STRUCTURAL AND GAS SENSING PROPERTIES OF TiO$_2$-BASED (Sn, Mg) NANO-STRUCTURES INDUCED BY MECHANICAL MILLING AND ANNEALING

AMOGELANG SYLVESTER BOLOKANG

A thesis submitted in fulfillment
of the requirements for the degree of

Doctor of Philosophy

in the

DEPARTMENT OF PHYSICS
UNIVERSITY OF THE WESTERN CAPE

Supervisors:
Dr. David E. Motaung, Council for Scientific and Industrial Research
Prof. Christopher J. Arendse, University of the Western Cape
Dr. Theophillus F.G. Muller, University of the Western Cape

OCTOBER 2015

KEYWORDS

"STRUCTURAL AND GAS SENSING PROPERTIES OF TiO$_2$-BASED (Sn, Mg) NANO-STRUCTURES INDUCED BY MECHANICAL MILLING AND NNEALING"

Mechanical milling

Sensing properties

Metal oxide

Titanium oxynitride

Metastable phases

Phase transformation

Face centered cubic

Crystal structure

Crystallinity

Annealing

ABSTRACT

"STRUCTURAL AND GAS SENSING PROPERTIES OF TiO$_2$-BASED (Sn, Mg) NANO-STRUCTURES INDUCED BY MECHANICAL MILLING AND NNEALING"

Titanium oxynitride has attracted research interest for the fact that it is a bioactive non-toxic material. It is suitable for surface coating of biomaterials and in other applications such as anti-reflective coatings, while oxygen-rich titanium oxynitride has been applied in thin film resistors and photocatalysis. Two common types of titanium oxynitrides are TiO$_x$N$_y$ and TiO$_{2-x}$N$_y$. In this work, titanium mixed metals oxynitrides (Ti-TiO$_2$, Mg-TiO$_2$ and Mg-Sn-TiO$_2$) were synthesized for the first time using ball milling (BM) and annealing processes. Their structural, morphological, surface, optical, and gas sensing properties were studied in detail. Structural analyses showed that upon milling a pure TiO$_2$ phase, tetragonal to orthorhombic phase transformation occurred. However, when milling TiO$_2$ mixed with Mg, Sn and Ti no evidence of the transformation was observed. Furthermore, scanning electron microscopy, transmission electron microscopy and atomic force microscopy showed that the milling process promotes particle refinement. The gas sensing analyses also demonstrated that the sensing response of the TiO$_2$, Mg-TiO$_2$ and Mg-Sn-TiO$_2$ materials improved upon milling.

Moreover, the Mg-TiO$_2$ showed improved sensing compared to pure TiO$_2$ due to incorporation of Mg, which might have resulted in a decrease of charge carrier

concentration. The Mg-TiO$_2$ sensing materials showed fast response-recovery time of ~32 s and ~48 s, respectively, as well as high selectivity to NH$_3$ gas compared to other gases (H$_2$, and CH$_4$). In addition, the improved response observed for the milled samples is due to increased surface area and pore diameter, providing more active sites for the target gas and allowing more gas adsorption with an increase in point defects related to oxygen vacancies (V$_O$), which are the most favorable adsorption sites for oxygen species and thus can enhance the possibility of interaction with gas molecules. A combination of photoluminescence, x-ray photoelectron spectroscopy, vibrating sample magnetometer and sensing analyses demonstrated that a direct relation exists between the magnetization, sensing and the relative occupancy of the V$_O$ present on the surface of TiO$_2$ nanoparticles.
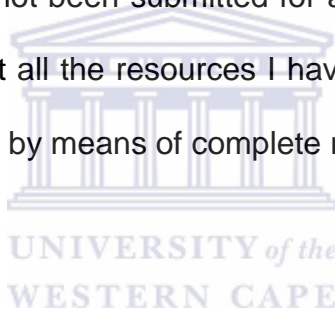
Therefore, based on these finding we conclude that the milling process promotes particle refinement, resulting in an increased BET surface and partial breaking of Ti–O bonds on the TiO$_2$ surface layer, which results in the formation of oxygen vacancies in the TiO$_2$ lattice, therefore anticipating improved sensing response.

DECLARATION

I declare that

"STRUCTURAL AND GAS SENSING PROPERTIES OF TiO$_2$-BASED (Sn, Mg) NANO-STRUCTURES INDUCED BY MECHANICAL MILLING AND ANNEALING"

is my own work, that it has not been submitted for any degree or examination in any other university and that all the resources I have used or quoted have been indicated and acknowledged by means of complete references.

UNIVERSITY *of the*
WESTERN CAPE

Signed: _____   OCTOBER 2015

Amogelang S. Bolokang

ACKNOWLEDGEMENTS

UNIVERSITY *of the*
WESTERN CAPE

Innovation is a true visionary leadership that improves the human life and
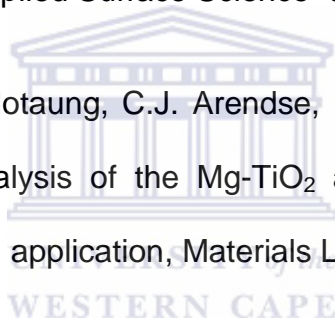
empowered by the Almighty

I dedicate this work to my wife (Oletlamang Mavis Bolokang), my daughters (Reamogetse Casey Bolokang and Tlotlego Daisy Bolokang), my son (Keaorata Sylvester Jnr. Bolokang), my mother (Basetsana Bolokang), my mother-in-law Kedisaletse Juliet Mocwiri and my uncle Magare Joseph Bolokang.

UNIVERSITY *of the*
WESTERN CAPE

LIST OF ARTICLES INCLUDED IN THIS THESIS

[1] A.S. Bolokang, D.E. Motaung, C.J. Arendse, T.F.G. Muller, "Formation of the metastable FCC phase by ball milling and annealing of titanium–stearic acid powder", Advanced Powder Technology, 26 (2) (2015) 632-639.

[2] A.S. Bolokang, D.E. Motaung, C.J. Arendse, T.F.G. Muller, Formation of face-centered cubic and tetragonal titanium oxynitride by low temperature annealing of ball milled titanium powder in air, Advanced Powder Technology 26 (2015) 169-174.

[3] A.S. Bolokang, D.E. Motaung, C.J. Arendse, T.F.G. Muller "Production of titanium-tin alloy powder by ball milling: Production of titanium-tin oxynitride composite powder produced by annealing in air, Journal of Alloys and Compounds 622 (2015) 824-830.

[4] A.S. Bolokang, D.E. Motaung, C.J. Arendse, T.F.G. Muller, "Morphology and structural development of reduced anatase-TiO_2 by pure Ti powder upon annealing and nitridation: Synthesis of TiO_x and TiO_xN_y powders, Materials Characterization 100 (2015) 41-49.

[5] A.S. Bolokang, D.E. Motaung, C.J. Arendse, T.F.G. Muller, "Structural transformation and surface properties of a new magnesium oxynitride upon annealing, Journal of Alloys and Compounds 646 (2015) 1143-1150.

[6]   A.S. Bolokang, F.R. Cummings, B.P. Dhonge, H.M.I. Abdallah, T. Moyo, H.C. Swart, C.J. Arendse, T.F.G. Muller, D.E. Motaung, "Characteristics of the mechanical milling on the room temperature ferromagnetism and sensing properties of TiO_2 nanoparticles, Applied Surface Science 331 (2015) 362-372.

[7]   A.S. Bolokang, B.P. Dhonge, H.C. Swart, C.J. Arendse, T.F.G. Muller, D.E. Motaung, Structural and optical characterization of mechanically milled Mg-TiO_2 and nitrided Mg-TiO_x-N_y nanostructures: Possible candidates for gas sensing application, Applied Surface Science 360 (2016) 1047-1058

[8]   A.S. Bolokang, D.E. Motaung, C.J. Arendse, S.T. Camagu, T.F.G. Muller, "Structure-property analysis of the Mg-TiO_2 and Mg-Sn-TiO_2 composites intended for biomedical application, Materials Letters 161 (2015) 328–331
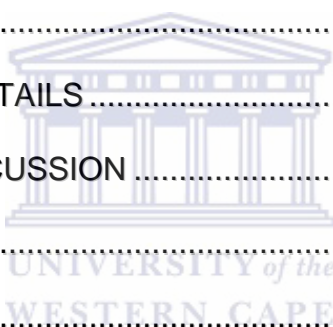
CONTENTS

CHAPTER ONE

BACKGROUND OF THE STUDY

1. GAS SENSING

MOTIVATION

The standard of living has improved quite remarkably because of the industrial revolution. Besides the benefits, the industrial revolution has introduced a negative aspect on human health due to emission of various gases and particles, which pollute the environment. Thus the development of gas sensors with high sensitivity, good selectivity, low-power consumption, and long-term stability to detect or monitor the leakage of poisonous (or flammable) gases that can be harmful to the environment and human health, has become more pressing. In 2009 an industrial market report in the United States of America (USA) reported that the demand for sensors increased with an annual average growth rate of 4.6% from 2004 **[1.1]**. The global gas sensors, detectors and analysers market 2013 reported that the market size for gas sensors was US$1,782.1 M in 2013; a market growth – Compound Annual Growth Rate of 5.1% is expected by 2020 **[1.2]**. Among all the materials, metal-oxide (MOX) semiconductors appear to be the most promising materials for gas sensing application, due to their good thermal stability and capability to operate at high temperatures and in harsh environments. Moreover, the structure and

morphology of metal oxides can be controlled to vary its electrical, chemical, optical and magnetic properties. So far, various MOX, such as tin oxide (SnO_2) [1.3-1.5], zinc oxide (ZnO) [1.6-1.10.], cerium oxide (CeO_2) [1.11], titanium dioxide (TiO_2) [1.12, 1.13], indium oxide (In_2O_3) [1.14], etc. have been used as gas sensing materials. However, among the above mentioned MOX, TiO_2 has been reported as the most promising material for gas sensing application, due to its novel properties such as stability, bio-compatibility, cost effectiveness and non-toxicity. It has a high corrosion resistance compared to other metal oxides and therefore has a longer life cycle. TiO_2 is known to display extraordinary changes in its electrical properties upon exposure to O_2, CO, NO_2 and other reactive gases. Generally, gas sensors based on MOX operate in air at temperatures between 100 and 400 °C, whereby the sensing porous surface layer are covered with adsorbates [1.15]. At these high temperatures the oxygen exchange reaction modifies the concentrations of electrically charged oxygen vacancies. The interaction of oxygen involves different reactions as follows:

$$O_{2\,(gas)} + V_{(ads)} \leftrightarrow O_{2\,(ads)} \tag{1.1}$$

$$O_{2\,(ads)} + e^- \leftrightarrow O^{2-}_{(ads)} \tag{1.2}$$

$$O_{2\,(ads)}^- + e^- \leftrightarrow O_2^{2-}{}_{(ads)} \tag{1.3}$$

$$O_2^{2-}{}_{(ads)} + V_{(ads)} \leftrightarrow 2O^-{}_{(ads)} \tag{1.4}$$

$$2O^-{}_{(ads)} + e^- \leftrightarrow O^-{}_{(ads)} + O^{2-}{}_{(ads)} \tag{1.5}$$

$$O^-{}_{(ads)} + O^{2-}{}_{(ads)} + e^- \leftrightarrow 2O^{2-}{}_{(ads)} \tag{1.6}$$

$$2O^{2-}{}_{(ads)} + V_O^{++}{}_{(ads)} \leftrightarrow O_o + O^{2-}{}_{(ads)} + V_{(ads)} \tag{1.7}$$

$$O^{2-}{}_{(ads)} + V_O^{++}{}_{(ads)} \leftrightarrow O_o + V_{(ads)} \tag{1.8}$$
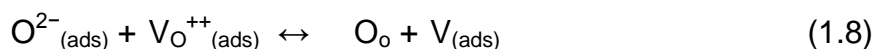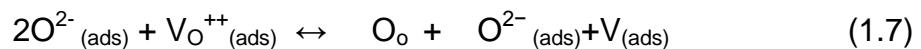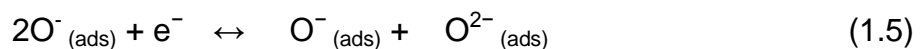
In the above reactions the adsorption site is denoted by (ads), vacant adsorption by ($V_{(ads)}$), and electron transferring from the sensor to the adsorbate and doubly ionized oxygen vacancy (V^{++}). The reactions between TiO_2 and O_2 are shown in Fig. 1.1
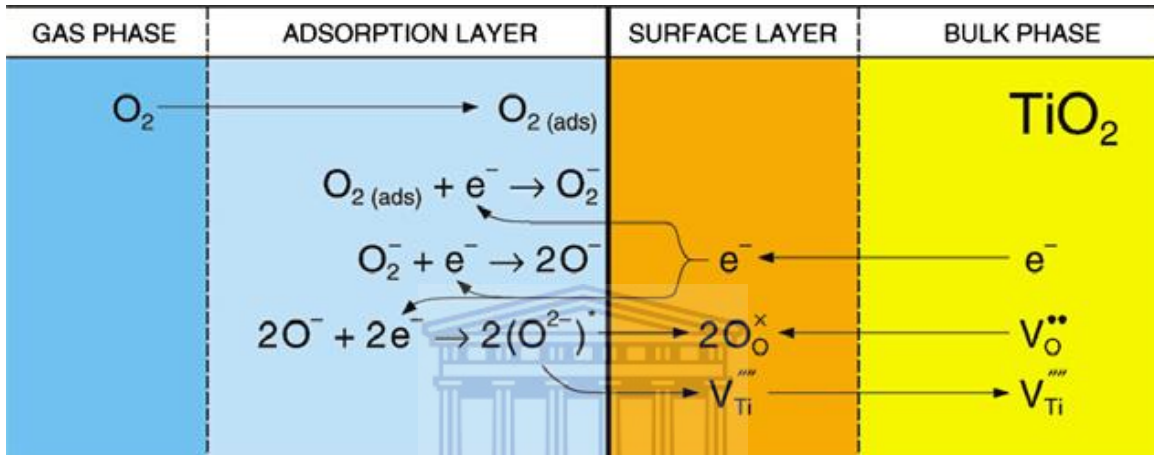
Fig. 1.1:   Plausible reactions occurring upon interaction of TiO_2 with oxygen from the surrounding gas phase **[1.16].**

It has been found that the sensor element based on Pd (1.0 wt.%) modified $Ni_{0.6}Zn_{0.4}Fe_2O_4$ exhibited an enhanced response to H_2S with excellent selectivity and can detect 10ppm H_2S, which is useful for practical applications **[1.17].** Previous studies have reported that the synthesized $Mg_{0.5}Zn_{0.5}Fe_2O_4$ nano-tubes possess promising gas sensing characteristics and response towards H_2, CO, and N_2O gases **[1.18]**. Currently, to the best of our knowledge, sensing properties based on Mg-doped TiO_2 has never been investigated. Furthermore, as compared to the conventional binary oxide based sensors, the gas sensing

characteristics of nanostructured Mg-TiO$_2$-N sensors are found to be limited in literature. The nanocrystalline size induced by mechanical milling (MM), the light weight of Mg-TiO$_2$, and the high surface-to-volume ratio of its nanostructures makes it a suitable candidate for improving capabilities to detect chemical and biological species. This is due to the material's strong oxidizing power, good chemical inertness, low cost, nontoxicity, large surface area, unique optical and sensing properties **[1.17].** Since gas sensing properties are usually affected by the morphology, grain sizes, and synthesis conditions a mechanical milling (MM) or ball milling (BM) treatment (discussed in detail below) has been selected for further structure refinement and size reduction of anatase TiO$_2$ powders (see detailed discussion) in this study. MM is an eminent solid-state powder process involving welding and fracturing of particles during high energy milling **[1.19]**. This technique has been shown to be proficient in synthesizing a variety of equilibrium and non-equilibrium phase (solid solution, metastable crystalline and quasi-crystalline phases, nanostructures and amorphous alloys), starting from blended elemental or pre-alloyed powders **[1.19]**. Furthermore, the use of MM or BM for gas sensing application has been limited to few cases so far **[1.20-1.22]**. Therefore, the present thesis focuses on the novel synthesis of the mixed metal oxynitrides and gas sensing performance of the mechanically milled TiO$_2$, Mg-TiO$_2$ based nanocrystalline powders. The sensing performace of these powders will be compared with the corresponding nitrided samples.

1.2. GAS SENSING PROPERTIES

1.2.1. Response

The sensor response (R) (see reactions 1.9 and 1.10) in percentage is defined as the ratio of the resistance change by introducing target gas in the air **[1.23]**. Generally, when the n-type semiconducting metal oxide material is exposed to a reducing target gas, the sensing resistance decreases (current increases), whereas when it is exposed to oxidizing gas, the resistance increases.

The ratio is given as:

$$R(\%) = \left(R_{air} \big/ R_{gas} \right) \times 100 \qquad \text{(for reducing gas)} \tag{1.9}$$

and

$$R(\%) = \left(R_{gas} \big/ R_{air} \right) \times 100 \qquad \text{(for oxidizing gas)} \tag{1.10}$$

where, R_{gas} and R_{air} are the resistance values of the sensor during gas exposure and ambient air, respectively. Fig. 1.2 shows the variation of resistance of the sensor versus time. As shown in Fig. 1.2, the sensing resistance increases rapidly when the target gas is introduced in the chamber and reaches its equilibrium. When the target gas is removed, the resistance decreased quickly to the baseline. This behaviour shows the high reproducibility of the sensor.
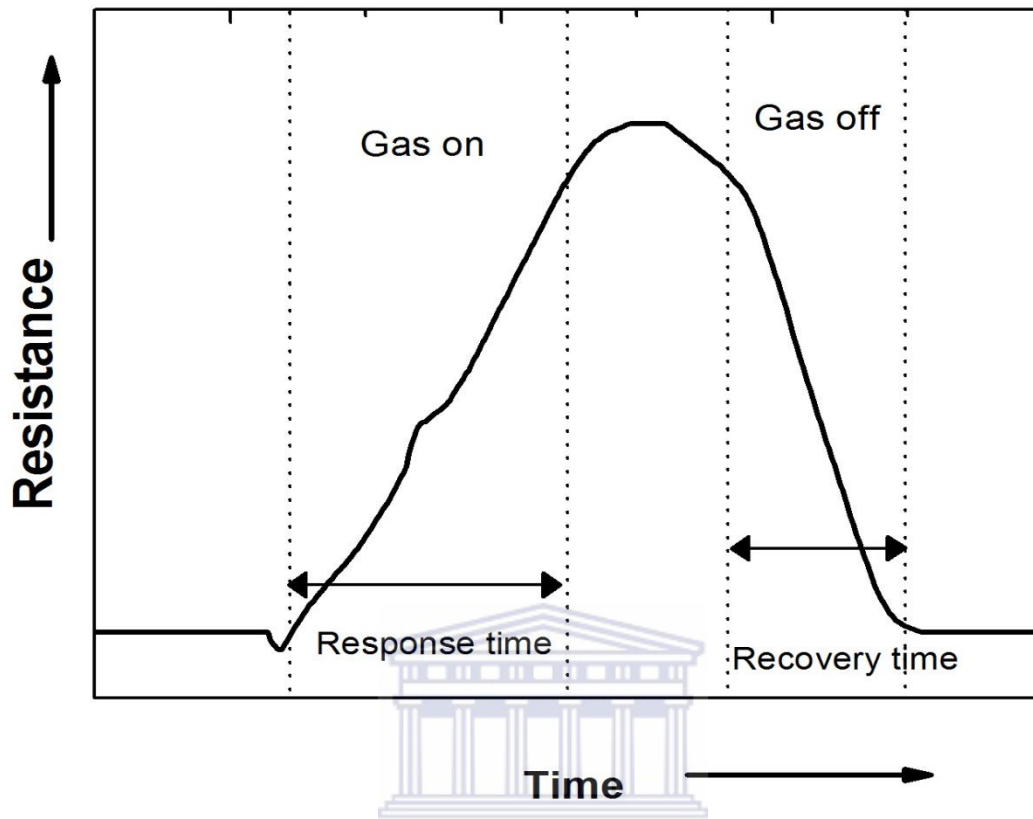
Fig. 1.2: A typical resistance curve of a gas sensing material **[1.23]**.

1.2.2. Response time and recovery time

The response time is defined as the time required for reaching 90% of the equilibrium value of the resistance after gas exposure, and the recovery time is defined as the time required for the resistance to return to 10% below the original resistance in air after the test gas is released (see Fig. 1.2).

1.2.3. Sensitivity

A change of measured signal per analyte concentration unit is called sensitivity. The change in electrical properties of the metal-oxide semiconductor

due to adsorption of gas molecules is mostly associated with the chemisorption of oxygen. Molecular oxygen adsorbs on the surface by trapping an electron from the conduction band of the semiconductor **[1.24]**.

1.2.4. Selectivity

The feature that determines if a sensor can respond selectively to a group of analytes or a single analyte is called selectivity. The metal-oxide gas sensors normally have challenges of high selectivity. The material is prepared to be sensitive to one compound and has low cross-sensitivity to other compounds that may be present in the working atmosphere. Normally it is challenging to attain a categorically selective metal oxide gas sensor. Most of the materials possess cross-sensitivity to humidity and other gases **[1.25].**
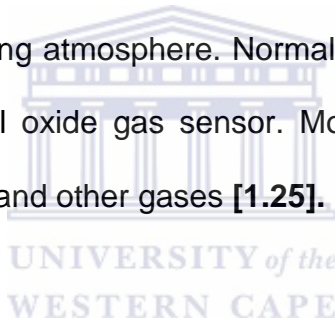
1.2.5. Stability

For practical application, the stability of response is of critical importance. Thus, the stability is the ability of a sensor to replicate results including the retention of the sensitivity, selectivity, response, and recovery time. The material-associated stability problem can lead to incorrect results such as false alarms. Little attention is paid in the literature to the problems of stability **[1.25, 1.26].** Generally, nanostructured oxides with small grains as well as nanotubes, nanorods etc. are subject to degradation because of their high reactivity. There is no unified approach to increasing the stability of metal-oxide gas sensors. It has

21

been reported that doping metal oxides with metal particles and synthesis of mixed oxides increase the stability of sensor elements **[1.26, 1.27]**.

1.2.6. Repeatability

It is important that commercialized sensor products show good cycle repeatability at ambient temperatures with reproducible data for a certain period of time **[1.28]**. For a polluted sensing environment, poor sensing performance will be experienced.

1.3.   MECHANICAL ALLOYING/MILLING PROCESS

Mechanical alloying (MA) was developed at the International Nickel Company in the late 1960's' by John Benjamin and his co-workers for production of oxide-dispersion-strengthened (ODS) alloys for high temperature structural applications **[1.29]**. However, an increase in interest in MA as a non-equilibrium processing method occurred after realizing that amorphous alloys could be made by MA. A variety of studies using the MA of dissimilar powders and mechanical milling (MM) has since increased reports of synthesized intermetallic compounds **[1.30]**, extended solid solution and carbides **[1.31-1.34],** metastable crystalline phases and nanocrystalline materials **[1.19].** MM involves microscopic deformation and welding of nano-sized powder particles during the ball-powder-ball collision. However, if a large exothermic heat reaction is involved, as for example with Ni+Al+NiAl, much higher local temperatures, perhaps even to the melting temperature, can be produced by milling **[1.30]**. It provides non-

equilibrium phases at low cost relative to some other fabrication techniques such as sputter deposition. Material production can take place at room temperature; however, if products with high strength are required there is still a need for thermal treatment to be applied. Novel structures are realized even after annealing and sintering of ball milled powders **[1.35, 1.36]**. In order to generate an understanding of the resultant crystal structures induced by MM/MA and annealing, it is appropriate to investigate pure metals phase transformation **[1.35, 1.36]**, for example, the FCC TiC powder synthesized by MA process. The question remains whether pure Ti does transform to FCC phase, or whether the interstitial elements drive the formation of TiC during MA. Therefore, thermal stability of ball-milled Ti is required.

1.4. TITANIUM

1.4.1. Hexagonal closed-packed to body-centered cubic (HCP→BCC) transformation

Pure Ti undergoes an allotropic HCP→BCC phase transformation above 883 °C. **Fig. 1.3a** shows the densely packed lattice planes and the lattice parameters at room temperature. The unit cell of the BCC phase is illustrated in **Fig. 1.3b**, exhibiting {110} lattice planes, and the lattice parameter at 900 °C.

(A) **(B)**
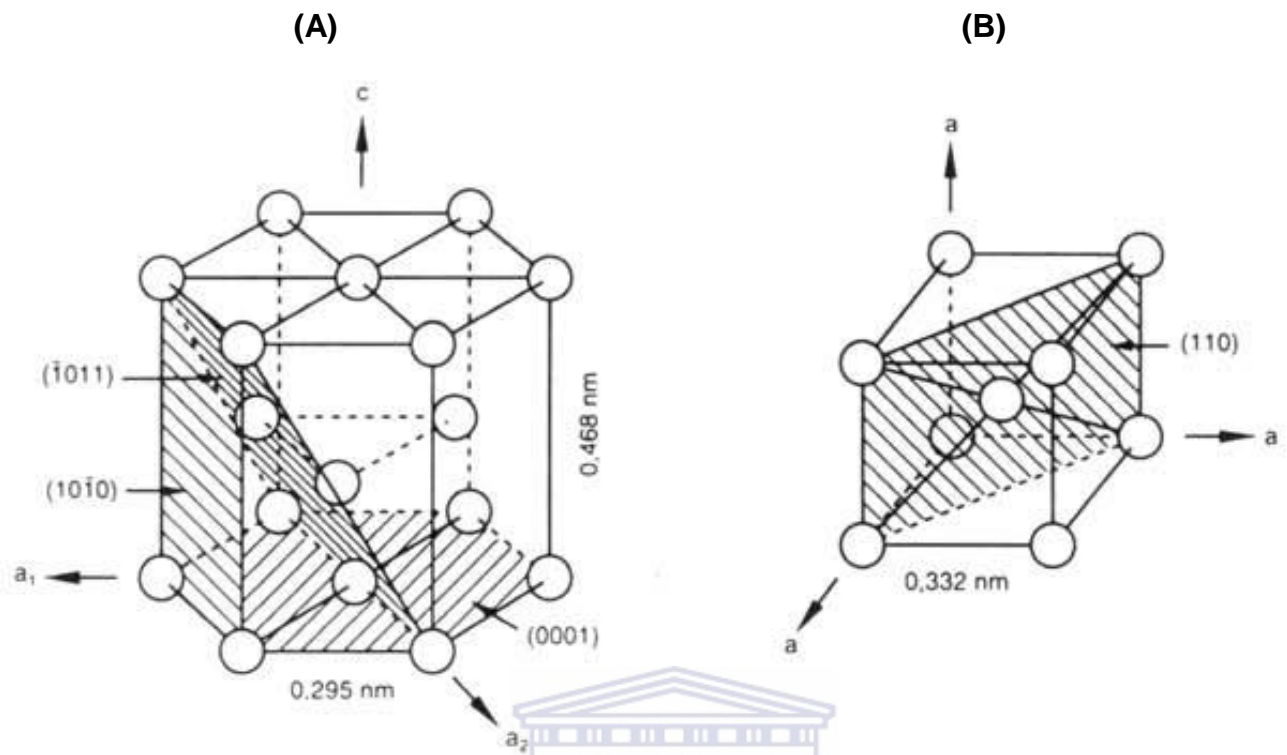
Fig. 1.3: The densely packed lattice planes and the lattice parameters of (A) HCP α-phase and (B) BCC β-phase Ti at room temperature **[1.37]**.

The HCP→BCC transformation temperature is influenced by the purity of Ti, hence interstitial and substitutional elements affect the transformation. Plastic deformation by grain refinement enhances strength as well as ductility, generating ultra-fine-grained (UFG) microstructure with excellent physical and mechanical properties in titanium and its alloys **[1.38, 1.39].** Commercially pure titanium (CP-Ti) has become widely used as a biomaterial for dental implants, orthopaedic implants, cardiovascular appliances, and implant-supported dental crowns because of outstanding high specific strength, high resistance to corrosion, greater biocompatibility, low modulus of elasticity, and high capacity to

be osseo-integrated with bone **[1.38]**. However, oxynitrides of Ti are potential materials for sensing and biomedical application. Titanium oxynitride is mainly obtained in FCC crystal structure.

1.4.2. Hexagonal closed-packed to face-centered cubic (HCP→FCC) transformation in Ti

Investigations have shown that polycrystalline Ti thin films gradually transform from FCC to HCP structure with increasing film thickness. The FCC phase is formed in a highly compressive HCP matrix, the magnitude of which decreases with increasing film thickness possible in the thickness range 144–720 nm, while HCP is stable at 720 nm **[1.40].** This theory implies that the FCC phase is stabilized easier in thin films, hence, during MM process, the shape and the size of the particles will be the driving force for the transformation in Ti. The FCC Ti phase induced by MM show lattice parameters in the range of 4.20-4.40 Å **[1.41, 1.42].** Manna et al. reported HCP (hexagonal-closed-packed) to FCC (face-centred-cubic) solid-state transformation in Ti governed by lattice expansion (negative hydrostatic pressure) as a result of grain refinement or nanocrystallization during milling **[1.41]**. The formation of FCC TiO_xN_y is driven by the ability of pure Ti transformation to FCC structure.

1.5. ANATASE-TIO$_2$

Titanium dioxide (TiO_2) is a strategic mineral for the South African economy due to abundant reserves. The oxidation of Ti yields TiO_2 with a tetragonal rutile

crystal structure. The driving force for the oxidation of Ti is its strong chemical affinity with oxygen (O) when compared with interstitial nitrogen (N). Anatase has a tetragonal lattice (*P42/mnm*) with four TiO_2 units per unit cell forming chains of slightly elongated TiO_6 octahedra as shown in **Fig. 1.4**. The Ti−O bonding is largely ionic with some covalent contribution **[1.43]**.
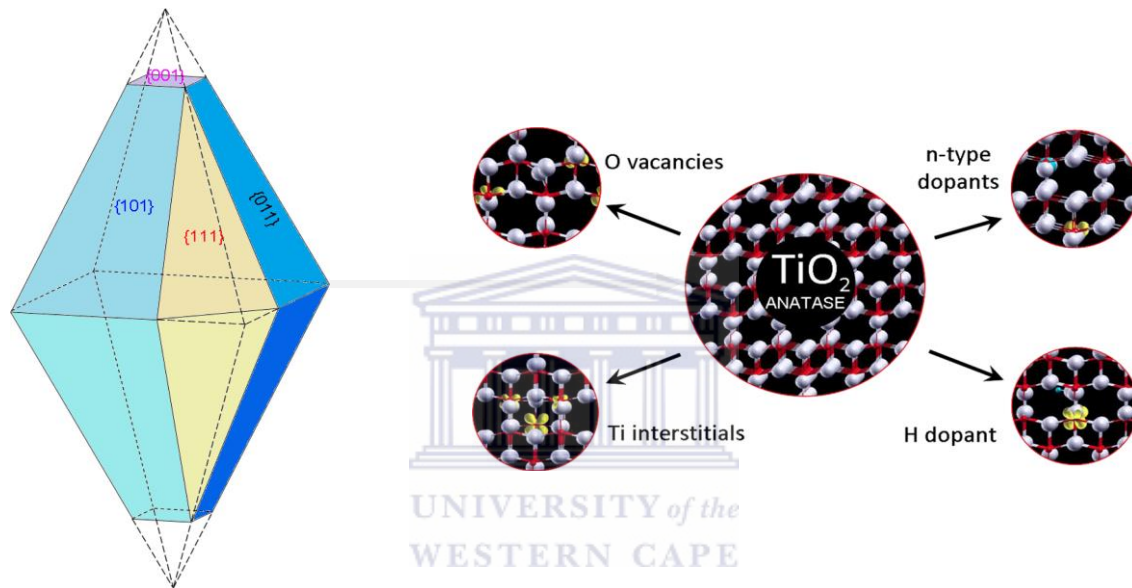
Fig. 1.4: Crystal structure, ball and stick representation of pure and stoichiometric anatase TiO_2 bulk structure **[1.43].**

TiO_2 is a reducible semiconducting oxide yielding electrical conductivity and colour change. The removal of a neutral oxygen atom from stoichiometric bulk anatase by thermal annealing treatment leaves two excess electrons in the lattice which becomes reduced partially while forming Ti^{3+} species **[1.43]**. The current thesis is aiming to exploit these characteristics of anatase TiO_2 with innovative synthesis of titanium oxynitride materials with unique applications. Extensive

milling will be used to create oxygen vacancies to be occupied by nitrogen atoms. For example, the un-doped thin films of anatase were found to possess room temperature ferromagnetism related to the presence of oxygen vacancies **[1.43].** It thus implies that ferromagnetism might be induced in anatase by high-energy ball milling. Although milling of TiO_2 with induced phase tarsnformation has been reported, TiO_xN_y was never synthesized from the technique used in the current study.

1.6. BALL MILLING OF ANATASE-TIO$_2$

BM induces phase transformations, chemical reactions and changes in the reactivity of solids. The Rutile-TiO_2 is formed during room-temperature milling of anatase TiO_2 **[1.44].** At the early stage of BM, anatase TiO_2 phase transformed to high-pressure srilankite phase due to high impact energy and highly broadened reflections of srilankite phase **[1.45, 1.46].** The transformations from anatase to srilankite and rutile were also induced at room temperature and ambient pressure when the nanocrystalline TiO_2 powders were milled in oxygen, air and nitrogen atmospheres, respectively **[1.47]**. An increase in oxygen vacancies can accelerate the milling-induced transformation of anatase in TiO_2. The Ti–O bonds on the TiO_2 surface layer are broken during mechanical activation, resulting in the release of oxygen from the TiO_2 lattice. As a result, oxygen vacancies are generated in the TiO_2 lattice **[1.48].**

1.7. NITROGEN-DOPED TIO$_2$ (TITANIUM OXYNITRIDE)

Due to partial breaking of Ti–O bonds on the TiO$_2$ surface layer by milling to release oxygen from the TiO$_2$ lattice (TiO$_{2-x}$), there is an opportunity to fill vacancies with nitrogen for the synthesis of titanium oxynitride (TiON). Two common types of titanium oxynitrides are TiO$_x$N$_y$ and TiO$_{2-x}$N$_y$. The nitrogen-doped photocatalyst TiO$_{2-x}$N$_y$ can be prepared during BM of TiO$_2$ in a NH$_3$ and H$_2$O solution **[1.49]**. When compared with TiO$_2$, the photoabsorption of nitrogen-doped TiO$_{2-x}$N$_x$ photocatalyst increases. However, the crystal phase composition of TiO$_{2-x}$N$_x$ remains the same, as TiO$_2$ without BM but the diffraction intensity of the TiO$_{2-x}$N$_x$ is comparatively weaker than that of TiO$_2$ **[1.49]**. Upon BM for 120 h, the amount of doped nitrogen reached 0.26 wt.% in the TiO$_{2-x}$N$_x$ **[1.49].** Nitrogen doped TiO$_2$ thin films were deposited by RF magnetron sputtering onto various substrates. The resulting TiO$_x$N$_y$ layers are influenced by the surface morphology, roughness, surface energy and phase content **[1.49]**. The aim of BM in the current work is to create oxygen vacancies in TiO$_2$, which can yield the TiO$_x$ monoxide structure which is believed to promote the TiO$_x$N$_y$ phase when nitrided. Due to the capability of MA to produce oxide-dispersion-strengthened (ODS) alloys, TiO$_x$ phase can be synthesized between TiO$_2$ and pure Ti. During milling, a layer of nanocrystalline TiO$_2$ will form a coating on a Ti particle. During annealing the exchange of oxygen atoms from TiO$_2$ to Ti will result in TiO$_x$ with oxygen vacancies. In the presence of nitrogen activated at elevated temperature, formation of TiO$_x$N$_y$ will be realized. Dissolution of N will be promoted by annealing the ball milled TiO$_2$ nanocrystalline powder. The material will be more

stable when compared to those synthesized by milling TiO_2 under a nitrogen source.

The interaction between the TiO_x metal surface and cell/tissue is important for the biocompatibility of metallic implants, and surface modification has been studied extensively to alter its surface characteristics, and improve biocompatibility. Titanium oxide (TiO_x) films were deposited by electron-beam evaporation system using TiO_2 as a source material [1.51]. Using air as a reactive gas in sputtering at different air/Ar ratios yields films with various colours [1.52]. The films turned from golden and dark golden colours in the air/Ar ratio range of 0.10–0.20 to diverse colours including purple, dark blue, cyan, etc. at higher air/Ar ratios [1.52]. Synthesis of TiO_xN_y has been investigated with different processing methods; one such is laser pyrolysis. The synthesis of FCC titanium oxide or oxynitride nanoparticles yields properties that are highly dependent on their structures [1.53]. Additionally, titanium oxynitride can be synthesized by reacting TiN and TiO [1.54]. Titanium oxynitrides exhibit the combination of properties of metallic oxides such as colour, optical properties and nitrides like hardness, and wear resistance [1.55]. In this work a novel reduction of TiO_2 with pure Ti will be synthesized to form TiO_x with oxygen vacancies, which upon nitridation yield TiO_xN_y powder.

1.8. MIXED METAL OXYNITRIDES

AlN and Al_2O_3 were used as starting powders and either MgO or $MgAl_2O_4$ was added as a source of magnesium to produce MgAlON refractories, while in the case of magnesia-based samples stoichiometric spinel formed instead of MgAlON but **[1.56]**. Indium tin oxide (ITO) with films stable up to a temperature of 550 °C is an n-type degenerate semiconductor with unique properties, such as high electrical conductivity, very high optical transmittance, high infrared reflectance, excellent hardness and chemical inertness. It is used for display devices, solar cells and many other optical applications **[1.57]**. Formation of $(Mg-Ti)O_xN_y$ was never reported in literature. In this study, for the first time TiO_2 will be milled with Mg and annealed in nitrogen to form $(Mg-Ti)O_xN_y$. Pure Mg will reduce O from TiO_2 and create vacancies that will be occupied by N atoms to form a new oxynitride powder.

1.9   AIMS AND OUTLINES

1.9.1. Background

The use of bio-active and/or sensing materials in the fabrication of low cost devices and products, pegs TiO_2 as a most favourable material for gas sensing application. Despite the numerous reports on ball milled and phase transformation of Ti powder, formation of titanium oxynitride synthesized from mixed metal oxide by ball milling and annealing is still limited. An extensive body of work was reported on the formation of titanium oxynitride prepared by
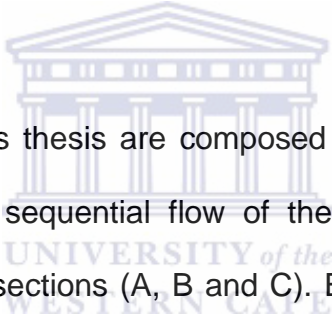
sputtering, but limited in the area of powder metallurgical synthesis. It is shown that mixed metal oxynitride formation synthesyzed with TiO_2 and the addition of reducing metals (pure Ti and Mg) is feasible while their sensing properties are reported for the first time. Therefore, the aim of this thesis is to study the structural, optical, surface morphology and gas sensing properties of the mechanically milled and annealed titanium mixed metals oxynitrides (Ti-TiO_2, Mg-TiO_2 and Mg-Sn-TiO_2) by nitridation. These mixed metal oxides were prepared by ball milling and annealing with Mg and Ti used as reducing metals to create oxygen vacancies.

1.9.2.   Structure of the thesis

This chapter provided the necessary background and physical theory involved in mechanical milling/alloying for the synthesis of nanocrystalline powders. The systematic characterization of Ti, Mg and TiO_2 was stadied in detail for structural transformation prior to synthesis of mixed metal oxides and oxynitrides. The theory explaining the synthesis of titanium oxynitride is discussed. The literature of gas sensing properties of oxide as well as mixed metal oxide powders addressing the gaps that the current study tries to fill is presented. The limitations and gaps deduced from the literature are:

- Lack of detailed thermal stability of ball-milled Ti and the formation of oxynitride formation in air.

- Formation of titanium oxynitride by reduction of TiO_2 by Ti to induce defects followed by nitridation of TiO_x thereof promoting the formation of titanium oxynitride powders.

- The use of Ti and Mg as reducing metal to TiO_2 prior to the formation of the mixed metal oxynitrides was never reported elsewhere.

- Sensing properties of ball-milled TiO_2, Mg-TiO_2 and Mg-Sn-TiO_2 powder and their oxynitrides.

- Novel synthesis of the Ti-Sn oxynitrides is presented for the first time.

Since the results of this thesis are composed of a total of eight published chapters, and to enable a sequential flow of the experiments, this thesis is hereafter divided into three sections (A, B and C). Each section is comprised of individual chapters, which are consistent with the general theme of the section. At the end of the section, a summary of provided. Finally, each section is concluded with a Summary. The references for different sections might appear similar due to the fact that the work has already been published and the chapters follow published paper style.

Section A

In Section A, chapter two and three presents only the formation feasibility of titanium oxynitride synthesized from pure Ti powder by milling and annealing in air and nitrogen, respectively.

Chapter four is the last chapter of Section A and it presents the formation of titanium oxynitride phases when Ti-Sn alloys powder produced by milling is nitrided. Therefore, this chapter addresses the formation of oxynitrides after ball milling and nitridation.

Section B

Due to successful formation of titanium oxynitrides from pure Ti and Ti-Sn alloys in Section A, investigations were done on anatase-TiO_2 powder.

Chapter five presents ball milling of TiO_2 followed by annealing. Characterization for optical, thermal, structural, morphology and humidity sensing properties were done. Chapter six entails milling and nitridation of Ti-TiO_2. Pure Ti was added to reduce oxygen from TiO_2 to create oxygen vacancies to promote a successful nitridation. The mechanism involves generation of defects caused by milling and Ti displacing oxygen atoms from their interstitial positions. The investigation presents microstructural and structural development of nonstoichiometric titanium oxides induced during the reduction of anatase by pure Ti and the resultant formation of TiO_xN_y powders upon nitridation.

Section C

Section C comprises of the last three chapters. Chapter seven focuses on the structural transformation and surface properties of magnesium upon annealing under nitrogen and nitrogen/oxygen gas mixture before doping in TiO_2 since it was established that formation of titanium oxynitrides are feasible. The

formation of magnesium oxynitride is a new contribution in literature; hence reported for the first time in this thesis. Chapter eight demonstrates the effect of added Mg-TiO$_2$ after milling and nitridation. This novel preparation process, reports the development of a new nanostructured ball milled Mg-TiO$_2$ powder material by nitridation. The surface morphology, structural and optical properties are studied in detail while the gas sensing responses of Mg-TiO$_2$ and Mg-TiO$_2$-N materials to hydrogen, ammonia, humidity and methane were examined. Lastly, Chapter nine details the effect of both Mg and Sn on Mg-TiO$_2$ on milling and the resultant properties after nitridation and their gas sensing properties.

UNIVERSITY of the
WESTERN CAPE

1.6. REFERENCES

[1.1] G. Kiriakidis, K. Moschovis, I. Kortidis, V. Binas, Vacuum, 86 (2012) 495-506.

[1.2] L. I. Trakhtenberg, G. N. Gerasimov, V. F. Gromov, T. V. Belysheva, O.J. Ilegbusi, Journal of Materials Science Research, 2012 (1) 56-68.

[1.3] D. Liu, T. Liu, H. Zhang, C. Lv, W. Zeng, J. Zhang, Materials Science in Semiconductor Processing 15 (2012) 438–444.

[1.4] B. Mondala, B. Basumataria, J. Dasb, C. Roychaudhuryc, H. Sahad, N. Mukherjee, Sensors and Actuators B 194 (2014) 389–396.

[1.5] F. Wei, H. Zhang, M. Nguyen, M. Ying, R. Gao, Z. Jiao, Sensors and Actuators B 215 (2015) 15–23.

[1.6] D.E. Motaung, P.R. Makgwane, S.S. Ray, Materials Letters 139 (2015) 475–479.

[1.7] Z. Liu, T. Fan, D. Zhang, X. Gong, J. Xu, Sensors and Actuators B 136 (2009) 499–509.

[1.8] D.E. Motaung, G.H. Mhlongo, I. Kortidis, S.S. Nkosi, G.F. Malgas, B.W. Mwakikunga, S.Sinha Ray, G. Kiriakidis, Applied Surface Science 279 (2013) 142– 149.

[1.9] G.H. Mhlongo, D.E. Motaung, I. Kortidis, N.R. Mathe, O.M. Ntwaeaborwa, H.C. Swart, B.W. Mwakikunga, S.S. Ray, G. Kiriakidisd, Materials Chemistry and Physics 162 (2015) 628e639

[1.10] W. Kim, M. Choi, K. Yong, Sensors and Actuators B 209 (2015) 989–996.

[1.11] W. Xie, B. Liu, S. Xiao, H. Li, Y. Wang, D. Cai, D. Wang, L. Wang, Y. Liu, Q. Li, T. Wang, Sensors and Actuators B 215 (2015) 125–132.

[1.12] B. Lyson-Sypien, M. Radecka, M. Rekas, K. Swierczek, K. Michalow-Mauke, T. Graule, K. Zakrzewska, Sensors and Actuators B 211 (2015) 67–76.

[1.13] Z.P. Tshabalala, D.E. Motaung, G.H. Mhlongo, O.M. Ntwaeaborwa, Sensors and Actuators B: Chemical 224 (2016) 841–856.

[1.14] C. Zhao, B. Huang, E. Xie, J. Zhou, Z. Zhang, Sensors and Actuators B 207 (2015) 313–320.

[1.15] Il-Doo Kim, A. Rothschild, H. L. Tuller, Acta Materialia 61 (2013) 974–1000.

[1.16] V.D. Kapse, S.A. Ghosh, F.C. Raghuwanshi, S.D. Kapse, Materials Chemistry and Physics 113 (2009) 638–644.

[1.17] J.M. Ducéré, A. Hemeryck, A.E.M.D. Rouhani, G. Landa, P. M'enini, C. Tropis, Journal of Computitional Chemistry 2011:247.

[1.18] K. Mukherjee, S.B. Majumder, Sensors and Actuators B 177 (2013) 55–63.

[1.19] C. Suryanarayana, Progress in Materials Science 46 (2001) 1–184.

[1.20] O.K. Tan, W. Cao, Y. Hu, W. Zhu, Solid State Ionics 172 (2004) 309–316.

[1.21] W. Cao, O.K. Tan, W. Zhu, B. Jiang, C.V. Gopal Reddy, Sensors and Actuators B 97 (2001) 1–6.

[1.22] Y. Hu, O.K. Tan, W. Cao, W. Zhu, Ceramic International 30 (2004) 1819–1822.

[1.23] D. Kohl, Sensors and Actuators **18**(1) (1989) 71-113.

[1.24] Y. Zhang, J. Liu Y. Zhang ; X. Tang, Optical Engineering **41** (3) (2002) 615-625.

[1.25] A.M. Soleimanpour, Y. Hou, A.H. Jayatissa, Applied Surface Science 257 (12) (2011) 5398-5402.

[1.26] M. Iwamoto, "Chemical Sensor Technology" (S. Yamauchi, Ed.), Vol. 4, p. 63. Kodansha, Tokyo, 1992.

[1.27] V. E Bochenkov, G. B Sergee, Sensitivity, Selectivity, and Stability of Gas-Sensitive Metal-Oxide Nanostructures, Chapter 2, Laboratory of Low Temperature Chemistry, Department of Chemistry.

[1.28] J. Riegel, H. Neumann, H.M. Wiedenmann, Solid State Ionics, 152–153 (2002) 783-800.

[1.29] J.S. Benjamin, R.D. Schelleng, Metallurg Trans. A 12A (1981) 1827.

[1.30] C.C. Koch, J.D. Whittenberger, Review, intemetallics 4 (1996) 339-355.

[1.31] Q. Yuan, Y. Zheng, H. Yu, International Journal of Refractory Metals and Hard Materilas 27 (2009) 696–700.

[1.32] A.S. Bolokang, M.J. Phasha, C. Oliphant, D. Motaung, Interanational Journal of Refractory Metals and Hard Materials 29 (2011) 108–111.

[1.33] S. Bolokang, C. Banganayi, M J. Phasha, Interanational Journal of Refractory Metals and Hard Materials 28 (2010) 211–216.

[1.34] A.S. Bolokang, Journal of Alloys and Compounds. 477 (2009) 905–908.

[1.35] A.S. Bolokang, M.J. Phasha, S. Bhero, Interanational Journal of Refractory Metals and Hard Materials 36 (2013) 111–115.

[1.36] A.S. Bolokang, Phasha MJ, Motaung DE, Bhero S, Journal of Metallurgy 2012, Article ID 290873, 1-7 doi:10.1155/2012/290873.

[1.37] S. E. Schoenfeld, Bimal Kad, International Journal of Plasticity 18 (2002) 461‑486

[1.38] R.R   Boyer, Advanced Performance Materials 2 (1995) 349-368.

[1.39] H. Tanaka, T. Yamada, E. Sato, I. Jimbo, Scripta Materialia. 54 (2006) 121-124.

[1.40] J. Chakraborty, K. Kumar, R. Ranjan, S. G. Chowdhury, S.R. Singh, Acta Materialia 59 (2011) 2615–2623

[1.41] I. Manna, P.P. Chattopadhyay, P. Nandi, F. Banhart, H.-J. Fecht, Journal of Applied Physics 93 (2003) 1520-1524.

[1.42] P. Chatterjee, S.P. Sen Gupta, Applied Surface Science 182 (2001) 372-376.

[1.43] De Angelis F, Di Valentin C, Fantacci S, Vittadini A, Selloni A, Chemical Reviews 114 (2014) 9708−9753.

[1.44] S. Begin-Colin, T. Girot, NanoStructructured Materials 12 (1999) 195-198.

[1.45] H. Dutta a, P. Sahu b, S.K. Pradhan a, M. De, Mater. Chemical Physics 77 (2002) 153–164.

[1.46] J. Hu, H. Qin, Z. Sui, H. Lu, Materials Letters 53 (2002) 421– 424.

[1.47] X. Pan, X. Ma, Journal of Solid State Chemistry 177 (2004) 4098–4103.

[1.48] X. Pan, X. Ma, Materials Letters 58 (2004) 513– 515.

[1.49] C. Shifu, C. Lei, G. Shen, C. Gengyu, Chemical Physics Letters 413 (2005) 404–409.

[1.50] K.G. Grigorov, I.C. Oliveira, H.S. Maciel, M. Massi, M.S. Oliveira, Jr., J. Amorim, C.A. Cunha, Surface Science 605 (2011) 775–782.

[1.51] Z. Lin, G.-H. Lee, C-M Liu, In-Seop Lee, Surface & Coatings Technology 205 (2010) S391–S397.

[1.52] M-H Chan, F-H Lu, Surface & Coatings Technology 210 (2012) 135–141.

[1.53] P. Simon, K. March, O. Stéphan, Y. Leconte, C. Reynaud, N. Herlin-Boime, A-M Flank. Chemical Physics 418 (2013) 47–56.

[1.54] H. Kiyono, T. Tsumura, T. Kiyo, M. Toyoda, S. Shimada, Ceramics International 37 (2011) 1813–1817.

[1.55] S. K. Rawal, A. K. Chawla, V. Chawla, R. Jayaganthan, R. Chandra, Applied Surface Science 256 (2010) 4129–4135.

[1.56] S. Pichlbauer, H. Harmuth, Z. Lencés, P. Sajgalík, Journal of European Ceramic Society 32 (2012) 2013–2018.

[1.57] M. Koufaki, M. Sifakis, E. Iliopoulos, N. Pelekanos, M. Modreanu, V. Cimalla, G. Ecke, E. Aperathitis, Applied Surface Science 253 (2006) 405–408.

SECTION A

CHAPTER TWO

Formation of metastable FCC phase by ball milling and annealing of titanium-stearic acid powder

ABSTRACT

Ball milling of titanium and stearic acid (SA) mixed together yields the hexagonal closed-packed (HCP) crystal structure. Upon thermal analysis, the known α→β phase transformation in pure Ti was disturbed. This implies that BM eliminates the crystal ordering in Ti powder. SA introduced the carbon to form Ti (C) solid solution. The Raman peaks suggest shiftining despite the crystal structure remaining HCP after milling.

2.1 INTRODUCTION

Due to their low density, high strength-to-weight ratio and good corrosion resistance; titanium (Ti) and its alloys are currently demanded in many structural applications; such as in aerospace, automotive and medical industries. There is a serious challenge in the processing of pure Ti due to its affinity for interstitial elements such as oxygen (O), nitrogen (N), carbon (C) and hydrogen (H). On the other hand, attempts to increase the strength of pure Ti without compromising elongation are achievable **[2.1]**. The use of oxygen to re-enforce Ti yields a high strength Ti composite. This nonferrous grey metal has a hexagonal closed packed (HCP) crystal structure at room temperature and undergoes a transition to body-centred cubic (BCC) above 883 ºC. Literature shows that metastable face- centred cubic (FCC) is an intermediate Ti phase that emerges due to ball milling (BM) and deformation of the powder. The reported lattice parameters of FCC Ti by BM **[2.2-2.4]** and other processes **[2.5-2.7]** are found in the range of 4.24 to 4.40 Å. So far, it is only Vullum et al. **[2.8]** investigation that resulted in the smallest lattice parameter of 4.10 Å for FCC Ti, which is attributable to small amount of H. In relation to these findings, the lattice parameter of 4.11 Å is regarded ideal by first-principle calculations and predictions **[2.4, 2.9, 2.10]**. Despite materials-embrittlement by hydrogen, studies show that the FCC Ti hydride has a low elastic modulus which is a positive property for biomedical implants **[2.11]**. At a nano-scale level Ti properties improve considerably, hence the application options also widen. BM of Ti does not only reduce the grain size but also induces phase transformation **[2.3]**. Up to this date, there are several

41

reports published on the solid-state transformation achieved by high-energy ball milling (HEBM) on elemental metals [2.3, 2.4]. Manna et al. [2.3] reported the metastable FCC solid-state transformation in Ti governed by lattice expansion (negative hydrostatic pressure) as a result of grain refinement during milling. However, there is an unclear underlying relationship between the metastable FCC phase and the microstructural development of Ti emerging from various processing techniques especially when SA is added. The FCC phase was earlier obtained by BM of Ti and an n-Heptane mixture whereby C and H decomposition influences the stabilization of the metastable phase that originates by milling-induced stacking faults [2.12]. These findings were based on differential scanning calorimetry (DSC) and x-ray diffraction (XRD) studies. Recently, high hardness values were attained in pure Ti due to Ti (C) reinforcement after MM and hot pressing [2.13]. The hardness of 800 Hv, far less than that of a stable TiC phase (2700 Hv) was reported [2.14]. The source of the interstitial could be the process control agents such as SA. SA is a low cost 18-carbon chain saturated fatty acid used in many industrial sectors to create protective coatings [2.15]. It is biocompatible and ideal for the pharmaceutical industry for coatings of controlled drug delivery [2.16]. SA is a possible carbon source for Ti [2.12] and can be detrimental or beneficial depending on the amount used [2.17]. The current work investigates the thermal stability of milled Ti and effect of SA. It aims to study preparation of pure Ti by BM prior to the synthesis of TiO_xN_y powder.

42

2.2   EXPERIMENTAL WORK

Titanium (Ti) powder of 99.5% purity with a particle size of 40 μm was used. It should be pointed out that the Ti powder was milled alone without SA and after milling the particle size of Ti reduced to about 32 μm. Previous studies indicated that BM treatment results in further structure refinement and size reduction of powder materials. BM is a solid-state powder process involving welding and fracturing of particles in a high energy milling process **[2.18]**. Stearic acid (SA) ($C_{18}H_{36}O_2$) with a purity of ~99% was mixed in 5 weight percentage (wt. %) with Ti to make a charge for milling. BM was performed for 15 hours (h) in a milling jar, under argon atmosphere at the speed of 800 rpm and ball-to-powder (BPR) ratio of 20:1. The unmilled and 15 h ball milled powders have undergone cold pressing (CP) at a pressure of 20 MPa into cylindrical compacts/discs of 17 mm in diameter and 3 mm thickness. **Fig. 2.1** illustrates the BM and CP processes.
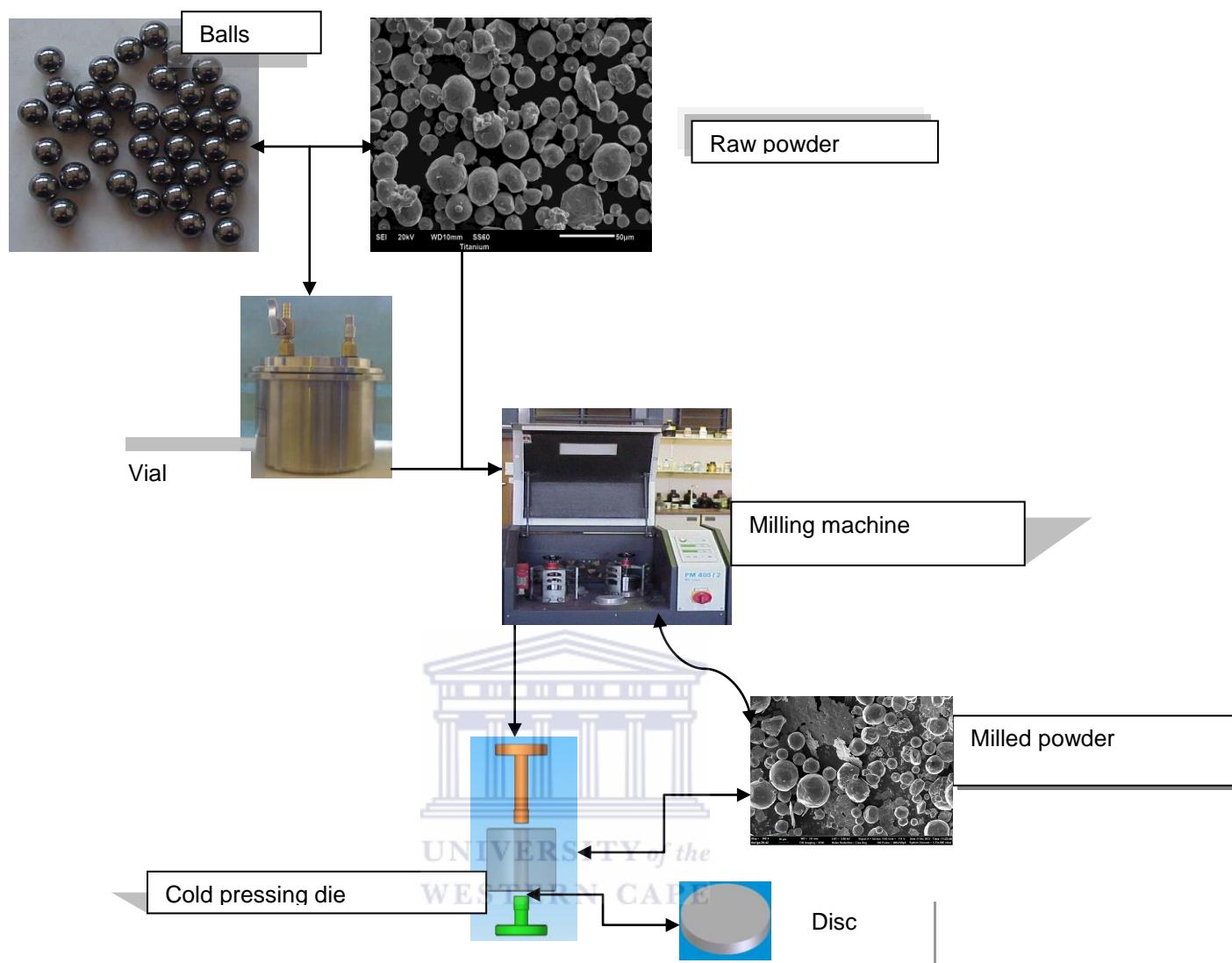
Fig. 2.1: The ball milling and cold pressing processes of Ti powder.

Thermal analysis of unmilled and 15 h milled Ti powders was carried out using DSC and TG incorporated in NETZSCH STA heated up to 1200 °C and cooled to room temperature using Al_2O_3 as a baseline. The thermal analyses were conducted at a heating rate of 20 °C min^{-1} and under an argon flow rate of 20 ml/min.

Phase evolution was traced with a PANalytical X' pert PRO PW3040/60 x-ray diffractometer with a Cu K_α (λ= 0.154 nm) monochromated radiation source, and 0.02 step size scanned from 20 to 90 ° (2θ). The XRD peak broadening was calculated from the full width at half maximum (FWHM) of the most intense Bragg peak. It should be noted that pure tungsten was used as a standard. To calculate the crystallites size, the Scherrer formula was used **[2.19]**:

$$L_{hkl} = \frac{0.9\lambda}{B_{2\theta}\cos(\theta)} \qquad (2.1)$$

where λ is the wavelength of the x-rays, $B_{2\theta}$ is the full width at half maximum intensity (FWHM) and θ is the diffraction angle. Powder morphology was analysed by LEO 1525 field-emission scanning electron microscope (FE-SEM) coupled with a Robinson Backscatter Electron Detector (RBSD) and an Oxford Link Pentafet energy dispersive x-ray spectroscopy (EDS) detector. Raman measurements were obtained using a Horiba Jobin-Yvon HR800 Raman microscope equipped with an Olympus BX-41 microscope attachment. An Ar + laser (514.5 nm) with energy setting 1.2 mW from a Coherent Innova Model 308 was utilized as an excitation source.

2.3. RESULTS AND DISCUSSIONS

2.3.1. Powder Characterization

SEM morphology of the unmilled and 15 h milled titanium-stearic acid (Ti-SA) powders are presented in **Fig. 2.2a and b**, respectively. As shown in **Fig. 2.2a,** the unmilled atomized Ti powder particles have a spherical shape. Due to the high energy impact resulting from ball-to-powder collisions, some spherical particles are flattened to thin flakes type **(Fig. 2.2b)**. These thin flakes are highly reactive to interstitial elements on thermal application. No welding of powders particles were experienced on milled with SA as it was the scenario with milled Ti powder without SA.
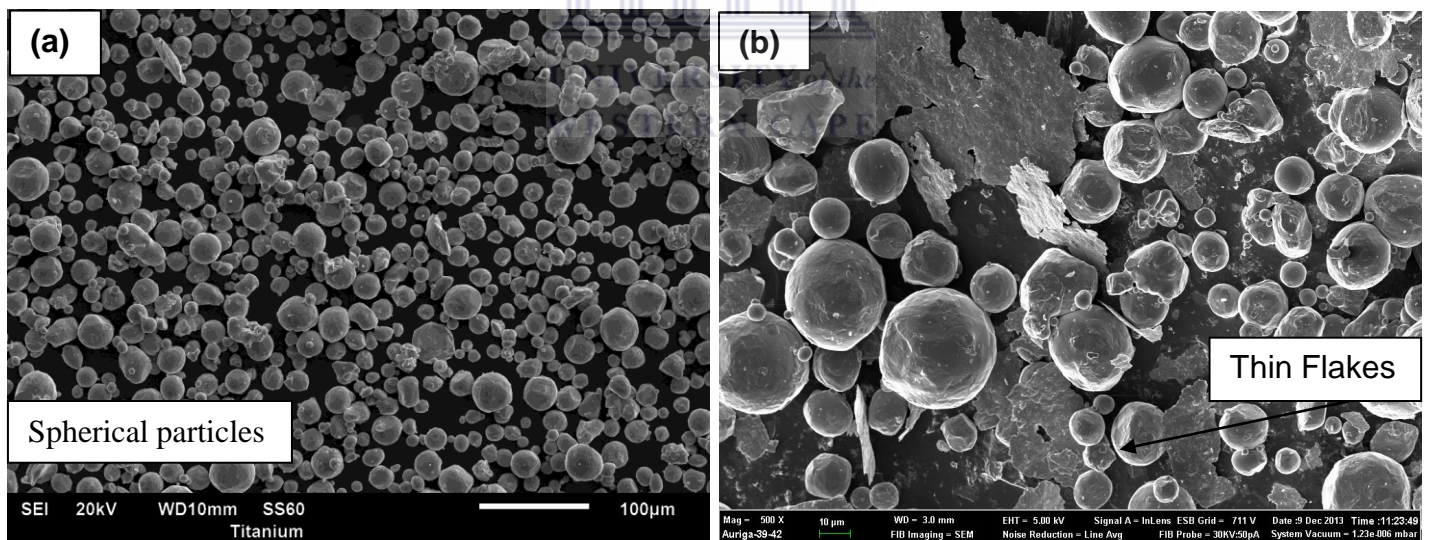
Fig 2.2: SEM images of Ti (a) unmilled and (b) 15 h ball-milled powders

Fig. 2.3 shows the crystal structures of unmilled and 15 h milled-SA Ti powders. XRD patterns display the HCP crystal structure in unmilled and 15 h

46

milled Ti-SA powders. Ti powder milled for 15 h without SA has HCP crystal structure. It appears that BM shortens and broadens the intensity peak heights as previously reported elsewhere **[2.20, 2.21]**. The peaks have slightly shifted to the higher 2 theta positions due to structural deformations and induced lattice strain by milling. The estimated crystallite sizes using Scherrer formula reduce from 73 nm (unmilled) to 47 nm (15 h milled-SA). On the contrary, for 15 h-milled without SA a crystallite size of 34 nm was achievable. This implies that milling in SA delays the crystallite refinement. The calculated lattice parameters of unmilled and 15 h milled Ti-SA powders are a=2.95 Å; c=4.68 Å and a=2.92 Å; c=4.67 Å, respectively.
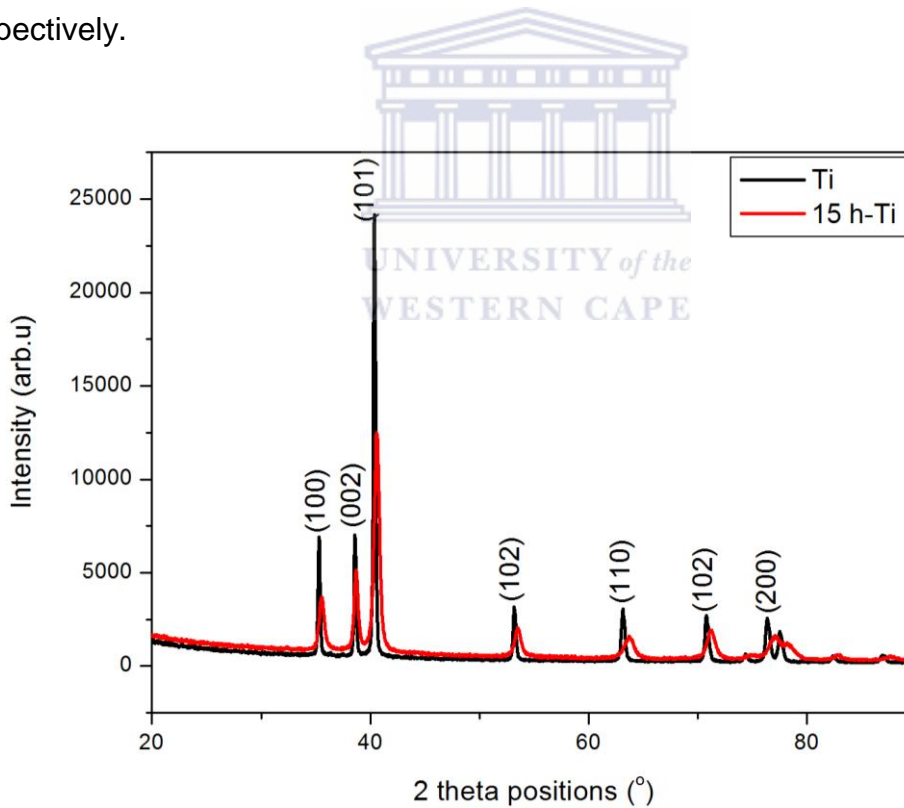
Fig 2.3: XRD patterns of unmilled Ti and 15 h milled powders

Fig. 2.4 shows the Raman spectra of 15 h Ti-SA and 15 h without SA. According to Lohse et al. **[2.22]**, pure Ti does not have Raman-active vibrational modes, which implies that milling induces the Raman-active vibrational modes shown in **Fig. 2.4.** Although C from SA could facilitate contamination on the Ti milled powder, the Raman peaks do not correspond to either C or TiC. Lohse et al. **[2.22]** reported Raman peaks at 260, 420 and 605 cm^{-1} for commercial TiC and carbon graphite peaks at 1320 and 1590 cm^{-1}. The two graphs in **Fig. 2.4** interfere with each other. In addition, the 15 h Ti-SA shows multiple peaks at 142 cm^{-1}, 257 cm^{-1}, 414 cm^{-1}, 609 cm^{-1}, 711 cm^{-1}, 834 cm^{-1}, 1322 cm^{-1} and 1611 cm^{-1} that are not attributable to TiC **[2.23]** but to nonstoichiometric titanium carbide (TiC_x) solid solution. The 15 h Ti, without SA sample, show peaks at 460, 541, 795, 1088, 1611 cm^{-1}. The shifting of peaks from Ti-SA together with Ti without SA is attributable to the defects created by milling operations that resulted in the refinement of crystallite size.
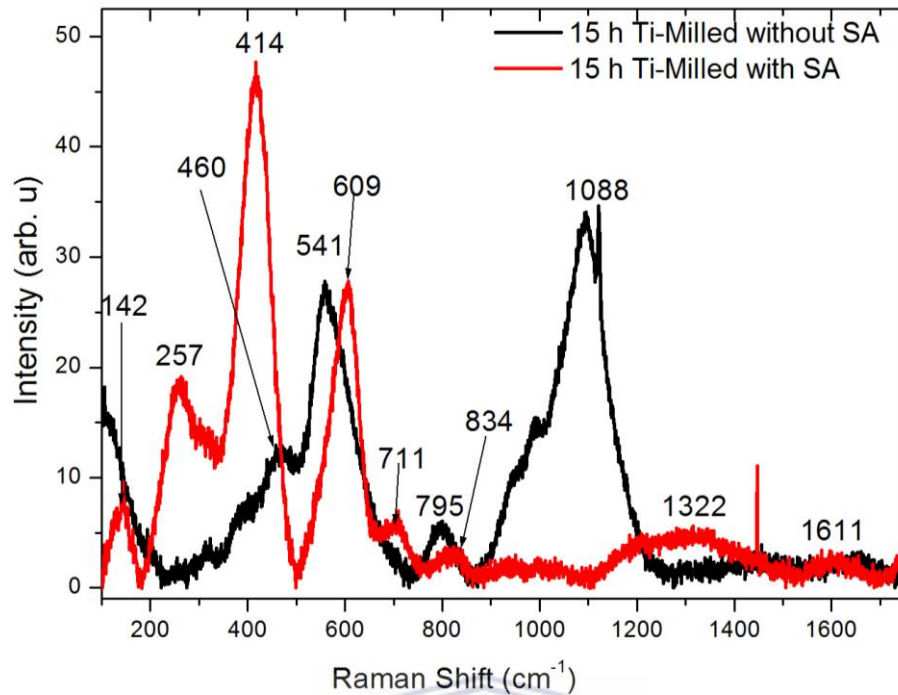
Fig. 2.4: Raman spectra of 15 h (Ti-SA) and (15 h without-SA) powders.

2.3.2.   Thermal Analysis of Ti

Thermal analysis is useful for phase transformation analysis and for choosing suitable sintering temperatures. **Fig. 2.5a-b** shows the DSC and TG curves of unmilled and 15h-Ti-SA powders, respectively. **Fig. 2.5a** shows the behaviour of pure atomised Ti powder upon thermal treatment. The DSC curve shows the α→β allotropic phase transformation in pure Ti powder with an endothermic peak at 909°C during heating and an exothermic peak at 886°C upon cooling. This behaviour confirms a reversible α↔β phase transformation in pure Ti. The emergence of endothermic (heating) and exothermic (cooling) peaks is in agreement with literature of the first order phase transformation [2.24-2.27]. It is similar to those of second order phase transitions such as ferromagnetic to paramagnetic [2.24, 2.27]. The corresponding TG curve shows no significant

49

change. **Fig. 2.5b** shows the DSC and TG curves for 15 h Ti-SA powder. It is evident that milling of the Ti-SA mixture induces the change in thermal properties of the Ti powder. The disappearance of a well-pronounced reversible α→β peak at 909 and 886 ^{o}C is evident. The disappearance of the phase transformation is in agreement with Porter et al.'s **[2.28]** findings obtained upon milling of the atomised Ti-Ni powder. This implies that BM eliminates the crystal ordering in Ti powder. Nevertheless, SA consists of long chain fatty acids that can establish hydrogen and carbon bonds. The melting temperature of SA is approximately 70 ^{o}C, decomposes at approximately 150 ^{o}C, and can decompose during BM. The exothermic peak representing the reactions between Ti and SA decomposed elements i.e. C and H appears at 442 ^{o}C. Suzuki and Nagumo **[2.12],** showed a similar reaction of pure Ti and n-Heptane ($CH_3(CH_2)_5CH_3$) after thermal processing of milled powder, whereby C and H atoms were distributed preferentially between the closed packed planes of the HCP structure. At 745 $^\circ$C, the endothermic peak appears, due to dissociation of H_2 gas dissolved in closed packed planes of Ti powder during milling. This endothermic peak shown at 728 $^\circ$C is reversible upon cooling. The decomposed H atoms dissolve again into the Ti lattice.
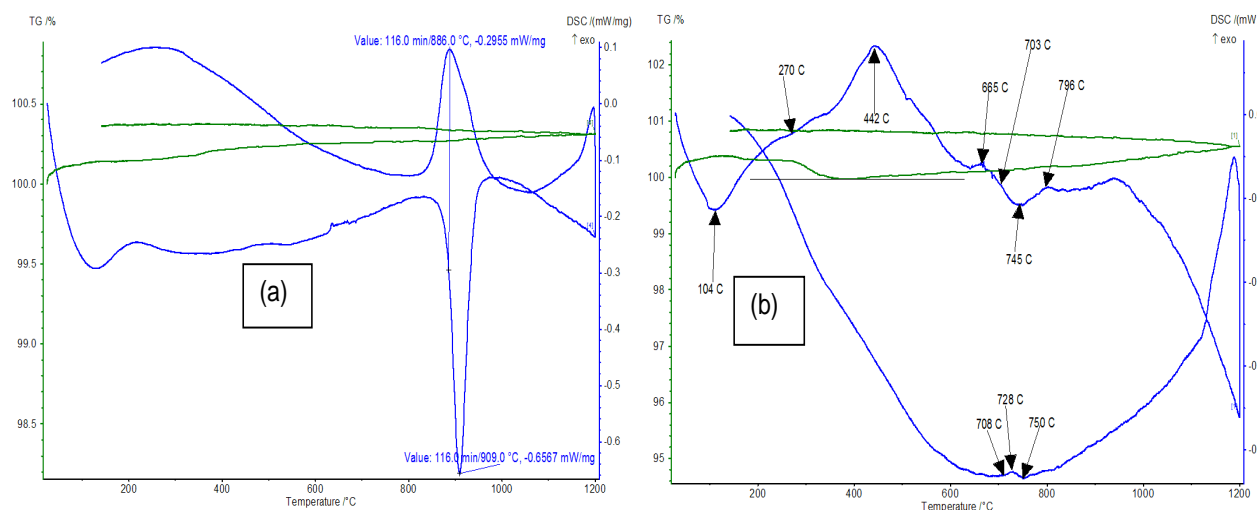
Fig 2.5: DSC graph of Ti (a) unmilled and (b) 15 h milled Ti powders

2.4 CONCLUSION

BM of Ti-SA mixture yields did not alter the lattice parameter of Ti. The 15 h Ti-SA shows multiple Raman peaks at 142 cm^{-1}, 257 cm^{-1}, 414 cm^{-1}, 609 cm^{-1}, 711 cm^{-1}, 834 cm^{-1}, 1322 cm^{-1} and 1611 cm^{-1} that are not attributable to TiC [2.23]. The 15 h Ti, without SA sample, show peaks at 460, 541, 795, 1088, 1611 cm^{-1}. The shifting of peaks from Ti-SA together with Ti without SA is attributable to the difference in the crystallite sizes. Thermal analysis shows that phase transformation occur at lower temperature for milled Ti powder. It was concluded in this study that pure Ti powder without control agent will be milled for the synthesis of titanium oxynitride in order to avoid contamination.

2.6 REFERENCES

[2.1] T. Yoshimura, T. Thotsaphon, H. Amai, K. Kondoh, Transaction JWRI 38 (2009) 37-41.

[2.2] P. Chatterjee, S.P. Sen Gupta, Applied Surface Science 182 (2001) 372-376.

[2.3] I. Manna, P.P. Chattopadhyay, P. Nandi, F. Banhart, H.-J. Fecht, Journal of Applied Physics 93 (2003) 1520-1524.

[2.4] M.J. Phasha, A.S. Bolokang, P.E. Ngoepe, Materials Letters 64 (2010) 1215-1218.

[2.5] D. Shechtman, D. van Heerden, D. Josell, Materials Letters 20 (1994) 329-334.

[2.6] D. Josell, D. Shechtman, D. Van Heerden, Materials Letters 22 (1995) 275-279.

[2.7] J.P.A. Lofvander, F.-C. Dary, U. Ruschewitz, C.G. Levi, Materials Science and Engineering A 202 (1995)188-192.

[2.8] P.E. Vullum, M. Pitt, J. Walmsley, B. Hauback, R. Holmestad, Applied Physics A: Materials Science & Processing 94 (2009) 787-793.

[2.9] A. Aguayo, G. Murrieta, R. de Coss, Physics Reviws B 65 (2002) 092106-092109.

[2.10] G. Ghosh, M. Asta, Acta Materialia 53 (2005) 3225-3252.

[2.11] D. Setoyama, J. Matsunaga, H. Muta, M. Uno, S. Yamanaka, Journal of Alloys Compounds 381 (2004) 215-220.

[2.12] T.S. Suzuki, M.Nagumo, Scripta Metallurgica et. Materialia 32 (8) (1995) 1215-1220.

[2.13] B. Srinivasarao, J.M. Torralba, M.A. Jabbari Taleghani, M.T. Pérez-Prado, Materials Letters 123 (2014) 75–78.

[2.14] H. Abderrazak, F. Schoenstein, M. Abdellaoui, N. Jouini, International Journal of Refractory Metals and Hard Materials 29 (2011) 170–176.

[2.15] W.F. Ng, M.H. Wong, F.T. Cheng, Surface Coatings and Technology 204 (2010) 1823–1830.

[2.16] Y.B. Li, W.J. Weng, Journal of Materials Science 19 (2008) 19–25.

[2.17] M. Yan, M. Qian, C. Kong, M.S. Dargusch, Acta Biomaterialia 10 (2014) 1014-1023.

[2.18] C. Suryanarayana, Progress in Mater Science 46 (2001) 1-184.

[2.19] D. Cullity, Elements of X-ray Diffraction, Addison-Wesley, Reading (MA), 1956, p. 363.

[2.20] A Fathy, A Wagih, M Abd El-Hamid, AA Hassan, Interantional Journal of Engineering 27 (4) (2014) 625-632.

[2.21] A Wagih, Advanced Powder Technology (2014), Article in press

[2.22] B.H. Lohse, A. Calka, D. Wexler, Journal of Applied Physics 97 (2005) 114912-1-1149-7.

[2.23] Y.W. Wang, X. Zhang, X. Wu, Q. Li, H. Zhang, X. Zhang, Materials Science Engineering A 488 (2008) 112-116.

[2.24] C. Papandrea, L. Battezzati, Philosophical Magazine 87 (10), (2007) 1601-1618.

[2.25] A.K. Rai, S. Raju, B. Jeyaganesh, E. Mohandas, R. Sudha, V. J. Ganesan, Journal of Nuclear Materials 383 (2009) 215-225.

[2.26] R.J. Contieri, M. Zanotello, R. Caram, Materials Science Engineering A 527 (2010) 3994-4000.

[2.27] A.S. Bolokang, M.J. Phasha, Advanced Powder Technology 22 (2011) 518-521.

[2.28] G.A. Porter, P.K. Liaw, T.N. Tiegs, K.H. Wu, Scripta Materialia, 43 (2000) 1111-1117.

UNIVERSITY of the
WESTERN CAPE

CHAPTER THREE

Formation of face-centered cubic and tetragonal titanium oxynitride by low temperature annealing of ball milled titanium powder in air

ABSTRACT

$TiO_{0.61}N_{0.29}$ was synthesized by annealing of ball milled Ti in air at 900 ºC for 5 hrs. A trace of rutile-type $TiO_{1.56}N_{0.56}$ phases was observed. The morphology of the synthesized powder displayed multiple interesting colours. Scanning electron microscopy, x-ray diffraction and Raman spectroscopy were used for characterization of the powders. Raman analyses showed a phase transformation upon annealing in air.

3.1 INTRODUCTION

For the past three decades, studies on ball milling (BM) or mechanical milling (MM) have aroused interest in the research field. The process induces deformations and grain refinement on elemental powders **[3.1-3.3]**. Although Ti shows allotropic phase transformation upon thermal stress, several authors reported on the intermediate metastable FCC phase using BM processes **[3.4-3.7]**.

However, the reaction of Ti with interstitial elements such as O, N, C, form stable compounds. The lattice parameters of the FCC phase reported after MM range from 4.24 to 4.40 Å **[3.4-3.7]**. The lattice parameters of titanium carbide (TiC), titanium nitride (TiN), and titanium monoxide (TiO_x) and titanium hydride (TiH_2) are found within this range. Literature shows that TiN can be synthesized with ball milled Ti powder at low temperatures **[3.8]**. The synthesis of nitride and oxynitride is feasible by milling Ti in air **[3.9]**. Lately, researchers show a high interest in titanium oxynitride (TiO_xN_y) that is proposed as a material of choice for biomedical applications **[3.10]**, since it has good electrical and optical properties, as well as good thermal stability **[3.11].** TiO_xN_y films provide a retarding diffusion barrier at the interface between a metal and silicon **[3.9]**. The preparation of TiO_xN_y involves sputtering **[3.9, 3.11-3.13]** as well as MM **[3.14].** It seems that hydroxyapatite (HA) implant material bond with TiO_xN_y due to its mixed-valence states on the Ti atoms surface by negative charge of oxygen, thus promoting the adsorption of Ca^{2+} ions **[3.10]**. Therefore, in this current work, TiO_xN_y and $TiO_{2-x}N_y$ structures were prepared by milling in Ar and subsequently annealed in air

due to the increasing interest in biomedical application. To study the surface morphology, elemental analysis and the phase composition of the obtained TiO_xN_y and $TiO_{2-x}N_y$, scanning electron microscopy, x-ray diffraction and Raman spectroscopy analyses were performed.

3.2   EXPERIMENTAL WORK

High purity titanium powder was subjected to BM. The powder was charged in a 50 l stainless steel milling vial with 5 mm diameter stainless steel balls filled with argon gas inside a glove box. BM was done for 30 h at 800 rpm and a 20:1 ball-to-powder weight ratio. The two samples were annealed at 900 °C under air and nitrogen (N_2) atmosphere, respectively. Phase evolution was traced with a PANalytical X'pert PRO PW 3040/60 X-ray diffraction (XRD) machine fitted with a Cu K_α radiation source. The XRD peak broadening was calculated from the full width at half maximum (FWHM) of the most intense Bragg peak. Pure tungsten was used as a standard, while the average crystallite size was estimated using the Scherer formula **[3.15].** The surface morphology of the annealed and polished samples was studied using LEO 1525 field-emission scanning electron microscope (FE-SEM) coupled with a Robinson Backscatter Electron Detector (RBSD) and an Oxford Link Pentafet energy dispersive x-ray spectroscopy (EDS) detector. Raman spectra were collected using a Horiba Jobin-Yvon HR800 Raman microscopy equipped with an Olympus BX-41 microscope attachment. An Ar+ laser (514.5 nm) with energy setting 1.2 mW from a Coherent Innova

Model 308 was used as an excitation source. Optical images were captured by digital camera.

3.3   RESULTS AND DISCUSSIONS

3.3.1   Morphology and microstructures

Fig. 3.1 shows the SEM images of (a) unmilled and (b) 30 h ball-milled Ti powders. The unmilled Ti powder particles show spherical shape morphology with a broad distribution of sizes ranging from 18 to 45 μm. Upon extensive and continuous milling for 30 h at 800 rpm, the spherical shape of the particles changes to thin flakes or pancakes. The two 30 h-milled Ti sample, has undergone annealing in nitrogen and air, respectively.
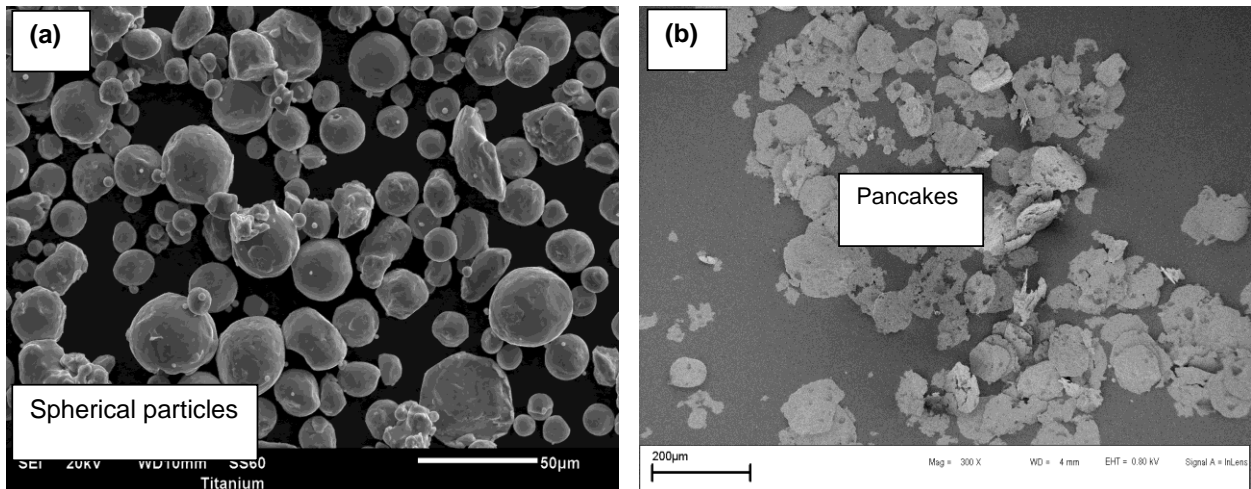

Fig. 3.1: SEM images of (a) 0 and (b) 30 h-milled Ti powders.

Fig. 3.2 shows the XRD patterns of Ti powders (a) unmilled, (b) 30 h-milled and (c) 30 h-annealed at 900 ºC. The unmilled and 30 h milled Ti retained the HCP crystal structure as shown in **Fig. 3.2a and b**. Moreover, the crystallite size reduced from 110.27 nm to 47.21 nm after milling. **Fig. 3.2c** shows the XRD pattern of the 30 h milled Ti powder in flowing air at 900 ºC. It is evident that new peaks have developed. The FCC and tetragonal phases confirm the formations of titanium oxynitride phases; $TiO_{0.61}N_{0.29}$ and rutile-type $TiO_{1.56}N_{0.56}$. The former has a lattice parameter a=4.260 Å while the latter has a=4.555 Å; c=2.962 Å. The crystallite size of FCC $TiO_{0.61}N_{0.29}$ is 66.72 nm while the rutile type has a larger crystallite size of 106.65 nm as shown in **Fig. 3.3**. The $TiO_{1.56}N_{0.56}$ phase is either of anatase **[3.16, 3.17]** or rutile nature **[3.18]**. This phase has a small N contamination compared to the TiO_xN_y phase **[3.16]**. The obtained XRD patterns for TiO_xN_y and rutile-type $TiO_{1.56}N_{0.56}$ phases are in agreement with the literature **[3.16]**. From the XRD patterns, the $TiO_{1.56}N_{0.56}$ showed (110), (200), (220) and (310) planes, while the $TiO_{0.61}N_{0.29}$ revealed (111), (200), (311) and (222) planes which are in agreement with the reported rutile phase of N_2-doped TiO_2 **[3.18]**. The majority of TiO_2 phases formed in the samples are because oxygen has higher electronegativity with Ti when compared to nitrogen **[3.19]**. Simon et al. **[3.20]** observed that annealing under air at 450 °C leads to complete oxidation of Ti (O, N) to titanium dioxide, mainly in the anatase form with a small contribution of the rutile phase.
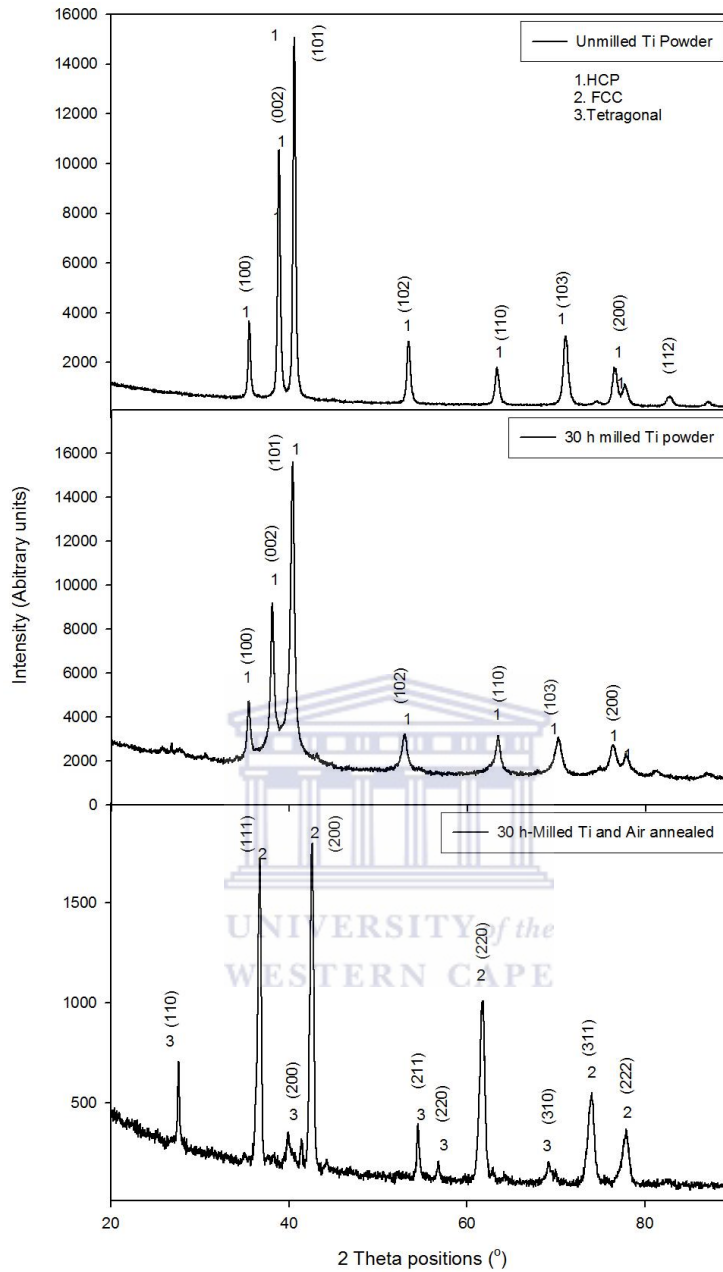
Fig. 3.2: XRD patterns of (a) unmilled, (b) 30 h-milled and (c) 30 h-annealed Ti powders in air.

The formation mechanism of oxynitride is proposed; equations, (1) and (2) shows that Ti has higher affinity to O_2 than N_2, although both reactions are exothermic. Air contains approximately 78 % nitrogen and 21 % oxygen.

$$Ti + \tfrac{1}{2} N_2 \rightarrow TiN \qquad\qquad \Delta H_f = -346.89 KJ/mol \qquad\qquad (3.1)$$

$$Ti + O_2 \rightarrow TiO_2 \qquad\qquad \Delta H_f = -959.75 KJ/mol \qquad\qquad (3.2)$$
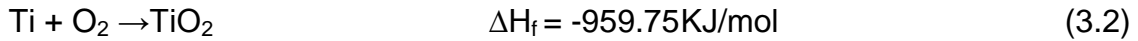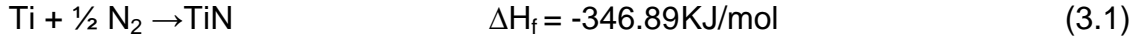
High temperatures induced during the exothermic reaction between Ti and oxygen facilitates the TiO_xN_y formation that occurs at lower temperatures. Due to stacking faults induced by BM **[3.21]**, the FCC $TiO_{0.61}N_{0.29}$ phase is preferable over tetragonal $TiO_{1.56}N_{0.56}$ phase. The smaller crystallite size (66.72 nm) of TiO_xN_y justifies that low heat input was involved. Crystallite growth improves at high temperatures in the case of $TiO_{1.56}N_{0.56}$.
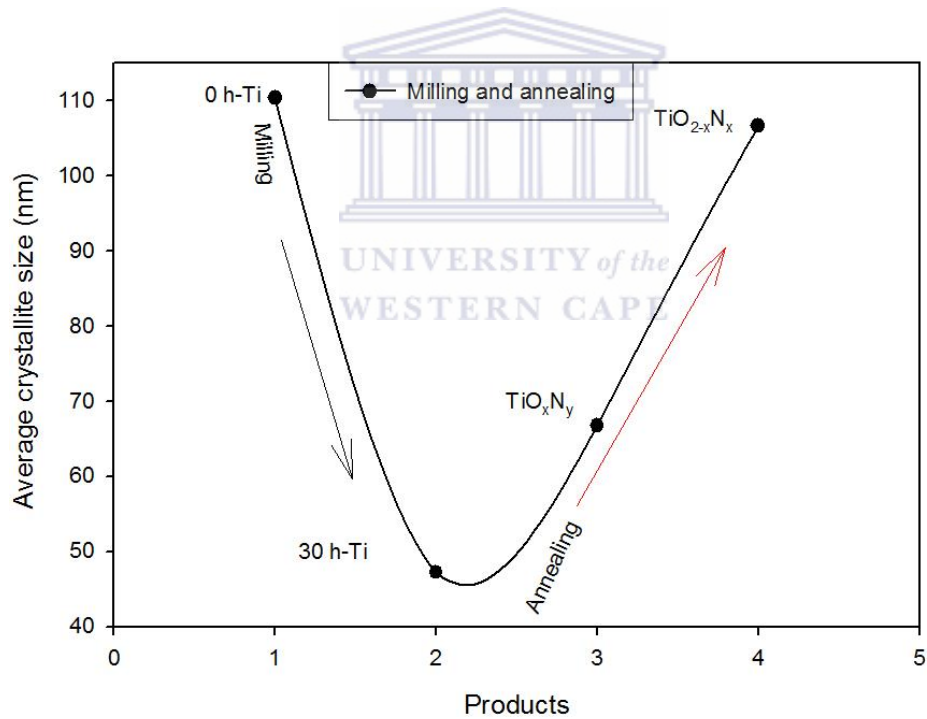
Fig. 3.3:   Evolution of average crystallite sizes of Ti powders before and after annealing in air.

Figs. 3.4a and b show the Raman spectra of the unmilled, milled Ti powders and $TiO_{1.56}N_{0.56}$ and $TiO_{0.61}N_{0.29}$ phases respectively. Raman peaks of the atomized Ti powder appear at 560, 795.8, and 1097 cm^{-1}. Upon milling, a peak shift was observed at 246, 403, 563, 770, 1227.5 and 1757 cm^{-1}, which is probably due to the change in the crystal orientation induced by the milling effect. Upon annealing at 900 in air, $TiO_{1.56}N_{0.56}$ and $TiO_{0.61}N_{0.29}$ phases were observed, which revealed Raman active modes at 144, 199, 248, 409, 436, 518 and 640 cm^{-1} corresponding to anatase and rutile phases **[3.22, 3.23]**. It is clear from the spectra that the Raman modes shift to higher wavenumber showing modes of $TiO_{1.56}N_{0.56}$. Therefore, the peaks observed at 248, 436 and 605 cm^{-1} are attributed to the Raman active modes of $TiO_{0.61}N_{0.29}$.
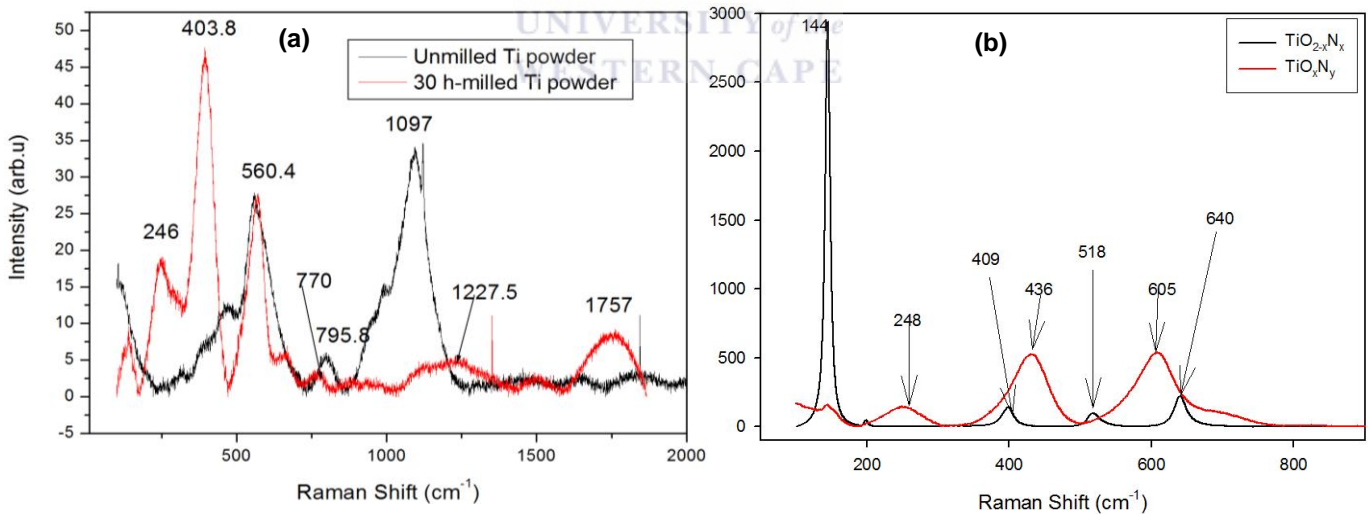
Fig. 3.4: Raman spectra of (a) unmilled and milled Ti powder in Ar and (b) 30 h milled-annealed powder in air done on $TiO_{1.56}N_{0.56}$ and $TiO_{0.61}N_{0.29}$ phases of the polished powder sample.

From the Raman analysis, we can conclude that there is a difference in crystal structure between two phases of annealed powder, $TiO_{2-x}N_x$ and TiO_xN_y. **Table 3.1** shows a summary of Raman peaks positions compared with the literature. Thus based on the literature **(Table 3.1)** it can be concluded that $TiO_{1.56}N_{0.56}$ and $TiO_{0.61}N_{0.29}$ phases were formed by annealing in air.

Table 3.1: Comparison of published Raman data of $TiO_{1.56}N_{0.56}$ and $TiO_{0.61}N_{0.29}$ with the current work

Raman shifts (cm^{-1}) TiO_xN_y	Raman shifts (cm^{-1}) $TiO_{2-x}N_y$	Reference
148, 200, 398, 518, 641		[3.24]
144, 400, 514, 639 214, 246, 646		[3.25]
143, 445, 615 200, 400, 640		[3.26]
144, 410, 520, 640, 240, 450, 620		[3.27]
	143.4, 396.1, 514.6, 641.1(A)	[3.16]
	147, 397, 443 R, 519, 637 150, 421 R, 613 A+R	[3.17]
248, 436, 605	144, 200, 409, 518, 640	Current work

Note: A corresponds to anatase and R to rutile phase

Fig. 3.5a shows the SEM image of the 30 h-milled powder after annealing in air, while its corresponding selected areas 1 and 2 is shown in **Figs. 3.5b** and

c, respectively. Two different morphologies are evident for area 1 and area 2. Area1 **(Fig. 3.5 b)** appear as the fine grains welded together, while area 2 illustrates larger particles **(Fig. 3.5c).**
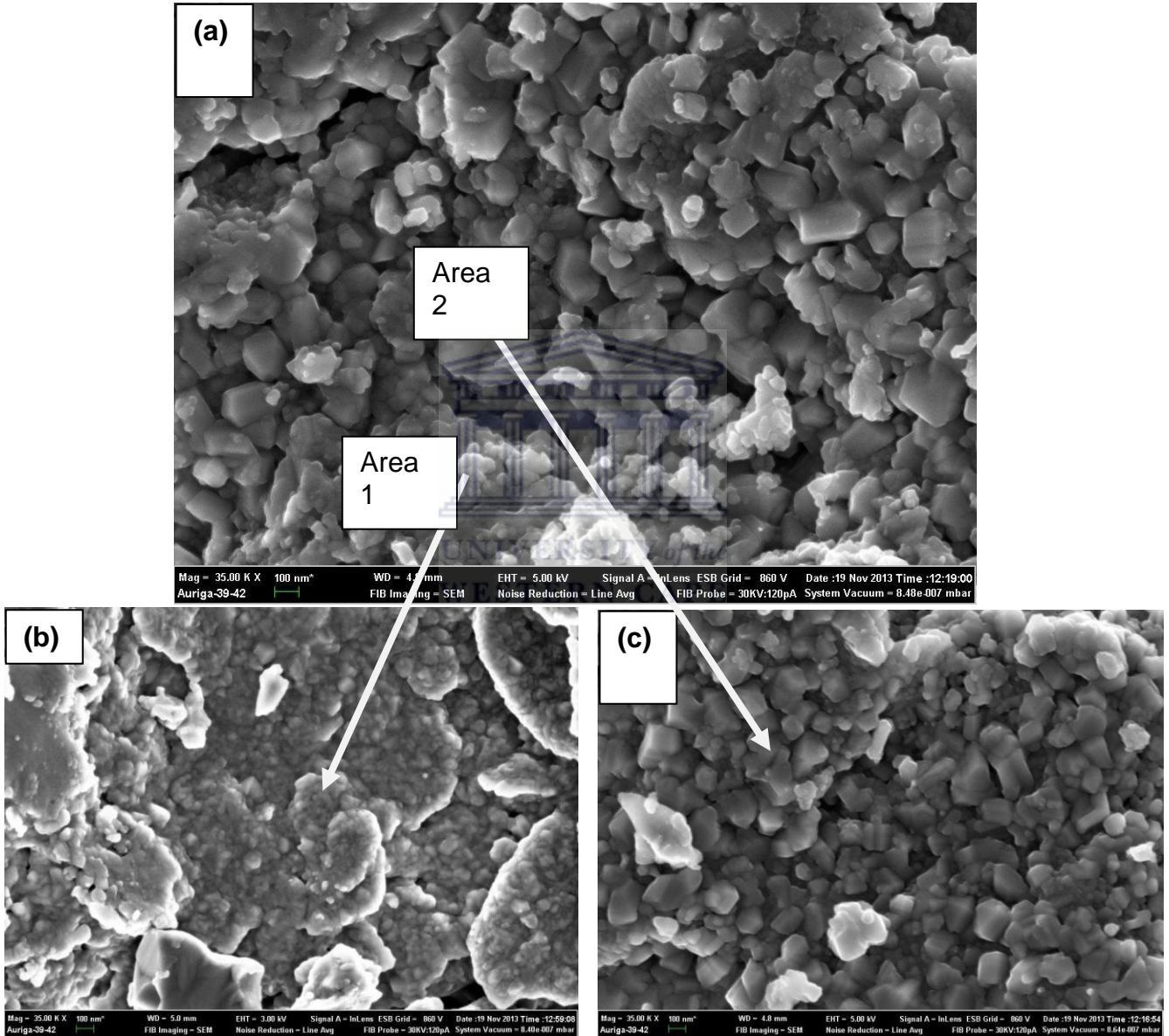
Fig. 3.5: SEM images of (a) 30h milled and annealed in air and (b-c) correspond to high-resolution images of (a) showing different shapes of the particle.

The EDS analysis in **Fig.3.6** confirms the existence of O and N. Minor peaks of carbon originate from the sample preparation carried out for the SEM analysis. The two Ti-phases, oxygen-rich $TiO_{1.56}N_{0.56}$ and nitrogen-rich $TiO_{0.61}N_{0.29}$ with varying N_2 content, exists. From the quantitative analysis determined from the EDS spectra the values were estimated as $TiO_{1.56}N_{0.56}$ and $TiO_{0.61}N_{0.29}$. These values are consistent with ones observed by Tessier et al. **[3.16]** for titanium oxynitride.
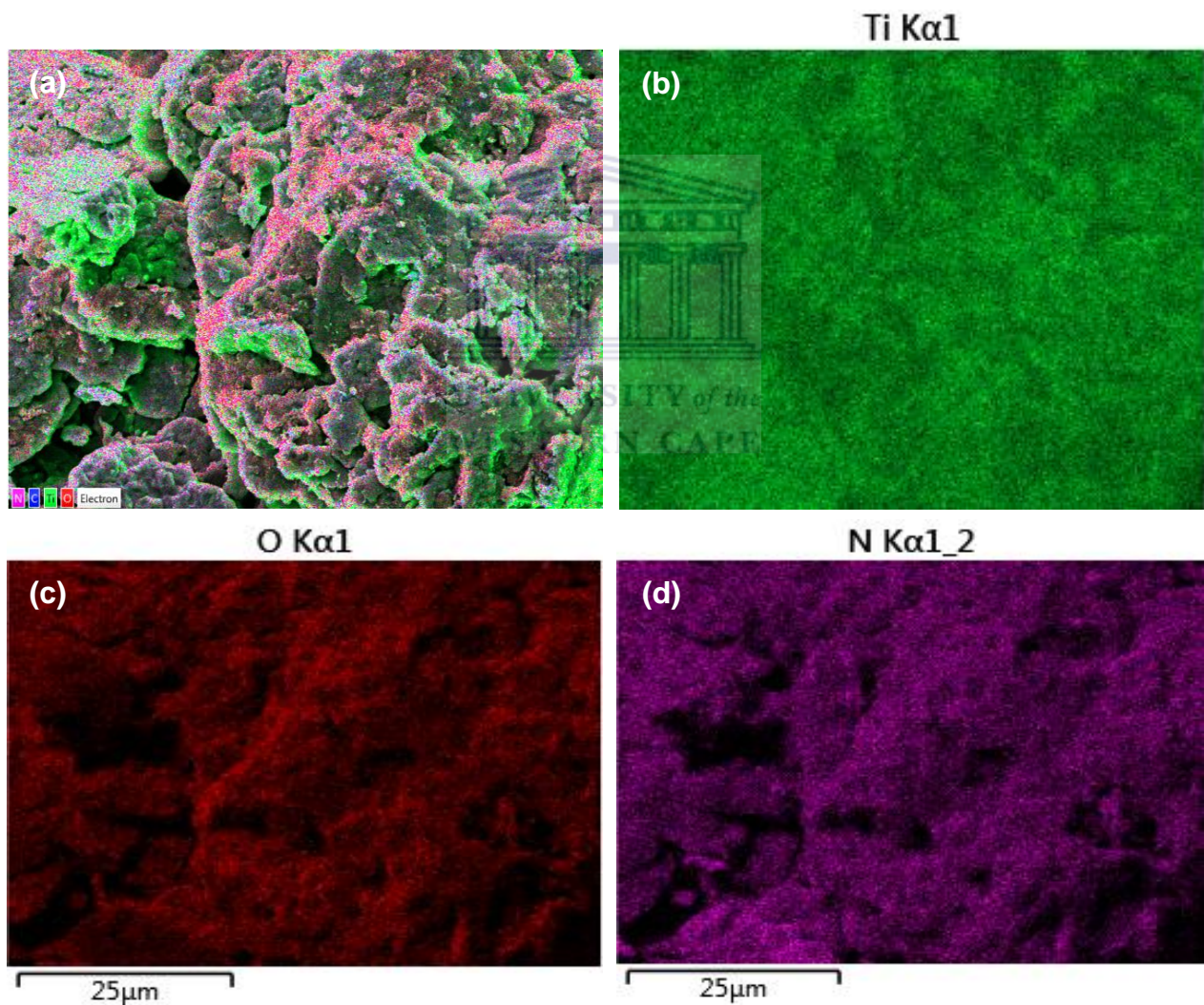
Fig. 3.6: EDS analysis of the 30 h milled Ti powder annealed in air

Fig. 3.7 shows the optical images of Ti powders annealed in air and N_2 as well as the SEM microstructure of the particles annealed in air. **Fig. 3.7a** shows the optical picture of air-annealed powder particles; displaying multiple interesting blue, gold and bright yellow colours. According to the published literature, the bright yellow and golden colours belong to low oxygen titanium oxynitride $TiO_{0.61}N_{0.29}$ and that can turn blue due to an increase in oxygen content **[3.29]**. Multiple colours are due to the temperature difference during the synthesis. TiN may have reddish to yellowish colours based on the processing temperatures **[3.28]**, as confirmed in **Fig. 3.7b.** Koopayeh et al **[3.29]** suggested that pale yellow and dark blue colours are due to stoichiometric and oxygen deficiency in tetragonal rutile, respectively. Therefore, the tetragonal TiO_2 structure can also accommodate small amounts of nitrogen. In order to differentiate TiO_xN_y and TiN, titanium powder was annealed in a N_2 atmosphere **(Fig. 3.7b).** Since the air-annealed sample has larger particles that are welded together, it was possible to do microstructural analysis on the sample. **Fig. 3.7c** shows the SEM microstructure of the polished sample obtained after annealing in air. The microstructure is comprised of globular TiO_xN_y (light and dark grey) phases. A light-grey TiO_xN_y phase is only due to smaller amounts of N_2 compared to the dark phase. The bright phase surrounding the TiO_xN_y is a nitrided TiO_2-rutile represented by $TiO_{2-x}N_x$. Due to the high amount of oxygen in $TiO_{1.56}N_{0.56}$ this phase is expected to be less ductile when compared with the $TiO_{0.61}N_{0.29}$ phase.
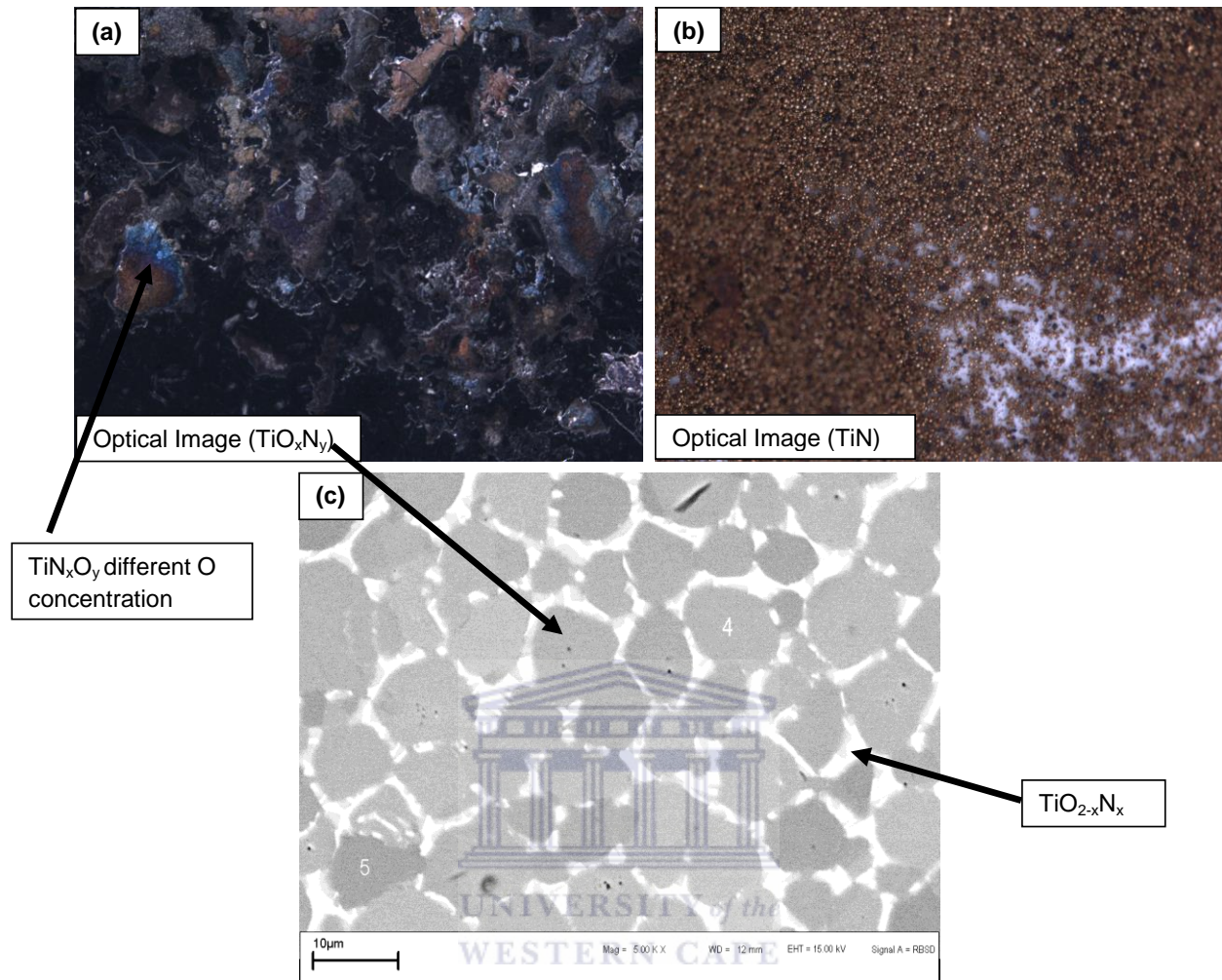
Fig. 3.7: Optical images of 30 h milled Ti (a) annealed in air, (b) milled Ti powder annealed in N_2 and (c) microstructure of the Ti sample annealed in air.

3.4 CONCLUSION

$TiO_{0.61}N_{0.29}$ was synthesized by annealing of ball milled Ti in air at 900 °C. In addition, traces of rutile-type $TiO_{1.56}N_{0.56}$ solid solution were detected. The morphology of the synthesized powder displayed multiple interesting colours. The estimated average crystallite sizes of $TiO_{0.61}N_{0.29}$ and $TiO_{1.56}N_{0.56}$ are 66.72 nm

106.65 nm, respectively. The formation mechanism of $TiO_{0.61}N_{0.29}$ and $TiO_{1.56}N_{0.56}$ is proposed. During the reaction at high temperature, the rutile-TiO_2 phase form first due to the higher heat of formation for TiO_2. As the temperature decreases, N_2 occupies the oxygen vacancies present in TiO_2 to induce $TiO_{2-x}N_x$ while at the same time, the N_2-rich particles promotes the formation of the $TiO_{0.61}N_{0.29}$ phase. The observed shift of the Raman active peaks to higher wavenumber was induced by formation of the $TiO_{0.61}N_{0.29}$ phase.

UNIVERSITY of the
WESTERN CAPE

3.6 REFERENCES

[3.1]   D. Gu, W. Meiners, Y. Hagedorn, K. Wissenbach, R. Poprawe, Journal of Physics D: Applied Physics 43 (2010) 135402-135412.

[3.2]   S. Bolokang, C. Banaganayi, M. Phasha, Interantional Journal of Refractory Metal and Hard Materials 28 (2010) 211-216.

[3.3]   A.S. Bolokang, M.J. Phasha, C. Oliphant, D. Motaung, Interantional Journal of Refractory Metal and Hard Materials 29 (2011) 108-111.

[3.4]   I. Manna, P.P. Chattopadhyay, P. Nandi, F. Banhart, H.-J. Fecht, Journal of Applied Physics 93 (3) (2003) 1520-1524.

[3.5]   P. Chatterjee, S.P. Sen Gupta, Applied Surface Scienec 182 (2001) 372-376.

[3.6]   P. Chatterjee, S.P. Sen Gupta, Philosophical Magazine A 81 (2001) 49-60.

[3.7]   M.J. Phasha, A.S. Bolokang, P.E. Ngoepe, Materials Letters 64 (2010) 1215-1218.

[3.8]   A.S. Bolokang, M.J.Phasha, Interantional Journal of Refractory Metal and Hard Materials 28 (5) (2010) 610-615.

[3.9]   P.K. Barhai, N. Kumari, S.K. Pabi, S.K. Mahapatra, Vacuum 84 (2010) 896-901.

[3.10] S. Piscanec, L.C. Ciacchi, E. Vesselli, G. Comelli, O. Sbaizero, S. Meriani, A. De Vitta, Acta Materialia 52 (2004) 1237-1245.

[11]   S.K. Rawal, A.K. Chawla, R. Jayaganthan, R. Chandra, Journal of Materials Science and Technology 28(6) (2006) 512-523.

[3.12] J-M. Chappé, N. Martin, G. Terwagne, J. Lintymer, J. Gavoille, J. Takadoum, Thin Solid Films 440 (2003) 66-73.

[3.13] M. Radecka, E. Pamula, A. Trenczek-Zajac, K. Zakrzewska, A. Brudnik, E. Kusior, N-TH. Kim-Ngan, A.G. Balogh, Solid State Ionics. 192 (2011) 693-698.

[3.14] H. Yang, P.G. McCormick, Journal of Materials Science 28 (1993) 5663-5667.

[3.15] D. Cullity, Elements of X-ray Diffraction, Addison-Wesley, Reading, MA (1956) 363

[3.16] F. Tessier, C. Zollfrank, N. Travitzky, H. Windsheimer, O. Merdrignac-Conanec, J. Rocherulé, P. Greil, Journal of Materials Science 44 (2009) 6110-6116.

[3.17] S. Bagaswi, Y. Niu, M. Nasir, B. Tian, J. Zhang, Applied Surface Science 264 (2013) 139-147.

[3.18] K. Kollbek, M. Sikora, Cz. Kapusta, J. Szlachetko, K. Zakrzewska, K. Kowalski, M. Radecka, Applied Surface Science 281 (2013) 100-104.

[3.19] M.S. Wong, H.P. Chou, T.S. Yang, Thin Solid Films 494 (2006) 244-249.

[3..20] P. Simon, K. March, O. Stéphan, Y. Leconte, C. Reynaud, N. Herlin-Boime, A.-M. Flank, Chemical Physics 418 (2013) 47-56.

[3.21] T.S. Suzuki, M. Nagumo, Scripta Metallurgica at. Materialia 32 (8) (1995) 1215-1220.

[3.22] J.-M. Wu, H.C. Shih, W.-T. Wu, Y.-K. Tseng, I-C. Chen, Journal of Crystal Growth 281 (2005) 384-390.

[3.23] P.W. Shum, K.Y. Li, Z.F. Zhou, Y.G. Shen, Surface Coatings Technology 185 (2–3) (2004) 245-253.

[3.24] B. Subramanian, C.V. Muraleedharan, R. Ananthakumar, M. Jayachandran, Surface Coatings Technology 205 (2011) 5014-5020.

[3.25] G. Hyett, M.A. Green, I.P. Parkin, $Ti_{3-\delta}O_4N$. Journal of Photochemical Photobio. A: Chemistry 203 (2009) 199-203.

[3.26] X. Song, D. Gopireddy, C. G. Takoudis, Thin Solid Films 516 (2008) 6330-6335.

[3.27] S. Lee, I.-S. Cho, D.K. Lee, D.W. Kim, T.H. Noh, C.H. Kwak, S. Park, K.S. Hong, J.K. Lee, H.S. Jung, J. Photochem Photobio A: Chemistry 213 (2010)129-135.

[3.28] S-Q. Wang, L.H. Allen, Journal of Applied Physics 79 (5) (1996) 2446-2457.

[3.29] S.M. Koohpayeh, D. Fort, J.S. Abell, Journal of Crystal Growth 282 (2005) 190-198.

CHAPTER FOUR

Production of titanium-tin alloy powder by ball milling: Formation of titanium-tin oxynitride composite powder produced by annealing in air

ABSTRACT

Phase transformation was induced by BM and annealing of Ti_{75}-Sn_{25} powder. HCP solid solution was induced by BM and yielded compressed lattice parameters a=2.929 Å; c=4.780 Å and c/a=1.63. Upon annealing in Ar at 700 °C, Ti_3Sn intermetallic with lattice parameters a=5.916 Å; c=4.764 Å with (c/a=0.80) was detected. Subsequent TGA analysis of HCP milled Ti-Sn and Ti_3Sn intermetallic in air have resulted in tetragonal oxynitride powders with lattice parameters a=4.985 Å; c=2.962 Å, c/a=0.594 for the former and a=4.582 Å; c=2.953 Å and c/a=0.644 for the latter, respectively. The powder morphology was monitored by high-resolution transmission electron microscopy while the roughness of the milled sample was analysed by atomic force microscopy. Phase transformation was monitored by x-ray diffraction and complemented by Raman spectroscopy.

4.1 INTRODUCTION

Research into metallic oxynitrides is a subject of interest due to their remarkable optical and electronic properties and chemical stability **[4.1, 4.2]**. In particular, titanium oxynitride (TiN_xO_y) has been widely applied in solar selective collectors **[4.3]**, biomaterials **[4.4]**, and decorative coatings **[4.5]**. However, TiN_xO_y properties depend significantly on the N:O ratio. On the other hand, combination of Ti and Sn in alloys brings an interesting properties such as two-stage B2–R–B19' martensitic transformation on cooling and the one-stage B19'–B2 on heating in Ti–Ni–Sn alloys **[4.6, 4.7]**. Elemental Sn is an important dopant for improvement of room temperature photoluminescence. The lattice defects caused by Sn doping could serve as favourable trap sites of the electrons or holes to reduce their recombination and consequently increase the photocatalytic activities **[4.8].** Moreover, Ti-Sn mixed oxide is a better protective film than the single Ti or Sn oxides. The optical properties obtained after the application of the protective film depend on the composition **[4.9]**. Nitrogen (N)-doped SnO_2 nanocrystals (NCs) has been investigated to gain insights about the optical properties and to promote further applications of NCs SnO_2 **[4.10]**. Similarly N-doping occur in TiO_2 powders **[4.11]**, therefore Ti-Sn doping is of interest in the current work. Formation of mixed metal carbides is feasible via ball milling (BM) with ultrafine particles **[4.12, 4.13]**. The ultrafine powder particles become very reactive when flattened due to surface deformation. As a result, synthesis of compounds such as nitride **[4.14]** and oxynitrides **[4.15]** is possible at low temperatures. Mixed metal oxynitride are available and has been fabricated in

indium-tin-oxynitride films by RF-sputtering for potential applications in electronics **[4.16].** Hence, the current paper presents the synthesis of the oxynitride phase, formed by annealing the ball-milled Ti-Sn powder in air.

4.2. EXPERIMENTAL WORK

Titanium-tin (Ti_{75}-Sn_{25}) powder mixture was prepared from pure Ti and Sn of 99.98% and subjected to BM. The powders were charged in a stainless steel milling vial filled with argon gas inside a glove box. BM was done for 30 hours at 600 rpm speed. Annealing of the milled powders was performed in a Carbolite tube furnace under flowing argon (Ar) at 700 °C. Thermal analysis of the milled and annealed powders was conducted at a heating rate of 20 °C min^{-1} and under industrial air flow rate of 20 ml/min to 1000°C. Morphology of the Ti-Sn samples was studied using field-emission scanning electron microscopy (FE-SEM, Zeiss-Auriga). Phase evolution was traced with a PANalytical X'pert PRO PW 3040/60 X-ray diffraction (XRD) machine fitted with a Cu K_α radiation source. To calculate the crystallites size, the Scherer formula was used:

$$L_{hkl} = \frac{0.9\lambda}{B_{2\theta}\cos(\theta)} \qquad (4.1)$$

where λ is the wavelength of the x-rays, $B_{2\theta}$ is the full width at half maximum intensity (FWHM) and θ is the diffraction angle.

Optical properties were measured using a Jobin-Yvon NanoLog photoluminescence (PL) spectrometer. The topography of Ti pellets was

74

analyzed using atomic force microscopy (AFM, Veeco, and Digital Instruments). Raman spectra were collected using a Horiba Jobin-Yvon HR800 Raman microscopy equipped with an Olympus BX-41 microscope attachment. An Ar+ laser (514.5 nm) with energy setting 1.2 mW from a Coherent Innova Model 308 was used as an excitation source.

4.3   RESULTS AND DISCUSSION

Figs. 1 a-d show the SEM images of Sn, Ti, 30 h-milled and 30 h-milled and annealed Ti-Sn powders, respectively. The Sn powder displays the rod and cucumber-shaped morphology (Fig 1a), while Ti powder (Fig 1b) is comprised of spherical particles. Fig. 2c shows the morphology of 30 h-milled Ti-Sn powder. During the milling process, irregular semi-spherical lumps of particles were developed. At this stage, elemental Sn is not distinguishable from Ti implying that both metals have welded. Fig. 2d shows SEM image of the milled Ti-Sn powder after annealing in Ar at 700 °C. However, the powder morphology appears similar to those of milled powder in Fig. 1c. Therefore, there is change in morphology due to annealing.
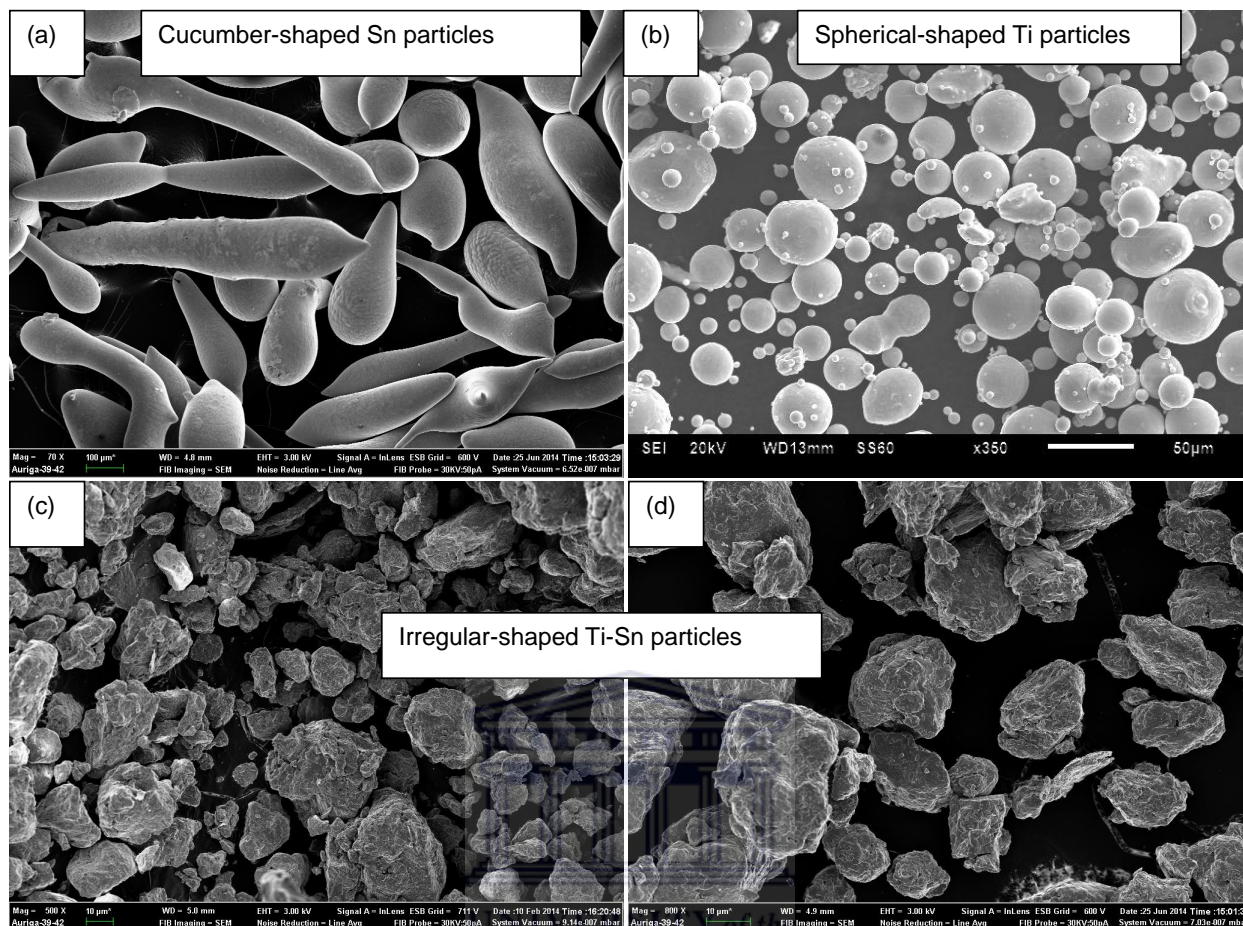
Fig. 4.1: SEM images of unmilled (a) Sn (b) Ti, (c) 30 h milled and (d) 30 h milled and annealed Ti-Sn at 700 ⁰C in Ar

To investigate structural development and phase transformation, XRD analysis was performed on the milled and annealed powders. **Figs. 4.2 a-b** show the XRD pattern of the 30 h milled and that of milled and annealed in Ar at 700 °C. **Figs. 4.2a** reveal a broad and shortened intensity peaks due to the crystallite refinement and defective structure induced by extensive BM. After milling, approximately 45 nm crystallite sizes were obtained. The crystal structure was

identified as HCP with lattice parameters a=2.902 Å; c=4.734 Å and c/a=1.631.

Fig. 4.1b reveals the crystallization of the 30 h-milled Ti-Sn powder upon annealing in Ar atmosphere at 700 ⁰C into HCP Ni_3Sn-type structure with a=5.828 Å; c=4.732 Å, and c/a=0.812. Its estimated crystallite size equals 65 nm. Moreover, intensity peaks of the Ar annealed sample show better crystallinity in agreement with the increased crystallite size. The c/a of 0.812 agrees with that of reported orthorhombic crystal structure on cast samples **[4.17, 4.18]**. The orientation relationships between orthorhombic and hexagonal phases $(110)_{orto}$ ||$(100)_{hex}$, $<001>_{orto}$||$<001>_{hex}$ has been proposed **[4.17].** The transition from hexagonal to orthorhombic phase is accompanied by a shortening of 1.5% along x axis and an elongation of 0.5% along y axis (into orthorhombic basis) leading to the reduction of crystal volume of 1% **[4.17].** Therefore, the XRD analysis confirms phase transformation of Ti-Sn to Ti_3Sn intermetallic. However since the intermetallic is in powder form, further transformation is expected upon thermal treatment at higher temperatures.
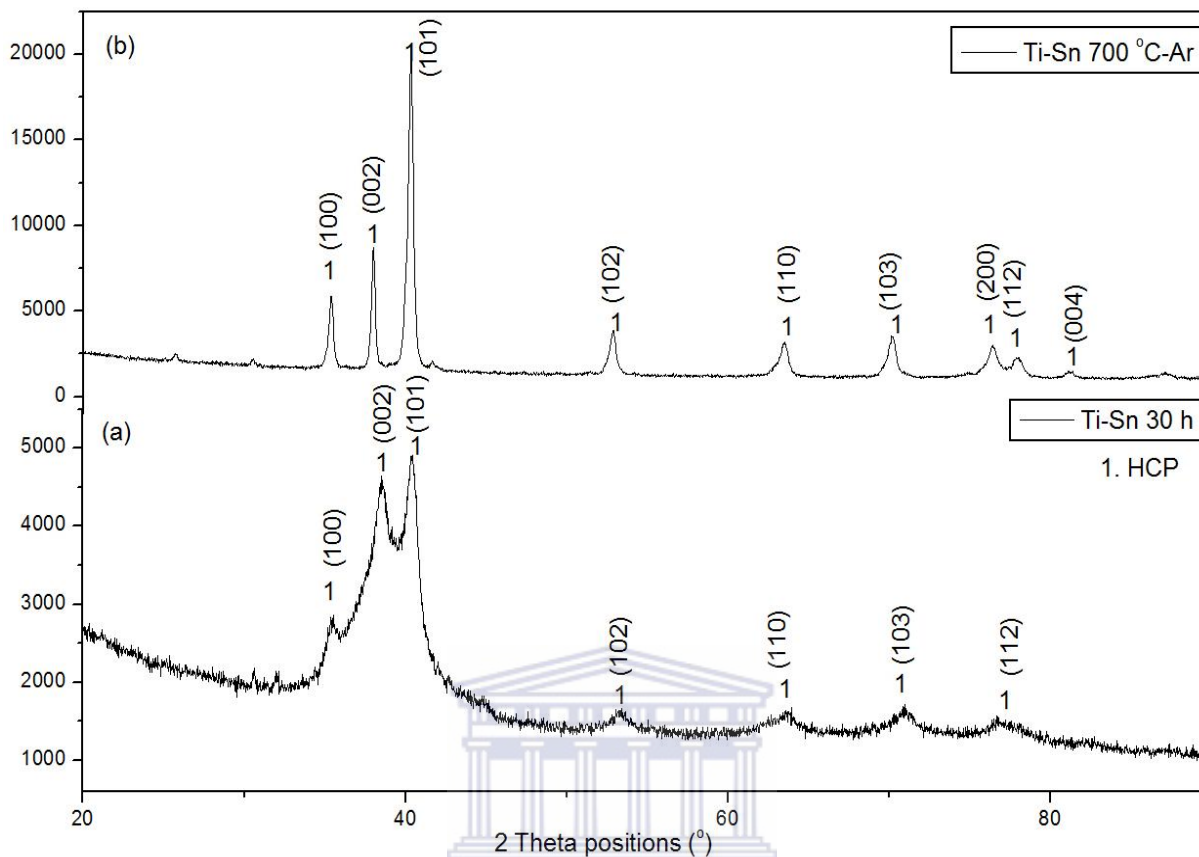
Fig. 4.2: XRD pattern of the (a) 30 h milled Ti-Sn (b) 30 h milled-annealed Ti-Sn powders in Ar at 700 °C.

Fig. 4.3 depicts the PL spectra of the 30 h-milled sample, and that of the sample annealed in Ar. The intense peak around the 395 nm wavelength of the 30 h-milled Ti-Sn powder is attributable to the structural defects and impurities induced after milling, which are in agreement with the XRD pattern in **Fig. 4.2a**. The PL emission peak of the Ar annealed sample is flat and small, indicating better crystallinity, in agreement with XRD peaks due to annealing **[4.19].**
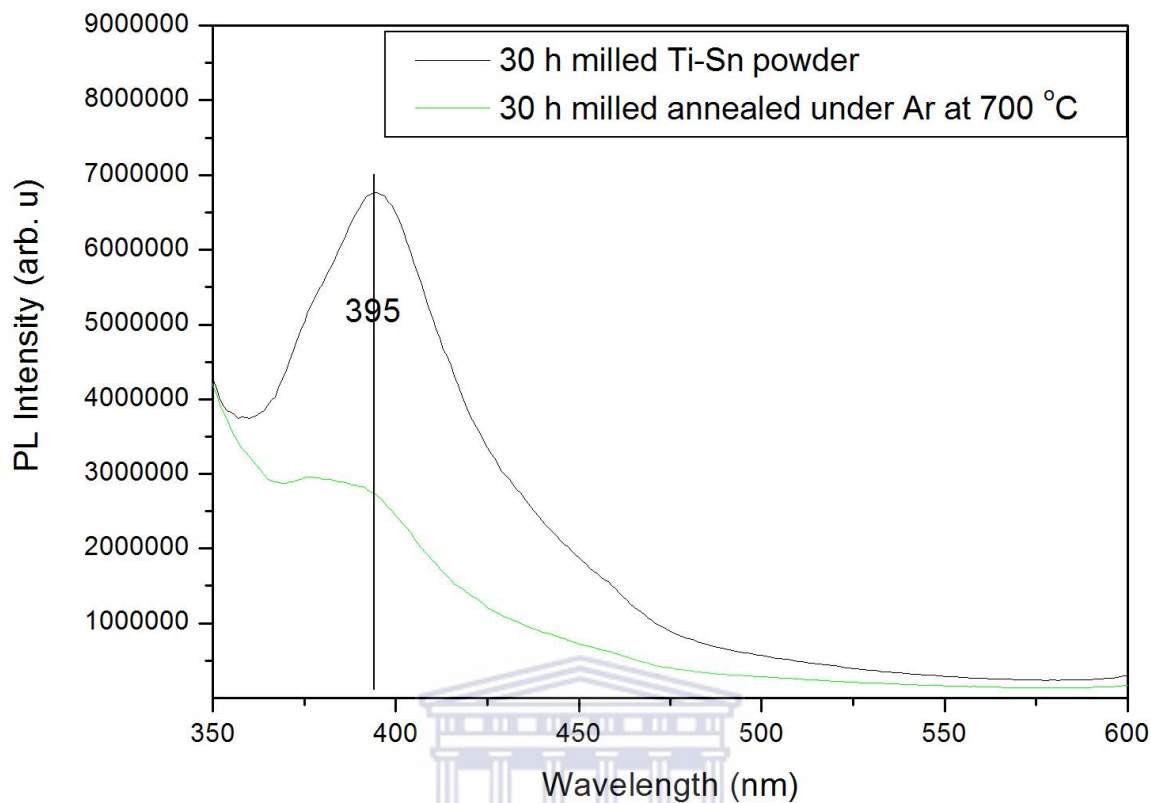
Fig. 4.3: Room temperature PL of the 30 h-milled and annealed Ti-Sn powder in Ar at 700°C.

It is thus logical to investigate the effect of milling and annealing on the particle surface roughness. Surface properties are crucial for bonding and adhesion, especially on biomedical products. AFM images of the 30 h-milled Ti-Sn and that of the annealed sample at 700 ^{o}C are shown in **Figs. 4.4a-b**. It is observed that the milled Ti-Sn powder contains fine grains resulting in surface roughness values around 1.08 nm. The observed low roughness value for 30 h-milled powder might relate to decreased crystallinity and smooth fresh surfaces on deformed particles. After annealing, the surface roughness increases to 3.45

nm, indicating better crystallinity and crystal growth during annealing as shown in

Fig. 4.4c-d.

(a) Homogenous mixture

(b)

(c)

(d) Core-Rim particles
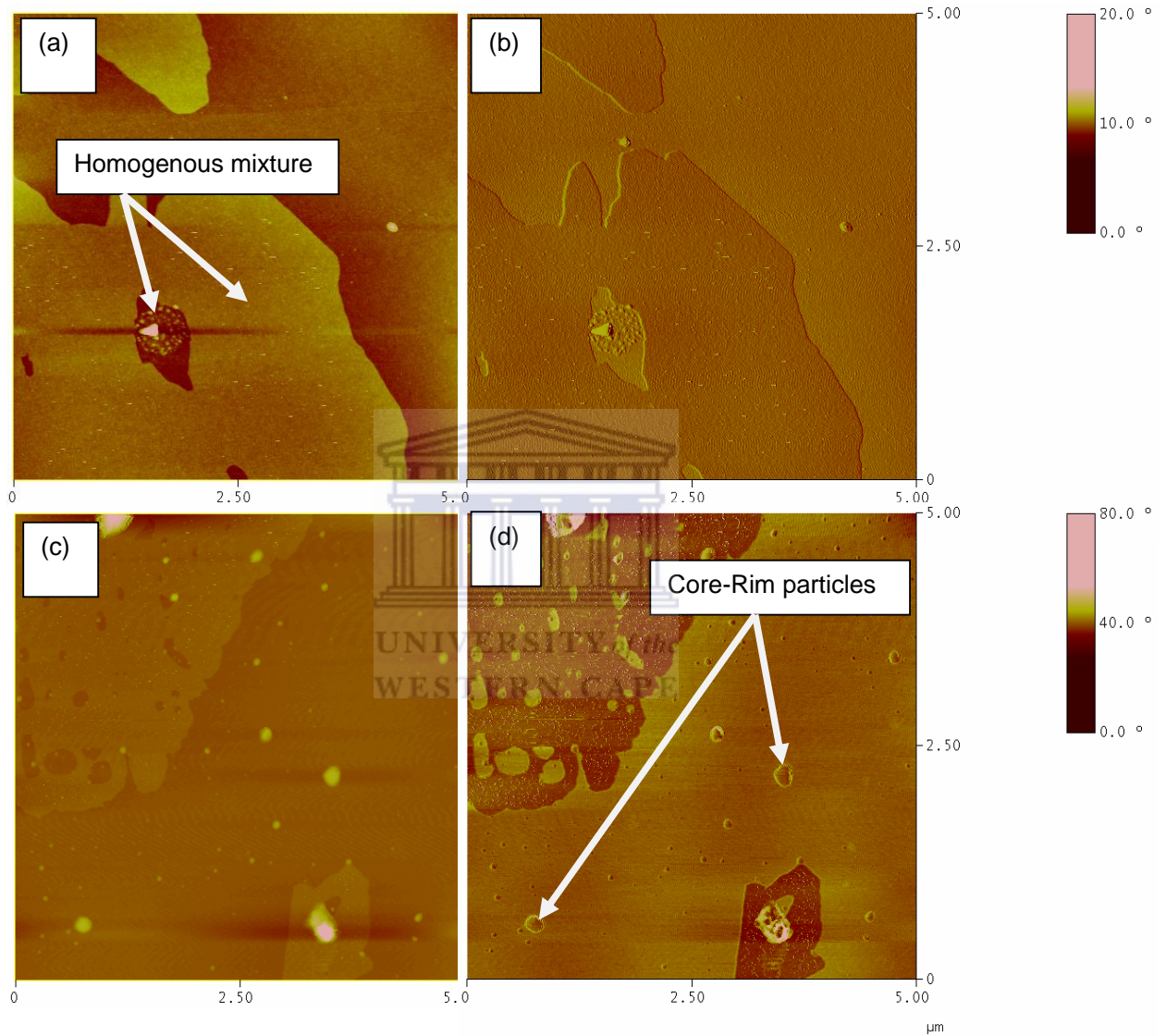
Fig. 4.4: AFM height and (a) Ti-Sn milled and (b) annealed at 700°C in Ar.

Due to interest in the study of oxynitride, new alloys will arouse research interest in this subject. Both synthesized 30 h-milled and annealed Ti_3Sn

powders were subjected to annealing by using the TGA analysis in air from 0 to 1000 °C. **Fig. 4.5** illustrates the TGA graphs of the 30 h-milled and pre-annealed Ti_3Sn powders, respectively. The milled powder increases mass slightly at a faster rate than the pre-annealed powder. This increase in mass starts at approximately 300 °C and reaches maximum at around 900 °C and clearly indicates the phase transformation of powders in air. The resultant powders after TGA analysis were carefully collected and characterized to gain insight into the structural and morphology properties upon annealing in air. The TGA results indicate that milling has affected the powder particle size hence its reactivity to nitrogen occurs earlier than that of the unmilled powder.
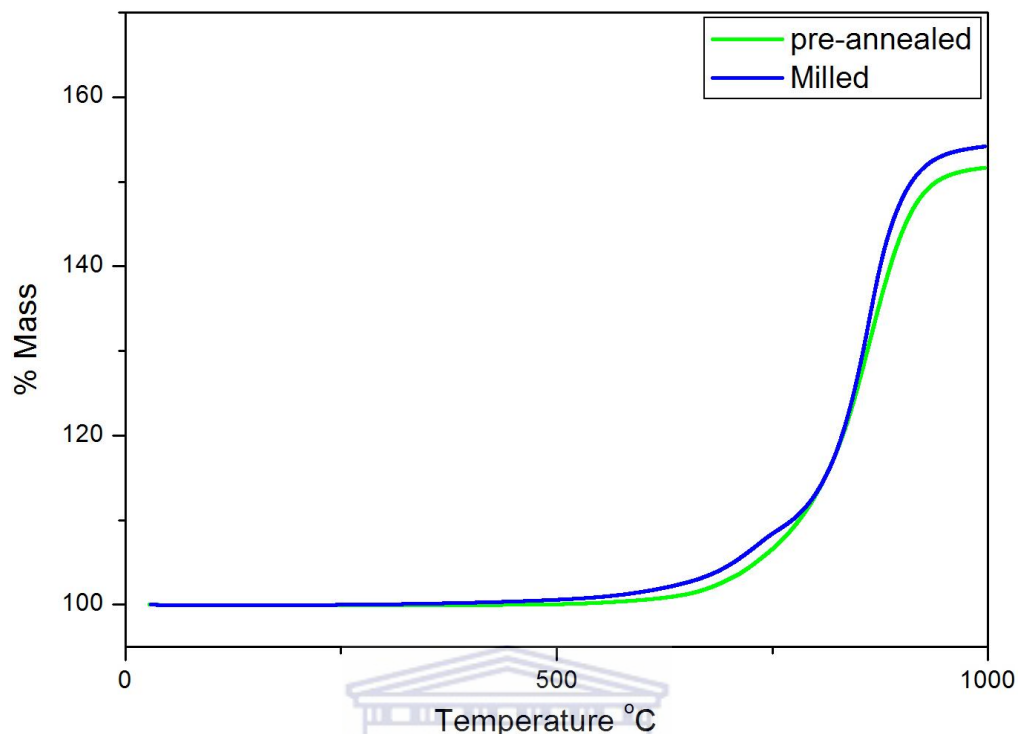
Fig. 4.5: TGA graphs of the 30 h-milled and the milled and pre-annealed Ti-Sn powders

The morphology of the samples obtained after TGA analysis is shown in **Fig. 4.6a-d**. **Fig. 4.6a-b** is the low and high magnification SEM images of the milled powder. The particles in **Fig. 4.6a** show porous features unlike those in the as-milled condition **(Fig. 4.1c)**. The high magnification image in **Fig. 4.6b** displays small rectangular rod-shaped particles of different sizes but improved crystallinity. **Fig. 4.6c** shows the pre-annealed sample after TGA analysis. A large irregular particle appears to be an agglomeration of finer particles. As shown in **Fig. 4.6d**, the particles are interconnected and appear as small grains with well-defined grain boundaries, which are also crystalline. EDS analysis has confirmed the presence of Ti, Sn, O and a small amount of N. In addition, the

corresponding powders have changed color from their original gray to golden/yellow.
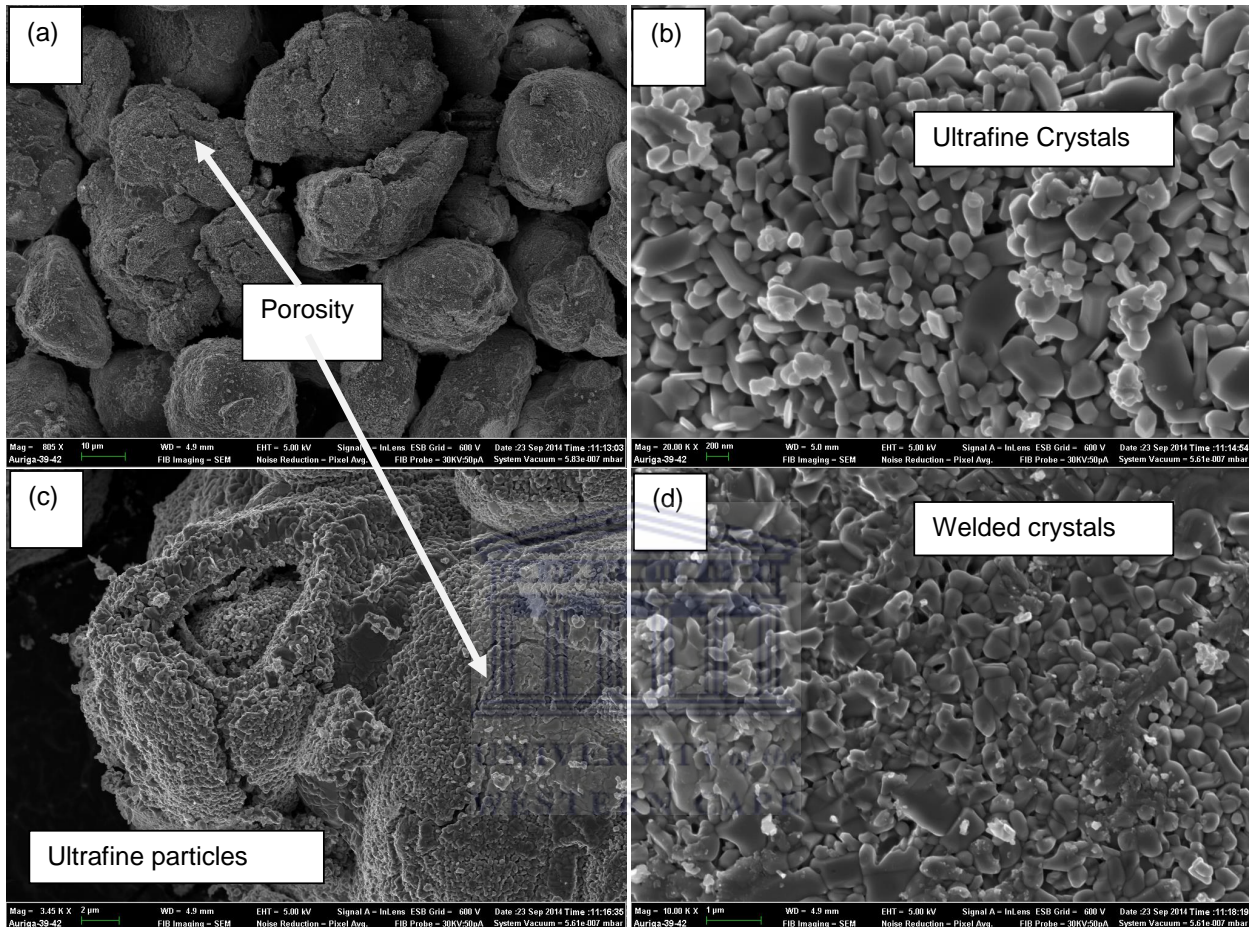
Fig. 4.6: SEM images of the Ti-Sn milled and pre-annealed samples obtained after TGA analysis in air. Low and high magnification (a)-(b) 30 h-milled and (c)-(d) 30 h milled and pre-annealed.

The crystal structure of the powder obtained after TGA analysis is shown in **Figs. 4.7a-b**. The XRD pattern of the milled powder shows a higher intensity peak, or improved crystallinity compared to that of the pre-annealed sample,

before TGA analysis. However, both powders were transformed from HCP to tetragonal crystal structures, respectively. The lattice parameters of the milled sample lattice parameters are a=4.985 Å; c=2.962 Å, c/a=0.594 while for the pre-annealed sample are a=4.582 Å; c=2.953 Å and c/a=0.644, respectively. These tetragonal oxynitride phases are of rutile-type and vary only in Sn, O and N content, respectively.
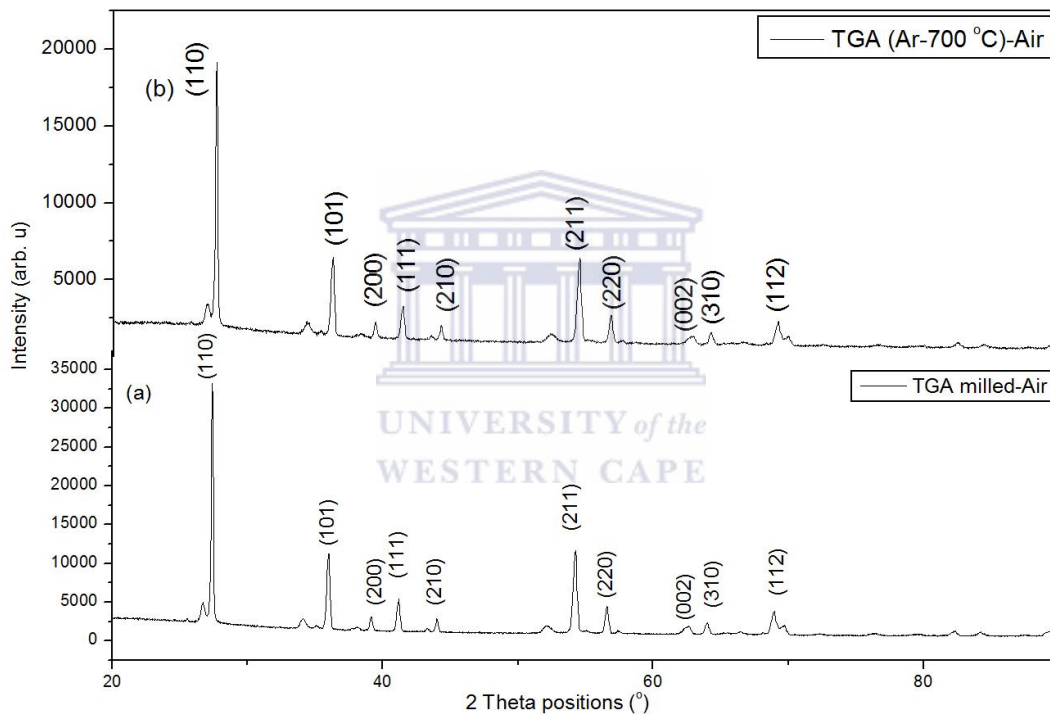
Fig. 4.7: XRD pattern of the milled Ti-Sn and milled pre-annealed samples obtained after TGA analysis in air.

Fig. 4.8a-c shows the Raman spectra of TiO_2, SnO_2 and Sn to use as comparison with the Raman spectra of the milled and powders obtained after TGA analysis. The anatase Raman vibration modes at 142, 197, 399, 518 and 640 cm^{-1}, respectively are shown in **Fig. 4.8a**. The TiO_2 exhibits six Raman

active modes ($1A_{1g}$ at 520 cm^{-1}, $2B_{1g}$ at 395 cm^{-1} and $3E_g$ at 144, 199 and 638 cm^{-1}). The most intense peaks observed at 144 cm^{-1}, 520 and 638 cm^{-1} are due to the anatase phase [4.20]. The analyzed SnO$_2$ Raman active modes appeared at 300, 359, 443, 574, 639 and 791 cm^{-1} while the Sn powder sample does not show any strong vibration modes, as shown in **Fig. 4.8c**. Moreover, some fundamental Raman peaks of nanocrystalline rutile SnO$_2$ may not be detectable in the rutile bulk SnO$_2$ [4.21]. For N-doped SnO$_2$, Raman peaks appear at 253.9, 302.1, 556.3 and 627.8 cm^{-1} [4.10].
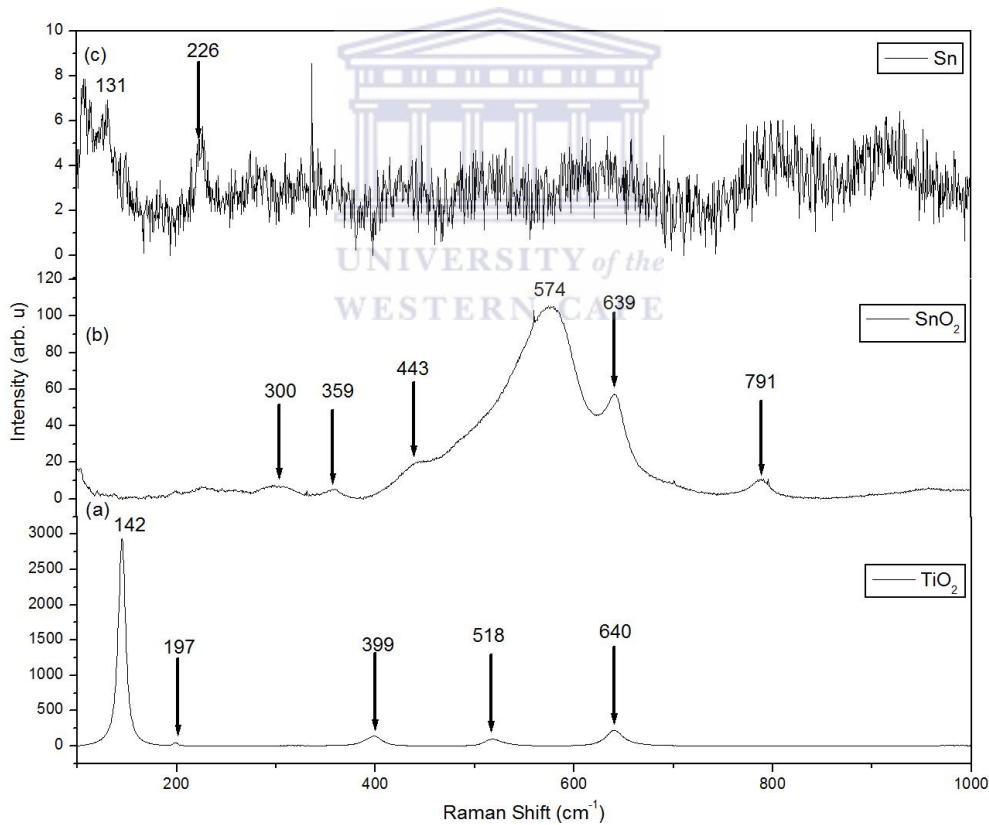
Fig. 4.8: Raman spectra of TiO$_2$, SnO$_2$ and Sn powders

Fig. 4.9a shows the Raman spectra of the 30 h-milled Ti-Sn powder. The Raman peaks are broad with low intensities, in agreement with the XRD results. The Raman peaks for milled powder appear at 288, 843, 1001 and 1042 cm^{-1}, respectively. In addition, the milled sample analysed using TGA in air shows Raman vibration modes at 190, 330, 442, and 573 cm^{-1} in **Fig 4.9b**. A Raman peak appearing at 574 and 580 cm^{-1} belongs to A$_{1g}$ mode intensity, which arises either as a consequence of an increase in the surface-to-volume atom ratio or due to conversion from crystalline to nanocrystalline form, induced by increasing the number of disordered atoms by milling **[4.22]**. These intensity peaks of the TGA sample are comparable to those obtained after Raman analysis of the TGA powder for the pre-annealed sample **(Fig 4.9c)**, in agreement with the XRD patterns shown in **Fig. 4.7.** Due to the presence of Sn, these Raman modes are different from those of pure TiO$_{2-x}$N$_y$ and TiO$_x$N$_y$ recently published **[4.15].** The difference in Raman intensity peaks are attributable to varying Ti:Sn and N:O ratios. Morever, It is known that the stretching wavenumber peaks are related to the force constants and lengths of the bonding; consequently Raman analysis can offer vital information on the Ti–O bond lengths of TiO$_x$N$_y$ **[4.23]**. The best known empirical relations between stretching wavenumbers (ν) and equilibrium bond lengths (R) are given below:

$$\nu = \exp(-BR) \quad \text{or} \quad \nu = A - BR \tag{4.2}$$

where A and B are experimentally derived fitting parameters **[4.23]**. Annealing in air has phased out all the Raman peaks found on the milled powder. This implies that crystallization and phase transformation has occurred, which was confirmed by the new Raman vibration modes of the TGA powder samples.
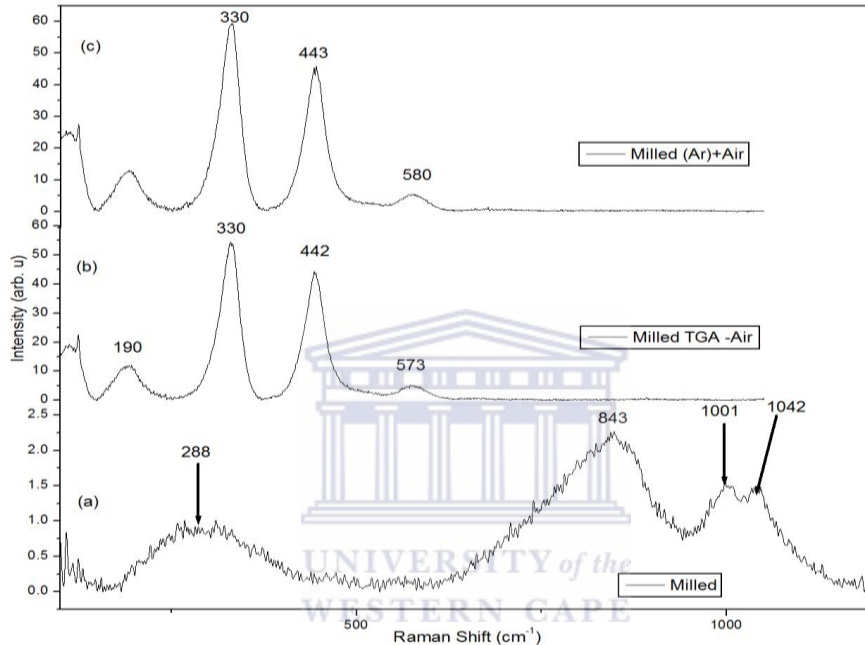
Fig. 4.9:   Raman spectra of 30 h-milled its sample after TGA and the pre-annealed TGA Ti-Sn powders. The TGA analysis of the powders was done air.

4.4. CONCLUSION

In conclusion, HCP solid solution was induced by Ball milling of Ti_{75}-Sn_{25} powder and yielded a compressed lattice parameters a=2.929 Å; c=4.780 Å and c/a=1.63. Upon annealing in Ar at 700 °C, lattice parameters a=5.916 Å; c=4.764 Å with (c/a=0.80) was detected. The XRD analysis confirms phase transformation

of Ti-Sn to Ti_3Sn intermetallic. The particles of the milled powder after TGA analysis show porous structure unlike those in the as-milled condition. The milled Ti-Sn has increased mass slightly at a faster rate than the pre-annealed Ti_3Sn intermetallic powder during TGA analysis. The high magnification image display shows agglomerated fine rectangular rod-shaped particles of different sizes. A large irregular particle appears to be an agglomeration of finer particles. The Ar pre-annealed particles are interconnected and appear as small grains with well-defined grain boundaries. The crystal structures of milled and pre-annealed powders show phase transformation from HCP to tetragonal phases, respectively. The former sample have the lattice parameters a=4.985 Å; c=2.962 Å, c/a=0.594, while the latter sample have a=4.582 Å; c=2.953 Å and c/a=0.644, respectively. These phases are attributed to tetragonal oxynitride of rutile-type. The roughness of the milled powder has increased from 1.078 nm to 3.448 nm after annealing. The high PL intensity was obtained on the milled powder due to defects generated by milling, and is agreement with broadening of the XRD peaks. Raman intensity is also consistent with the XRD results. This powder will be useful to industries interested in the biomedical, structural and damping capacity applications. The milled sample analysed using TGA in air shows Raman vibration modes at 190, 330, 442, and 573 cm^{-1}. A Raman peak appearing at 574 and 580 cm^{-1} is well-known as the A_{1g} mode intensity, which arises either as a consequence of the increase in the surface-to-volume atom ratio, or is due to conversion from crystalline to nanocrystalline forms induced by

an increasing number of disordered atoms on milled and annealed samples in air **[4.22].**

4.6. REFERENCES

[4.1] F. Vaz, P. Cerqueira, L. Rebouta, S.M.C. Nascimento, E., Thin Solid Films, 447-448 (2004) 449-454.

[4.2] J.M. Chappe, N. Martin, J. Lintymer, Applied Surface Science 253 (2007) 5312-5316.

[4.3] C. Nunes, V. Teixeira, M.L. Prates, N.P. Barradas, A.D. Sequeira, Thin Solid Films 442 (2003) 173-178.

[4.4] R.J. Koerner, L.A. Butterworth, I.V. Mayer, R. Dasbach, H.J. Busscher, Biomaterials 23 (2002) 2835-2840.

[4.5] F. Vaz, P. Cerqueira, L. Rebouta, S.M.C. Nascimento, E. Alves, Ph. Goudeau, J.P. Riviere, Surface Coatings & Technology 174-175 (2003) 197-203.

[4.6] J-H. Kim, Y.-M. Im, J.-P.l. Noh, S. Miyazaki, T.H. Nam, Scripta Materialia 65 (2011) 608–610.

[4.7] H.J. Choi, J.-H. Kim, J.P. Noh, S. Miyazaki, Y.-W, Kim T.H. Nam, Scripta Materialia 65 (2011) 611–614.

[4.8] C. Wu, L. Shen, H. Yu, Q. Huang, Y. C. Zhang, Materials Research Bulletin 46 (2011) 1107–1112.

[4.9] E Barrera, T Viveros, A Montoya, M Ruiz, Solar Energy Materials & Solar Cells 57 (1999) 127-140.

[4.10] G.X. Zhou, S.J. Xiong, X.L. Wu, L.Z. Liu, T.H. Li, Paul K. Chu, Acta Materialia 61 (2013) 7342–7347.

[4.11] S. Lee, In-Sun Choa, D. Kyu Lee, D. W Kim, T.H. Noh, C.H. Kwak, S. Park, K.S. Hong, J-K Lee, H.S. Jung, J Photochemistry Photobiology A: Chemistry 213 (2010) 129–135.

[4.12] A.S. Bolokang, Journal of Alloys Compounds 477 (2009) 905–908.

[4.13] A.S. Bolokang, M.J. Phasha, C. Oliphant, D. Motaung, International Journal of Refractory Metals and Hard Materials 29 (2011) 108–111.

[4.14] A.S. Bolokang, MJ Phasha, International Journal of Refractory Metals and Hard Materials 28 (2010) 610-615.

[4.15] A.S. Bolokang, M.J. Phasha, D.E. Motaung, F.R. Cummings, T.F.G. Muller, C.J. Arendse, Materials Letters 132 (1) (2014) 157-161.

[4.16] M. Koufaki, M. Sifakis, E. Iliopoulos, N. Pelekanos, M. Modreanu, V. Cimalla, G. Ecke, E. Aperathitis, Applied Surface Science 253 (2006) 405–408.

[4.17] O. Ivanova, M. Karpets, A.R. Yavari, K. Georgarakis, Y. Podrezov, Journal of Alloys Compounds 582 (2014) 360-363.

[4.18] J.W. O'Brien, R.A. Dunlap, J. Dahn, Journal of Alloys Compounds 330-332 (2002) 60-64.

[4.19] S. A. Pawar, R.S. Devan, D.S. Patil, V.V. Burungale, T.S. Bhat, S.S. Mali, S.W. Shin, J.E. Ae, C.K. Hong, Y.R. Ma, J.H. Kim, P.S. Patil, Electrochimica Acta 117 (2014) 470– 479.

[4.20] S. Daothong, N. Songmee, S. Thongtem, P. Singjai, Scripta Materialia 57 (2007) 567-570.

[4.21] A. Ayeshamariam, S. Ramalingam, M. Bououdina, M. Jayachandran, Molecular and Biomolecular Spectroscopy 118 (2014) 1135–1143.

[4.22] L. Popovic, D. de Waal, J.C.A. Boeyens, Journal of Raman Spectroscopy 36 (2005) 2–11.

[4.23] G.D. Chryssikos, Journal of Raman Spectroscopy 22 (1991) 645–650.

SUMMARY

BM of Ti-SA mixture did not change the lattice parameter of pure Ti. The 15 h Ti-SA shows multiple Raman peaks at 142 cm^{-1}, 257 cm^{-1}, 414 cm^{-1}, 609 cm^{-1}, 711 cm^{-1}, 834 cm^{-1}, 1322 cm^{-1} and 1611 cm^{-1}. The 15 h Ti sample prepared without SA, shows peaks at 460, 541, 795, 1088, 1611 cm^{-1}. The shifting of peaks is attributed to the difference in the crystallite sizes.

FCC TiO_xN_y was synthesized by annealing of ball-milled Ti in air at 900 ºC. The traces of rutile-type $TiO_{2-x}N_x$ solid solution were detected while morphology of the synthesized powder displayed multiple colours. The estimated average crystallite sizes of $TiO_{0.61}N_{0.29}$ and $TiO_{1.56}N_{0.56}$ are 66.72 nm 106.65 nm, respectively. During the high temperature reaction, the rutile-TiO_2 phase form first due to the higher heat of formation favorable for TiO_2. As the temperature decreases, N_2 occupies the oxygen vacancies present in TiO_2 and induce $TiO_{2-x}N_x$ formation. Concurrently, N_2-rich particles promote the formation of $TiO_{0.61}N_{0.29}$ phase. The observed shift of the Raman active peaks to higher wavenumber is attributed to the formation of $TiO_{0.61}N_{0.29}$ phase.

After alloying Ti with Sn (Ti_{75}-Sn_{25}) using BM, HCP solid solution was induced with lattice parameters a=2.929 Å; c=4.780 Å and c/a=1.63. Upon annealing in Ar at 700 °C, lattice parameters a=5.916 Å; c=4.764 Å with (c/a=0.80) was formed. The XRD analysis confirms phase transformation of Ti-Sn to Ti_3Sn intermetallic. The particles of the milled powder after TGA analysis show porous structure unlike those in the as-milled condition. The milled Ti-Sn has increased mass
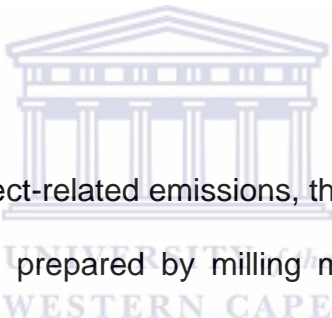
slightly at a faster rate than the pre-annealed Ti_3Sn intermetallic powder during TGA analysis. The image display agglomerated fine rectangular rod-shaped particles of different sizes. The pre-annealed sample under Ar shows particles that are interconnected and appear as small grains with well-defined grain boundaries. The crystal structures of milled and pre-annealed powders has transformed from HCP to tetragonal structure. The former sample have the lattice parameters a=4.985 Å; c=2.962 Å, c/a=0.594 while the latter sample have a=4.582 Å; c=2.953 Å and c/a=0.644, respectively. These phases are attributed to tetragonal oxynitride of rutile-type. The roughness of the milled powder has increased from 1.08 nm to 3.45 nm after annealing. The high PL intensity was obtained on the milled powder due to the high volume of defects generated by the milling operation. This is in agreement with the broadening of XRD peaks and is also consistent with Raman results. This powder will be useful to industries interested in the biomedical, structural and damping capacity applications. The milled sample that was analyzed with the TGA in air shows Raman vibration modes at 190, 330, 442, and 573 cm^{-1}. A Raman peak appearing at 574 and 580 cm^{-1} is assigned to the A_{1g} mode intensity, which arises either as a consequence of the increase in the surface-to-volume atom ratio or due to conversion from crystalline to nanocrystalline form, induced by an increasing number of disordered atoms on milled and annealed samples in air **[4.22].**

SECTION B

CHAPTER FIVE

Characteristics of the Mechanical Milling on the Room Temperature Ferromagnetism and Sensing Properties of TiO$_2$ Nanoparticles

ABSTRACT

The correlation between defect-related emissions, the magnetization and sensing of TiO$_2$ nanoparticles (NPs) prepared by milling method, is reported. Surface morphology analyses showed that the size of the TiO$_2$ NPs decreases with milling time. Raman and XRD studies demonstrated that the structural properties of the TiO$_2$ transform to orthorhombic structure upon milling. Magnetization improved with an increase of a defect-related band originating from oxygen vacancies (V$_O$), which can be ascribed to a decrease in the size of the NPs due to the milling time. Moreover, the longer-milled TiO$_2$ exhibited enhanced gas-sensing properties to humidity in terms of sensor response, with about 12 s response time at room temperature. A combination of photoluminescence, x-ray photoelectron spectroscopy, vibrating sample magnetometer and sensing

analyses demonstrated that a direct relation exists between the magnetization, sensing and the relative occupancy of the V_O present on the surface of TiO_2 NPs.

5.1. INTRODUCTION

After the theoretical prediction of room temperature ferromagnetism (RTFM) in manganese (Mn)-doped zinc oxide (ZnO) and its high Curie temperature due to strong p-d hybridization, the emerging field of spintronics generated a widespread interest due to its potential to provide new functionalities and enhanced performance in conventional electronic devices **[5.1, 5.2]**. Despite some initial promising results on dilute magnetic semiconductor (DMS), the basis of RTFM in DMS is not fully understood, and the mechanism behind the magnetic ordering is still under debate; in addition it is not clear if they can display this required high-temperature magnetism, that is, Curie temperature (T_C) (above 300 K) in order to be useful for spintronic applications **[5.3-5.5]**. More importantly, to achieve spintronic devices, RTFM should be an intrinsic property of the semiconducting host matrix. Recent reports using innovative characterization tools such as X-ray absorption spectroscopy and X-ray magnetic circular dichroism (XMCD) ruled out the possibility of RTFM being due to extrinsic effects associated with 3d cations, demonstrating that the 3d electronic shells of the cations in these diluted magnetic oxides (DMOs) do not carry any measurable ferromagnetic moment. Scientists also reported RTFM in undoped oxides such as TiO_2, HfO_2, ZnO, and In_2O_3. RTFM in these materials could be related to surface defects and/or interface defects **[5.6-5.9]** which are induced during the preparation process. Previous results calculated that the FM observed in undoped TiO_2 largely originates from the d-orbitals of low-charge-state Ti cations converted from Ti^{4+} cations, which are induced by the surface oxygen vacancies

[5.10, 5.11].

Furthermore, most recent reports by Chaboy et al. **[5.12]** and Guglieri et al. **[5.13, 5.14]** using XMCD analyses carried out on ZnO nanoparticles (NPs) capped with organic molecules and without any 3d doping, have shown the existence of an intrinsic ferromagnetic contribution. They suggested that it branches from the interface formed between the ZnO core of the NP and the capping region created by bonding to the organic molecules. Additionally, there is a need for reproducibility of a FM signal in undoped oxides systems prepared with the same growth conditions, which add to the controversy about the origin of FM. Céspedes et al. **[5.15]** and Straumal et al. **[5.16, 5.17]** reported that magnetism in undoped oxides depends on the structural details of the sample, especially at the near-surface regions (surface, grain boundaries, or interfaces). Therefore, since magnetic properties are usually affected by the synthesis conditions, morphology and grain sizes, we have chosen in this study to carry out mechanical milling (MM) treatment for further structure refinement and size reduction of TiO_2 powders. MM is a well-known solid-state powder process involving welding and fracturing of particles in a high energy milling process **[5.18]**. Despite all the achievements, the use of MM for spintronic applications has been limited to few cases. It has been found that ball milling induces the phase transformation from anatase to rutile which results in FM above room temperature in the milled TiO_2 doped with Fe **[5.19]**. Chen et al. **[5.20]** reported that by doping TiO_2 with a non-magnetic Al in a $(TiO_2)_{1-x}Al_x$ (x = 0-0.5) composition. Using X-ray absorption near-edge structures spectroscopy they

found that there is a charge transfer from Al to O at the interface of nanograins, signifying that the charge-transfer ferromagnetism is a possible mechanism in the nanostructured TiO_2-Al system.

However, apart from spintronic applications, systems for monitoring the air quality are vital for quality control of products in different industries that includes electronic devices, precision instruments production, textile area, food storage, and human comfort in domestic environments **[5.21]**. Humidity control is very imperative in a wide range of our daily life and for industrial processes, air conditioning, electronics processing, since higher relative humidity also induces the outside temperature to be hotter in the summer and reduces the effectiveness of sweating to cool the body, by preventing the evaporation of perspiration from the skin. As a result intensive research has been carried out in a large range of metal oxide (MOX) materials as humidity sensor elements in order to achieve the necessary requirements for practical application of humidity sensors, with good sensitivity over a wide range of humidity and temperature, short response time, good reproducibility, etc. **[5.22-5.25]**. The principle of humidity measurement with MOX-based sensors is the change in electrical capacitance or conductivity owing to water vapour chemisorption and physisorption on the surface of the sensing element. Despite the many successes there are few reports on humidity sensors based on milled anatase-TiO_2, as well as studies on the correlation between magnetism and sensing. Therefore, in the current study we investigate the effect of MM time on the magnetic and structural properties of milled anatase-TiO_2 NPs. Additionally a

simple approach to fabricate humidity sensors based on TiO_2 NPs is presented and these results are correlated with the optical and magnetic properties.

5.2. EXPERIMENTAL PROCEDURE

Anatase titanium dioxide (TiO_2) powder of high purity was subjected to high energy ball/mechanical milling (MM). The powders were charged in a milling vial filled with argon gas inside a glove box. MM was done for 60 and 120 h intervals. Small samples were collected inside the glove box for characterization. The surface morphology of the TiO_2 samples was studied using field-emission scanning electron microscopy (FE-SEM, Zeiss-Auriga). Phase evolution was traced with a PANalytical X'pert PRO PW 3040/60 X-ray diffraction (XRD) machine fitted with a Cu K_α radiation source. High-resolution transmission electron microscopy was employed to investigate the localized phase formation and crystal growth of the milled NPs. Electron micrographs and selected area diffraction patterns (SAED) were collected with an FEI Tecnai G^{2}20 FE-TEM. Raman measurements were collected using a Horiba Jobin-Yvon HR800 Raman microscope equipped with an Olympus BX-41 microscope attachment. An Ar^+ laser (514.5 nm) with energy setting 1.2 mW from a Coherent Innova Model 308 was used as an excitation source.

Optical properties were measured using a Perkin-Elmer Lambda 750 UV-vis and a Jobin-Yvon NanoLog photoluminescence spectrometer. Nitrogen (N_2) adsorption-desorption isotherms were obtained using Micrometiritics TRISTAR 3000 surface area analyzer (USA) after samples were outgassed at 110 °C

under 10^{-2} mm Hg for 6 h. Specific surface area analyses were carried out by the Brunauer-Emmet–Teller (BET) method using desorption isotherms. X-ray photoelectron spectroscopy measurements were carried using a PHI 5000 Versaprobe-Scanning ESCA Microprobe. The survey scans were recorded with a 100 µm, 25 W, 15 kV beam using monochromatic Al K_α radiation (hv = 1486.6 eV) and for the higher resolution spectra the hemispherical analyzer pass energy was maintained at 11.8 eV (C1s, O1s, Ti_{2p}) for 50 cycles. Measurements were performed using either a 1 eV/step and 45 min acquisition time (binding energies ranging from 0-1400 eV) for survey scans or a 0.1 eV/step and 20-30 min acquisition times for the high resolution scans. The pressure during acquisition was typically under 1×10^{-8} Torr. The surfaces were also cleaned by sputtering for 30 s using an Ar ion gun (2 kV energy ions), and measurements were repeated. A minicryogen-free measurement system with a vibrating sample magnetometer, VSM (type J3505 mini CFM-VSM) was used to study the magnetization properties for TiO_2 semiconductor nanoparticles milled for 120 h. Since this type of samples tend to exhibit small magnetization signals, special care was taken during measurements as to avoid magnetic contamination **[5.26, 5.27]**. Magnetic measurements carried out on different batches of TiO_2 powders displayed consistent and reproducible results, demonstrating RTFM behaviour. These measurements included magnetic hysteresis loops, zero-field-cooling (ZFC) and field-cooling (FC) magnetizations. The magnetic hysteresis loops were obtained at various isothermal temperatures between 4 K and 300 K in applied magnetic fields of up to 50 kOe. ZFC and FC magnetization curves as a function of

temperature were recorded in applied magnetic fields of 0.1, 0.5, 15 and 30 kOe. The lower curve of ZFC was obtained after the sample was cooled down in zero-field from 300 K to 4 K. The magnetization curve (M_{ZFC}) was recorded while warming up the sample in a static applied magnetic field from 4 to 300 K. During the field cooling procedure the sample was cooled from 300 K to 4 K in the presence of an external static magnetic field. The magnetization curves (M_{FC}) were recorded while warming up the sample in the same field.

The TiO$_2$ NPs were dispersed in ethanol and drop-coated on alumina substrates (size: 2 mm × 2 mm) with two Pt electrodes (on its top surface) and a micro-heater (on its bottom surface). The deposited sensitive layer was heated to 250 °C to remove the organic solvent used and to obtain good adhesion. The sensing measurements were carried out at room temperature. To test the device, the desired level of relative humidity (RH) was achieved by bubbling the water by air and mixed with dry air before entering in the sensing chamber. The humidity inside the chamber was monitored using an in-built humidity sensor. The humidity response of the device was surveyed through monitoring the variation of the resistance of the sensors using a gas sensing station KSGAS6S (KENOSISTEC, Italy).

5.3. RESULTS AND DISCUSSION

Fig. 5.1a shows that the un-milled TiO_2 nanoparticles (NPs) are almost spherical in shape, well resolved and agglomerated with an average size ranging from 80 to 130 nm. Upon milling for 60 hrs, the NPs are less agglomerated, as shown in **Fig. 5.1b. Fig. 5.1c** shows that the degree of agglomeration also increases with increasing duration of milling (120 hrs) and the particle size reduces to about 40 nm upon milling for 120 hrs.
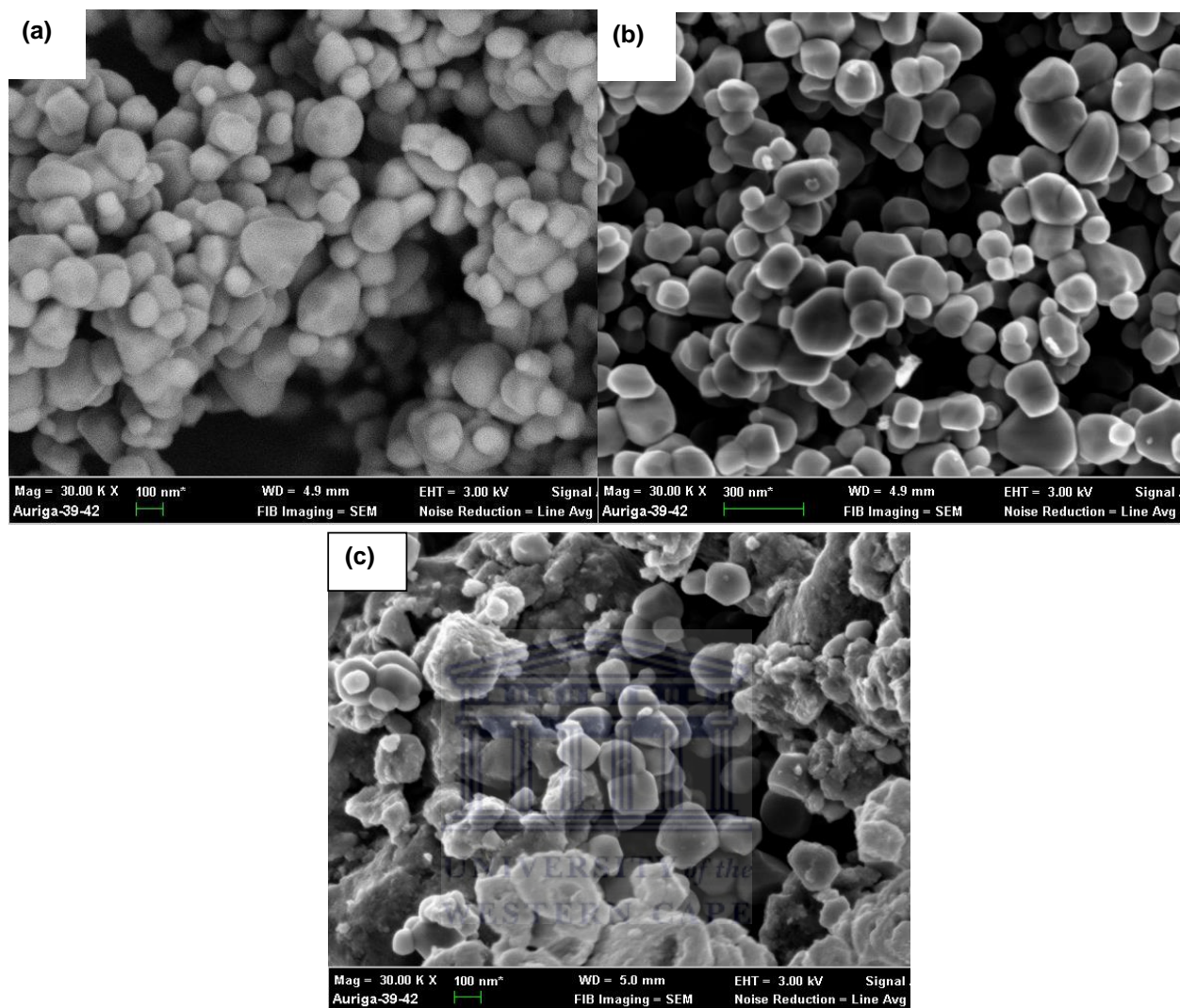
Fig. 5.1: SEM micrographs of the (a) 0 (b) 60 (c) 120 hrs milled TiO_2 powders.

Fig. 5.2a presents the XRD patterns of un-milled anatase-TiO_2 NPs with tetragonal crystal structure and lattice parameters of a=3.782 Å; c=9.502 Å. It is clear from **Fig. 5.2b** that the anatase structure remained stable after milling for 60 h, while its lattice constants *a* and *c* reduced slightly to 3.777 and 9.501 Å, respectively. Upon milling for 120 hrs the XRD intensity reduced while the full-width at half maximum (FWHM) broadened **(Fig. 5.2c).** The broadening of peaks

is associated with crystallite refinement and the disordering of the crystal structure. This ordering is confirmed by the detected metastable orthorhombic phase which has lattice parameters a=4.523 Å; b=4.696 Å; c=2.962 Å, respectively. Traces of the anatase-TiO_2 phase with lattice parameters a=3.783 Å; c=9.497 Å was detected. The orthorhombic structure detected after milling do not share a similar crystal structure with the known Brookite orthorhombic (TiO_2-II). Bose et al. **[5.28]** reported the lattice parameters a=4.536 Å; b=5.502 Å; c=4.942 Å of orthorhombic TiO_2-II after 100 h ball milling. In addition, orthorhombic $TiO_{1.94}$ structure was established with lattice parameters a=9.38 Å; b=9.19 Å; c=5.88 Å **[5.29]**. These results were supported by reduction of TiO_2 by hydrogen, whereby orthorhombic $TiO_{2-\delta}$ with lattice parameter a= 9.31 Å was achieved **[5.30]**. Rezaee et al. **[5.29]** reported the orthorhombic Brookite transformation at varying milling speeds. The lattice parameters a=9.101 Å; b=9.195.455 Å; c=4.942 Å and crystallite size of 64 nm were obtained **[5.31]**. Therefore, it is evident that the orthorhombic lattice parameters observed in the current work is not similar to those already reported in literature.
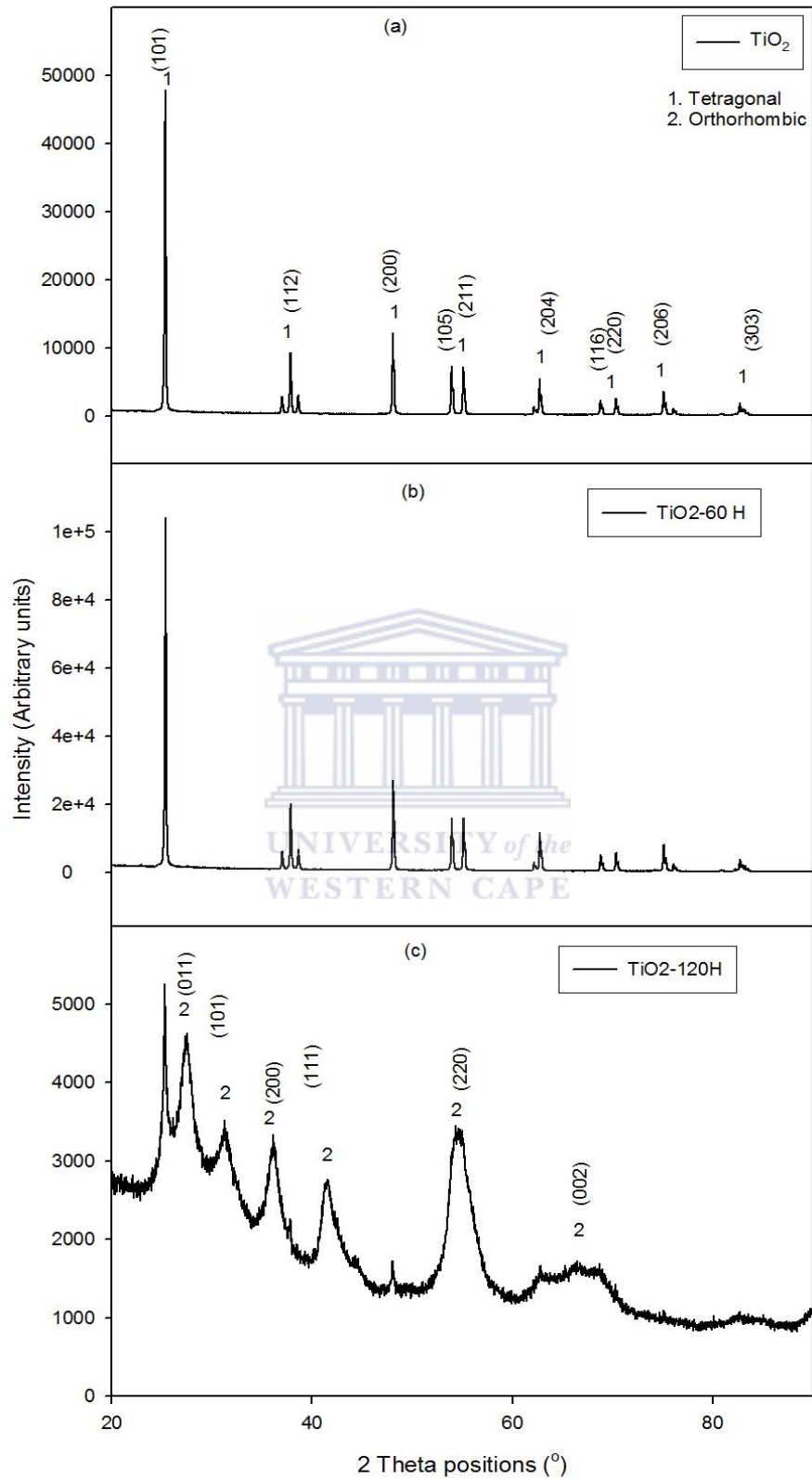
Fig. 5.2: (a-c) XRD profiles of the un-milled and milled TiO$_2$ powders.

The TEM image in **Fig. 5.3a** confirms that the un-milled TiO_2 NPs are mainly of spherical shape with a diameter of 116 ± 0.5 nm, which corresponds to the crystallite size calculated from XRD patterns. **Fig. 5.3b** shows the high resolution TEM image for an isolated TiO_2 NP. The uniform fringes with an interval of 0.355 nm, corresponding to (101) lattice spacing of anatase phase, are observed over the entire particle **[5.32]**. Selected area electron diffraction (SAED) shown in the inset of **Fig. 4.3b** clearly indicates that the TiO_2 NPs are highly crystalline in nature. The HRTEM image in **Fig. 5.3c** shows that the anatase grain sizes decrease from 115 nm for pure TiO_2 powder to about 40 nm for 120 h-milled TiO_2 powders as confirmed by the size distribution (see insets). This is very close to the average particle size determined from XRD analysis. It is also evident from the micrographs that the NPs almost retain their spherical shapes even after long durations of milling. A similar result has also been obtained from XRD analysis. SAED patterns of the milled samples **(Fig. 5.3d)** reveal that the number of diffraction rings decreases with increasing milling time and that the rings are quite broad, which indicates that the particles are very small in size. This is consistent with the XRD patterns which indicated that the peak broadening increases with increasing milling time.
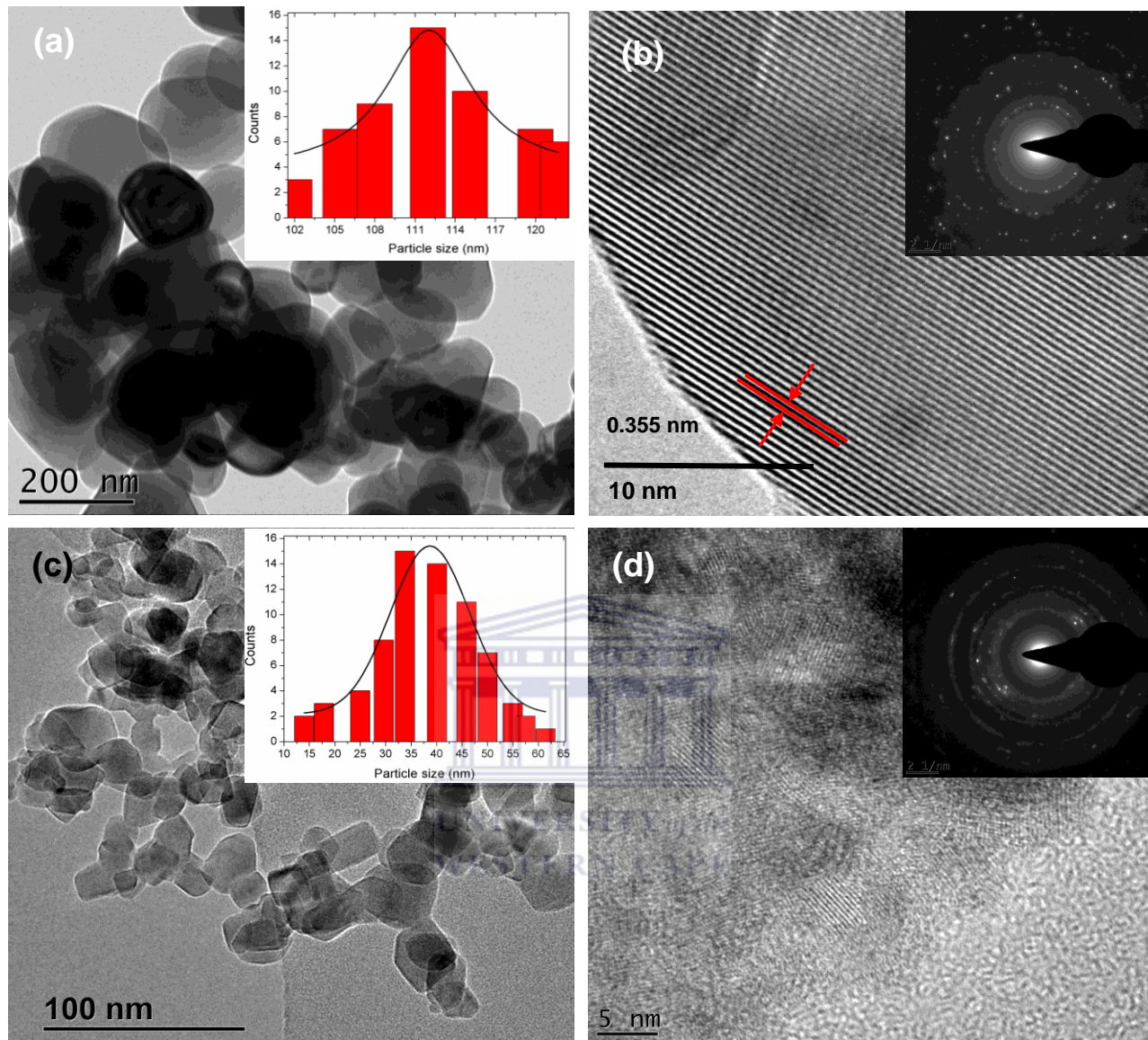
Fig. 5.3: HR-TEM images of the (a-b) 0 h and (c-d) 120 hrs-milled TiO$_2$ NPs and their corresponding SAED patterns. Inset in (a) and (c) corresponds to the particle size distribution of the 0 h and 120hrs-milled powders.

The Raman spectra of the TiO$_2$-NPs milled at different times are shown in **Fig. 5.4**. The un-milled and 60 h-milled TiO$_2$ NPs exhibit six Raman active

modes ($1A_{1g}$ at 518 cm^{-1}, $2B_{1g}$ at 399 and 518 cm^{-1} and $3E_g$ at 144, 199 and 641 cm^{-1}) **[5.33]**. The strongest peaks at 144 cm^{-1}, 520 and 639 cm^{-1} due to anatase phase are in agreement with the one reported in ref **[5.34]**. An increase of milling time induces a shift in the peak positions to higher wavenumbers. The intensity and the FWHM are often used as an indication of the ordering in the material. Therefore the high intensity of the unmilled and 60 milled TiO$_2$ indicates a highly ordered/crystalline material.
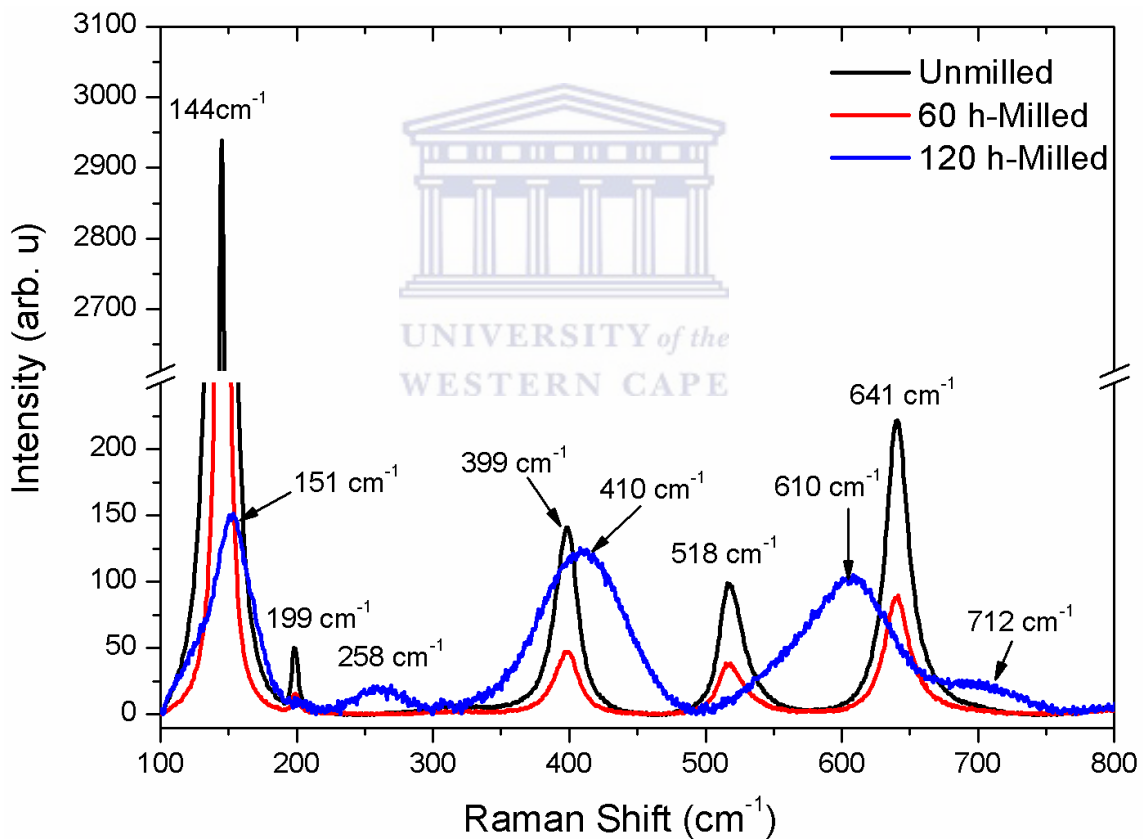

Fig. 5.4: Raman spectra of the un-milled and milled TiO$_2$ NPs at different milling times.

When milling for 120 h, the intensities of the peaks reduce while the FWHM increases, which indicates a disordering in the TiO_2 structure, entirely consistent with the XRD analysis. In addition, it is clear that the peaks positions shift to higher wavenumbers with broad bands around 151, 260, 410 and 610 cm^{-1}. The broad peaks at 410 and 610 cm^{-1} can be attributed to the Raman active modes E_g and $A1_g$ of rutile TiO_2, respectively [5.35]. The broad band at around 260 cm^{-1} results from second-order scattering [5.36], while the peak at around 151 cm^{-1} is due to the anatase phase, suggesting that traces of the anatase-TiO_2 phase are still present.

Fig. 5.5 (a) shows the UV-vis absorption spectra of the un-milled and milled TiO_2 NPs. The un-milled TiO_2 exhibits an absorption peak in the region of 360-380 nm. However, when the NPs are milled, an improvement in the absorption and a slight blueshift are observed, due to reduction of the particle size observed by SEM and TEM analyses. The band gap of these samples can be calculated using Tauc's formula [5.37]:

$$\alpha h v = A(h v - E_g)^{n/2} \quad (1)$$

where α is the absorption coefficient, A is a constant, hv is the energy and n depends on whether the transition is indirect (n = 4) or direct (n = 1). It is clear from **Fig. 5.5b** that the band gap reduces with milling time and from this plot, the band gaps of the un-milled, 60 and 120 h milled TiO_2 NPs were estimated to be 4.183, 4.182 and 4.179 eV, respectively.
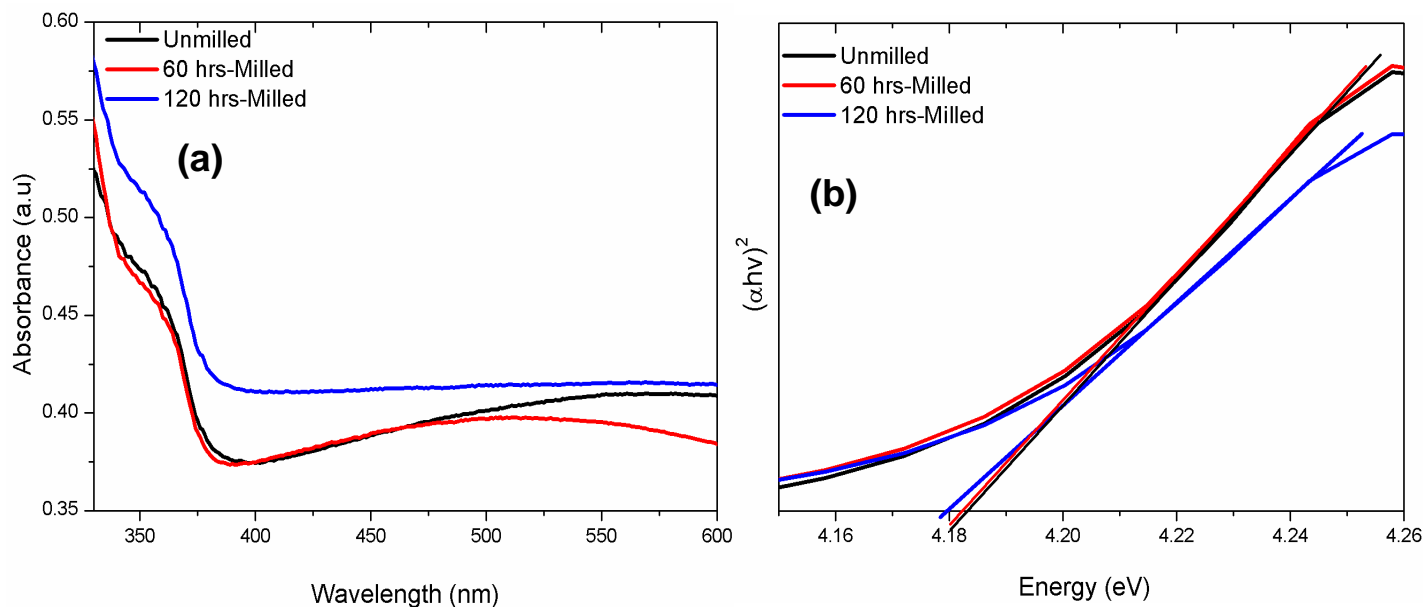
Fig. 5.5: (a) UV-vis absorption spectrum of the un-milled and milled TiO_2 NPs and (b) Tauc plots of $(\alpha h\nu)^2$ as a function of energy.

Fig. 5.6 depicts the PL spectra of the un-milled and milled TiO_2 NPs at various times. It can clearly be seen that the PL intensity increases with an increase in milling time. For detailed analysis, we have de-convoluted the spectrum into three peaks (400, 428 and 455 nm) with Gaussian functions. The PL emission band at 400 nm (3.0 eV) was suggested to be due to self-trapped excitons localized on TiO_6 octahedrals **[5.38, 5.39]**. An emission band located around 455 nm is attributed to the oxygen vacancy (V_O) on the surface area of TiO_2 and this emission is prominent for the 120h-milled TiO_2. PL emissions of TiO_2 at longer wavelengths (460 and 530 nm) result from the V_O on the surface area of TiO_2 nanowires **[5.38]**.
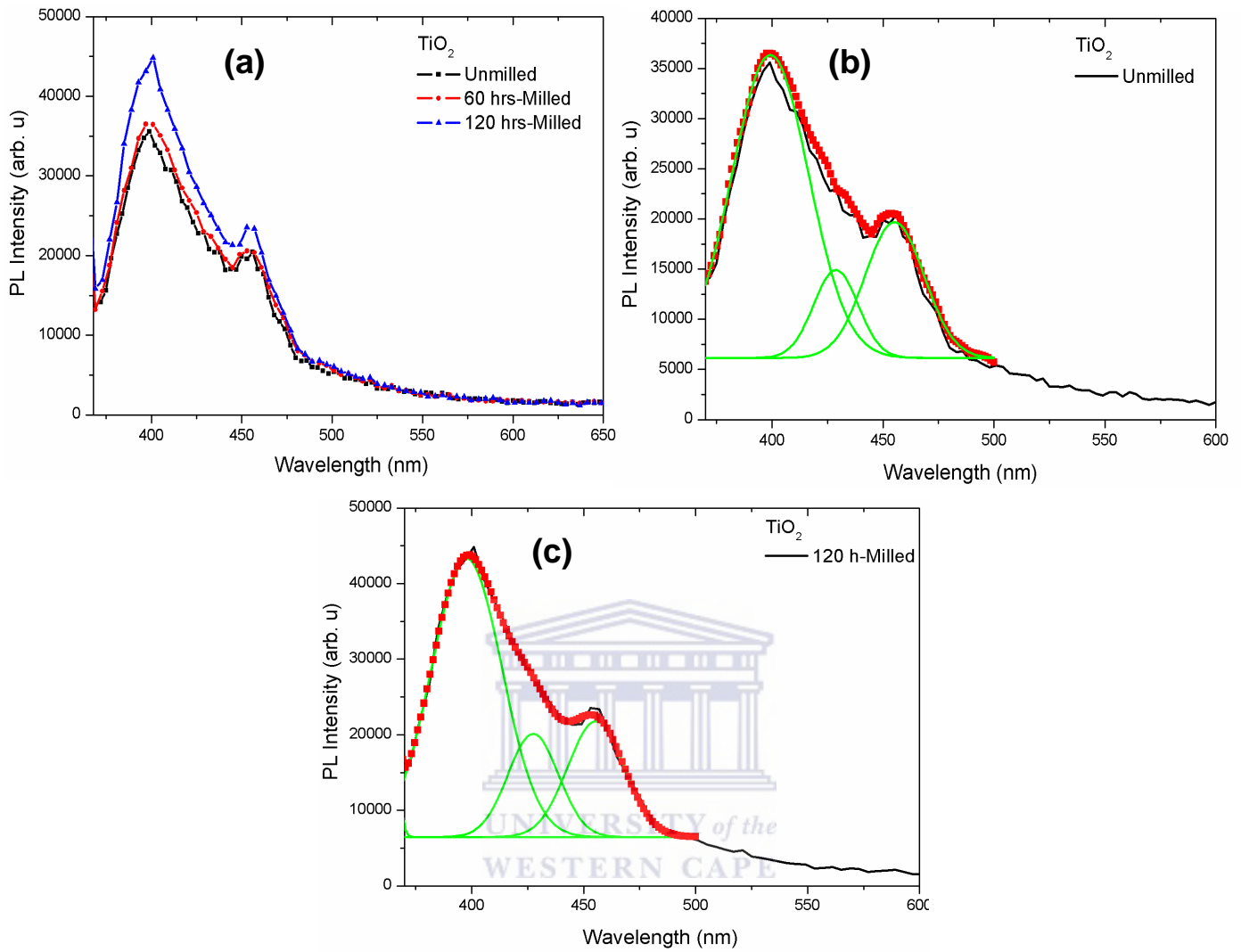
Fig. 5.6: (a) PL spectra of the un-milled and milled TiO_2 NPs. (b−c) Gaussian fits of each PL spectrum (the black lines are the experimental results and the red circles are Gaussian fits).

Fig. 5.7 depicts the typical N_2 adsorption/desorption isotherm curves of the unmilled and milled TiO_2 NPs. The hysteretic activity is related to both connectivity and the broadening of the pore size distribution in porous materials. It is clear that as the milling time increases, the isotherms shift downward while

111

the hysteresis loops at high relative pressure increases, denoting higher pore size distribution as well as higher BET surface area as depicted in **Table 5.1**.

Fig. 5.7: Typical N_2 adsorption and desorption isotherm curves.

Table 5.1: Surface areas (BET), total pore volumes (V_{pore}), pore diameters (d_{pore}), crystallites size (D) and energy band gap (E_g) of milled TiO_2 NPs.
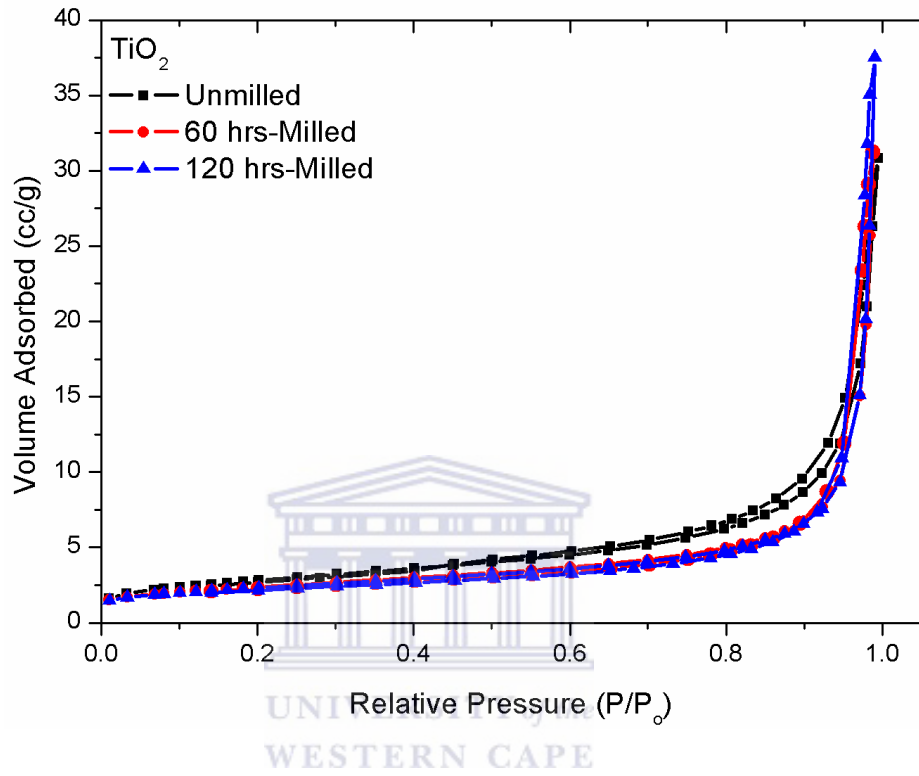
Milling time (hrs.)	BET ($m^2 g^{-1}$)	V_{pore} ($cm^3 g^{-1}$)	d_{pore} (nm)	D (nm)	FWHM (cm^{-1})	E_g (eV)
0	8.255	0.059	21.537	128.451	16.929	4.183
60	8.493	0.048	32.557	127.102	9.621	4.182
120	10.263	0.049	40.334	41.125	36.416	4.179

To complement the PL analyses, the chemical composition of the pure anatase TiO_2 in comparison to that of milled for 60 and 120 h was investigated by X-ray photoelectron spectroscopy (XPS), and the corresponding results are shown in **Fig. 5.8.** As observed in **Fig. 5.8,** the fully scanned spectra demonstrated that only Ti, O, and C elements existed in the pure and milled TiO_2, and no impurities are evident in the entire spectrum. The detected carbon is associated with the carbon tape used during the measurements, which adsorbed on the surface during the exposure of the sample to the ambient atmosphere. The binding energy for the C1s peak at 284.6 eV was used as the reference for calibration **[5.9]**.
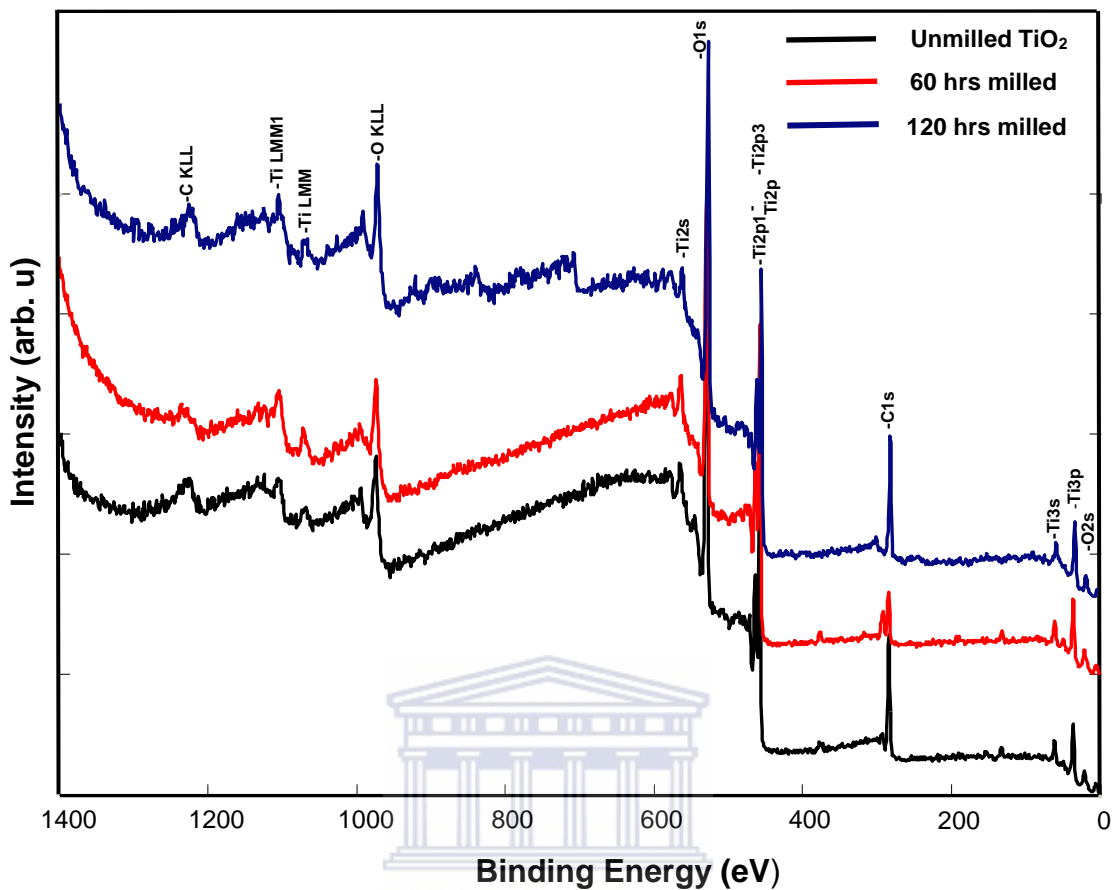
Fig. 5.8: XPS survey scan of unmilled and milled TiO_2 nanostructures

Fig. 5.9 displays high resolution XPS spectra of the Ti2p core-level of the pure and milled TiO_2. For the unmilled TiO_2 **(Fig. 5.9a),** the peaks centred at around 458.7 eV and 464.2 eV are assigned to Ti^{4+} ($2p_{3/2}$), and Ti^{4+} ($2p_{1/2}$) respectively **[5.40, 5.41]**. However upon milling for 60 hrs **(Fig. 5.9b)** the peaks become broad denoting that the milling induced significant changes in the nanocrystalline structure of TiO_2 and this is consistent with the XRD and Raman results. The 60 hrs milled sample show two peaks centred at 458.6 and 463.1 eV and two peaks at 459.1 and 464.8 eV. Upon milling for 120 hrs **(Fig. 5.9c),** the

114

broadening of the peaks becomes more discernible revealing two fitted peaks centred at 458.4 and 464.6 eV, assigned to Ti^{4+} ($2p_{3/2}$) and Ti^{4+} ($2p_{1/2}$) respectively, as well as two peaks at 457.0 and 463.3 eV. The peaks located at 457.0 and 463.3 eV are assigned to Ti^{3+} ($2p_{3/2}$) and Ti^{3+} ($2p_{1/2}$) respectively **[5.40]**.

Figs. 5.9d-f presents the O 1s core level spectra of the pure and milled TiO_2 at various times. It can be clearly seen that each O 1s signal of the pure TiO_2 and that milled for 60 hrs **(Fig. 5.9d and e)** could be fitted into two symmetric peaks. The peaks located at 529.67 and 531.55 eV corresponds to the oxygen vacancy-Ti^{4+} and oxygen vacancy-Ti^{3+}, respectively **[5.41, 5.42]**. It is observed from **Fig. 5.9f** that when the sample is milled for 120 hrs, broadening of the oxygen peaks also became more apparent and oxygen on the sample surface exists at least in three forms at the binding energies of 528.92, 529.85, and 531.61 eV, corresponding to oxygen vacancy-Ti^{2+}; oxygen vacancy-Ti^{4+} and oxygen vacancy-Ti^{3+}, respectively **[5.41, 5.42]**. This suggests that more oxygen vacancies are produced in the milled TiO_2 powder.
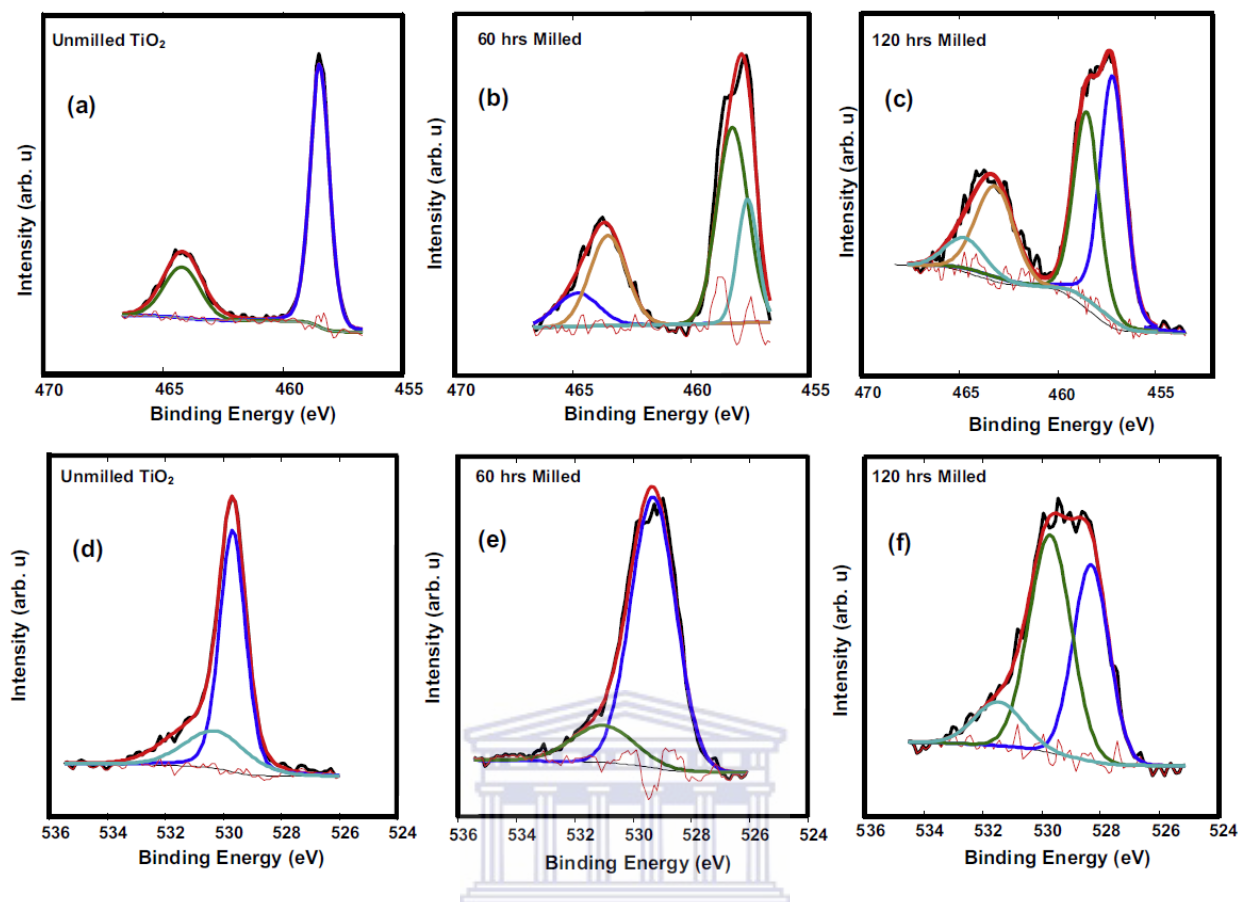
Fig. 5.9: Experimental and fitted curves for normalized Ti2p (a) unmilled, (b) 60 hrs milled, (c) 120 hrs milled and (d-f) corresponds to O1s XPS spectra of (d) unmilled, (e) 60 hrs milled and (f) 120 hrs milled TiO_2 nanostructures

Previous studies reported that during ball milling, partial Ti–O bonds on the TiO_2 surface layer may be broken due to mechanical activation and oxygen is released from the TiO_2 lattice. Therefore, oxygen vacancies are produced in the TiO_2 lattice **[5.42]**. Magnetic characterization of the un-milled and milled TiO_2 nanostructures was performed using VSM in the magnetic field range of 0-14kOe at various temperatures as shown in **Fig. 5.10.** It is evident from **Fig. 5.10a** that

116

the un-milled TiO_2 NPs reveal a paramagnetic signal. When milling for 60 hrs **(Fig. 5.10b)**, a weak ferromagnetic hysteresis loop with a contribution of paramagnetism is observed. The observed coercivity (H_c), remnant (M_r) and saturation magnetism (M_s) values are 158.04 Oe, 10.33 $\times 10^{-3}$ emu/g, and 1.26 $\times 10^{-3}$ emu/g respectively. The observed paramagnetism may be induced by possible interaction/impurity phases or TiO_2 clusters. When increasing the milling time to 120 hrs **(Fig. 5.10c),** clear magnetic hysteresis loops are observed for the NPs demonstrating room temperature ferromagnetism (RTFM) recorded at 19 different isothermal temperatures 4 - 300 K (some loops are not shown). The observed RTFM is thought to be due to higher V_O on the TiO_2 NPs surface (see PL results) and structure defect induced by the milling process, which result in coalescence of the ferromagnetic domains **[5.44]** such as reduced crystallites size (see Table 1). Previous studies **[5.9, 5.45-5.47]** showed that larger crystals are detrimental to magnetic properties. The origin of ferromagnetism for TiO_2 NPs diluted magnetic semiconductors can be explained by various carrier mediated mechanisms that include double-exchange, super-exchange or Ruderman-Kittel-Kasuya-Yosida (RKKY) exchange interactions **[5.44]**. Experimental magnetic moment per molecular unit (μ) in the Bohr magneton was calculated using the relation $\mu = M_w M_S / 5585$ where M_w is the molar mass **[5.48]**.
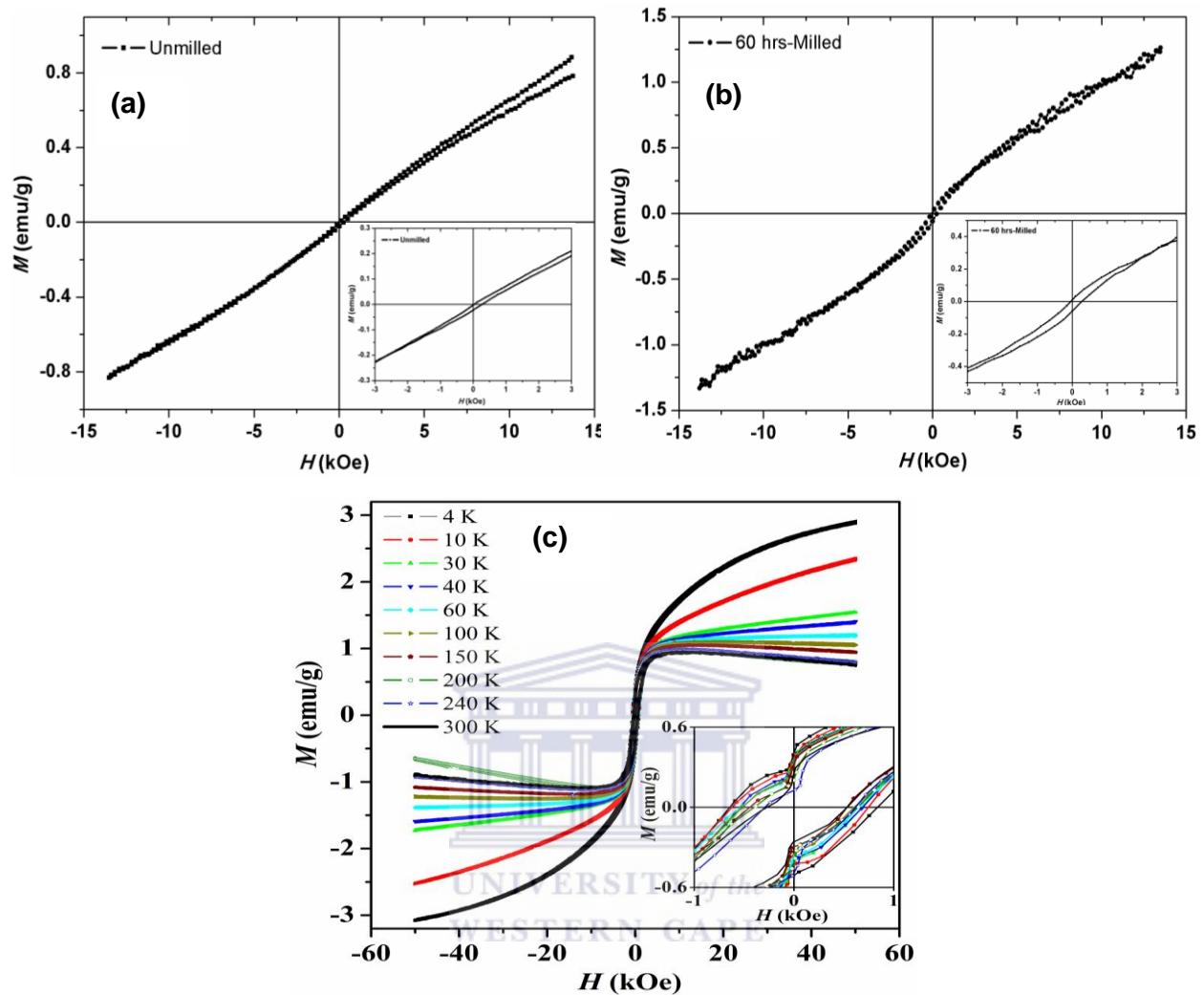
Fig. 5.10: Magnetic properties of (a) 0, (b) 60 and (c) 120 h milled TiO_2 NPs measured at various temperatures. The inset shows the magnified view of the $M - H$ curves.

The magnetic properties such as H_C, exchange bias field (H_E), M_S, μ and M_R as a function of measuring temperature (T) deduced from hysteresis loops are illustrated in **Fig 5.11.** It is evident from this figure that H_C, M_S, M_R and μ tend to increase by decreasing temperature. H_C, M_S, M_R and μ increases

from about 465 Oe, 0.75 emu/g, 0.16 emu/g and 0.0107 μ_B at room-temperature

to 754 Oe, 2.54 emu/g, 0.45 emu/g and 0.0363 μ_B at 4 K respectively. Above 60

K, the magnetization decreased with increasing applied magnetic field (H).

Below 80 K, the sample did not saturate even in a maximum field of 50 kOe. The

current results appear to confirm that there at least two magnetic phases in the

sample which leads to magnetic exchange bias effects (H_E) in the TiO$_2$ NPs.

The exchange bias field was obtained from hysteresis loops using the following

formula: **[5.49]** $H_E = |H_{C+} - H_{C-}|/2$ where H_{C+} and H_{C-} are the coercive fields at

right and left side of the shift of $M-H$ loops respectively. The temperature

dependence of the exchange bias field of the sample is also shown in **Fig 5.11.**

Some enhancement of the coercive field for TiO$_2$ NPs may be attributed to

existence of H_E. We observed that all the loops are shifted along the magnetic

field axis which confirm the existence of the so-called exchange bias field (H_E)

due to the coexistence of ferromagnetic (FM) and antiferromagnetic (AFM)

nanostructures, as a result of surface effects in milled TiO$_2$ NPs **[5.49]**.
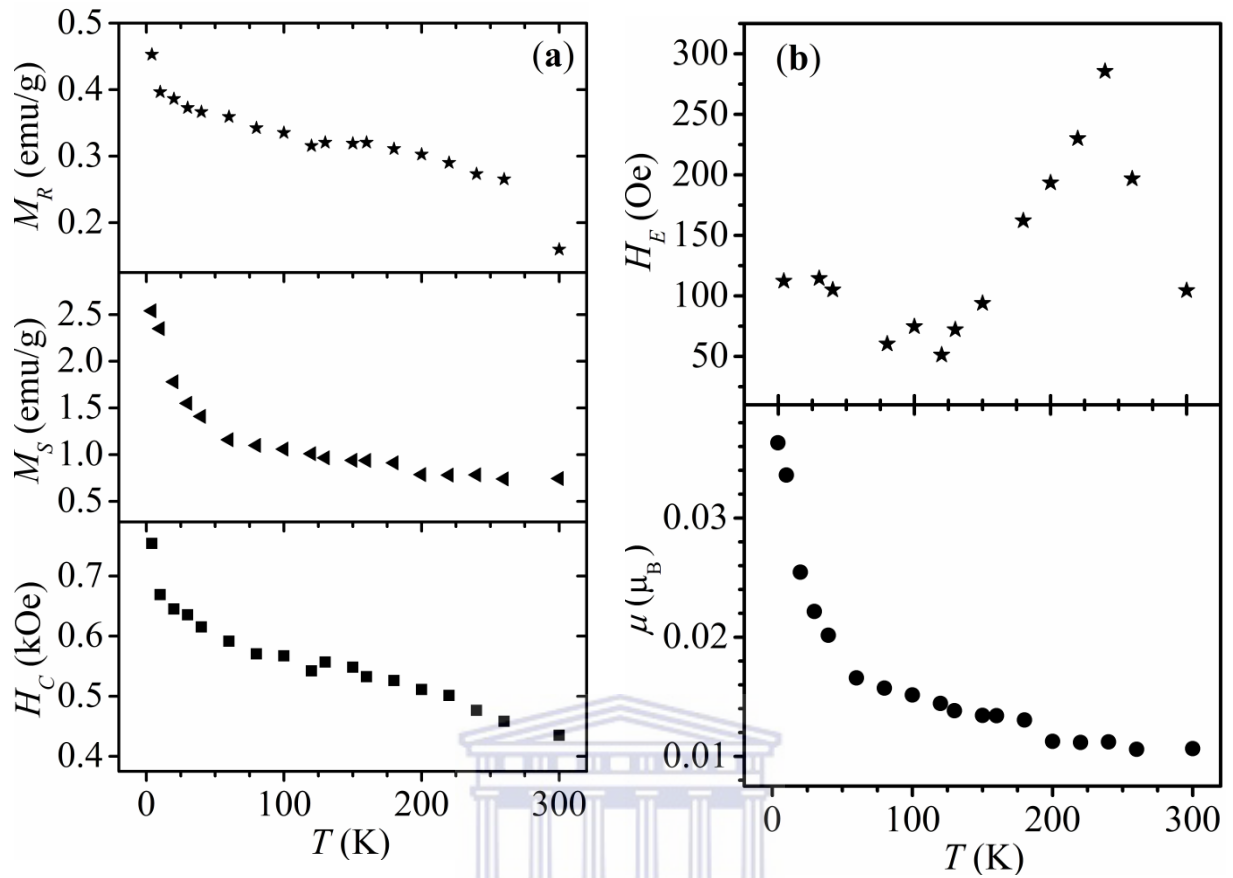
Fig. 5.11: The evolution of the coercive field H_C, saturation magnetization M_S, remnant magnetization M_R, experimental magnetic moment per molecular unit μ and exchange bias field H_E as a function of temperature for 120 h-milled sample.

The temperature-dependence of ZFC and FC magnetizations curves of the milled TiO_2 sample in applied magnetic fields of 0.1, 0.5, 1, 15 and 30 kOe are shown in **Fig. 4.12.** The FC magnetization curves decrease continuously with increasing temperature. Sharp reproducible cusps are observed for measurements in static applied fields of at least 0.5 kOe at about 60 K. The results show splitting between FC and ZFC shown typically at a field of 0.5 kOe.

Similar behavior has been reported for $BiFeO_3$ **[5.50, 5.51]**. Spin-reorientation transitions with increasing temperature have also been observed in $(Er, Tm)_2Fe_{16}SiC_2$ intermetallic compounds **[5.52]**. In the present case the cusps appear to be enhanced at higher field and persist on both FC and ZFC magnetizations. The cusps may be associated with AFM domain pinning effect due to non-uniformly distributed defects **[5.51-5.53]**. Domain wall pinning develops as a result of the non-uniformity distributed defects that affect the movement of the domain wall **[5.50]**. We suspect the peak positions of the cusps to be the Néel point of the AFM phase which also appear to reduce at higher measuring field. The splitting of the ZFC and FC curves has been attributed to the coexistence of ferromagnetism and anti-ferromagnetism phases **[5.50]** and appears consistent with the magnetic exchange bias effect observed.
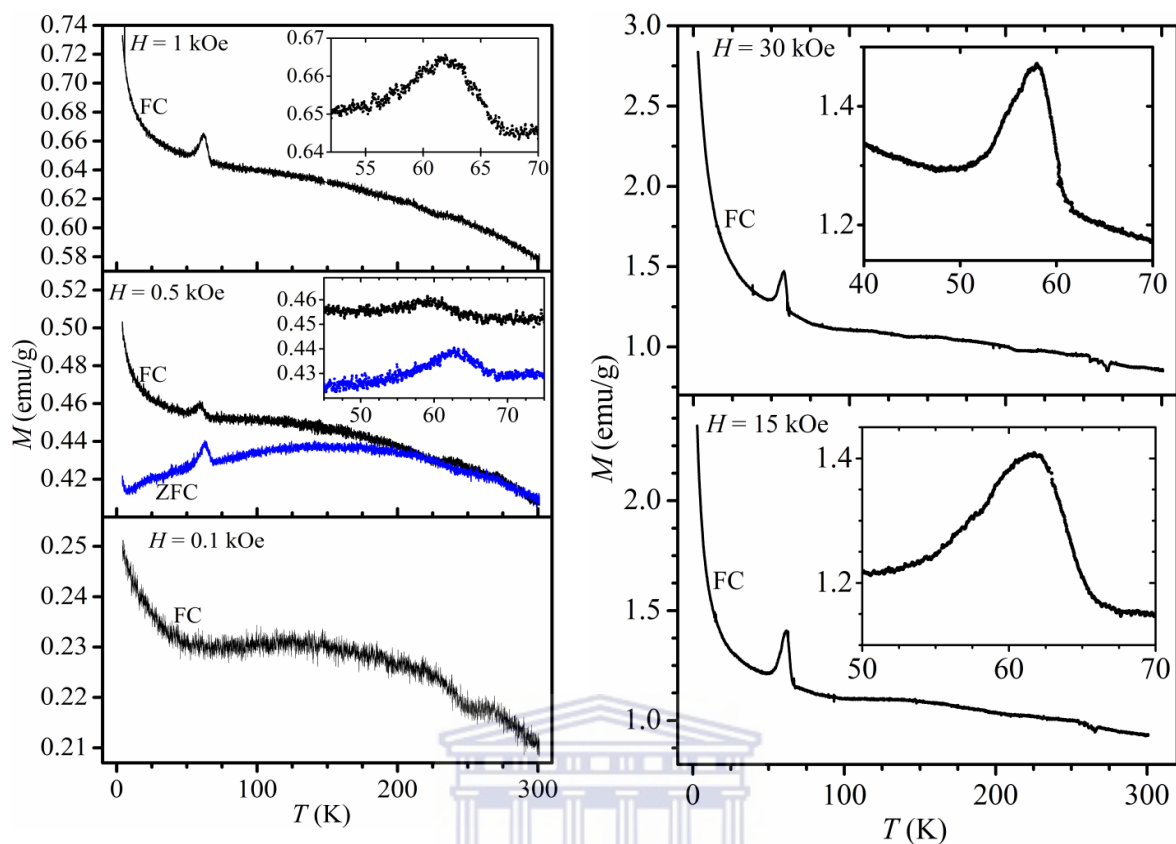
Fig. 5.12: Temperature-dependence magnetization curves for TiO$_2$ measured in different static applied magnetic fields 0.1, 0.5, 1, 15 and 30 kOe. The insets show magnified view of reproducible cusps around 60 K.

To evaluate humidity sensing properties of the fabricated devices, we measured the I-V characteristics of the sample at room temperature (25 °C) with various RHs. A chamber was employed to provide different humidity levels in incremental steps. **Fig. 5.13a** shows that the current of TiO$_2$ NPs milled for 120 h increases with an increase in humidity up to 100 % RHs. Additionally, Fig. 13b shows the TiO$_2$ NPs sensor response at different RH values. It is clear from **Fig. 5.13b** that the 120 h milled TiO$_2$ NPs shows improved response as compared to

the un-milled powder, probably due to improved oxygen vacancies (V_O) on the TiO$_2$ surface as evidenced by PL and XPS analyses **(Figs. 5.6 and 5.9)**, and high surface area **(Table 5.1).** Moreover, the RTFM feature was observed in the 120h milled TiO$_2$ sample, induced by V_O **(see Fig. 5.10)**; therefore, this indicates that there is a correlation between magnetism and sensing. In addition, the increased response under relative humidity can be explained as follows. It is well-known that TiO$_2$ is an n-type semiconductor due to localized donor levels in the bandgap caused by V_O and interstitial TiO$_2$ atoms in the lattice. It was demonstrated previously by Schaub et al. **[5.54]** that the V_O are active sites for dissociation of the water molecule. At high RHs, humidity molecules start to condensate on the surface of the TiO$_2$ NPs and both protonic transport and electrolytic conduction contribute to increase of the current **[5.55]**.
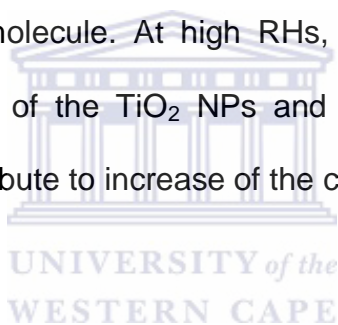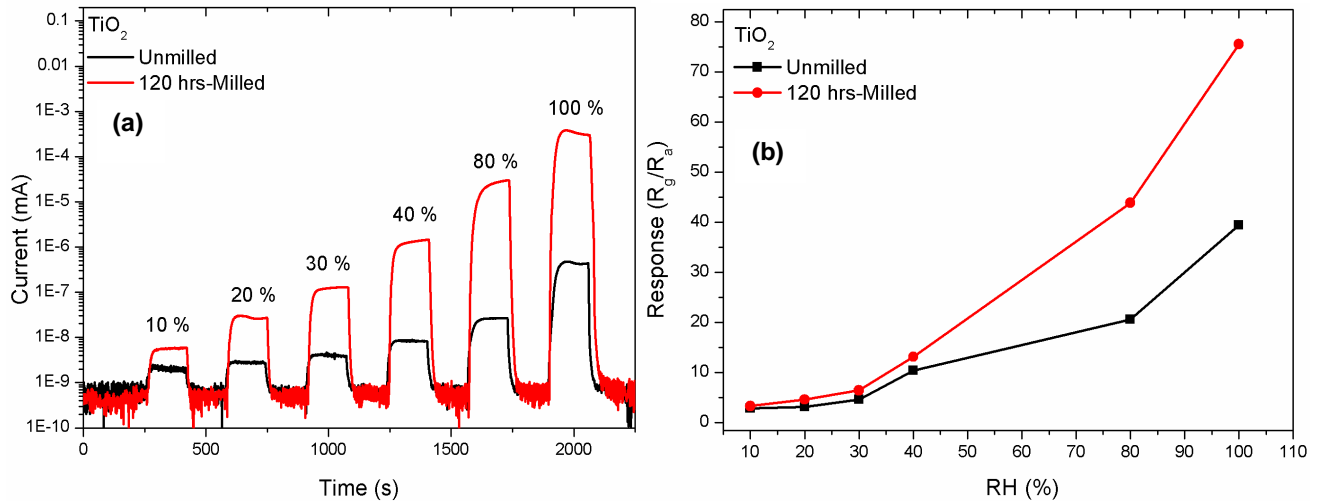
Fig. 5.13: (a) The measured current of the sensor, extracted from different RH pulses (b) RH (%) sensing response.

5.4 CONCLUSION

In conclusion, anatase TiO_2 NPs of high purity was subjected to high energy ball/mechanical milling (MM) at different hours. We have utilized XRD, TEM, PL, VSM, BET and XPS as characterization tools to investigate the morphology, structural, magnetic properties, and defect chemistry of the milled TiO_2 NPs. The findings show that when the size of the NPs decrease due to milling time the magnetization improves with an increase of a defect-related band originating from V_O. The enhanced humidity sensing performance was also observed for the NPs milled for 120 hrs. This improved sensing is attributed to higher V_O concentration on the TiO_2 surface, and increased surface area and higher pore size distribution. We have therefore demonstrated that there is a good correlation between the magnetism and humidity response characteristics of the milled TiO_2 NPs. It was established that V_O is the most probable point defect in these

124

structures and the concentration of these defects varies both with the milled duration and microstructure of the TiO_2 NPs. Thus we conclude that the concentration of V_O in turn controls the magnetization and humidity sensing characteristics of the milled TiO_2 NPs.

5.6 REFERENCES

[5.1]   T. Dietl, H. Ohno, F. Matsukura, J. Cibert, D. Ferrand, Science 287 (2000) 1019-1022.

[5.2]   S.J. Pearton, D.P. Norton, M.P. Ivill, A.F. Hebard, J.M. Zavada, W.M. Chen, I.A. Buyanova, Journal of Electronic Materials 36 (2007) 462-471.

[5.3]   R. Knut, J. M. Wikberg, K. Lashgari, V.A. Coleman, G. Westin, P. Svedlindh, O. Karis, Physics Review B 82 (2010) 094438-094444.

[5.4]   S.S. Nkosi, I. Kortidis, D.E. Motaung, J. Keartland, E. Sideras-Haddad, A. Forbes, B.W. Mwankakinga, G. Kiriakidis, S. Sinha-Ray, Applied Surface Science 280 (2013) 79-88.

[5.5]   S. Ghosh, G.G. Khan, S. Varma; K. Mandal, ACS Applied Materials Interfaces 5 (2013) 2455-2461.

[5.6]   S. Ghosh, G.G. Khan, K. Mandal, ACS Applied Materials Interfaces 4 (2012) 2048-2056.

[5.7]   M. Venkatesan, C.B. Fitzgerald, J.M.D. Coey, Nature 430 (2004) 630-630

[5.8]   A. Sundaresan, R. Bhargavi, N. Rangarajan, U. Siddesh, C.N.R. Rao, Physics Review B 74 (2006) 161306-161309

[5.9]   D.E. Motaung, G.H. Mhlongo, S.S. Nkosi, G.F. Malgas, B.W. Mwakikunga, E. Coetsee, H.C. Swart, H.M.I. Abdallah, T. Moyo, S.S. Ray, ACS Applied Materials Interfaces 6 (2014) 8981-8995.

[5.10] T. Wu, H. Sun, X. Hou, L. Liu, H. Zhang, J. Zhang, Microporous and Mesoporous Materials 190 (2014) 63-66.

[5.11] Q. Wan, X. Wei, J. Dai, J. Jiang, X. Huo, Materials Science Semiconductor Processings 21 (2014) 111-115.

[5.12] J. Chaboy, R. Boada, C. Piquer, M. A. Laguna-Marco, M. Garciá-Hernández, N. Carmona, J. Llopis, M.L. Ruìz-González, J. González-Calbet, J.F. Fernández, M.A. García, Physics Review B 82 (2010) 064411-064419.

[5.13] C. Guglieri, M.A. Laguna-Marco, M.A. Garcìa, N. Carmona, E. Ceśpedes, M. Garcìa-Hernández, A. Espinosa, J. Chaboy, Journal of Physical Chemistry C 116 (2012) 6608-6614.

[5.14] C. Guglieri, E. Ceśpedes, A. Espinosa, M.A. Laguna-Marco, N. Carmona, Y. Takeda, T. Okane, T. Nakamura, M. García-Hernández, M.A. Garcìa, J. Chaboy, Advanced Functional Materials 24 (2014) 2094-2100.

[5.15] E. Céspedes, M.A. Laguna-Marco, F. Jiménez-Villacorta, J. Chaboy, R. Boada, C. Guglieri, A. de Andrés, C. Prieto, Journal of Physics and Chemistry C 115 (2011) 24092- 24101.

[5.16] B.B. Straumal, S.G. Protesova, A.A. Mazilkin, G. Schütz, E. Goering, B. Baretzky, P.B. Straumal, JETP Letters 97 (2013) 367- *377*.

[5.17] B.B. Straumal, A.A. Mazilkin , S.G. Protesova, P.B. Straumal, A.A. Myatiev, G. Schütz, E.J. Goering, T. Tietze, B. Baretzky, Philosophical Magazine 93 (2013) 1371-1383

[5.18] C. Suryanarayana, Progress in Materials Science 46 (2001) 1-184.

[5.19] P. Xiaoyan, J. Dongmei, L. Yan, M. Xueming, Journal of Magnetizm and Magnetic Materials 305 (2006) 388–391.

[5.20] S.J. Chen, J.S. Garitaonandi, D. Ortega, K. Suzuki, Journal of Alloys and Compounds 536S (2012) S287– S290.

[5.21] G.N. Chaudhari, A.M. Bende, A.B. Bodade, S.S. Patil, V.S. Sapkal, Sensors and Actuators B Chemistry 115 (2006) 297-302.

[5.22] H.-S. Hong, D.-T. Phan, G.-S. Chung, Sensors and Actuators B 171-172 (2012) 1283-1287.

[5.23] K.O. Rocha, S.M. Zanetti, Sensors and Actuators B 157 (2011) 654-661.

[5.24] X.J. Huang, Y.F. Sun, L.C. Wang, F.L. Meng, J.H. Liu, Nanotechnology 15 (2004) 1284-1288.

[5.25] J.T.W. Yeow, J.P.M. She, Nanotechnology 17 (2006) 5441-5448.

[5.26] M.A. García, J.M. Merino, E.F. Pinel, A. Quesada, J. de la Venta, M.L.R. González, G.R. Castro, P. Crespo, J. Llopis, J.M. González-Calbet, Hernando, A. Nano Letters 7 (2007) 1489-1494.

[5.27] M.A. García, E.F. Pinel, J. de la Venta, A. Quesada, V. Bouzas, J.L. Fernández, J.L. Romero, M.S. Martn-González, J.L. Costa-Krämer, Journal of Applied Physics 105 (2009) 013925-013925-7

[5.28] P. Bose, S.K. Pradhan, S. Sen, Materials Chemical Physics 80 (2003) 73-81.

[5.29] M. Rezaee, S. Khoie, H.K. Liu, Crystal Engineering Communications 13 (16) (2011) 5055-5061.

[5.30] I. Tsuyumoto, H. Uchikawa, $TiO_{1.94}$, Journal of Materials Science 19 (2000) 2075-2076.

[5.31] I. Tsuyumoto, H. Uchikawa, Materials Research Bulletin 39 (2004) 1737-1744.

[5.32] H. Duttaa, Y.-C. Lee, S.K. Pradhan, Physica E 36 (2007) 17-27.

[5.33] K. Huo, X. Zhang, J. Fu, G. Qian, Y. Xin, B. Zhu, H. Ni, P. Chu, J. Nanoscience and Nanotechnology 9 (2009) 3341-3346.

[5.34] X. Wang, J. Shen, Q. Pan, Journal of Raman Spectroscopy 42 (2011) 1578-1582.

[5.35] J.-M. Wu, H.C. Shih, W.-T. Wu, Y.-K. Tseng, I-C. Chen, Journal of Crystal Growth 281 (2005) 384-390.

[5.36] H.L. Ma, J.Y .Y ang, Y.Dai, Y.B. Zhang, B. Lu, and G.H. Ma, Applied Surface Science 253, (2007) 7497-7500.

[5.37] X. Zhang, X.M. Li, T.L. Chen, J.M. Bian, C.Y. Zhang, Thin Solid Films 492 (2005) 248-252.

[5.38] Y. Lei, L.D. Zhang, G.W. Meng, G.H. Li, X.Y. Zhang, C.H. Liang, W. Chen, S.X. Wang, Applied Physics Letters 78 (2001) 1125-1127.

[5.39] J.-M. Wu, H.C. Shih, W.-T. Wu, Y.-K. Tseng, I.-C. Chen, Journal of Crystal Growth 281 (2005) 384-390.

[5.40] X. Zhang, H. Tian, X. Wang, G. Xue, Z. Tian, J. Zhang, S. Yuan, T. Yub, Z. Zou, Materials Letters 100 (2013) 51-53.

[5.41] Y. Yu, K.J. Wu, D.L. Wang, Appl. Phys. Lett. 99 (2011) 192104-7.

[5.42] X. Pan, X. Ma, Journal of Solid State Chemistry 177 (2004) 4098-4103.

[5.43] P.M. Kumar, S. Badrinarayanan, M. Sastry, Thin Solid Film 358 (2000) 122-130.

[5.44] S.K.S. Patel, N.S. Gajbhiye, Materials Chemistry and Physics 132 (2012) 175-179.

[5.45] S.S. Nkosi, I. Kortidis, D.E. Motaung, G.F. Malgas, J. Keartland, E. Sideras-Haddad, A. Forbes, B.W. Mwakikunga, G. Kiriakidis, S. Sinha-Ray, Journal of Alloys and Compounds 579 (2013) 485-494.

[5.46] X. Xu, C. Xu, J. Dai, J. Hu, F. Li, S. Zhang, Journal of Physicas and Chemistry C 116 (2012) 8813-8818.

[5.47] D.E Motaung I. Kortidis, D. Papadaki, S.S. Nkosi, G.H. Mhlongo, J. Wesley-Smith, G.F. Malgas, B.W. Mwakikunga, E. Coetsee, H.C. Swart, G. Kiriakidis, S.S. Ray, Applied Surface Science 311 (2014) 14-26.

[5.48] H.M.I. Abdallah, T. Moyo, J.Z. Msomi, Journal of Magnetizm and Magnetic Materials 332 (2013) 123-129.

[5.49] J. Nogués, J. Sort, V. Langlais, V. Skumryev, S. Suriñach. J.S. Muñoz and M.D. Baró, Physics Reports 422 (2005) 65-117.

[5.50] F. Huang, Z. Wang, X. Lu, J. Zhang, K. Min, W. Lin, R. Ti, T.T. Xu, J. He, C. Yue, J. Zhu, Scientific Reports 3:2907 (2013) DOI: 10.1038/srep02907.

[5.51] T. Park, G.C. Papaefthymiou, A.J. Viescas, A.R. Moodenbagh, S.S. Wong, Nano Letters 7 (3) (2007) 766-772.

[5.52] B. Liang, B. Shen, Z. Cheng, H. Gong, J. Zhang, F. Wang, S. Zhang, W. Zhan, Journal of Alloys and Compounds 226 (1995) 65-69.

[5.53] C.R. Sankar, P.A. Joy, Physics Review B 72 (2005) 024405- 024405-10

[5.54] R. Schaub, P. Thostrup, N. Lopez, E. Laegsgaard, I. Stensgaard, J.K. Norskov, F. Besenbacher, Physics Review Letters 87 (2001) 26104-1– 266104-2.

[5.55] Y. Zhang, K. Yu, D. Jiang, Z. Zhu, H. Geng, L. Luo, Applied Surface Science 242 (2005) 212-217

CHAPTER SIX

Morphology and structural development of reduced anatase-TiO$_2$ by pure Ti powder upon annealing and nitridation: Synthesis of TiO$_x$ and TiO$_x$N$_y$ powders

ABSTRACT

It is well known that nitriding of titanium is suitable for surface coating of biomaterials and in other applications such as anti-reflective coatings, while oxygen-rich titanium oxynitride has been applied in thin film resistors and photocatalysis. Thus in this work anatase was reduced with pure titanium powder during annealing in argon. This was done to avoid any metallic contamination and unwanted residual metal doping. As a result, interesting and different types of particle morphology were obtained when the pre-milled elemental anatase and titanium powders were mixed. The formation of metastable face centred cubic and monoclinic titanium monoxide were detected by the x-ray diffraction technique. The phases were confirmed by energy dispersive x-ray spectroscopy analysis. Raman analysis revealed weak intensity peaks for samples annealed in argon as compared to those annealed under nitrogen (N$_2$).

6.1 INTRODUCTION

Studies on modification of TiO_2 are of interest to research based on applications such as photocatalysis **[6.1, 6.2]**. Previous attempts to enhance photocatalysis properties of TiO_2 by doping with nitrogen have led to the formation of titanium oxynitride (TiO_xN_y). The structure modifications of TiO_2 are initiated by creating oxygen vacancies, decreasing the grain size and by annealing **[6.3]**. High-energy ball milling (BM) triggers the phase transformation in TiO_2 **[6.4]**. Moreover, the reaction of TiO_2 by pure Ti yields metastable phases such as FCC and monoclinic TiOx **[6.5]**. Accordingly, the reduction of TiO_2 by Ti yields oxygen vacancies without contaminating with other reducing metals. Properties such as resistance switching for memory devices **[6.6]**, photocatalysis **[6.7]**, bioactivity **[6.8]** and insulators **[6.9]** are found in titanium oxynitrides. TiO_xN_y powder was synthesized by mechanical alloying of pure titanium (Ti) powder in air at ambient temperature **[6.10]**. In addition, production of TiO_xN_y from TiO_2 powder may involve generation of defects by displacing oxygen atoms from their interstitial positions. The current investigation presents microstructural and structural development of nonstoichiometric titanium oxides induced during the reduction of anatase by pure Ti and the resultant formation of TiO_xN_y powders upon nitridation.

6.2 EXPERIMENTAL WORK

Anatase TiO_2 and pure Ti elemental powders were pre-milled separately in a milling vial filled with argon gas inside a glove box. BM was done for 30 hours

133

(h) at 600 rotations per minute (rpm) speed for each charge. Small samples were collected inside the glove box for characterization. The mixtures of anatase and Ti powders were prepared from three combinations of compositions:

1. unmilled Ti mixed with unmilled TiO_2 (Ti + TiO_2)

2. unmilled Ti mixed with 30 h milled TiO_2 (Ti + 30 h TiO_2) and

3. 30 h milled Ti mixed with 30 h milled TiO_2 (30h Ti + 30h TiO_2).

These compositions were mixed in a 1:1 weight ratio and annealed at 900 ºC in a tube furnace under argon (Ar) for two hours. The resultant products were then annealed under nitrogen (N_2) at 900 ºC for two hours. The powder morphology was studied using an Auriga ZEISS field-emission scanning electron microscope (FE-SEM) coupled with a Robinson Backscatter Electron Detector (RBSD) and an energy dispersive x-ray spectroscopy (EDS) detector. Optical properties were measured using the Jobin-Yvon NanoLog photoluminescence (PL) spectrometer. Raman spectra were obtained using a Horiba Jobin-Yvon HR800 Raman microscope equipped with an Olympus BX-41 microscope attachment. An Ar^+ laser (514.5 nm) with power setting 1.2 mW from a Coherent Innova Model 308 was used as an excitation source. Phase evolution was traced with a PANalytical X'pert PRO PW 3040/60 X-ray diffraction (XRD) machine fitted with a CuK_α radiation source.

6.3 RESULTS AND DISCUSSION

6.3.1 Morphology of the unmilled and milled Ti and TiO2 powders

Figs. 6.1a-d display the morphology of unmilled and milled Ti and TiO_2 powders, respectively. Unmilled Ti powder is comprised of spherical particles with varying sizes as shown in **Fig. 6.1a.** Upon milling, large particles retained their spherical shape. **Fig. 6.1b** shows the 30 h milled Ti powder comprised of the mixture of spherical and thin flake type particles due to the milling effect. **Fig 6.1c** shows irregular shaped unmilled anatase-TiO_2 powder. It is clear from **Fig. 6.1d** that BM did not evidently change the shape of the anatase powder upon milling.
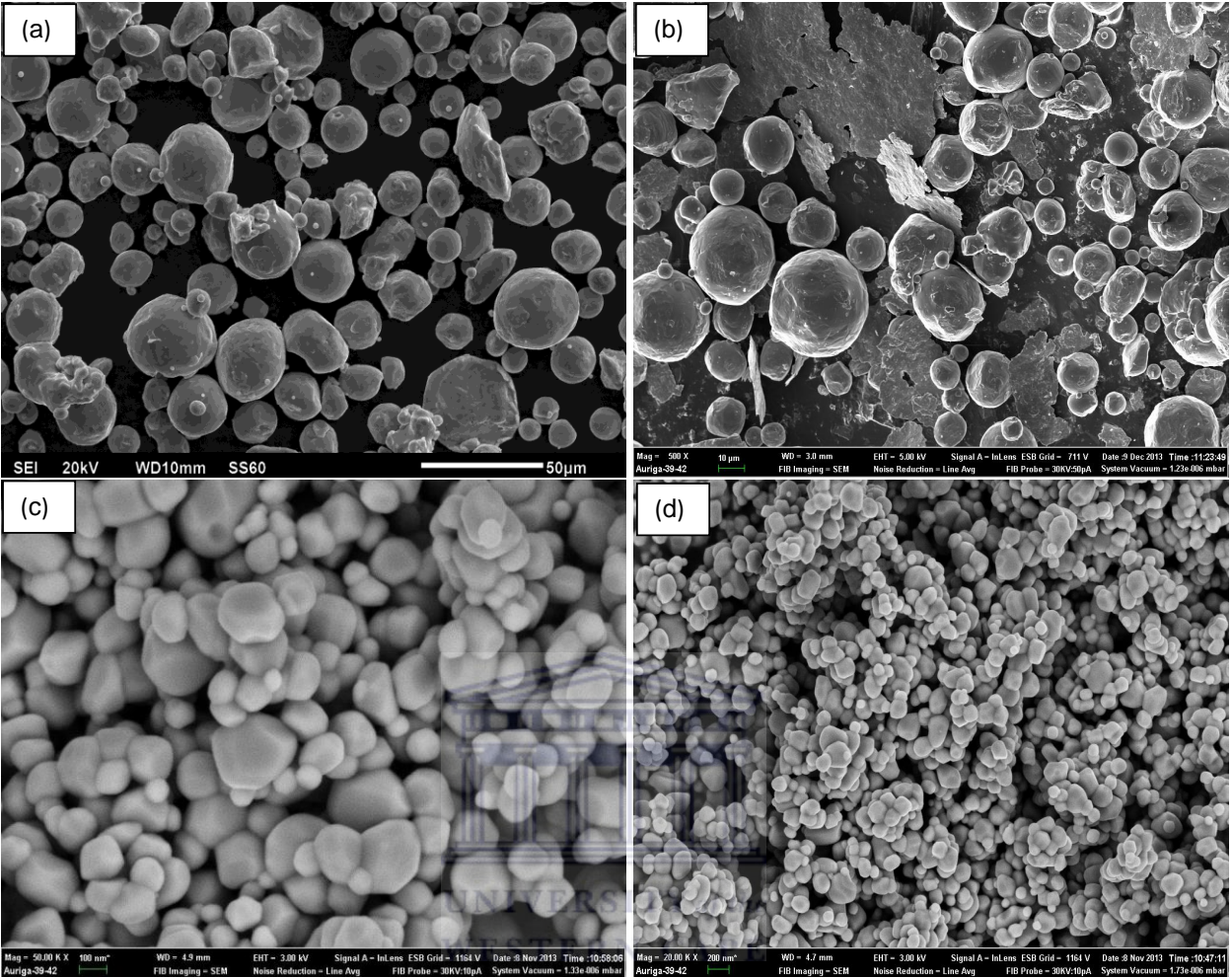
Fig. 6.1: SEM images of Ti (a) unmilled, (b) 30 h milled, (c) unmilled TiO_2 and (d) 30 h milled TiO_2 powders

6.3.2 Morphology of the Ti + TiO2 powders after annealing under Ar and N_2

Figs. 6.2a-f show the SEM images of the annealed (Ti + TiO_2) powder mixtures at 900 °C in Ar with three different combinations of unmilled and milled Ti and TiO_2, respectively. **Figs. 6.2a-b** show the mixed phase morphology of the unmilled combination of Ti + TiO_2. The presence of original spherical shape of Ti

nanostructures and the fine TiO_2 particles is evident. Finer TiO_2 particles are embedded on the surface of the large spherical Ti particles after annealing. **Fig. 6.2b** confirms the presence of TiO_2 particles after annealing of Ti + TiO_2. The unmilled and milled combination of Ti + 30 h TiO_2 powder mixture is shown in **Figs. 6.2c-d.** This powder also shows the mixture of the two different particle morphologies; the rod type particles that are well alligned and interconnected **(Fig. 6.2c)** and smooth crystalline particles **(Fig. 6.2d). Figs. 6.2e-f** illustrate the morphology of the 30 h milled Ti + 30 h milled TiO_2 powder mixture. The two different partcle morphologies illustrate irregular shape that is also comprised of thin plates **(Fig.6.2e)** and the smooth curved crystalline particles **(Fig.6.2f).**
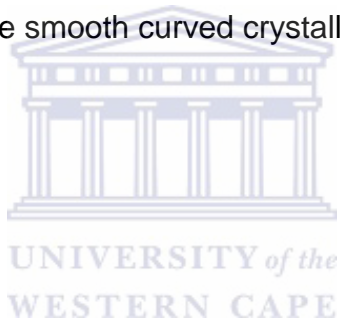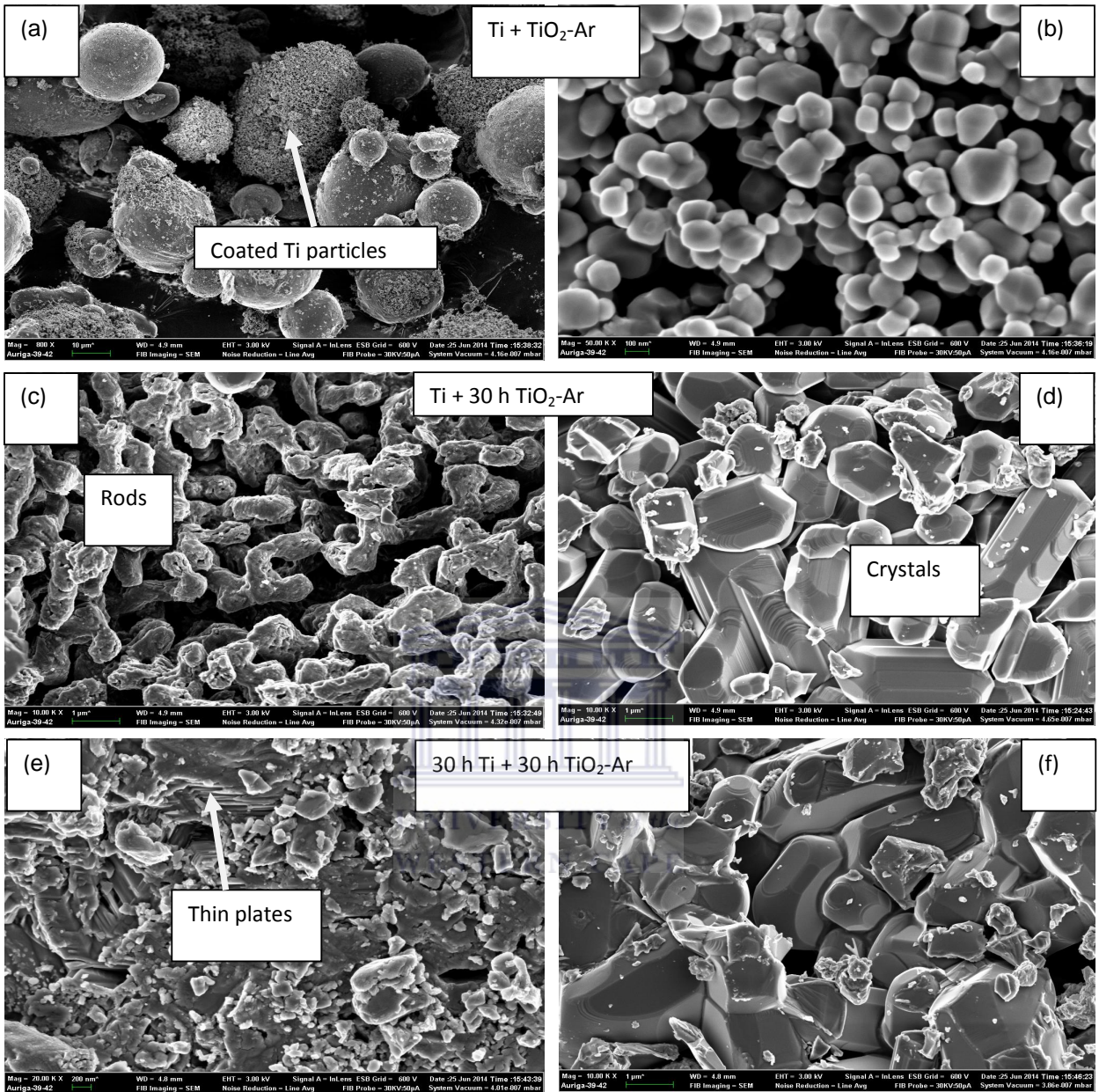
Fig. 6.2: SEM images of the (a-b) (Ti + TiO$_2$), (c-d) (Ti + 30 h TiO$_2$) and (e-f) (30h Ti + 30h TiO$_2$) powder mixtures annealed under Ar.

Fig. 6.3 presents the elemental mapping and EDS analysis of Ti and O of a Ti + 30 h TiO$_2$ sample annealed in Ar at 900 °C. The oxygen content measured

is 25.2 wt. %, which is below the stoichiometric amount to justify a stable TiO_2 structure. This oxygen content confirms that reduction of TiO_2 by pure Ti and formation of metastable TiO_x has occurred, and this is in agreement with the reported $TiO_{0.99}$ **[6.11]**. The 30 h Ti + 30 h TiO_2 and Ti + TiO_2 samples show slightly higher oxygen content of 26.1 and 32.4 wt. %, respectively.
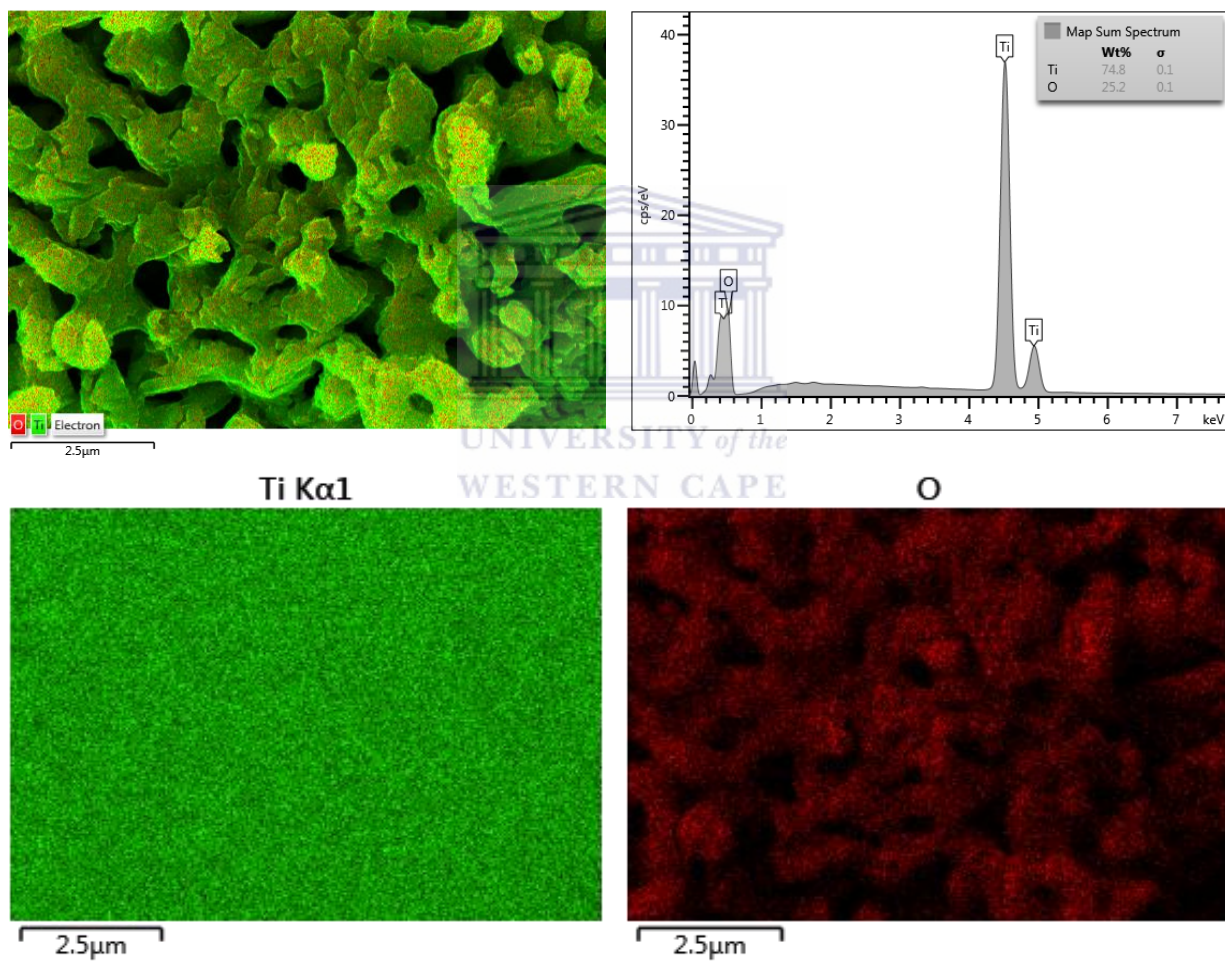

Fig. 6.3: EDS analysis of the Ti + TiO_2 powders after annealing under Ar.

Figs. **6.4a-f** show the SEM images of the Ti + TiO$_2$ powder mixtures of different combinations, pre-annealed under Ar, and further treated under N$_2$ at 900 °C. **Figs. 6.4a and b** show the morphology of nitrided Ti + TiO$_2$ sample. The spherical shape of original Ti particles appears entirely coated with fine TiO$_2$ particles. This phenomenon is clearly visible in **Fig. 6.4b.** The reacted particles appear grey while the segregated TiO$_2$ particles are white in color. **Figs. 6.4c-d** represents the Ti + 30 h TiO$_2$ sample. These particles appear light grey in color with irregular shapes welded together as shown in **Fig. 6.4c.** These large welds are evident in **Fig. 6.4d**. **Figs. 6.4e-f** represent the 30 h Ti + 30 h TiO$_2$, revealing large angular particles which are coated (or covered) by smaller particles. In general, the annealing process carried out in nitrogen ambient has changed the particle morphology of all powder samples that were previously annealed under Ar. Moreover, the formation of different particle shapes during annealing in N$_2$ indicates a phase transformation of powders. In addition, a colour change to pale yellow and reddish is observed.
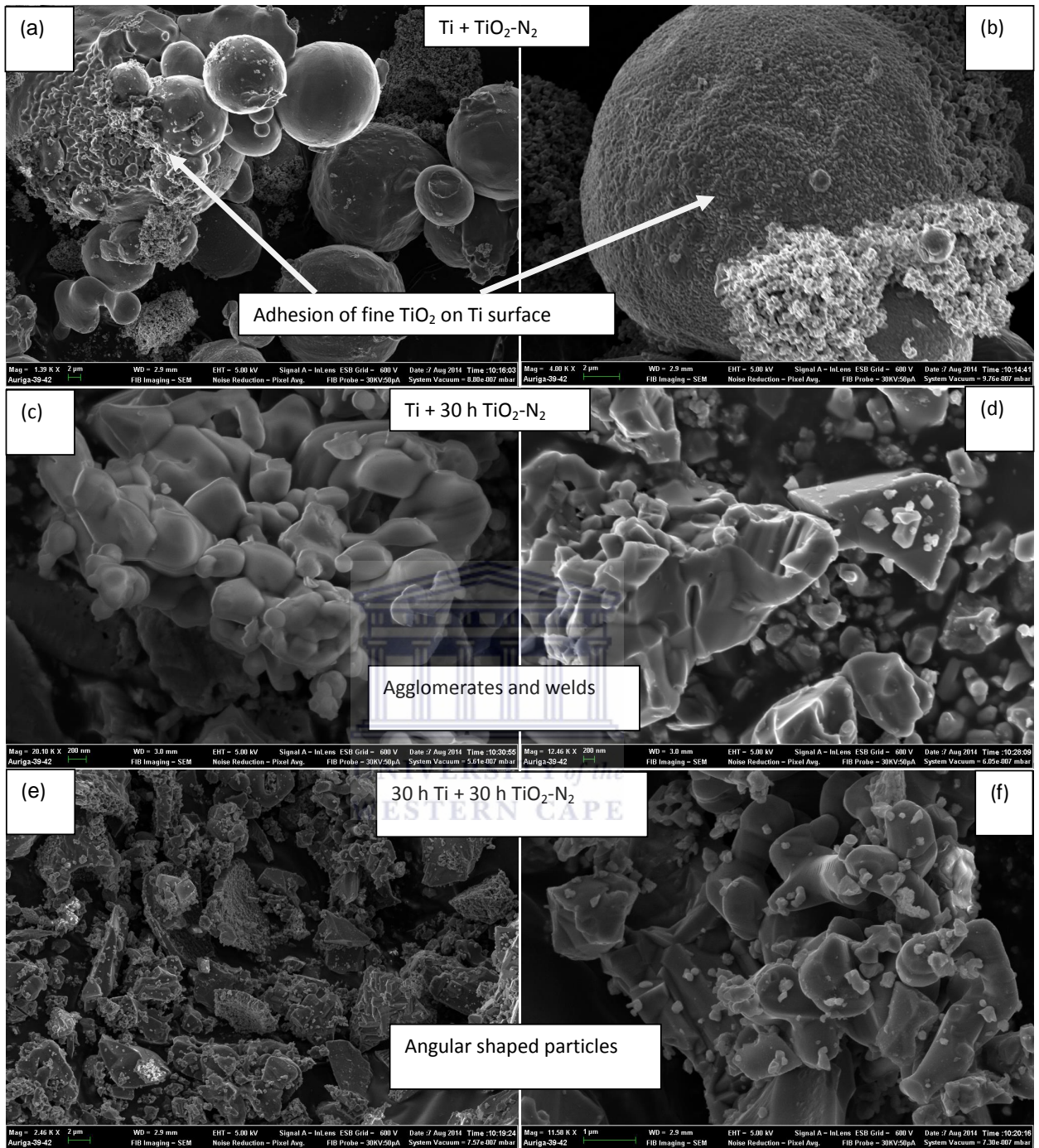
140

Fig. 6.4:   SEM images of the (a-b) (Ti + TiO_2), (c-d) (Ti + 30 h TiO_2) and (e-f)

(30h Ti + 30h TiO_2)   powder mixtures annealed under N_2.

6.3.3 XRD analysis of the Ti + TiO$_2$ mixture after annealing under Ar and N$_2$

Figs. 6.5a-d show the XRD patterns of Ti-TiO$_2$ powder mixtures of un-annealed and annealed samples at 900 ºC under Ar gas. **Fig. 6.5a** shows the elemental Ti and anatase-TiO$_2$ peaks characterized by their ground state HCP and tetragonal crystal structures, respectively. Upon annealing the powder mixture at 900 °C under Ar, new peaks emerged as shown in **Fig. 6.5b.** The XRD intensity peak heights of the annealed sample reduced as compared to the original elemental Ti and TiO$_2$ powders, respectively. The anatase to rutile phase transformation was induced. The lattice parameters of rutile are *a*=4.566 Å; *c*=2.948 Å with *c/a* ratio of 0.65. Additionally, a metastable phase attributed to FCC TiO$_x$ with lattice parameter a= 4.209 Å was induced. This FCC lattice parameter is consistent with that obtained after mechanical milling of the Ti and TiO$_2$ mixture **[6.11]**. In addition, a monoclinic TiO$_x$ phase with lattice parameters a=9.071Å; b=5.781 Å; c=4.541 Å was obtained. These observations are also in agreement with the results reported by Veljković *et* al. **[6.11]**. **Fig. 6.5c** shows the XRD patterns of the annealed Ti + 30 h TiO$_2$ under Ar sample. The height of the intensity peaks decreases upon annealing. This is an indication of induced defects created in the TiO$_2$ powder crystal structure. Minor peaks of tetragonal and HCP phase are still observable, but the metastable FCC and monoclinic TiO$_x$ phases dominate on the XRD patterns. The lattice parameters of FCC and monoclinic phases were *a*=4.230 Å; and a=9.071 Å; b=5.781 Å; c=4.541 Å, respectively. The variation in lattice parameters of the different samples is due to a slight difference in oxygen content, as confirmed by EDS analysis. **Fig. 6.5d**

shows the XRD pattern of the 30 h Ti + 30 h TiO_2 sample after annealing under Ar. Similarly, metastable FCC and monoclinic TiO_x phases were detected with lattice parameters a=4.177 Å and a=9.071Å; b=5.781 Å; c=4.541 Å, respectively. This implies that a phase transformation took place during the annealing of Ti and TiO_2. Veljković *et* al **[6.11]** reported the variation in lattice parameters of TiO_x upon annealing after mechanical alloying of the Ti and TiO_2 powder mixture. The FCC TiO_x has varying oxygen content, hence the difference in lattice parameter. In addition, deformation by milling has an effect on the lattice parameter by disturbing the equilibrium path for the formation of TiO_x structure. Ti reduces the oxygen content of TiO_2 during high temperature application according to the reaction process:

$$2TiO_2 + 2Ti \rightarrow 4TiO_x \qquad\qquad (7.1)$$

Upon heating, the anatase-TiO_2 phase becomes unstable, leading to a weakening of Ti-O bonds due the removal of a neutral oxygen atom from the stoichiometric anatase, which creates two excess electrons in the reduced lattice after annealing in Ar **[6.12]**. Since pure Ti has a high affinity for O, it attracts oxygen due to electron vibrations induced by the annealing of TiO_2, leaving O vacancies. This process yields metastable FCC and monoclinic TiO_x phases. FCC TiO_x with NaCl structures has large vacancies at both Ti and O sites **[6.13]**.
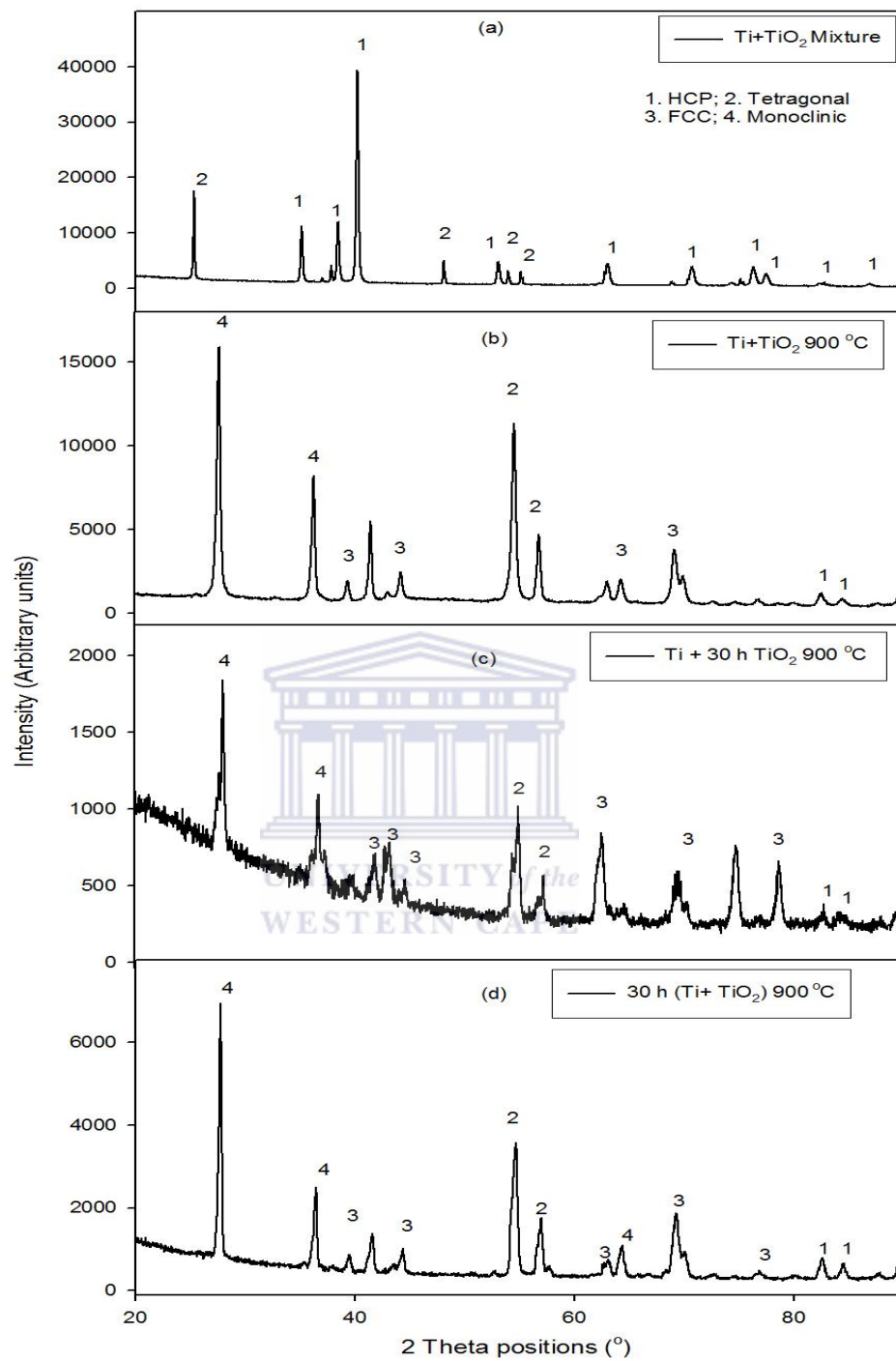
Fig. 6.5: XRD patterns of untreated (a) elemental (Ti + TiO$_2$) mixture and annealed (b) (Ti + TiO$_2$), (c) (Ti + 30 h TiO$_2$), (d) (30 h Ti + 30h TiO$_2$) under Ar at 900 °C.

Avar et al. **[6.5]** and Veljković et al. **[6.11]** have previously reported the synthesis of TiO_x from TiO_2 and Ti. Furthermore, Aghababazadeh et al. **[6.14]** proposed the systematic analysis of the transformation path in carbon-TiO_2 as $TiO_2 \rightarrow Ti_3O_5 \rightarrow Ti_2O_3 \rightarrow TiO_x$. As a result, we propose the formation mechanism of TiO_x in the current study as follows: due to higher thermal expansion (α) of the TiO_2 lattice a (13.28 10^{-6} K^{-1}) as compared to pure Ti (9.7 10^{-6} K^{-1} for β phase) **[6.15]**, TiO_2 expands better than the Ti powder. Atoms of TiO_2 gain thermal energy and start to vibrate, thereby weakening the Ti-O bonds. Hence, some of the O atoms are attracted by Ti and trapped upon cooling. The composition of TiO_x ranged from 0.92<x<1.26 **[6.11]**.
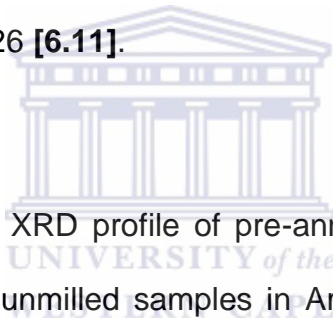
Figs. 6.6a-c show the XRD profile of pre-annealed Ti + TiO_2 of different combinations of milled and unmilled samples in Ar that has been subjected to nitridation at 900 ºC. **Fig. 6.6a** shows the XRD pattern of Ti + TiO_2 after nitridation. The rutile $TiO_{2-x}N_x$ was formed, co-existing with FCC, with minor HCP peaks of metastable TiO_xN_y phases detected, respectively. The lattice parameters of tetragonal rutile are a=4.594 Å; c=2.959 Å with c/a ratio of 0.64, while HCP consists of a=2.970 Å; c=4.775 Å and c/a ratio of 1.61. The FCC TiO_xN_y was detectable with a lattice parameter 4.225 Å. There were no traces of the monoclinic phase that was induced after annealing under Ar. Upon nitridation of the 30 h TiO_2 + Ti sample, no HCP phases were detected as shown in **Fig. 6.6b.** Only two phases exist; the rutile $TiO_{2-x}N_x$ and FCC TiO_xN_y phases. Rutile has lattice parameters a=4.566 Å; c=2.948 Å and c/a ratio of 0.65. The

145

metastable FCC oxynitride has a=4.236 Å. However, the heights of the intensity peaks are smaller than the intensities of **Figs. 6.6a and c.** The rutile and FCC phases were formed for the 30 h Ti + 30 h TiO_2 sample upon nitridation. Rutile has lattice parameters a=4.584 Å; c=2.953 Å with c/a ratio of 0.64, while the metastable FCC phase has a=4.220 Å. The estimated crystallite sizes for the phases calculated by the Scherrer method, on Ar and N_2 annealed samples are presented in **Table 6.1.**
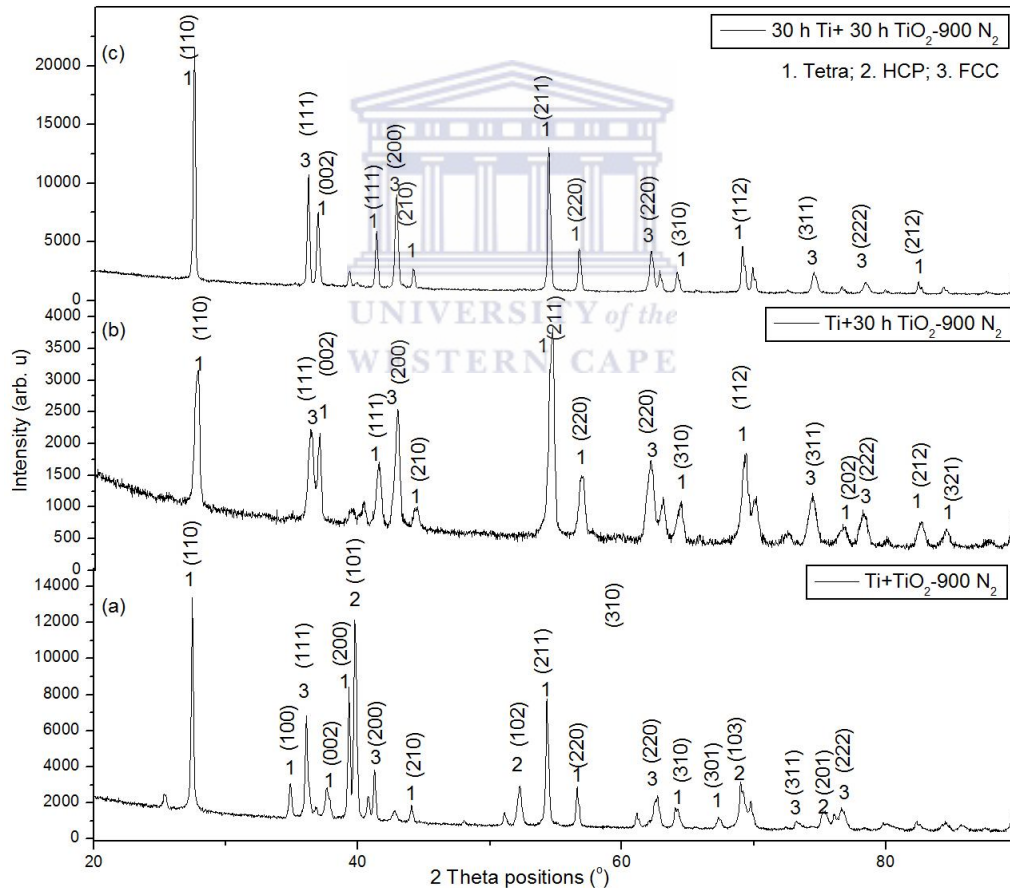

Fig. 6.6: XRD patterns of annealed (a) Ti + TiO_2, (b) Ti + 30 h TiO_2 and (c) 30 h Ti + 30h TiO_2 under N_2 at 900 °C

146

Table 6.1: Estimated crystallite sizes of Ti and TiO_2 samples annealed in Ar and N_2

Samples	Phases after annealing in Ar	Cryst. Sizes (nm)	Phases after annealing in N_2	Cryst. Sizes (nm)
Ti + TiO$_2$	Rutile (TiO_{2-x})	106.63	Rutile ($TiO_{2-x}N_x$)	106.60
	FCC (TiO_x)	132.85	FCC (TiO_xN_y)	66.74
Ti + 30 h TiO$_2$	Rutile (TiO_{2-x})	45.06	Rutile ($TiO_{2-x}N_x$)	71.11
	FCC (TiO_x)	55.75	FCC (TiO_xN_y)	48.07
30 h Ti + 30 h TiO$_2$	Rutile (TiO_{2-x})	80.04	Rutile ($TiO_{2-x}N_x$)	91.43
	FCC (TiO_x)	111.21	FCC (TiO_xN_y)	74.32

Figs. 6.7a-b depict the PL spectra of the three samples of (a) Ti + TiO_2, (b) Ti + 30 h TiO_2 and (c) 30 h Ti + 30h TiO_2 obtained after annealing at 900 °C in Ar and N_2, respectively. It is clear that PL intensity of Ti + 30 h TiO_2 is the highest of the three samples while its corresponding XRD intensity heights are short and broad. This behaviour is attributed to nanocrystallite sizes of rutile-TiO_{2-x} and FCC-TiO_x with 45.06 nm and 55.75 nm, as shown in **Table 6.1,** respectively. However, upon nitridation the intensity of the Ti + 30 h TiO_2-N_2 peak reduces as shown in **Fig. 6.7b.** Additionally, it is clear from **Fig. 6.7b** that the Ti + TiO_2-N_2 sample demonstrates improved PL intensity upon nitridation as compared to its counterparts. Furthermore, a peak shifts towards lower wavelengths is observed in all the samples after nitridation.
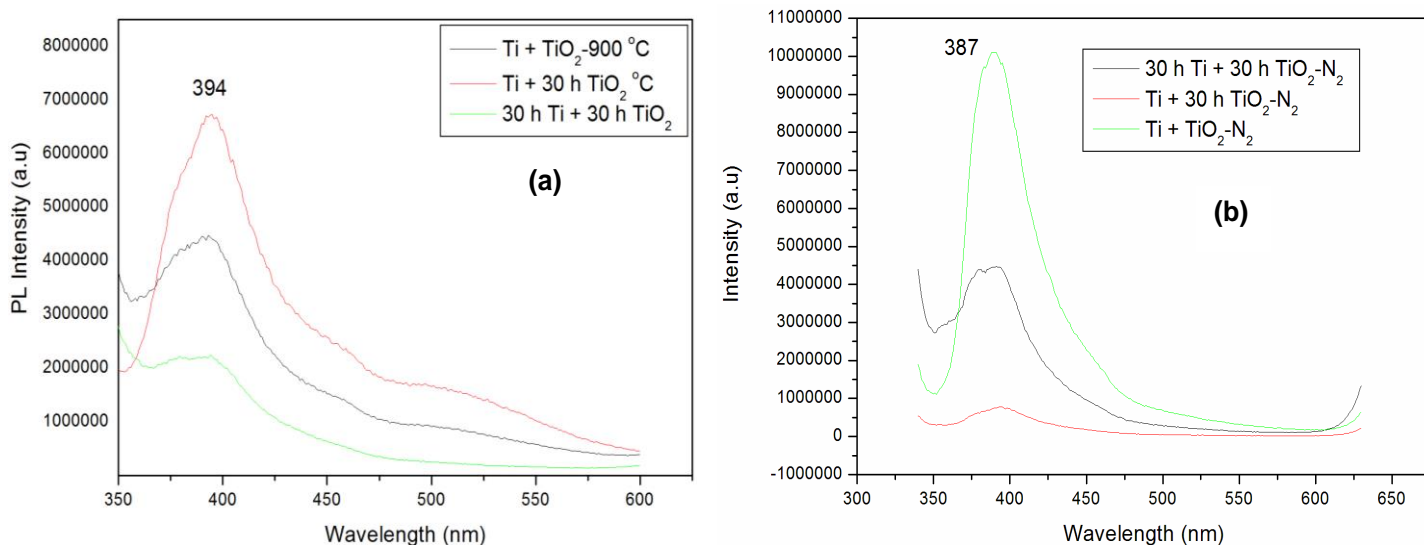
Fig. 6.7:　(a) PL spectra of the Ti + TiO$_2$ samples annealed under Ar at 900 °C.

Figs. 6.8a-c show the Raman spectra of annealed Ti + TiO$_2$ samples at 900 °C in Ar conditions. It is well known that in the anatase TiO$_2$ phase, Raman active modes around 144, 200 and 641 cm^{-1} can be attributed to 3E$_g$, while the modes at 399 and 518 cm^{-1} are ascribed to 2B$_{1g}$ **[6.16, 6.17]**. However, it is clear from **Fig. 6.8a** that the unmilled Ti and TiO$_2$ mixture illustrate Raman peaks at 146, 205, 392, 515 and 633 cm^{-1}, which are sligthly shifted as compared to the pure anatase TiO$_2$ phase. In addition, the Ti + 30 h TiO$_2$ sample shown in **Fig. 6.8b** shows Raman peaks at 142, 608 and 800 cm^{-1}, while the 30 h Ti + 30 h TiO$_2$ sample in **Fig. 6.8c** reveals the bands at 142, 265, 422, 613 and 800 cm^{-1}. The intensity peaks are generally weakly attributable to metastable TiO$_x$ phases **[6.18]**.
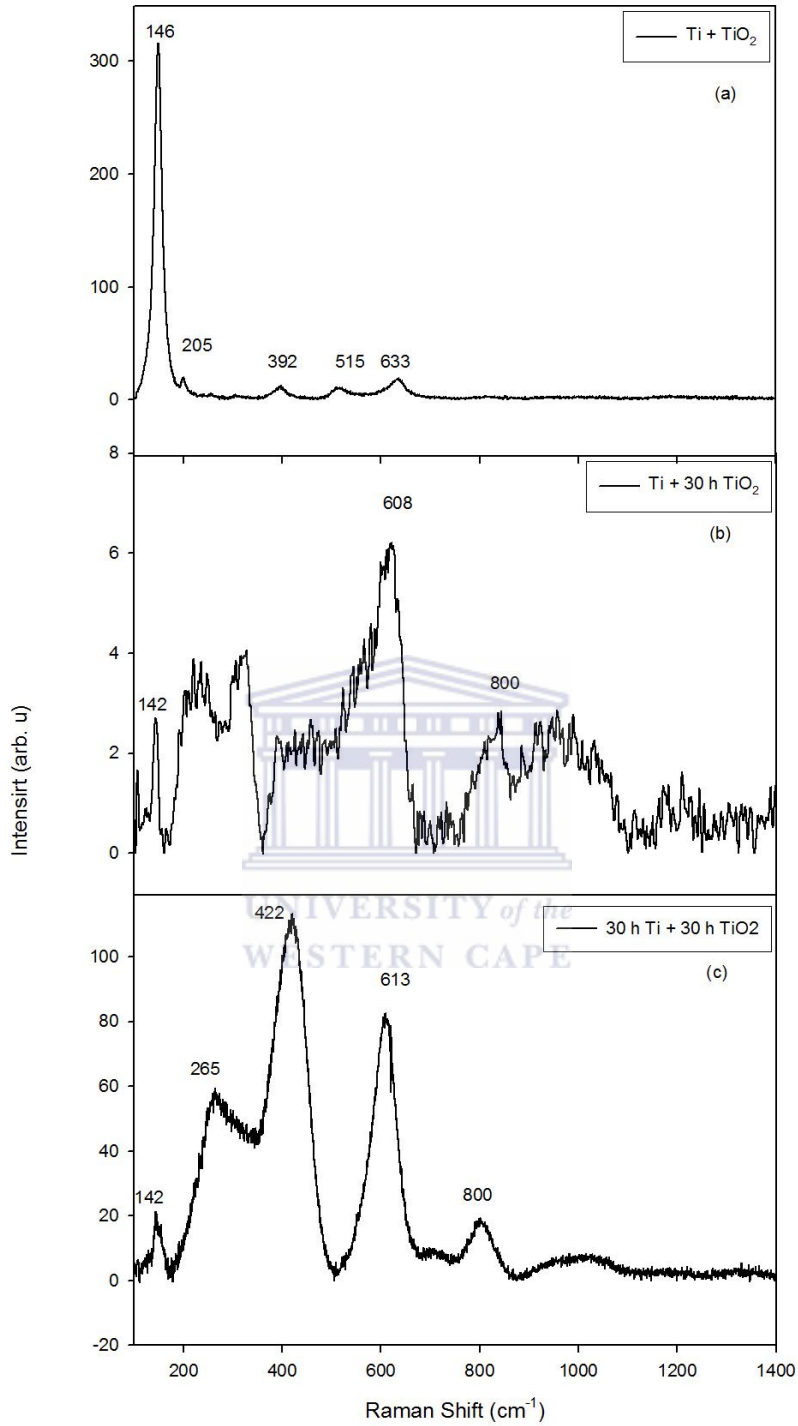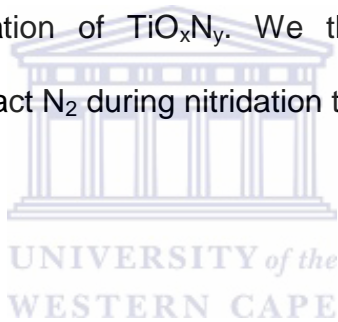
Fig. 6.8:   Raman spectra of annealed (a) Ti + TiO$_2$, (b) Ti + 30 h TiO$_2$ and (c)

30 h Ti + 30h TiO$_2$ under Ar at 900 °C

149

Figs. 6.9a-c show the Raman spectra of the nitrided samples. Three predominant Raman peaks of unmilled Ti + TiO_2 after annealing under N_2 are depicted in **Fig. 6.9a.** Raman peaks appear at 250, 433 and 613 cm^{-1}, while 243, 444 and 613 cm^{-1} peaks were detected in the spectrum for the Ti + 30 h TiO_2 sample, shown in **Fig. 6.9b.** Raman peaks of the 30 h Ti + 30 h TiO_2 milled and nitrided samples are shown in **Fig. 6.9c.** The peaks appear at 250, 437 and 605 cm^{-1}. As displayed in **Table 6.2**, most Raman peaks obtained in titanium oxynitrides are related and linked with either anatase or rutile in literature. However, it is clear that the most intense peak at 142 cm^{-1} for anatase reduced drastically upon the formation of TiO_xN_y. We therefore conclude that the metastable TiO_x phases attract N_2 during nitridation to induce oxynitride phases.
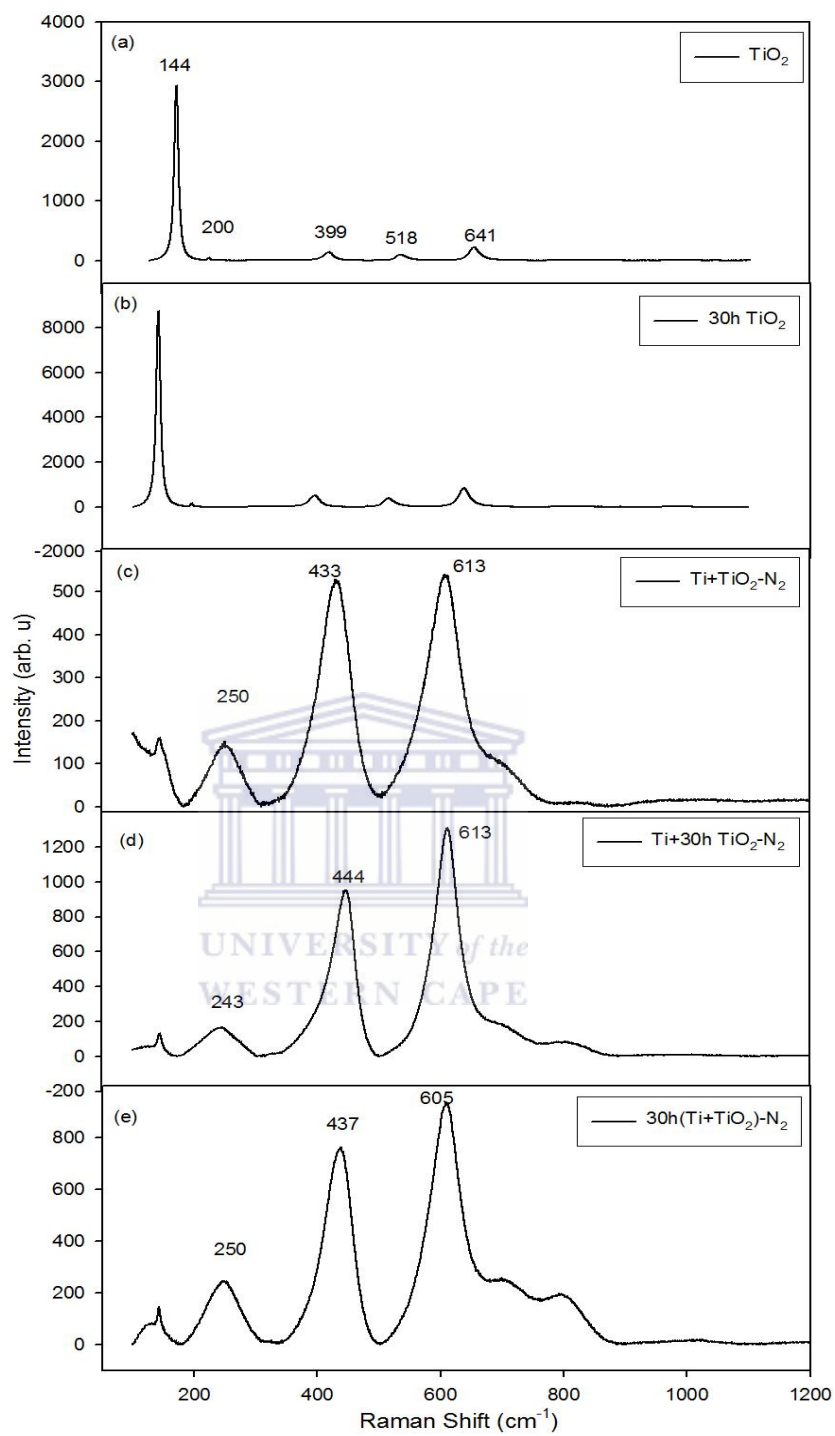
Fig. 6.9: Raman spectra of annealed (a) Ti + TiO$_2$, (b) Ti + 30 h TiO$_2$ and (c) 30 h Ti + 30h TiO$_2$ under N$_2$ at 900 °C

Table 6.2: Published Raman data of TiO_x and TiO_xN_y

Raman shifts (cm^{-1}) TiO_x	Raman shifts (cm^{-1}) TiO_xN_y	Process/comment	Reference
-	148, 200, 398, 518, 641	Deposition	[6.19]
144, 198, 399, 516, 640 and 143, 240, 447, 612		Plasma spraying	[6.20]
158, 420, 622 and 155, 265, 422, 612		UV laser IR laser	[6.21]
144, 399, 529, 639 440, 612		Laser deposition	[6.22]
	144, 400, 514, 639 214, 246, 646	Pressure chemical vapour deposition	[6.7]
	143, 445, 615 200, 400, 640	chemical vapour deposition	[6.9]
	144, 410, 520, 640, 240, 450, 620	Sol-gel and heat treatment	[6.23]
146, 205, 392, 515, 633 142, 608, 800 142, 265, 422, 613, 800	250, 433, 613 243, 444, 613 250, 437, 605	Reduction and nitridation	**current**

6.4   CONCLUSION

TiO_2 was reduced with pure Ti powder during annealing under Ar to avoid any metallic contamination and unwanted doping. As a result, different types of particle morphology were obtained when the Ti + 30 hTiO_2 was annealed. The formation of metastable FCC and monoclinic TiO_x was detected by the XRD

technique and confirmed by the EDS analysis. The metastable FCC TiO_x phases with lattice parameters a=4.209 Å; a=4.230 Å and a=4.177 Å was detected. Due to the vacancies in TiO_x, nitridation at 900 °C has yielded the formation of TiO_xN_y phases. The Raman analysis revealed weak intensity peaks for samples annealed under Ar when compared to those annealed under N_2. The most intense Raman peak for anatase (142 cm^{-1}) was drastically reduced upon nitridation. The detected lattice parameters of the FCC TiO_xN_y phase are a=4.225 Å, a=4.236 Å and a=4.220 Å for Ti + TiO_2, Ti + 30 h TiO_2 and 30 h Ti + TiO_2 samples, respectively.

6.6 REFERENCES

[6.1] S. Bagaswi, Y. Niu, M. Nasir, B. Tian, J. Zhang, Applied Surface Science 264 (2013) 139-147.

[6.2] G. Halasi, I. Ugrai, F. Solymosi, Journsl of Catalysis 281 (2011) 309-317.

[6.3] B. Choudhury, A. Choudhury, International Nano Letters 3 (2013) 1-9.

[6.4] X. Pan, X. Ma, Materials Letters 58 (2004) 513-515.

[6.5] B. Avar, S. Ozcan, Ceramic International 40 (2014) 11123-11130.

[6.6] A.R. Lee, Y.C. Bae, H.S. Im, J.P. Hong, Applied Surface Science 274 (2013) 85-88.

[6.7] G. Hyett, M.A. Green, I.P. Parkin, Journal of Photochemical Photobio. A: Chemistry 203 (2009) 199-203.

[6.8] S. Piscanec, L.C. Ciacchi, E. Vesselli, G. Comelli, O. Sbaizero, S. Meriani, A. De Vitta, Acta Materialia 52 (2004) 1237-1245.

[6.9] X. Song, D. Gopireddy, C.G. Takoudis, Thin Solid Films 516 (2008) 6330-6335.

[6.10] H. Yang, P.G. McCormick, Journal of Materials Science 28 (1993) 5663-5667.

[6.11] I. Veljković, D. Poleti, M. Zdujić, L. Karanović, Ć. Jovalekić, Materials Letters 62 (2008) 2769-2771.

[6.12] F.D. Angelis, C.D. Valentin, S. Fantacci, A. Vittadini, A. Selloni, Chemical Reviews 114 (19) (2014) 9708–9753.

[6.13] B. Jiang, G. Zhou, K. Huang, J. Hou, S. Jiao, H. Zhu, Physica B 421 (2013) 110-116.

[6.14] R. Aghababazadeh, A. R. Mirhabibi, B. Rand, S. Banijamali, J. Pourasad, M. Ghahari, Surface Science 601 (2007) 2881-2885.

[6.15] N. Jagtap, M. Bhagwat, P. Awati, V. Thermochimica Acta 427 (2005) 37-41.

[6.16] K, Huo, X, Zhang, J, Fu, G. Qian, Y. Xin, B. Zhu, H. Ni, P. Chu, Journal of Nanoscience and Nanotechnology 9 (2009) 3341-3346.

[6.17] X. Wang, J. Shen, Q. Pan, Journal of Raman Spectroscopy 42 (2011) 1578-1582.

[6.18] J. Blazevska-Gilev, V. Jandova, J. Kupcık, Z. Bastl, J. Subrt, P. Bezdick, J. Pola, Journal of Solid State Chemistry 197 (2013) 337–344.

[6.19] B. Subramanian, C.V. Muraleedharan, R. Ananthakumar, M. Jayachandran, A, Surface Coatings & Technology 205 (2011) 5014-5020.

[6.20] H. Podlesak, L. Pawlowski, J. Laureyns, R. Jaworski, T. Lampke, Surface Coatings & Technology 202 (2008) 3723-3731.

[6.21] R.J. Betsch, H.L. Park, W.B. White, Materials Research Bulletin 26 (1991) 613-622.

[6.22] M. Fusi, E. Maccallini, T. Caruso, C.S. Casari, B.A. Li, C.E. Bottani, P. Rudolf, K.C. Prince, R.G. Agostino, Surface Science 605 (2011) 333–340.

[6.23] S. Lee, I-S. Cho, D.K. Lee, D.W. Kim, T.H. Noh, C.H. Kwak, S. Park, K.S. Hong, J.K. Lee, H.S. Jung, J. Photochemical Photobio A: Chemistry 213 (2010)129–135.

SUMMARY

Milling of anatase TiO_2 NPs showed that when the size of the NPs decreases due to milling time; the magnetization improves with an increase of a defect-related band originating from V_O. The enhanced humidity sensing performance was observed for the NPs milled for 120 hrs, attributed to higher V_O concentration on the TiO_2 surface and increased surface area and higher pore size distribution. There is a good correlation between the magnetism and humidity response characteristics of the milled TiO_2 NPs. The concentration of V_O controls the magnetization and humidity sensing characteristics of the milled TiO_2 NPs.

TiO_2 reduced with pure Ti (Ti + 30 h TiO_2) powder by milling, and annealing yielded different types of particle morphology. The formation of metastable FCC and monoclinic TiO_x (a=4.209 Å and a=4.230 Å and a=4.177 Å) was confirmed by the XRD technique and EDS analysis, respectively. Due to V_O in TiO_x, nitridation at 900 °C has yielded the formation of TiO_xN_y phases. The Raman analysis revealed weak intensity peaks for samples annealed under Ar when compared to those annealed under N_2. The detected lattice parameters of the FCC TiO_xN_y phase are a=4.225 Å, a=4.236 Å and a=4.220 Å for Ti + TiO_2, Ti + 30 h TiO_2 and 30 h Ti + TiO_2 samples, respectively.

SECTION C

CHAPTER SEVEN

Structural transformation and surface properties of magnesium annealed under nitrogen and nitrogen/oxygen gas mixture

ABSTRACT

Cubic Mg_3N_2 and MgO_xN_y phases were synthesized via annealing under nitrogen and nitrogen-oxygen gas mixture. The nanosized stepped flower with triangular grains and thin layers powder morphology was obtained. Powders were characterized by XRD, SEM, TEM, Raman spectroscopy which confirmed the different phases synthesized during annealing. A complete synthesis of Mg_3N_2 was obtained after nitridation at 550 ºC, while at 650 ºC, metastable FCC Mg-N phase was induced.

7.1. INTRODUCTION

Magnesium (Mg) is a promising engineering material with low melting point (650 ^oC), modulus of elasticity (41 GPa) and density (1.74 kg/m^{-3}). It has a potential to replace some conventional materials that are used in automotive, aircraft and other industry branches. However, its major disadvantage attributes poor corrosion resistance which can be enhanced by nitridation **[7.1]**. The known nitride phase is a cubic Mg_3N_2 which is synthesized by various techniques **[7.1-7.6]**. Zong et al. **[7.2]** reported the formation of magnesium nitride at temperatures between 650 and 800 ^oC. Recently, research by Mei and Li (2009) proposed Mg_3N_2 as hydrogen storage material **[7.7]**. The Mg_3N_2 refines the grain in Mg alloys when added in small amounts **[7.8]**. In addition, it is used as a catalyst in preparing metal nitrides such as silicon nitrides and in preparation of cubic boron nitride **[7.4, 7.8]**. The prediction of high pressure Mg_3N_2 behavior resulted in a body-centered cubic (BCC) structure with a=3.3381Å **[7.9]**. Soto et al **[7.10]** reported on amorphous magnesium nitride films produced by reactive pulsed laser deposition. In this study, Mg matrix prefers a polar bonding from x>0.4 to be ionic saturated at nominal Mg_3N_2 stoichiometry **[7.10]**. It has been established that titanium oxynitride (TiO_xN_y) are potential bioactive material **[7.11]**. It implies magnesium oxynitride can be used as a catalyst for TiO_xN_y and as reinforcement for pure Ti. During synthesis of Mg_3N_2, the traces of FCC phase formed were attributable to MgO **[7.7-7.12]**. In addition, the conversion of Mg_3N_2 to MgO is reported around 500 C in air **[7.4]**. Despite the increasing interest in the development of oxynitride, magnesium oxynitride catalysts are still lacking.

The current paper reports on the structural transformation and morphology of magnesium upon annealing under N_2 and (N_2+O_2) gas mixture. Mg is also a reducing metal for TiO_2 and can assist in the formation of (Mg,Ti) oxynitrides.

7.2. EXPERIMENTAL PROCEDURE

In this work, only pure magnesium (Mg) powder (99.%) was subjected to high temperature annealing in flowing nitrogen (N_2) and N_2/O_2 gas mixture, respectively. The powders charged in a tube furnace at 550 and 650 ^{o}C were collected for characterization after annealing. The surface morphology of the Mg samples was studied using field-emission scanning electron microscope (FE-SEM, Zeiss-Auriga) coupled with energy dispersive x-ray spectroscopy detector. Phase evolution was traced with a PANalytical X'pert PRO PW 3040/60 X-ray diffraction (XRD) machine fitted with Cu K_α radiation. Electron micrographs and selected area diffraction patterns (SAED) were collected with an FEI Tecnai $G^2$20 FE-TEM. Raman measurements were collected using a Horiba Jobin-Yvon HR800 Raman microscope equipped with an Olympus BX-41 microscope attachment. An Ar+ laser (514.5 nm) with energy setting 1.2 mW from a Coherent Innova Model 308 was used as an excitation source.

7.3. RESULTS AND DISCUSSION

7.3.1 Magnesium-nitrogen reaction

Fig. 7.1 shows the XRD patterns of pure Mg and its structural transformation under nitrogen at elevated temperatures. A pure magnesium XRD pattern is shown in **Fig. 7.1a** with its hexagonal crystal structure. The lattice parameters of pure Mg are a=3.21 Å; c=5.21 Å displayed in **Table 8.1**. **Fig. 7.1b** shows the XRD pattern of Mg subjected to annealing at 550 ^{o}C under flowing nitrogen gas. Upon annealing, the number of intensity peaks increases in the XRD analysis. Pure Mg has completely transformed from HCP into cubic Mg_3N_2 as shown by equation 8.1. The intensity heights were also reduced when compared to those of a pure Mg powder. As displayed in **Table 1**, formation of Mg_3N_2 is accompanied by the reduction in crystallite size from 92.10 nm (Mg) to 57.69 nm. The obtained lattice parameter of Mg_3N_2 is a=9.849 Å. This lattice parameter seems to differ based on the processing methods as shown in literature (9.974 Å) **[7.13]**.

$$3Mg + N_2 \rightarrow Mg_3N_2 \qquad\qquad (8.1)$$

The sample that was annealed at 650 ^{o}C is presented in **Fig. 7.1c.** The intensity peaks becomes short and broadened, attributable to the formation of a disordered FCC Mg-N phase with lattice parameter a=4.209 Å as well as minor peaks of cubic Mg_3N_2**.** The EDS analysis shows no identifiable oxygen contamination to suggest the MgO compound formation. The investigation by Vissokov and Pirgov shows the co-existance of the FCC and Mg_3N_2 phase but

attributed the FCC phase to MgO **[7.12]**. Mei et al. **[7.7]** reported the oxygen contamination prior to combustion of Mg in N_2/Ar. However, since there is no significant amount oxygen that is detectable, we attribute this phase to the metastable supersaturated FCC Mg-N phase. It is reported that it has three allotropic modifications (α→β; β→γ) **[7.13]**.
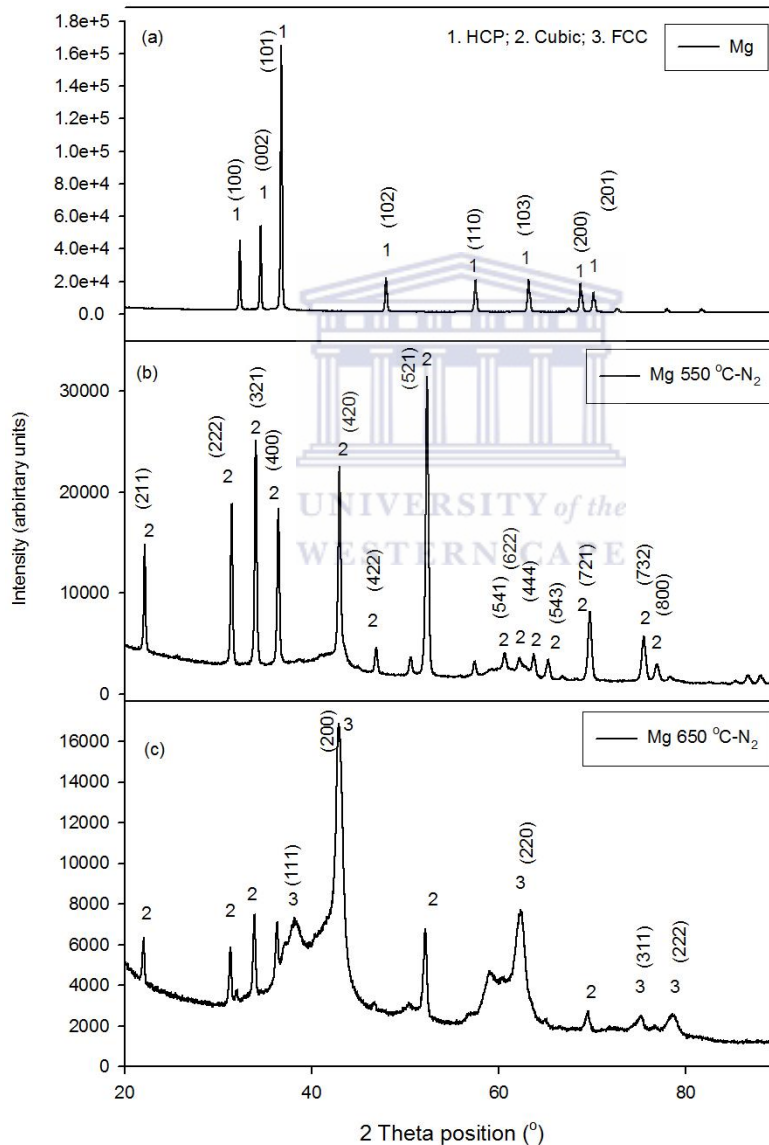

Fig. 7.1: XRD patterns of (a) pure Mg (b) annealed (b) 550 ^{o}C (c) 650 ^{o}C in flowing N_2 gas.

Fig. 7.2 shows the Raman spectra of pure Mg and corresponding samples annealed under N_2. Pure Mg spectrum is shown in **Fig. 7.2a.** Five peaks were identified at 125, 255, 379, 556 and 939 cm^{-1}, respectively. The most intense peak at 125 cm^{-1} is sharp while the remaining four peaks are broad. **Fig. 7.2b** represents the Raman peaks of Mg_3N_2 as identified by the XRD in **Fig. 7.1b.** The first peak at 125 cm^{-1}, drastically decreases due to nitridation at 550 ^oC. The intense Raman peaks for the synthesized Mg_3N_2 appears at 436 cm^{-1} followed by 269 cm^{-1} together with several weak peaks. The Raman spectrum of Mg annealed under nitrogen at 650 ^oC is shown **Fig 7.2c.** It appears the first three peaks that were obtained in **Fig. 7.2b** (Mg_3N_2), still exist, and are in agreement with the XRD results **(Fig. 7.1c).** Raman peaks at 619, 805, 906 and 1160 cm^{-1} are attributable to the metastable FCC Mg-N phase.
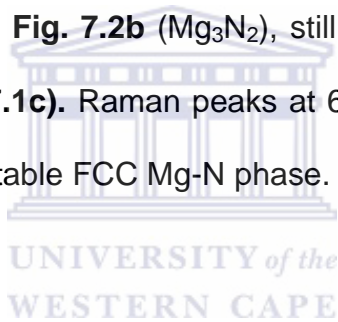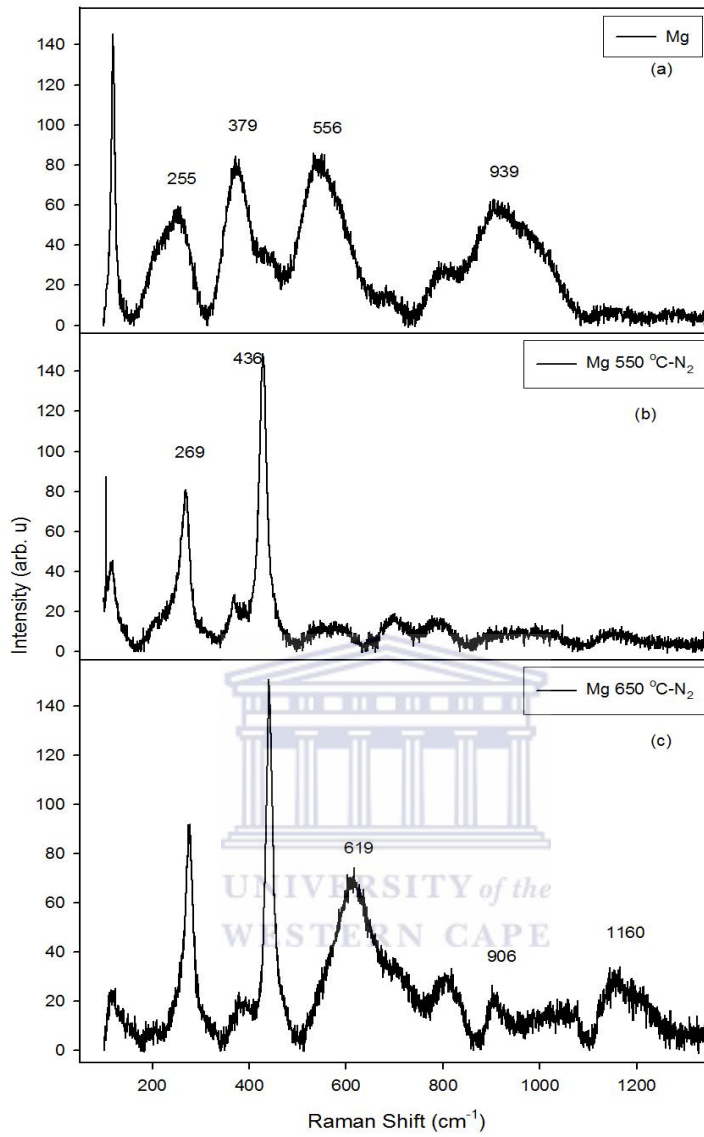
Fig. 7.2: Raman spectra of (a) Mg, (b) 550 °C, 650 °C annealed in flowing nitrogen

Table 7.1: Structural properties of Mg annealed in N_2 and $N_2 + O_2$ mixture

Annealed Samples (ºC)	Phases	Lattice parameters (Å)			Crystallite sizes (nm)
		a	*b*	*c*	
Mg	HCP	3.209	-	5.211	92.10
Mg (N₂) 550	Cubic		9.950		57.69
Mg (N₂) 650	FCC	4.209	-	-	59.84
	Cubic	9.849	-	-	60.66
Mg (ON) 550	FCC		4.209		60.84
	Orth	4.437	4.312	2.862	70.83
Mg (ON) 650	FCC		4.190		66.78
	HCP	3.203		5.194	60.75
Mg (ON) 650-	CUBIC		9.950		91.96
ºC aged	FCC		4.209		65.86

7.3.2. Magnesium-nitrogen/oxygen reaction

Fig. 7.3 shows the XRD patterns of Mg treated under N_2/O_2 flowing gas at 550 and 650 ºC. The XRD pattern of Mg subjected to annealing at 550 ºC under flowing N_2/O_2 gas represented by **equation 7.2**, is shown in **Fig. 7.3b.** Upon annealing, pure Mg powder transform to FCC phase with lattice parameter a=4.209 Å. In addition, a metastable orthorhombic phase with lattice parameters a=4.437Å; b=4.312Å; c=2.862Å was detectable. The calculated crystallite size was 60.84 nm.
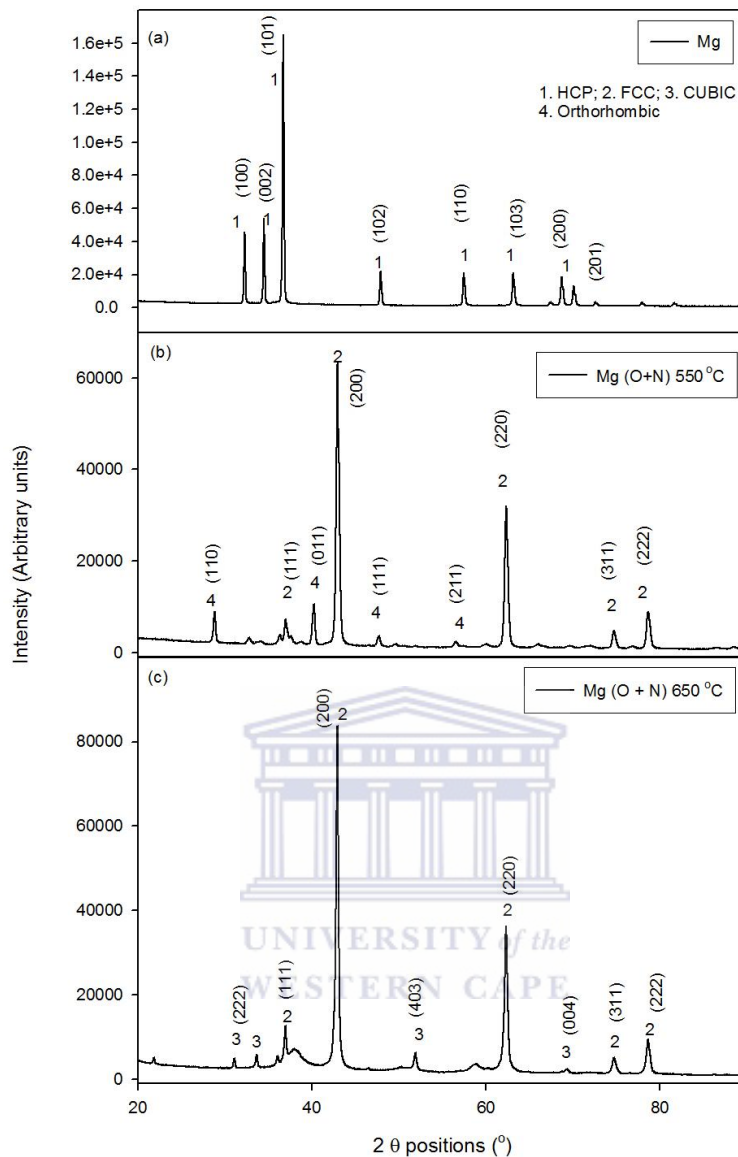
Fig. 7.3: XRD patterns of (a) pure Mg (b) annealed (b) 550 ^{o}C (c) 650 ^{o}C in a mixture of N_2-rich (N_2/O_2) gas mixture.

$$2Mg + O_2 + N_2 \rightarrow 2Mg(O_xN_y) \tag{7.2}$$

Upon annealing at 650 ^{o}C, the orthorhombic phase disappears and minor HCP peaks is detected **(Fig. 7.3c)** with lattice parameter a=3.203 Å; c=5.194 Å. This phase is attributed to metastable magnesium oxynitride with estimated crystallite size of 60.75 nm. Moreover, the FCC peaks with a=4.209 Å was

165

detected. The EDS analysis confirms the presence of oxygen and nitrogen. There are two FCC phases detected that are attributed to MgO or MgO_xN_y coexisting and sharing similar XRD peaks. Samples obtained after annealing appeared as lumps but increased in surface area after being characterized by XRD, hence the second XRD measurement was performed on the sample. The results are presented in **Fig. 7.4b**.
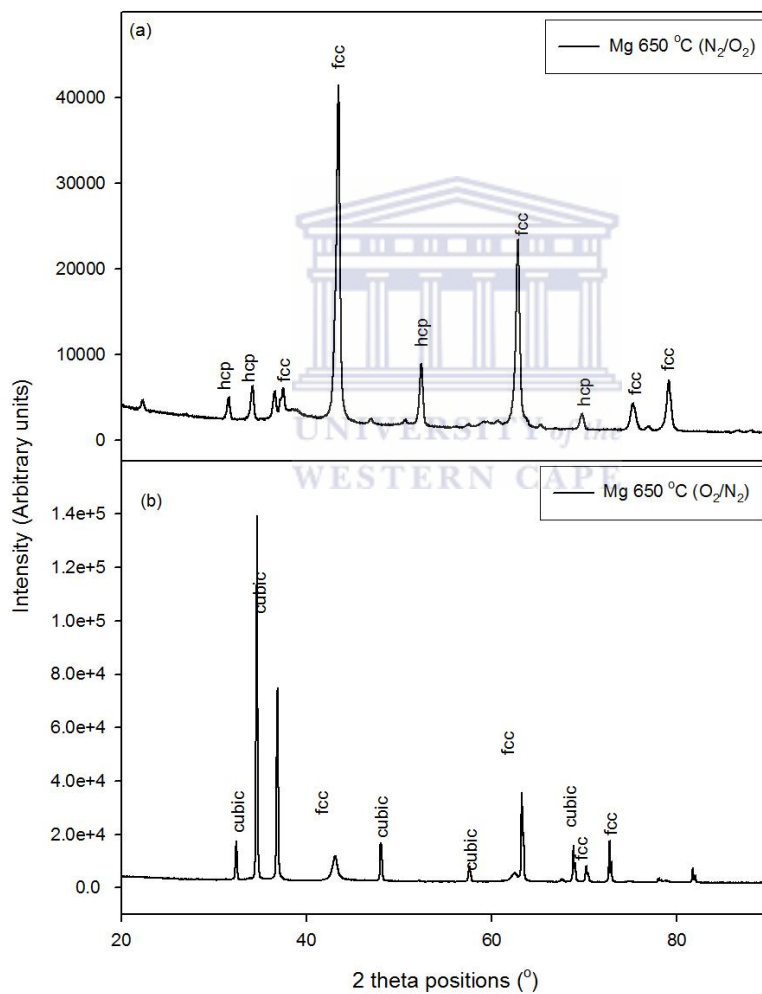

Fig. 7.4: XRD patterns of Mg annealed at 650 $^{\circ}$C (a) initial and (b) second oxidized sample.

Fig. 7.4 shows XRD patterns of annealed at 650 ^{o}C under N_2/O_2 gas mixture for lumps (initial) and fine samples (second). The XRD peaks in **Fig. 7.4b** indicate higher crystallinity when compared with **Fig. 7.4a.** This behavior implies the second samples shows stress relaxation compared to the initial sample. In addition, the FCC peaks remain stable with lattice parameter a=4.209 (MgO-Type), while the HCP phase transform to cubic Mg_3N_2 with estimated crystallite size of 91.96 nm.

Fig. 7.5 shows the Raman spectra of pure Mg and of the annealed sample under N_2/O_2. The Raman spectra of Mg_3N_2 phase in **Fig. 7.5b** is included only for comparison sake. Raman measurements were performed on two different phases after annealing at 650 ^{o}C, namely area **(A1) and (A2)**, respectively. The four intense peaks at 279, 374, 460, 628 cm^{-1} and weak peaks 805, 1203 cm^{-1}) were identified in **A1**. The peak at 374 cm^{-1} could be related to the MgO_xN_y phase since it was not visible in Raman spectra of the synthesized Mg_3N_2 phase. The peak at 805 cm^{-1} confirms the traces of the Mg_3N_2 phase. **Fig. 7.5d** shows the three intense Raman peaks at 279, 374 and 446 cm^{-1}, respectively. Raman peaks in **Fig. 7.5c** are broader compared to those in **Fig. 7.5d.** The Raman peak at 374 cm^{-1} could belong to new metastable HCP oxynitride with estimated crystallite size of 60.75 nm.
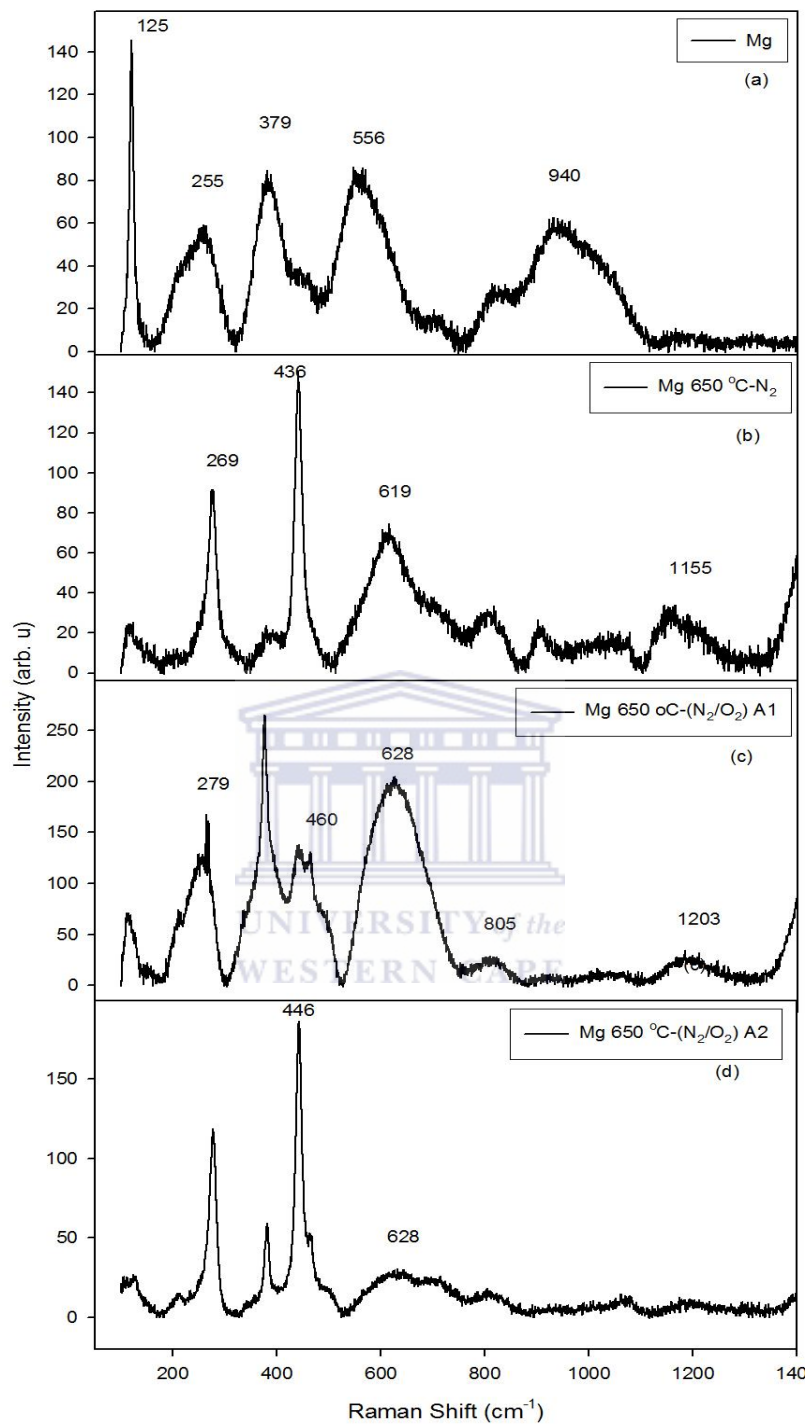
Fig. 7.5: Raman spectra of (a) Mg, (b) 550 ⁰C, 650 ⁰C annealed in a flowing mixture of nitrogen and oxygen.

Fig. 7.6 shows SEM images of pure Mg and annealed at 650 ^{o}C for 5 hours in N_2 and N_2/O_2, respectively. Large and elongated particles of pure Mg are displayed in **Fig. 7.6a.** The grey Mg powder becomes bright yellow after nitridation confirming the formation of Mg_3N_2 **(Fig. 7.6b)** in agreement with literature **[7.3]**. **Fig 7.6c** shows the Mg powder treated in a mixture of oxygen and nitrogen gases. The golden-yellow powder consisting of lumps was induced after annealing as shown in **Fig. 7.6d.** However, after XRD characterization, the powder surface area has increased as shown in **Fig. 7.6e.** It is known that Mg_3N_2 powder react rapidly with atmospheric moisture to form MgO **[7.5]**. Chen et al. **[7.14]** started to observe MgO whiskers if the temperature is increased to 700 ^{o}C. The microstructure or morphology of MgO is probably determined by the preparation method **[7.15, 7.16].** In the current study, the oxynitride formation is more favourable than the Mg_3N_2 phase. Three types of morphologies with different features are observable in **Fig. 7.6c** (Insets), the nanosized stepped, flower with triangular grains and thin layers. It is also evident that thin Mg_3N_2 layers are present **(Fig. 7.6b)** in agreement with the XRD and Raman analysis. The presence of cubic Mg_3N_2 is confirmed by both the XRD and Raman spectra while the morphology is attributed to the thin layers.
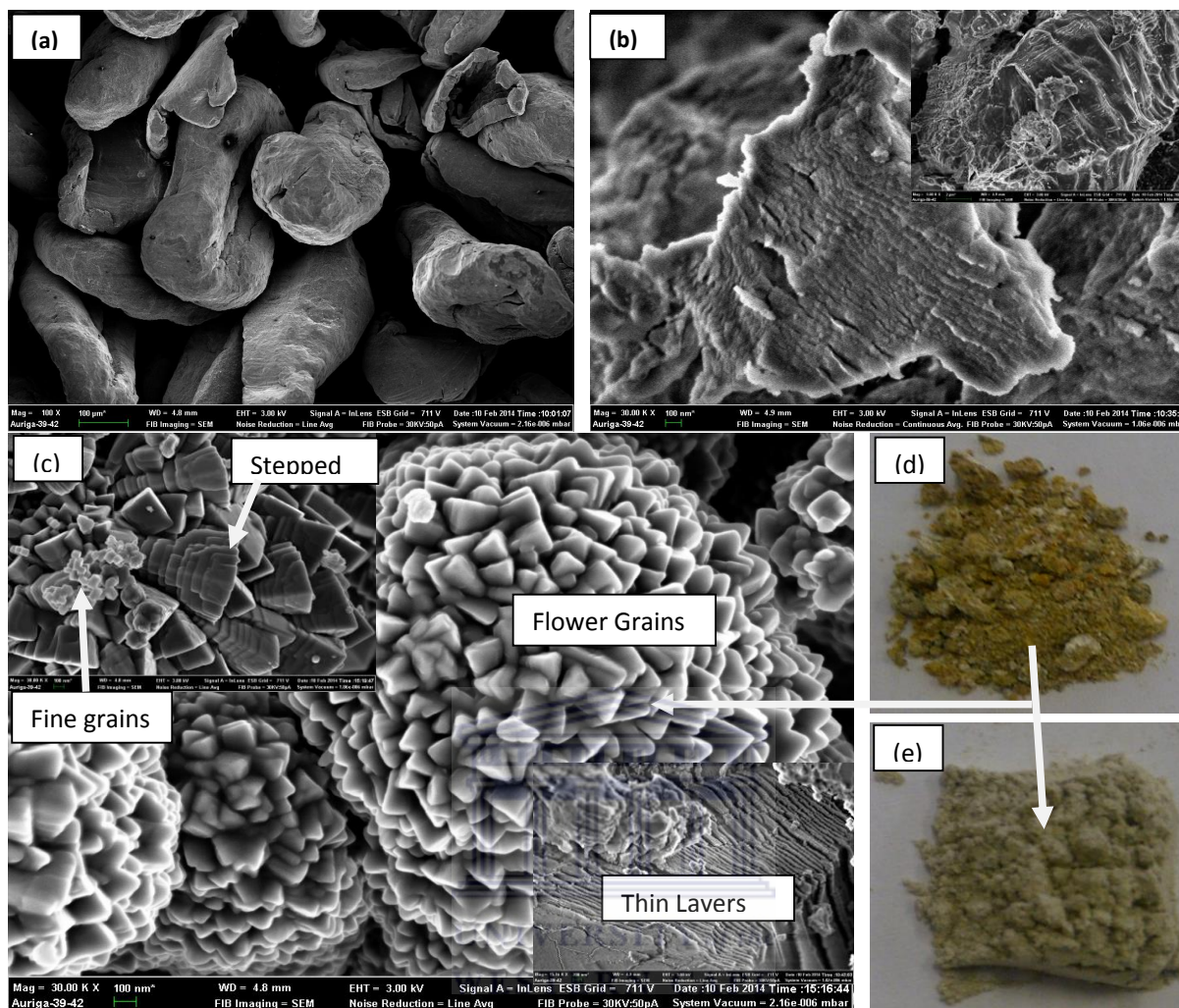
Figure 7.6: SEM images of Mg powders (a) pure, (b) annealed at 650 in N_2, (c) annealed at 650 in (N_2+O_2) (d)-(e) optical images.

Table 7.2: EDS compositional analysis in weight percentage (wt.%)

Mg	N	O
93.12	0.36	6.52
86.53	3.18	10.29

The TEM image in **Fig. 7.7(a)** depicts pure Mg powder showing large particles in correlation with the SEM image. **Fig. 6b** shows the corresponding

170

SAED pattern for pure Mg. The high resolution TEM image for Mg nitrided powder at 650 º C is shown in **Fig. 7.7(c).** The mixture of small and large NPs was observed in **Fig. 7.7 (e).** It is also evident from the micrographs that particles exhibit cubic shapes after high temperature annealing under (N_2+O_2) gas mixture. The SAED patterns of annealed samples display the rings that are quite broad **(Fig. 7.7d, 7.7f).** This behavior indicates the presence of ultrafine particles.
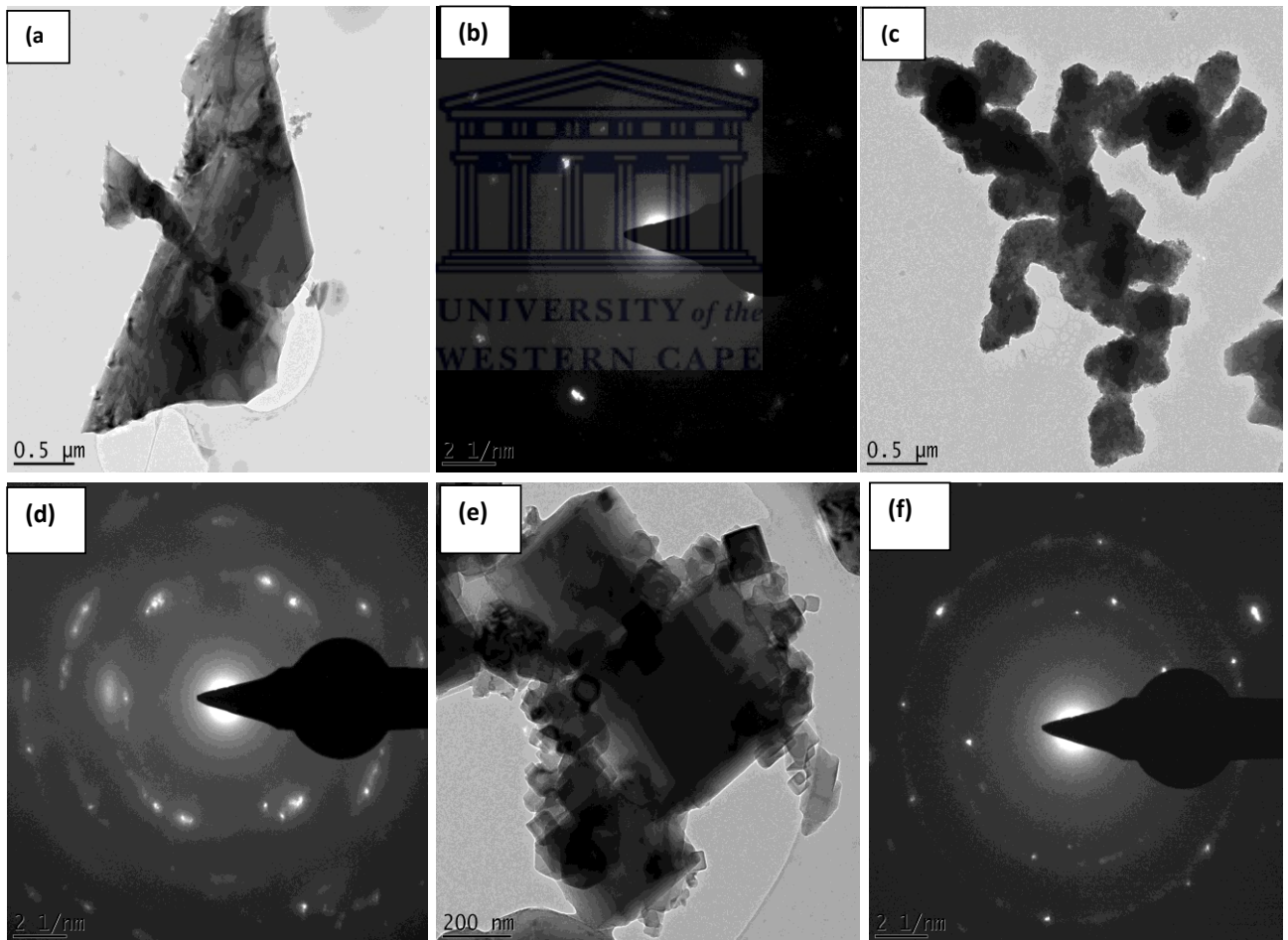
Fig. 7.7: HR-TEM images of Mg (a-b) pure, (c-d) annealed in N_2 and (e-f) annealed in N_2/O_2 at 650 ^{o}C with corresponding SAED.

7.4 CONCLUSION

A complete synthesis of $Mg_3N_2$was obtained after nitridation at 550 ^{o}C, while at 650 ^{o}C, a metastable FCC Mg-N phase was induced. Thin porous layers of Mg_3N_2 was observed and remained after 650 C. The annealing under the mixture of (N_2+O_2) gases altered the microstructure into three different phases; steps, triangular and thin slices NPs. EDS confirmed the presence of N_2 in Mg_3N_2 powder and (N_2+O_2) in MgOxNy. The direct correlation between XRD and Raman spectra analysis was realized. Raman spectra showed shifting of peaks with annealing under N_2 and (N_2+O_2), respectively.
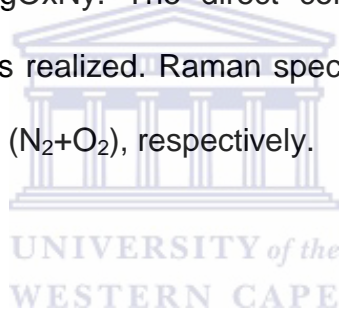
7.6 REFERENCES

[7.1]   D. Höche, C. Blawert, M. Cavellier, D. Busardo, T. Gloriant, Applied Surface Science 257 (2011) 5626-5633.

[7.2]   F. Zong, C. Meng, Z. Guo, F. Ji, H. Xiao, X. Zhang, J. Ma, H. Ma, Journal of Alloys and Compounds 508 (2010) 172-176.

[7.3]   K. Toyoura, T. Goto, K. Hachiya, R. Hagiwara, Electrochimica Acta 51 (2005) 56-60.

[7.4]   D-W. Kim, T-H. Kim, H-W. Park, D-W. Park, Applied Surface Science 257 (2011) 5375-5379.

[7.5]   M. Gajewska, J. Dutkiewicz, J. Morgiel, Archives of Metallurgical Materials 58 (2013) 433-436.

[7.6]   O. Reckeweg, J.C. Molstad, F.J. DiSalvo, Journal of Alloys and Compounds 315 (2001) 134-142.

[7.7]   L. Mei, J-T. Li, Scripta Materialia 60 (2009) 141-143.

[7.8]   I.S. Gladkaya, G.N. Kremkova, N.A. Bendeliani, Journal of Materials Science Letters 12 (1993) 1547-1548.

[7.9]   M.A. Brogan, R.W. Hughes, R.I. Smith, D.H. Gregory, Journal of Solid State Chemistry 185 (2012) 213-218.

[7.10] G. Soto, J.A. Diaz, W. de la Cruz, A. Reyes, E.C. Samano, Journal of Non-Crystal Solids 342 (2004) 65-69.

[7.11] S. Piscanec, L.C. Ciacchi, E. Vesselli, G. Comelli, O. Sbaizero, S. Meriani, A. De Vitta, Acta Materialia 52 (2004) 1237-1245.

[7.12] G.P. Vissokov, P.S. Pirgov, Journal of Materials Science 31 (1996) 3685-3690.

[7.13] G. Vissokov, Journal of University Chemistry and Technology Metallurgical 40 (3) (2005), 193-198.

[7.14] S-H. Chen, D-F. Zhang, J-Q. Li, G. Sun, Powder Technology 253 (2014) 677-680.

[7.15] M.H. Bocanegra-Bernal, Powder Technology 186 (2008) 267-272.

[7.16] F. Meshkani, M. Rezaei, Powder Technology 199 (2010) 144-148.

UNIVERSITY *of the*
WESTERN CAPE

CHAPTER EIGHT

Structural and optical characterization of mechanically milled Mg-TiO$_2$ and nitrided Mg-TiO$_x$-N$_y$ nanostructures: Possible candidates for gas sensing application

ABSTRACT

For the first time gas sensing properties of novel ball milled and nitrided Mg-TiO$_2$ prepared powder is presented. BM was performed on an Mg-TiO$_2$ powder mixture for 60 hours (h), yielding a reduction in crystallite sizes. The milled powder was annealed in nitrogen at 650 °C, and crystalized into two face centred cubic (FCC) phases with different lattice parameters. The nitrided powder sample exhibited various morphologies including nanorods, as well as nanoparticles showing porous behaviour. The AFM and BET analyses showed high roughness and surface area for 60 h milled Mg-TiO$_2$ nanostructures. The Mg-TiO$_2$ 60h and Mg-TiO$_2$-60h-N$_2$ materials were tested for their sensing performance towards H$_2$, NH$_3$ and CH$_4$ gases at various temperatures. The Mg-TiO$_2$ 60h sensing material showed high sensing response to NH$_3$, disclosing fast response-recovery time and high selectivity to NH$_3$.

8.1   INTRODUCTION

Studies on the modification of titanium dioxide (TiO_2) are of interest to researchers for its applications **[8.1, 8.2]**, while the increasing demands for lightweight materials in aerospace and automotive applications encourage continuous development of magnesium (Mg) based materials. Attempts to enhance the properties of TiO_2 by nitrogen doping yields titanium oxynitride (TiO_xN_y). The structure modifications of TiO_2 are initiated by creating oxygen vacancies, decreasing the grain size and by annealing **[8.3]**. High-energy ball milling (BM) triggers phase transformation in TiO_2 **[8.4]**. TiO_2 can also be reduced by using Mg **[8.5]**. Among the resultant phases of reduction of TiO_2 by Mg is a bioactive magnesium titanate oxide ($MgTiO_3$) phase **[8.6]**. Thermal analysis by DSC revealed that the unmilled Mg-TiO_2 powders showed no reaction when heated to about 500 °C, while in the mechanically milled powders an exothermic reaction appeared at about 390 °C, and complete disappearance of TiO_2 after annealing at 400 °C **[8.6]**. The reduction of ileminite by Mg was confirmed during mechanical milling, while the XRD patterns of the products exhibited MgO, Mg_2TiO_4 and $MgTiO_3$ phases present in the powders **[8.7]**. Mg_2TiO_4 is a metastable system, and the material is used as a heat resistor, dielectric for microwave technology, capacitor for temperature compensation and as refractory material **[8.8]**. It crystallizes in the cubic system, with inverse spinel structure complex oxides, with a regular structure that consists of a FCC close-packed oxygen sub-lattice, in which 1/3 of the metal ions are located in tetrahedral sites and the remaining ions are situated in octahedral sites **[8.9]**.
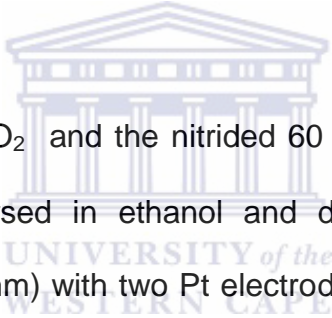
With respect to gas sensing, it is compulsory to monitor the concentrations of hazardous/explosive gasses such as H_2, NH_3, CH_4, etc., in the workplace and environment for health and safety due to their toxicity and explosive possibility. Among the metal oxides (MOX) for gas sensing applications, TiO_2 is one of the most attractive MOX semiconductor materials because of its wide band gap (3.2 eV), low cost, non-toxic nature, strong oxidizing power, and high resistance to chemical or photo-induced corrosion, etc. Previous studies showed that the physical, chemical characteristics and the performance of TiO_2 nanostructures are strongly dependent on its crystalline structure, morphology and dimension [8.10-8.12]. Additionally, TiO_2 has three different crystalline polymorph phases namely, anatase, rutile, and brookite. Each phase exhibits different characteristics appropriate for specific applications. Trinchi et al. [8.13] reported a good sensing performance of TiO_2-CeO_2 thin films towards 100-10,000 ppm O_2 in the temperature range 300-470 °C. Moreover, studies reported several sensing results on pure TiO_2 and that doped with other MOX, such as TiO_2-WO_3 [8.14], TiO_2-V_2O_5 [8.15], TiO_2-SnO_2 [8.16], and TiO_2 [8.17]. An improved selectivity to trimethylamine and NH_3 was reported by Hayakawa et al. [8.18] using Pt dispersed-TiO_2 nanoparticles. Doping of metal elements or surface modification of oxides was reported to be one of the effective methods in improving the sensing behaviour of semiconductor MOX. Liu et al. [8.19] reported much higher H_2 sensing performance for Mg-doped ZnO films than undoped ZnO films. By incorporating Mg in the TiO_2 matrix, nanostructures with tuneable properties can be produced that are promising for gas sensing

177

applications. In general, incorporation of Mg ions in the TiO_2 lattice may modify the value of the optical band of TiO_2 and this will raise the probability of band gap engineered nanostructures for sensing applications **[8.19]**. To the best of our knowledge, there are no reports on the sensing properties of Mg-TiO_2 and Mg-TiO_2-N_2. Therefore, in the present work, a novel preparation process for developing a new nanostructured material by doping ball milled Mg-TiO_2 powder with nitrogen during annealing is reported for the first time. The surface morphology, structural and optical properties are studied in detail using atomic force microscopy, X-ray diffraction, high resolution transmission electron microscopy, Raman and photoluminescence spectroscopy. The responses of Mg-TiO_2 and Mg-TiO_2-N sensing materials to hydrogen, ammonia and methane were examined, and the significant factors influencing the gas sensing performance were revealed by PL and XPS analyses. Moreover, the sensing response towards humidity is also investigated and discussed in detail.

8.2. EXPERIMENTAL DETAILS

Magnesium (purity 99.9%) and TiO_2 (purity 99.9%) were mixed in a 1:1 weight ratio; then ball milled for 60 hours (h) and annealed at 650 ºC in a tube furnace at ambient conditions and under nitrogen (N_2) gas flowing for two hours. The surface morphology of the powders was characterized by Zeiss-Auriga field-emission scanning electron microscope. The structural property was studied using a PANalytical X'pert-PRO PW 3040/60 X-ray diffraction (XRD) machine fitted with a CuK_α radiation source. The crystallite sizes were estimated using the

Scherrer formula **[8.20]**. Optical properties were measured using a Jobin-Yvon NanoLog photoluminescence (PL) and Perkin-Elmer Lambda 750 UV-vis spectrometer. The topography of the films prepared on an alumina substrate was analyzed using atomic force microscopy (AFM, Veeco, Digital Instruments). The Raman spectra were carried out using a Horiba Jobin-Yvon HR800 Raman microscopy equipped with an Olympus BX-41 microscope attachment. Nitrogen (N_2) adsorption–desorption isotherms were obtained using a Micrometiritics TRISTAR 3000 surface area analyzer (USA). X-ray photoelectron spectroscopy measurements were carried out using a PHI 5000 Versaprobe-Scanning ESCA Micro-probe.

The 60 h milled Mg-TiO_2 and the nitrided 60 h milled Mg-TiO_2 at 650 °C nanostructures were dispersed in ethanol and drop-coated on the alumina substrates (size:2 mm × 2 mm) with two Pt electrodes (on its top surface) and a micro-heater (on its bottom surface). Prior to the measurements, the sensor was heated at 500 °C for 24 hrs to remove any residual organic content. The sensors were then exposed to multiple analyte concentrations (hydrogen (H_2), ammonia (NH_3) and methane (CH_4) gas – 5, 10, 20, 40, 60 80 and 100 ppm) diluted in synthetic air at various operating temperatures (300, 350 and 400 °C). A computerized gas calibration system was used to vary the analyte concentrations balanced in synthetic air. The film resistance was measured by a Keithley 3706 source meter using a gas sensing station KSGAS6S (KENOSISTEC, Italy).

8.3. RESULTS AND DISCUSSION

The phase transformation of a 60 h-milled Mg-TiO$_2$ powder was investigated by TGA analysis. **Fig. 8.1** shows the TGA graph of the 60 h-milled powder. The derivative of TGA analysis (inset) shows two decomposition temperatures for the Mg-TiO$_2$ during absorption of nitrogen gas. The first stage of decomposition is mild and starts at 523 °C and ends at 575 °C with a minimum weight gain of about 3%. The second stage shows a significant weight gain, which occurs around 653 °C, resulting to a maximum weight gain of about 40%. The resultant powders after TGA analysis changed in colour from light grey to golden/reddish.
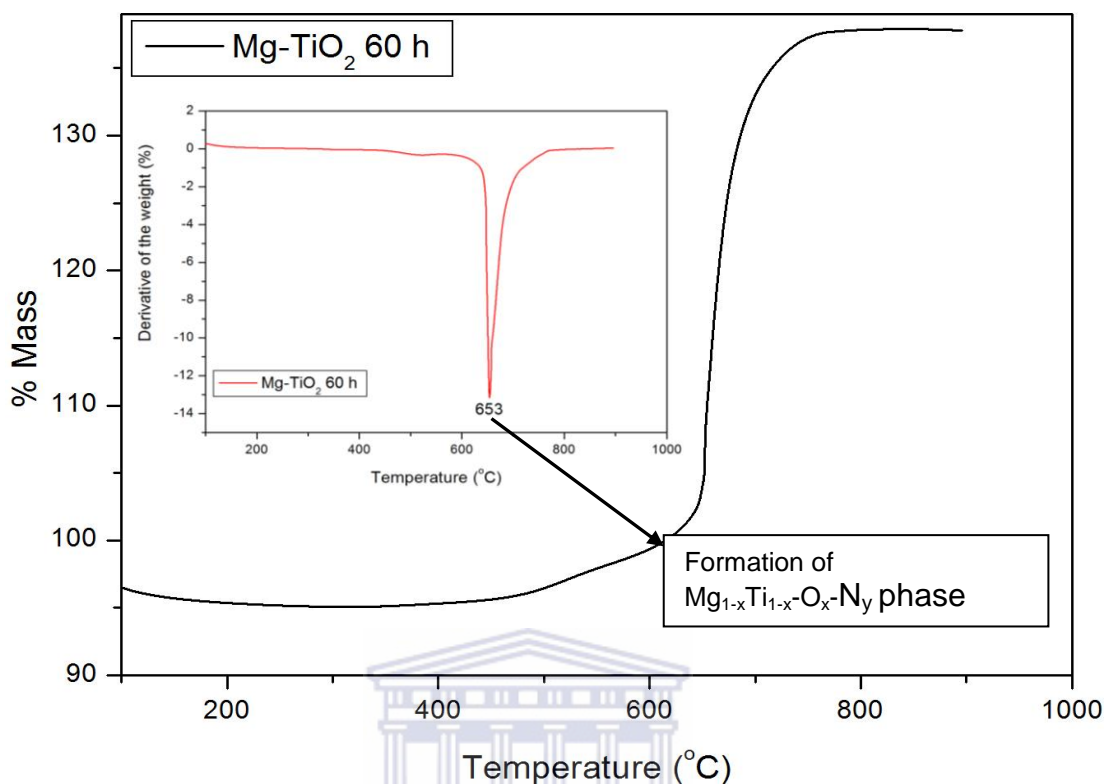
UNIVERSITY of the
WESTERN CAPE

Fig. 8.1: TGA curve of the 60 h milled Mg-TiO$_2$ powder. Inset corresponds to derivative plot showing the decomposition stages in N$_2$ atmosphere at heating rate 10 °C min^{-1}.

It is known that an Mg-TiO$_2$ powder mixture annealed in Ar yields spinel Mg$_2$TiO$_4$ with lattice parameter a=8.444 Å. The formation of Mg$_2$TiO$_4$ is an intermediate phase caused by the reaction between un-reacted TiO$_2$ and MgO formed **[8.21].** Possible reactions could yield phases according to the following reactions:

$$TiO_2 + Mg \rightarrow TiO + MgO \qquad\qquad (8.1)$$

$$Mg + 2TiO_2 = Ti + Mg_2TiO_4 \qquad\qquad (8.2)$$

$$1.5TiO_2 + Mg \rightarrow MgTiO_3 + 0.5Ti \qquad\qquad (8.3)$$

On the other hand, the following free energy formations were reported **[8.22]**:

$$\Delta G_f: \ MgTiO_3 = -1308.779 \text{ to } -1158.464 \qquad\qquad (8.4)$$

$$\Delta G_f: \ Mg_2TiO_4 = -1815.309 \text{ to } -1610.318 \qquad\qquad (8.5)$$

$$\Delta G_f: \ MgO = -504.255 \text{ to } -442.919 \qquad\qquad (8.6)$$

Due to indications obtained from the TGA results, the 60 h Mg-TiO$_2$ powder was annealed in a tube furnace at 650 °C in nitrogen atmosphere for 2 hours. **Fig. 8.2** shows the XRD patterns of the 60 h milled sample and after nitridation at 650 °C. XRD peaks of HCP Mg and tetragonal TiO$_2$ are denoted as 1 and 2 respectively. Based on the results, for the milled 60 h Mg-TiO$_2$, there is no obvious phase transformation after milling, although the TiO$_2$ (101) and (200) peaks were reduced and almost completely eliminated. The crystallite sizes as a function of milling time and nitridation are shown in **Table 8.1**. Despite the difference in the starting crystallite sizes of both Mg and TiO$_2$ powders, they reduced to approximately 30 nm after 60 h milling. The XRD pattern of nitrided 60 h milled powder at 650 °C shows the two FCC phases with space group and number *Fm-3m* # 225 but with corresponding different lattice parameters of 4.19 Å and 5.57 Å, respectively. Their corresponding crystallite sizes are 89 nm and 11 nm, respectively. It implies that nitridation has induced phase transformation.

Moreover, nitridation has altered the transformation path, since none of the spinel Mg_2TiO_4-type was obtained, which normally forms under argon. The induced two phases are attributed to both Ti-rich and Mg-rich oxynitrides, respectively. MgO is a highly stoichiometric oxide with lattice parameter a=4.21 Å. The lattice parameter obtained in the current work is smaller (4.190 Å), hence this phase is attributed to Mg-Ti-O_xN_y. Moreover, the calculated lattice parameters of the TiN and (Ti,Mg)N are a = 4.248 Å and a = 4.253 Å, respectively **[8.23]**, ruling out the existence of these phases. Due to the occupancy of N in oxygen interstitial positions, the formation of stoichiometric MgO was disturbed in order to follow the normal stoichiometric reaction that would have resulted in the formation of the Mg_2TiO_4 spinel phase.
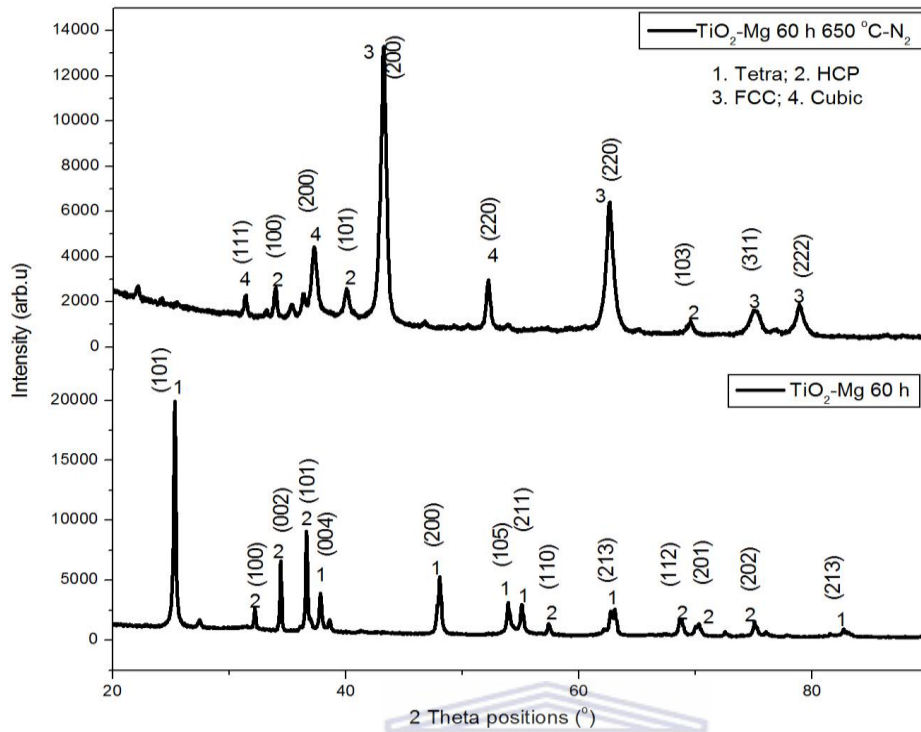
Fig. 8.2: XRD patterns of Mg-TiO$_2$ unmilled, 60 h milled and annealed powders.

Table 8.1:   Summary of crystallite sizes and phases of Mg-TiO$_2$ after ball milling and nitridation at 650 °C.

Elements	Milling time (h)	Crystallite sizes (nm)	Phases
Mg	0	93	HCP
TiO$_2$	0	127	Tetragonal
Mg	60	72	HCP
TiO$_2$	60	70	Tetragonal
Mg-Ti-O-N	60 Anneal 650 °C-N$_2$	89	FCC
		11	FCC

184

Fig. 8.3 shows the Raman vibration modes of the milled and nitrided Mg-TiO$_2$ powder, respectively. The characterized Raman vibration modes of the pure Mg and TiO$_2$ anatase powders are presented in the inset **(Fig. 8.3)**. Due to the presence of Mg, the original Raman vibration modes of anatase have shifted. The Raman peaks of the 60 h milled sample appear at 141, 195, 395, 515 and 637 cm^{-1}. In addition to these peaks, a small shoulder peak at 170 cm^{-1} appears induced by refinement of the crystallite size. The Mg-TiO$_2$ milled powders exhibits six Raman active modes belonging to (1A$_{1g}$ at 515 cm^{-1}, 2B$_{1g}$ at 395 and 515 cm^{-1} and 3E$_g$ at 141, 197 and 633 cm^{-1}) **[8.24]**. The Raman modes of the nitrided sample confirm that phase transformation has occurred on the 60 h milled Mg-TiO$_2$. The most intense Raman peak appears at 375 cm^{-1}, in addition to 208, 335, 487, 643 cm^{-1} attributed to the cubic solid solutions. The Raman E_g modes of MgTiO$_3$ are found at 282, 330, 356, and 487 cm^{-1} **[8.25]**. Therefore, Raman peaks appearing at 335 and 487 cm^{-1} are close to those obtained for *Eg* modes of the MgTiO$_3$ phase. However, MgTiO$_3$ has a rhombhohedral crystal structure with lattice parameters a=b= 5.0557 Å; c = 13.9003 Å **[8.26]**.
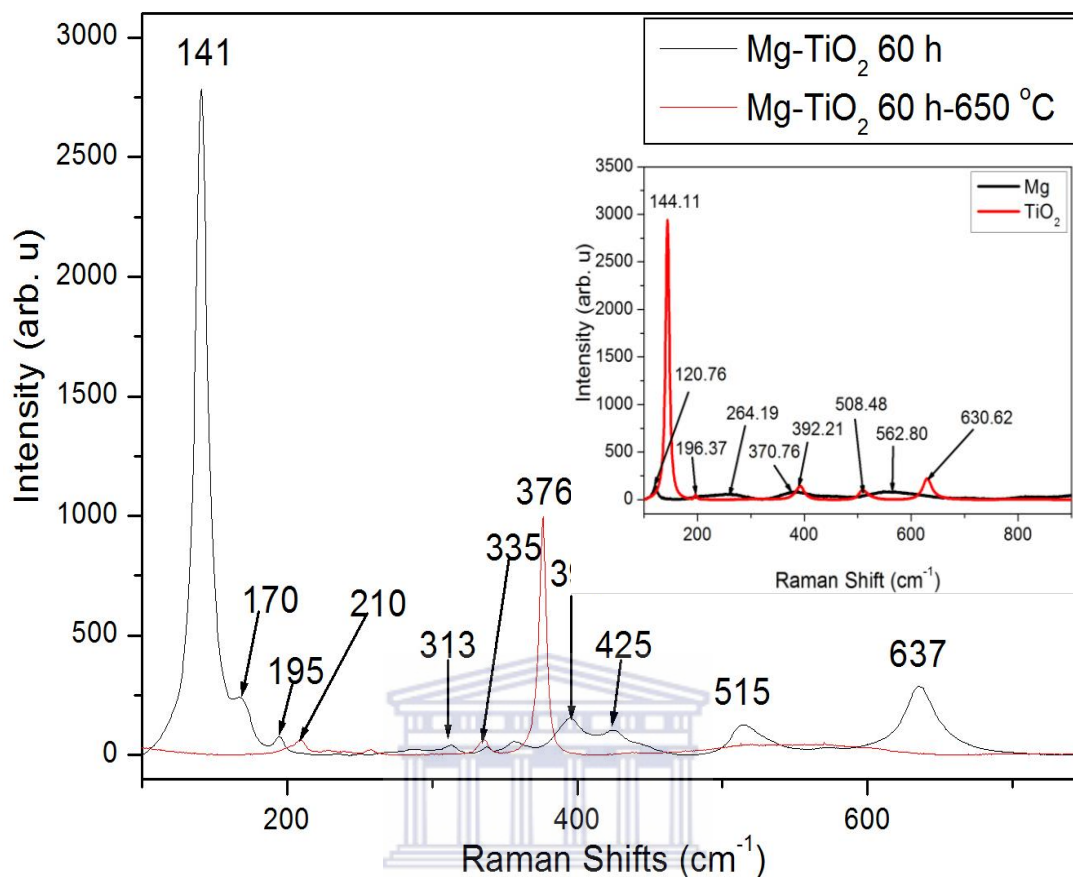
Fig. 8.3: Raman spectra of Mg-TiO$_2$ powder after milling and annealing in N$_2$

Fig. 8.4a-e depicts the milled and nitrided TiO$_2$-Mg nanostructures. The 60 h milled Mg-TiO$_2$ powder mixture in **Fig. 8.4a** shows spherical nanoparticles with diameter in range of 10-50 nm. It is observed that the nanoparticles are clustered together and showing some porous behaviour. **Fig. 8.4b-e** shows the SEM images of the 60 h-nitrided powder treated at 650 °C, displaying different morphology such as nanorods, and nanoparticles revealing porous structures. The rods vary in thickness and lengths, while some rods appear interconnected. In **Fig. 8.9d**, the nanorods appear nested together and fibrous with porous ball-

186

shaped ultrafine particles. The diameter of the rods ranges from 30 to 200 nm.

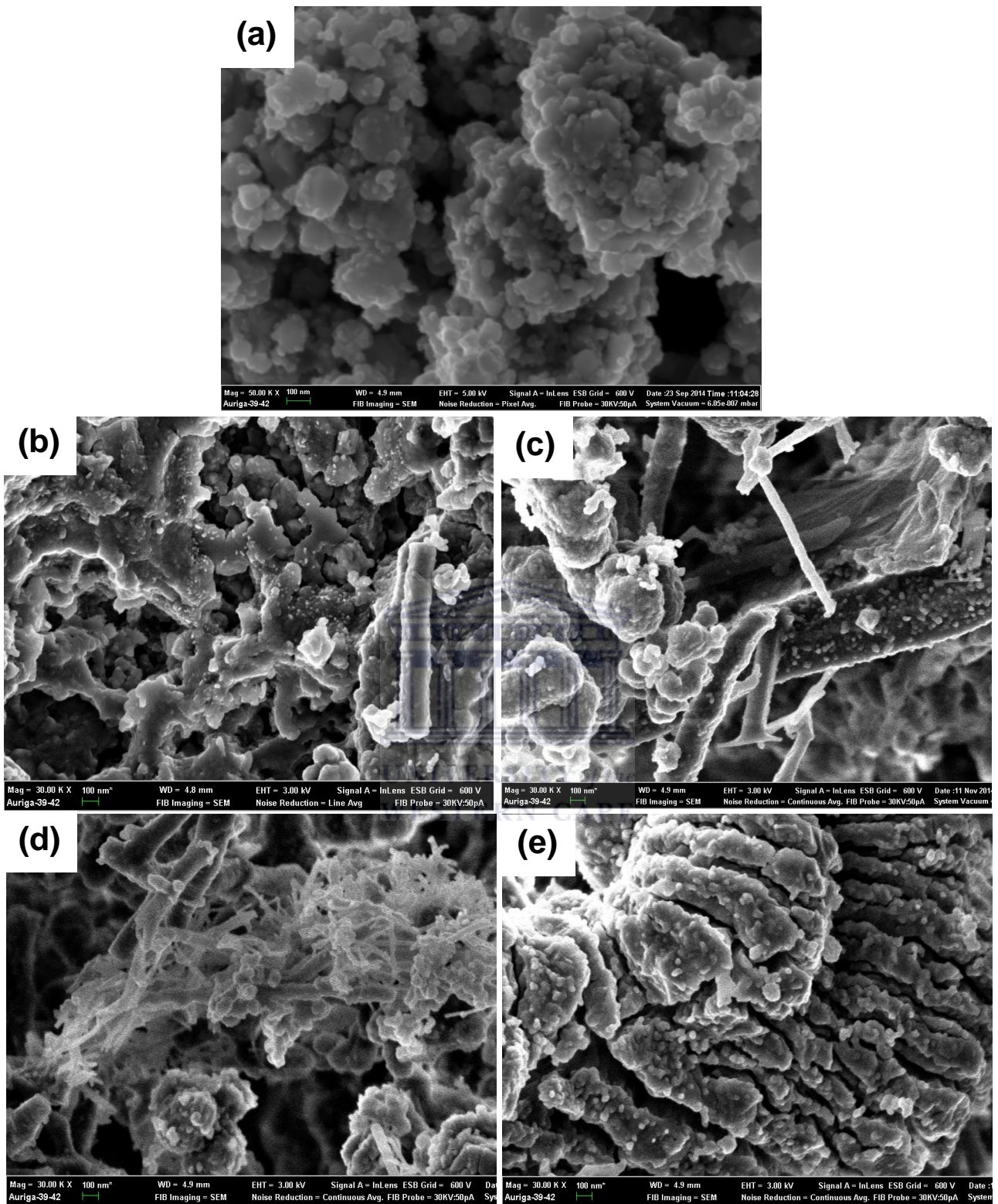**Fig. 8.9e** displays a pattern of shaped porous particle networks.

(a)

(b)

(c)

(d)

(e)

Fig. 8.4: SEM images of (a) 60 h-milled Mg-TiO$_2$. (b-e) nitrided 60 h-milled Mg-TiO$_2$ powder illustrating various phases.

The internal structure of the milled and annealed Mg-TiO_2 powders annealed in N_2 was studied using transmission electron microscopy (TEM). The 60 h milled Mg-TiO_2 demonstrates spherical nanoparticles as shown in **Fig. 8.5.** Their diameter ranges from 10-40 nm, which corresponds to the crystallite size calculated from XRD patterns. Selected area electron diffraction (SAED) shown in the inset of **Fig. 8.5b** clearly indicates that the Mg-TiO_2 nanoparticles are polycrystalline in nature. **Fig. 8.5c** depicts the TEM image of annealed Mg-TiO_2 in N_2. It is clear from **Fig. 8.5c** that upon annealing the samples in N_2, a "rod-like" structure forms. The diameter of these rods ranges from 100-150 nm, while their length is more than 1 μm. Furthemore, it can clearly be seen in the image that there are dark areas across the rods, which might be related to N_2 adsorbed on the surface of the rods. SAED patterns of the annealed milled Mg-TiO_2 sample **(Fig. 8.5d)** reveal that the number of diffraction rings increases upon annealing in nitrogen revealing that there is a structural change induced by nitrogen.
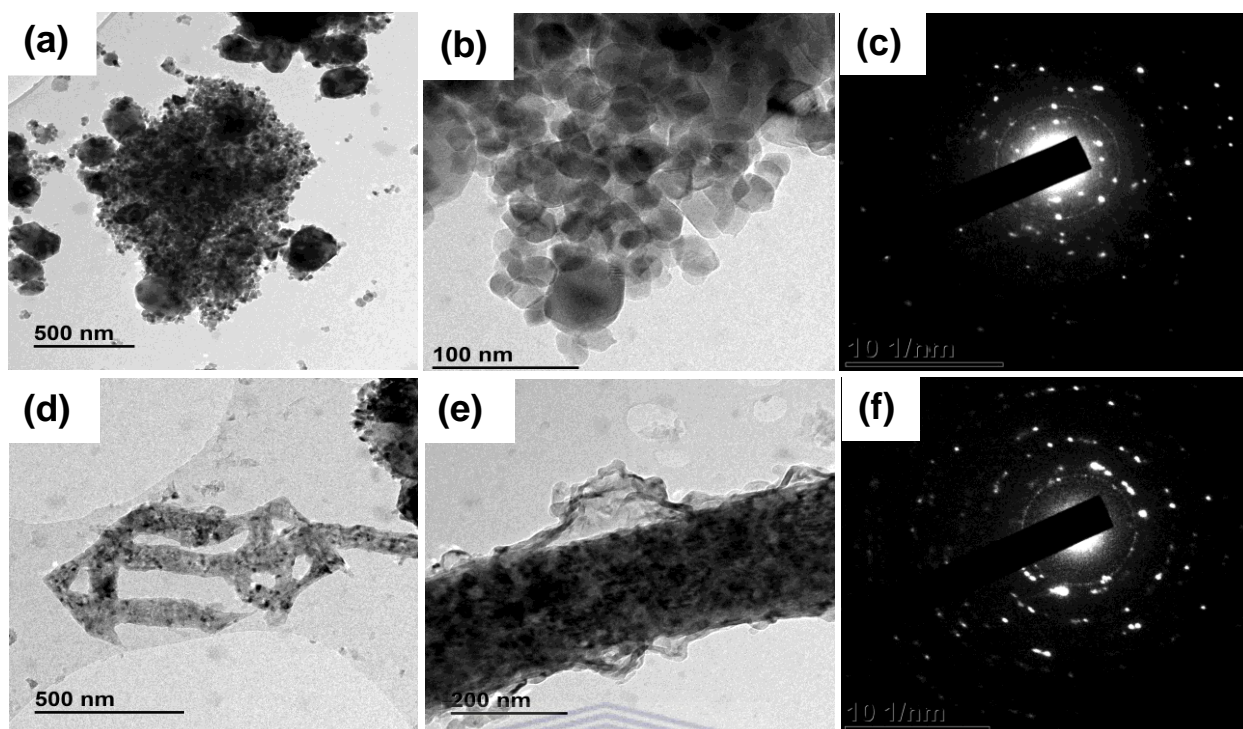
Fig. 8.5: HR-TEM images of the (a) 60 h milled and (b) milled and annealed Mg-TiO$_2$ powders in N$_2$.

It was previously reported by Egashira et al. **[8.27]** that the gas-sensing mechanism of metal oxides (MOX) is the surface-controlled type. This suggests that gas response generally depends on the amount of point defects on the MOX surface, crystallinity and particle size of the nanoparticles. Typically, the PL results are used to investigate the defects of semiconductor materials. **Fig. 8.6** depicts the PL spectra of the 60 h-milled sample, and that of the sample annealed in N$_2$. The 60 h milled sample could be fitted into three Gaussian peaks (380, 400 and 433 nm), while that annealed in N$_2$ only showed a small peak (or a hump) at 380 nm. The PL emission band at 380-400 nm (3.0 eV) was suggested

to be due to self-trapped excitons localized on TiO_6 octahedral **[8.28, 8.29]**. A PL emission band positioned around 433 nm is ascribed to the oxygen vacancy (V_O) on the surface of TiO_2.
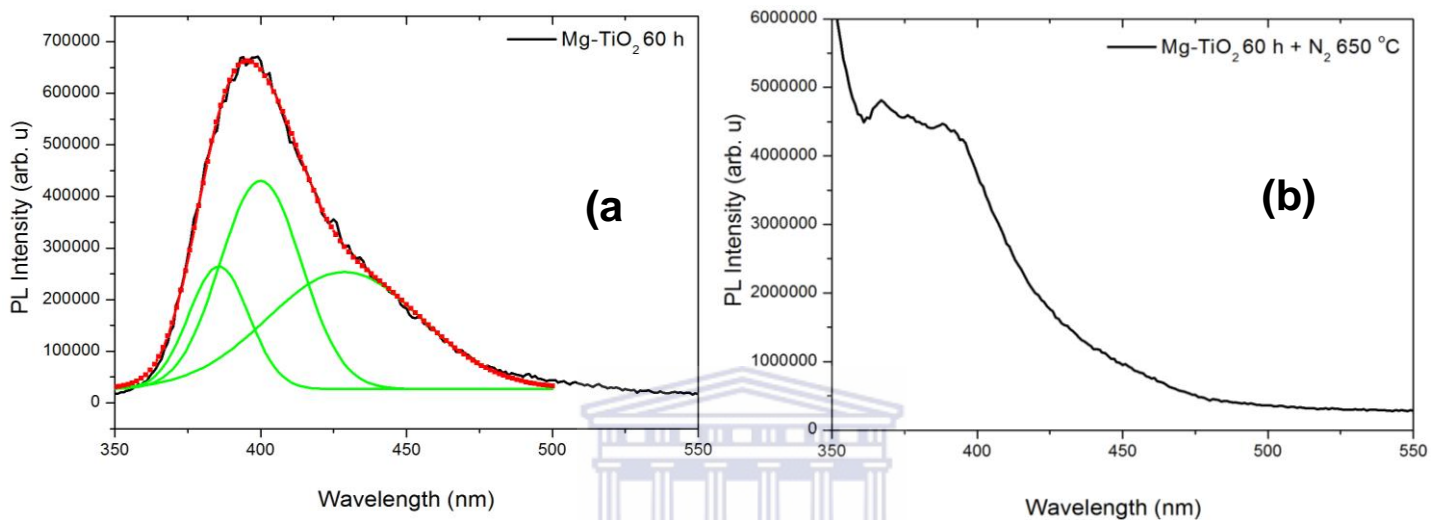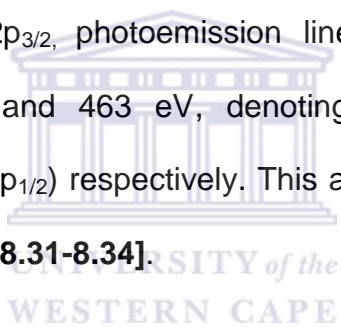

Fig. 8.6: PL spectra of the 60 h-milled and nitrided powders.

To confirm TEM speculation and complement the PL analyses, the chemical composition of the pure anatase TiO_2 in comparison to 60 h milled was investigated by X-ray photoelectron spectroscopy (XPS) analysis, and the corresponding results are shown in **Fig. 8.7**. As observed in **Fig. 8.7a**, the fully scanned spectra demonstrated that only Ti, O, and C elements existed in the pure and milled TiO_2 powder and that impurities are not evident. The detected carbon is ascribed to the carbon tape used during the measurements that adsorbed on the surface during the exposure of the sample to the ambient atmosphere. The binding energy for the C1s peak at 284.6 eV was used as the

reference for calibration. According to the literature **[8.30-8.34]**, the Ti $2p_{3/2}$ line is expected to be at the binding energies of 454.7-455.1 eV; 456.0-456.7 eV and 458.1-458.3 eV for TiN, TiO_xN_y, and TiO_2, respectively. From **Fig. 8.7b**, the $Ti2p_{3/2}$ photoemission line of the 60 h milled $Mg-TiO_2$ can be fitted into two components at 458.58 eV and 463.55 eV, assigned to $Ti^{4+}(2p_{3/2})$ and $Ti^{4+}(2p_{1/2})$. The XPS signal with nitrogen incorporation in $TiO_{2-x}N_x$ **(Fig. 8.7c)** shifts toward the lowest binding energy. According to the previous results **[8.35, 8.36]**, a shift toward lower binding energy upon nitrogen treatment reveals the successful incorporation of nitrogen into the TiO_2 lattice. Thus, the nitrided $Mg-TiO_2$ sample shows a deconvulated $Ti2p_{3/2,}$ photoemission line revealing components at 455.83, 457.62 eV, 461, and 463 eV, denoting the presence of TiO_xN_y, $Ti^{4+}(2p_{3/2})$, TiO_xN_y and $Ti^{4+}(2p_{1/2})$ respectively. This assignment is consistent with the results observed in refs **[8.31-8.34]**.
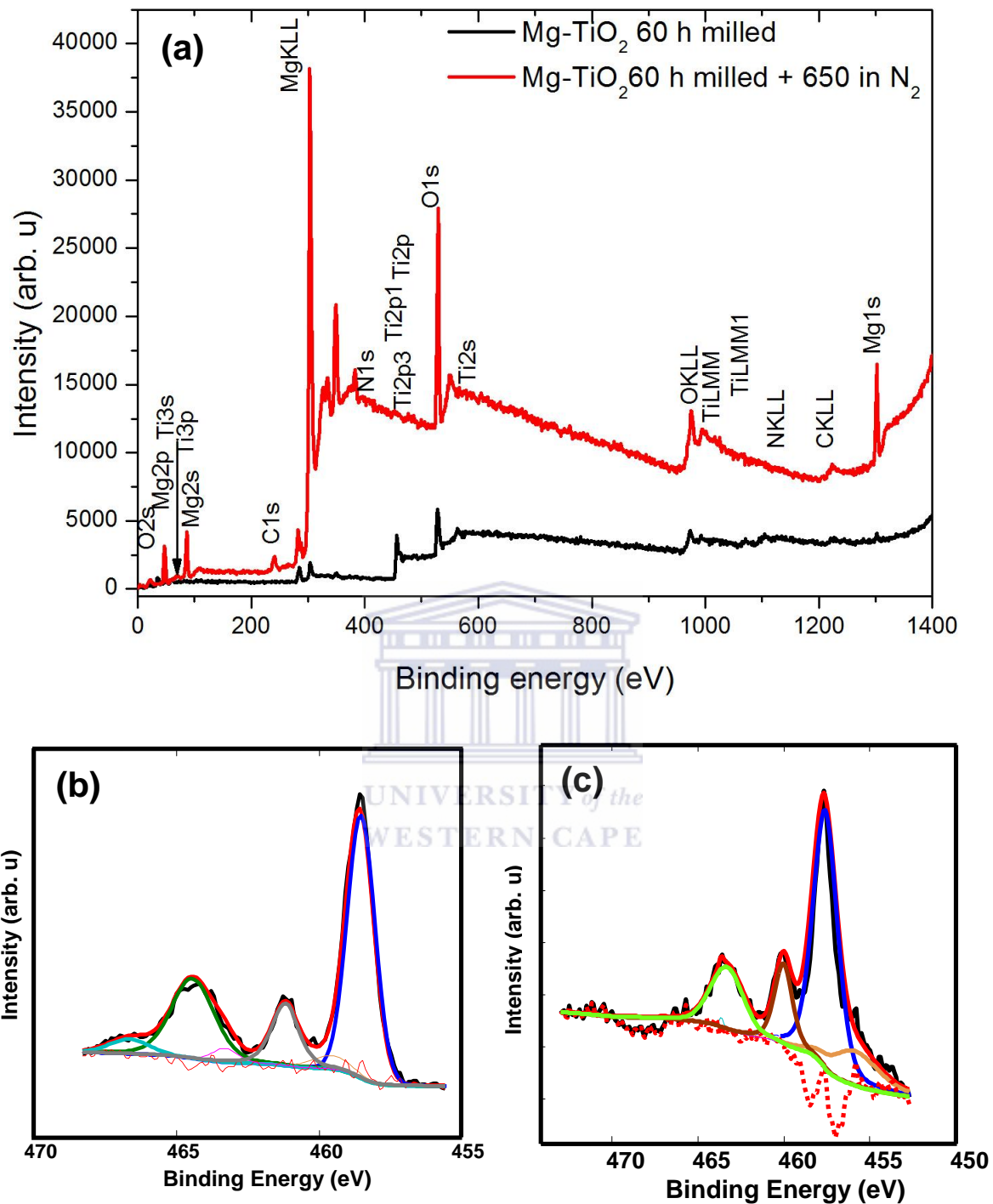
Fig. 8.7: XPS survey scan of milled and nitrided Mg-TiO$_2$ under nitrogen at 650 °C, (b-c) experimental and fitted curves for normalized Ti2p (a) Mg-TiO$_2$ 60h, (b) Mg-TiO$_2$ 60h-nitrided at 650 °C.

Fig. 8.8a-b presents the O 1s core level spectra of the 60 h milled Mg-TiO$_2$ and nitrided Mg-TiO$_2$ under nitrogen at 650 °C. The 60 h milled Mg-TiO$_2$ shows two oxygen peaks, and oxygen on the sample surface exists at least in three forms at the binding energies of 529.20 and 532.78 eV, which corresponds to the oxygen vacancy-Ti^{4+} and surface –OH, respectively **[8.37]**. After nitridation, a broad surface peak exists at least in three forms at the binding energies of 530.27, 531.3 and 532.23 eV, corresponding to oxygen vacancy-Ti^{2+}, Ti–N–O and oxygen vacancy-Ti^{4+}, respectively **[8.37-8.39]**. Previous results **[8.33]** reported O1s photoelectrons composed of two components centered at 530.2 and 531.8 eV, related to characteristics of Ti oxide and Ti oxynitride, respectively.

The photoelectron peak of Mg$_{2p}$ on the 60 h milled Mg-TiO$_2$ and nitrided Mg-TiO$_2$ under nitrogen at 650 °C is observed at 49.54 and 49.57 eV respectively, and this is shown in Fig. 8c-d. This clearly shows substantial evidence that the Mg 2p$_{3/2}$ **[8.40]** is indeed doped in the TiO$_2$ matrix. In **Fig. 8.8e**, a major N 1s peak located at 396.5 eV is a characteristic for nitrogen shifts in metal nitrides and oxynitrides **[8.33, 8.38]** while the minority line located at 394.58 could be due to the adsorbed nitrogen released during nitridation of Ti-O sites, or surface oxynitride species.
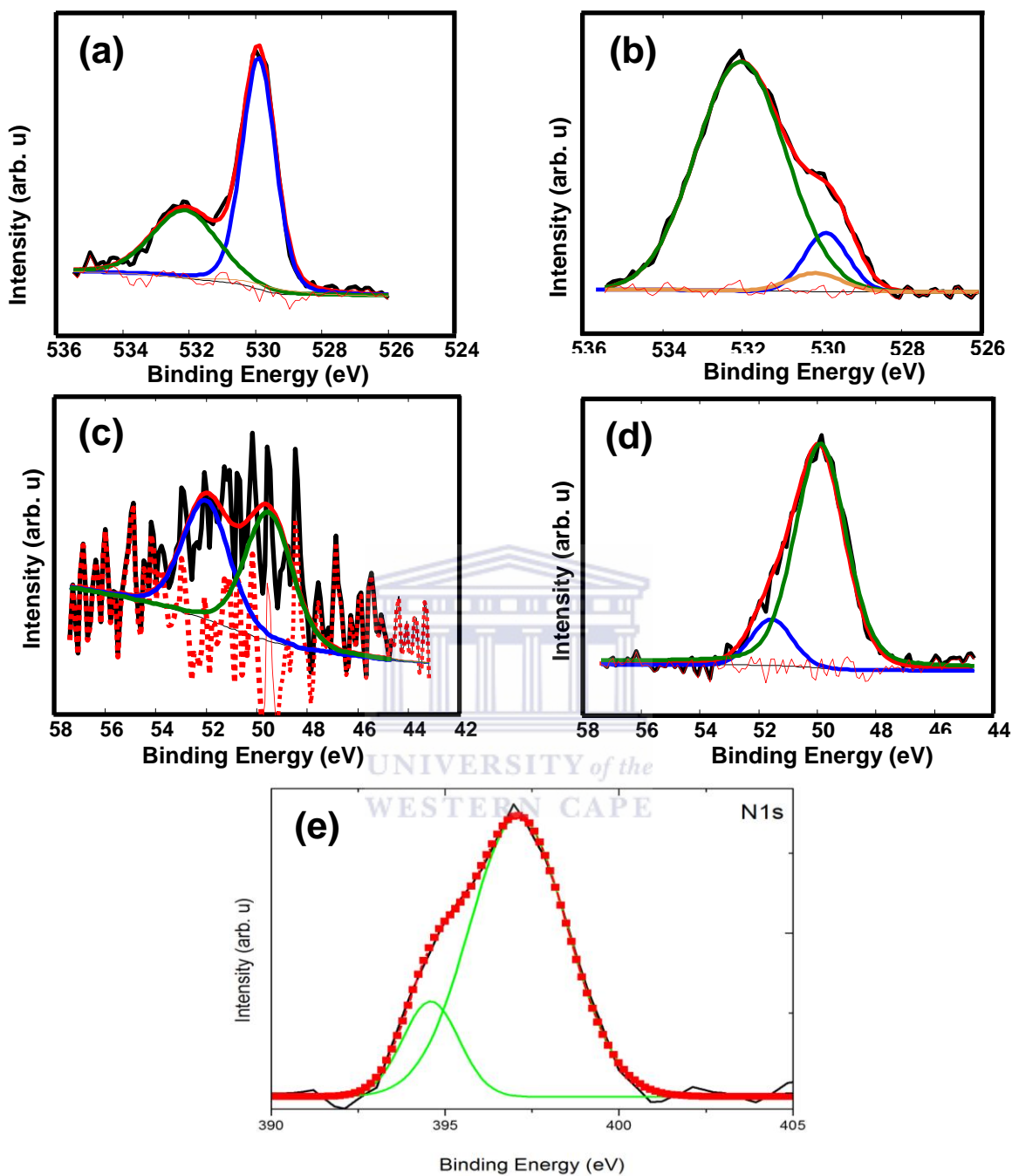
Fig. 8.8: Experimental and fitted curves for O1s XPS spectra of (a) Mg-TiO$_2$ 60h, (b) Mg-TiO$_2$ 60h nitrided and (c-d) correspond to Mg$_{2p}$ of Mg-TiO$_2$ 60h and Mg-TiO$_2$ 60h nitrided nanostructures and (e) N1s core level.

Fig. 8.9 shows atomic force microscopy (AFM) height and 3D micrographs of Mg-TiO$_2$-60 h and nitrided Mg-TiO$_2$-60 h deposited on an alumina substrate. The 60 h milled Mg-TiO$_2$ sample **(Fig. 8.9a)** is mainly composed of nanoparticles, which are clustered together revealing a surface roughness of 55.12 nm. Previous studies showed that larger surface roughness is beneficial for sensing properties **[8.41]**. The Mg-TiO$_2$-60 h nanoparticles having more rough surfaces might result in a larger surface area. The high surface area provides more active sites for gas molecule adsorption. However, upon annealing the powder under nitrogen gas (N$_2$) the size of the particles reduced resulting in a roughness of 34.24 nm. The influence of milling and annealing on the surface roughness **(Fig. 8.9a and b)** for the Mg-TiO$_2$ and Mg-TiO$_2$-N powders can be correlated to the changes in crystallite size and orientation in these alloys.
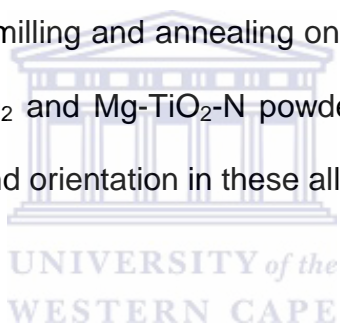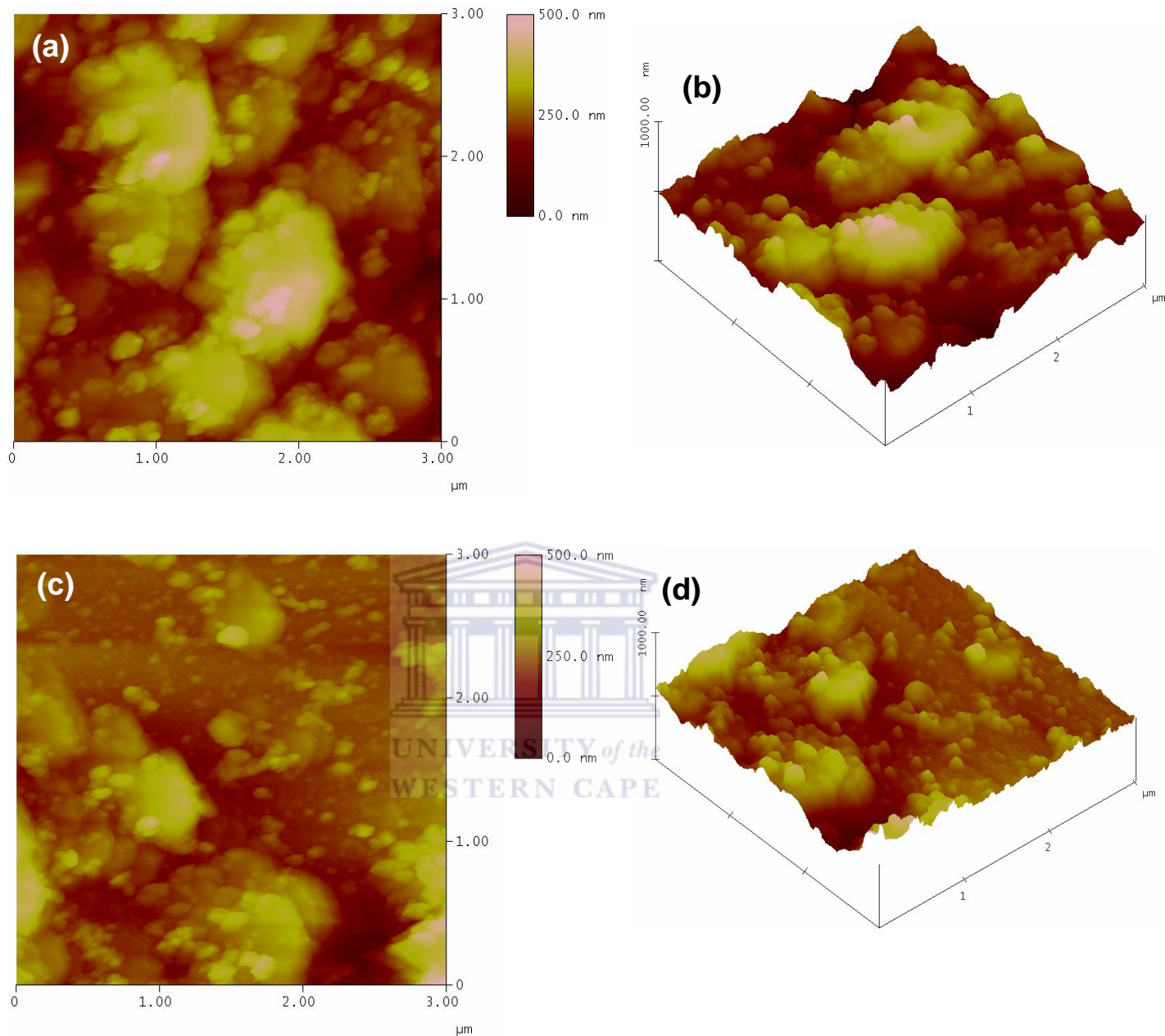
Fig. 8.9: AFM height and 3D micrographs of (a-b) 60 h milled and (c-d) milled and annealed Mg-TiO$_2$ powder in N$_2$.

Fig. 8.10 shows typical N$_2$ adsorption/desorption isotherm curves of the 60 h milled and nitrided Mg-TiO$_2$ powders annealed at 650 ^{o}C under the flow of

nitrogen gas. **Fig. 8.10** shows that the isotherms shift upwards while the hysteresis loops at high relative pressure increases, denoting higher pore size distribution on the 60 h milled Mg-TiO$_2$ powder as shown in **Table 8.2**. However, for the Mg-TiO$_2$ nitrided sample, the isotherms shift downwards while the hysteresis loops at high relative pressure decreases, signifying lower pore size distribution as well as low BET surface area. This clearly indicates that annealing under nitrogen appears to have reduced the surface area by shrinking the ultrafine particles induced by BM, but improving the crystallinity of powder particles.
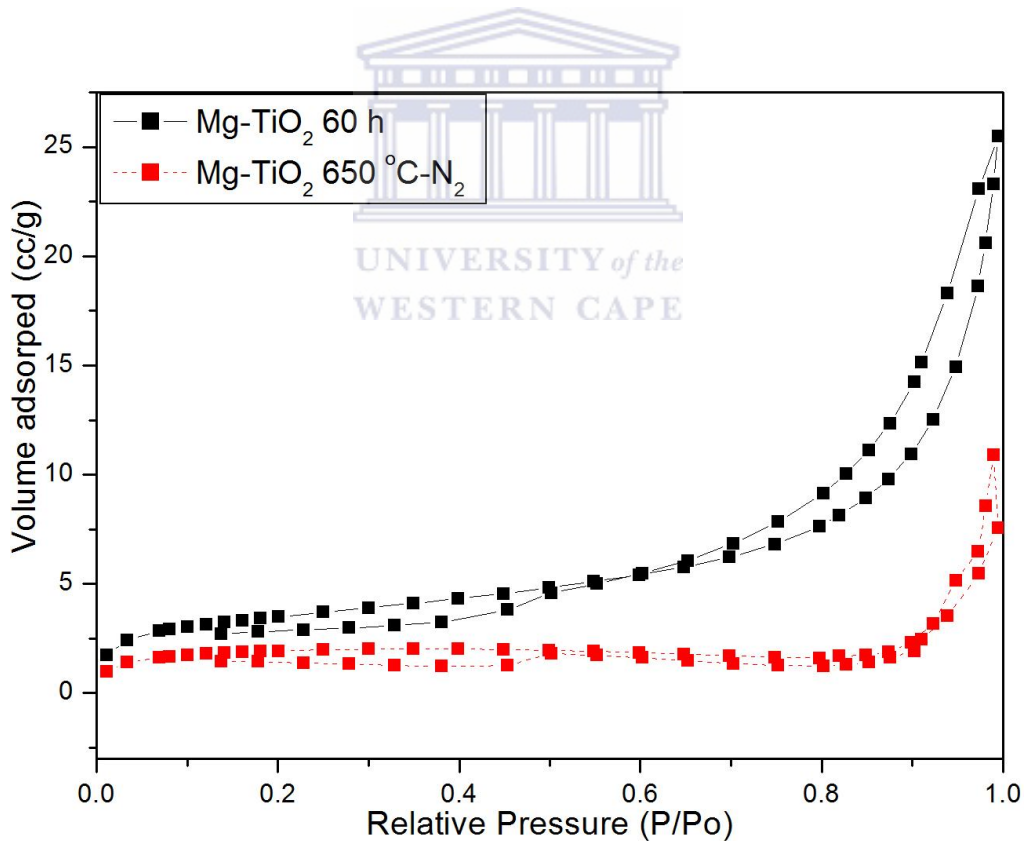

Fig. 8.10:   N$_2$ adsorption/desorption isotherm curves of 60 h milled and nitrided Mg-TiO$_2$ powders annealed at 650 $^{\circ}$C.

Table 8.2: Summary of surface area, pore volume and pore size of the milled and nitrided Mg-TiO$_2$ powders

Sample	Surface area (m²/g)	Pore Volume (cm³/g)	Pore size (nm)
60 h Mg-TiO$_2$	12.4792	0.036043	11.55282
60 h Mg-TiO$_2$-650 °C-N$_2$	6.8656	0.013268	7.73014

Fig. 8.11 shows the UV-vis absorption spectra of milled TiO$_2$, Mg and 60 h milled and nitrided Mg-TiO$_2$ powders annealed at 650 °C. It is evident from **Fig. 8.11** that by milling the Mg-TiO$_2$ mixture improved absorption has resulted when compared to elemental TiO$_2$ and Mg that were milled separately. It is noteworthy to point out that when the 60 h milled Mg-TiO$_2$ powder was annealed, the absorption spectra improved. This observation is consistent with the results observed from PL analysis. The band gap of these samples was calculated using Tauc's formula **[8.42]**:

$$\alpha h v = A(h v - E_g)^{n/2} \qquad (8.7)$$

where ͺ α is the absorption coefficient, A is a constant, $h v$ is the energy and n depends on whether the transition is indirect (n = 4) or direct (n = 1). The spectra of $(\alpha h v)^2$ as a function of $h v$ are shown in **Fig. 8. 11b and c**. From the plots, the band gaps of the milled TiO$_2$, 60 h milled and nitrided Mg-TiO$_2$ powders were estimated to be 3.26, 3.24, 3.15 and 3.06 eV, respectively. It is clear that the band gap reduces upon nitridation of the 60 h milled Mg-TiO$_2$ powder at 650

°C. This behaviour confirms the structural transformation observed in XRD and HR-TEM analyses.
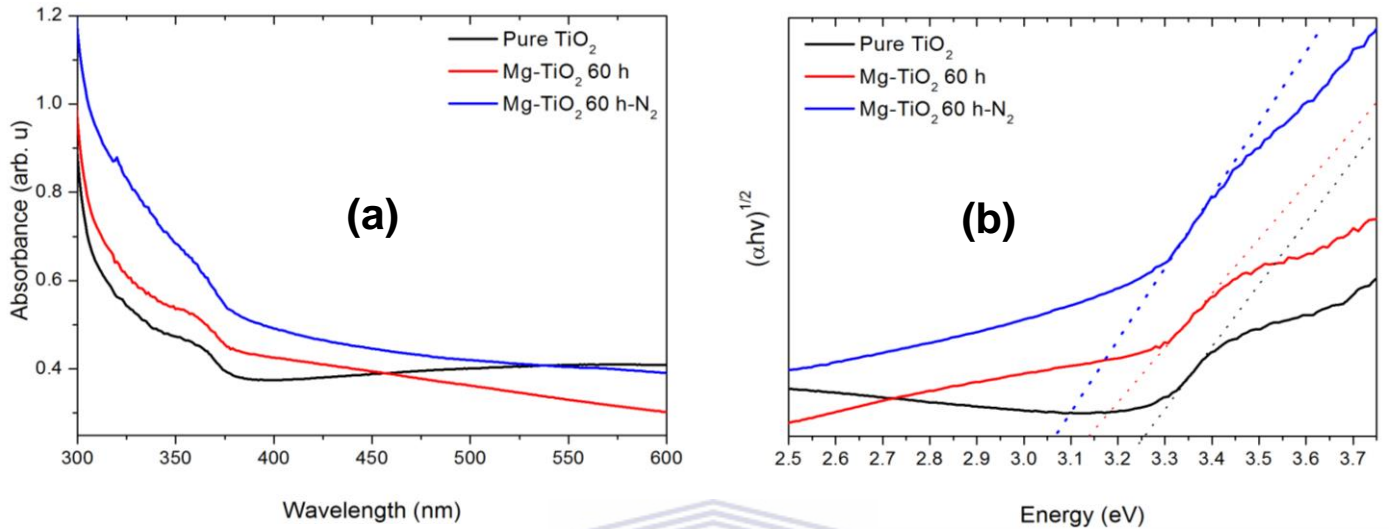

Fig. 8.11: (a) UV-vis absorption spectra of the milled TiO_2, Mg and 60 h milled and nitrided $Mg-TiO_2$ powders annealed at 650 °C and (b) Tauc plots of $(\alpha h\nu)^2$ as a function of energy.

The gas sensing performance of the sensor was studied by measuring the conductance change of the sensing material in the presence and absence of of H_2, CH_4, and NH_3. The response percentage in terms of change in resistance of the sensor on gas exposure such as reducing is defined as:

$$S(\%) = \frac{R_a}{R_g} \times 100 \qquad (8.8)$$

where R_g is the resistance measured with the presence of the gas, and R_a is the resistance measured in synthetic air (in the absence of reactive gas). The real-

time response curve of the sensors to various concentrations (5–100 ppm) of H_2, CH_4, and NH_3 operated at various temperatures are presented in **Fig. 8.12**. The response time (t_{res}) is defined as the time required for reaching 90% of the equilibrium value of the resistance after gas exposure, and the recovery time (t_{rec}) is defined as the time required for the resistance to return to 10% below the original resistance in air after the test gas is released **[8.43]**. It clear from the **Fig. 8.12** that in all conditions, the response of all the sensing materials increases (or resistance is decreases) when they are exposed in reducing gasses and settles back to the original value when the test gas is vented. A very good reproducibility is thus clearly observed. This behavior is typical for n-type semiconductor gas sensing material **[8.44]**. **Table 8.3** shows the t_{res} and t_{rec} of 60h milled Mg-TiO_2 and nitrided 60h milled Mg-TiO_2 nanostructures tested for the 40 ppm of different gases. It is observed from the table that sensors tested in NH_3 gas reveal improved t_{res} compared to other gases suggesting that the sensor responds quickly to both the injction and removal of the target gas.
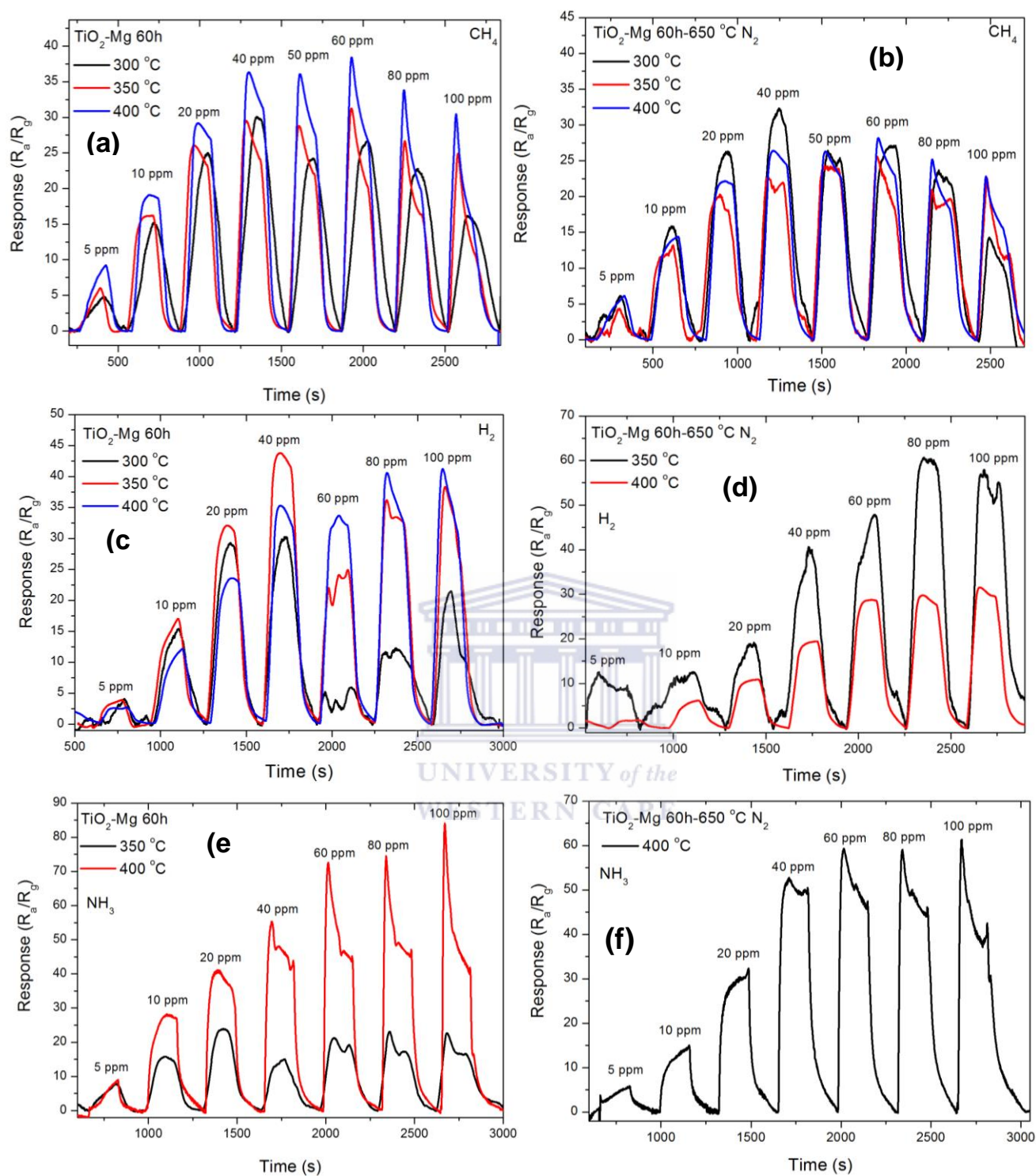
Fig. 8.12: Real-time response curves of the sensor device upon exposure to different concentrations of (a-b) CH_4, (c-d) H_2 and (e-f) NH_3 at working temperatures of 300, 350 and 400 °C.

Table 8.3: Summary of t_{res} and t_{rec} of Mg-TiO$_2$ 60h and 60h-650 °C N$_2$ nanostructures for different gases.

Materials	CH$_4$ (40 ppm)		NH$_3$ (40 ppm)		H$_2$ (40 ppm)	
	t_{res} (s)	t_{rec} (s)	t_{res} (s)	t_{rec} (s)	t_{res} (s)	t_{rec} (s)
Mg-TiO$_2$ 60h	50	56	32	48	53	82
Mg-TiO$_2$ 60h+-650 °C N$_2$	55	59	35	82	58	70

Fig. 8.13 shows the responses of Mg-TiO$_2$ 60 h milled and nitrided Mg-TiO$_2$ sensing films versus concentration (5-100 ppm) of H$_2$, CH$_4$, and NH$_3$ at various working temperatures. Fig. 13 displays that the response of all the sensors increases rapidly with the growth of the concentration up to 40 ppm at 300 °C, then saturates thereafter **[8.45]**. The dependence of the sensor response on the gas concentration is noticeable. However, both 60 h milled Mg-TiO$_2$ and nitrided sensors showed no response when tested for NH$_3$ at 300 °C. When increasing the testing temperature, the response of sensing materials increases with incresing the concentration of the tested gasses. The increase in response with increase in temperature is due to the increase of electron concentration on the surface of Mg-TiO$_2$ nanostructures with increasing temperature **[8.46]**. In addition, the nitrided sensing material shows less response to almost all the gases compared to the unitrided sample, and in addition it is only responding at higher temperature (400 °C) when tested for NH$_3$. Chou et al. **[8.47]** indicated that nitrogen fills up holes and defects which were promoted for sensing by

milling and the presence of Mg due to nitridation at 650 °C. The higher response observed for Mg-TiO$_2$ 60 h sensing material is due to larger surface area and pore diameter (Table 2) provides more active sites for the target gas and allowing more gas adsorption. Furthermore, based on the PL and XPS results, we suggest that the higher relative concentration of V$_O$ defects are the most favorable adsorption sites for oxygen species, which can enhance the possibility of interaction with gas molecules. Previous reports indicated that the response of the metal-oxide gas sensors depends also mainly on the grain size (D) of the sensing materials [8.48]. If the grain size is close to the size of the Debye length (L$_D$), then the sensing material can display excellent sensing response. However, if the grain size is larger than the Debye length (D>L$_D$), then a moderate response will be observed, since the conduction channel with high conductivity will exists. If the grain size is much larger than the Debye length (D>> L$_D$), then, the sensing mechanism is controlled by the grain boundaries, and thus low sensing response will be observed, since only a small portion of the semiconductor is affected by interaction of the target gas. Nonetheless, for our nanostructures, such small grains ($\sim$ 6 nm) were not obtained [8.49]. Therefore, we confirm that our sensing properties are induced by larger surface area and pore diameter, which provide more active sites for the target gas and allowing more gas adsorption, as well as higher relative concentration of V$_O$ defects, which are the most favorable adsorption sites for oxygen species. The higher response of Mg-TiO$_2$ 60 h is due to high surface area **(Table 8.2)** and improved oxygen vacancies observed in PL and XPS analyses.
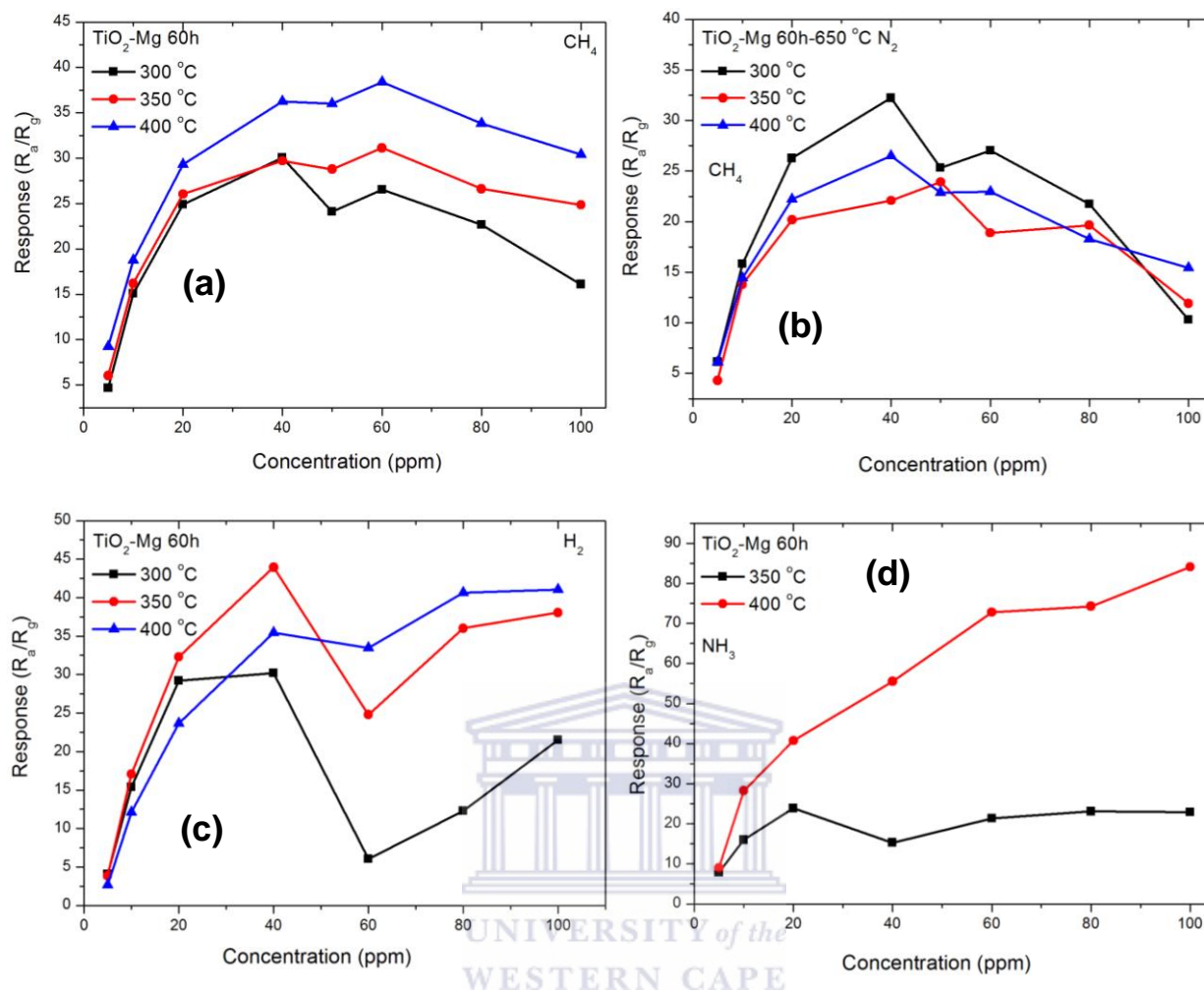
Fig. 8.13: Response curves of the sensor device upon exposure to different concentrations of (a-b) CH_4, (c-d) H_2 and (e-f) NH_3 at working temperatures of 300, 350 and 400 °C.

Generally, in semiconducting metal oxides, when the sensing material is exposed in air oxygen molecules are chemisorbed and capture electrons from the conduction band of the Mg-TiO_2 60 h milled and nitrided Mg-TiO_2, resulting in the following reaction **[8.48, 8.49]**:

$$O_2 \text{ (gas)} \quad \leftrightarrow \quad O_2 \text{ (absorbed)} \tag{8.9}$$

$$O_2 \text{ (absorbed)} + e^- \quad \leftrightarrow \quad O^{2-} \text{ (absorbed)} \tag{8.10}$$

$$O^- \text{ (absorbed)} + e^- \quad \leftrightarrow \quad O^{2-} \text{ (absorbed)} \tag{8.11}$$
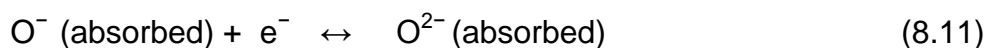
When the sensing material is exposed to a reducing gas such as CH_4, it will dissociate at the O_2 sites on the Mg-TiO_2 nanoparticles' surface, which will facilitate interaction between the resulting CH_4 and the chemisorbed O_2 ions as shown in **equation 8.11**. Then the extracted electrons are released to the conduction band of the sensing film, causing an increase of electron concentration in the conduction band. As a result the resistance of the sensing film increases **[8.50]**:

$$CH_4 + 4O^- \leftrightarrow CO_2 + 2H_2O \text{ (gas)} + e^- \tag{8.12}$$
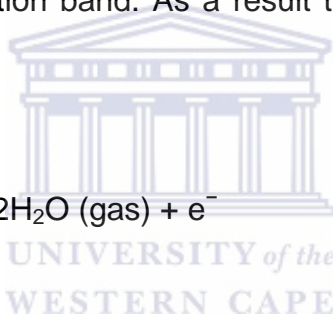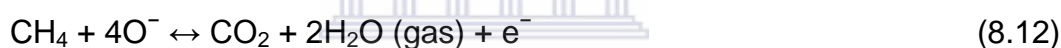
However, when H_2 gas is introduced in the chamber, the gas will react with chemisorbed oxygen species on the surface of the sensing film, producing H_2O molecules and releasing electrons back into the conduction band as shown in the following reaction **[8.51-8.53]**:

$$O_{ads}^- + H_2 \rightarrow \quad H_2O + 2e^- \tag{8.13}$$

When the Mg-TiO_2 60 h or nitrided sensing material is exposed to NH_3, the gas–solid interaction leads to the following reaction **[8.54]**:

$$4NH_3 + 3O^{-2}_{ads} \leftrightarrow 2N_2 + 6H_2O + 6e^- \tag{8.14}$$

The selectivity of the sensors based on Mg-TiO$_2$ 60 h and nitrided Mg-TiO$_2$ 60 h towards CH$_4$, H$_2$ and NH$_3$ is also examined, as shown in **Fig. 8.14.** It is observed that the response of the sensor to 40 ppm NH$_3$ is 55.05 % at 400 °C for Mg-TiO$_2$ 60 h, which is much larger than other gases, which indicates that the NH$_3$ sensor based on Mg-TiO$_2$ 60 h exhibits good selectivity and can be used for selective detection of NH$_3$. Moreover, the nitrided Mg-TiO$_2$ 60 h also showed a response of about 50.1% towards NH$_3$ at 400 °C, confirming that these sensing materials are both selective to NH$_3$.
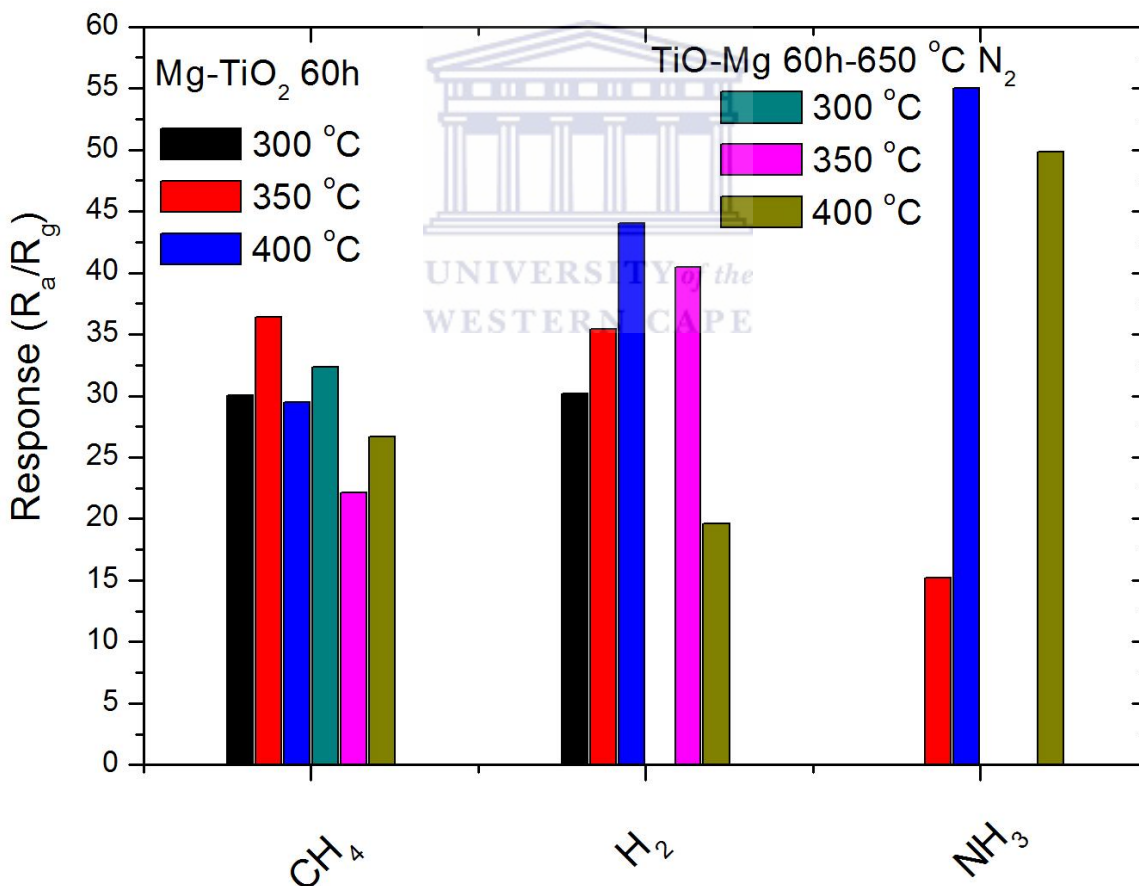

Fig. 8.14: The selectivity test for (a) 40 ppm of CH$_4$, H$_2$, and NH$_3$ at various temperatures.

To evaluate the humidity sensing properties of the fabricated devices, we measured the change in conduction of the sample at room temperature (25 °C) with various RHs. A chamber was employed to provide different humidity levels in incremental steps. **Fig. 8.15a** shows that the current of Mg-TiO$_2$ NPs milled for 60 h and nitrided 60 h Mg-TiO$_2$ increases with an increase in humidity up to 100 % RHs. The 60 h milled Mg-TiO$_2$ sensing material shows improved response compared to the nitrided sensing material, probably due to higher surface area and increased concentration of oxygen vacancies (V$_O$) on the surface of the milled material as evidenced by PL and XPS analyses **[8.55]**.
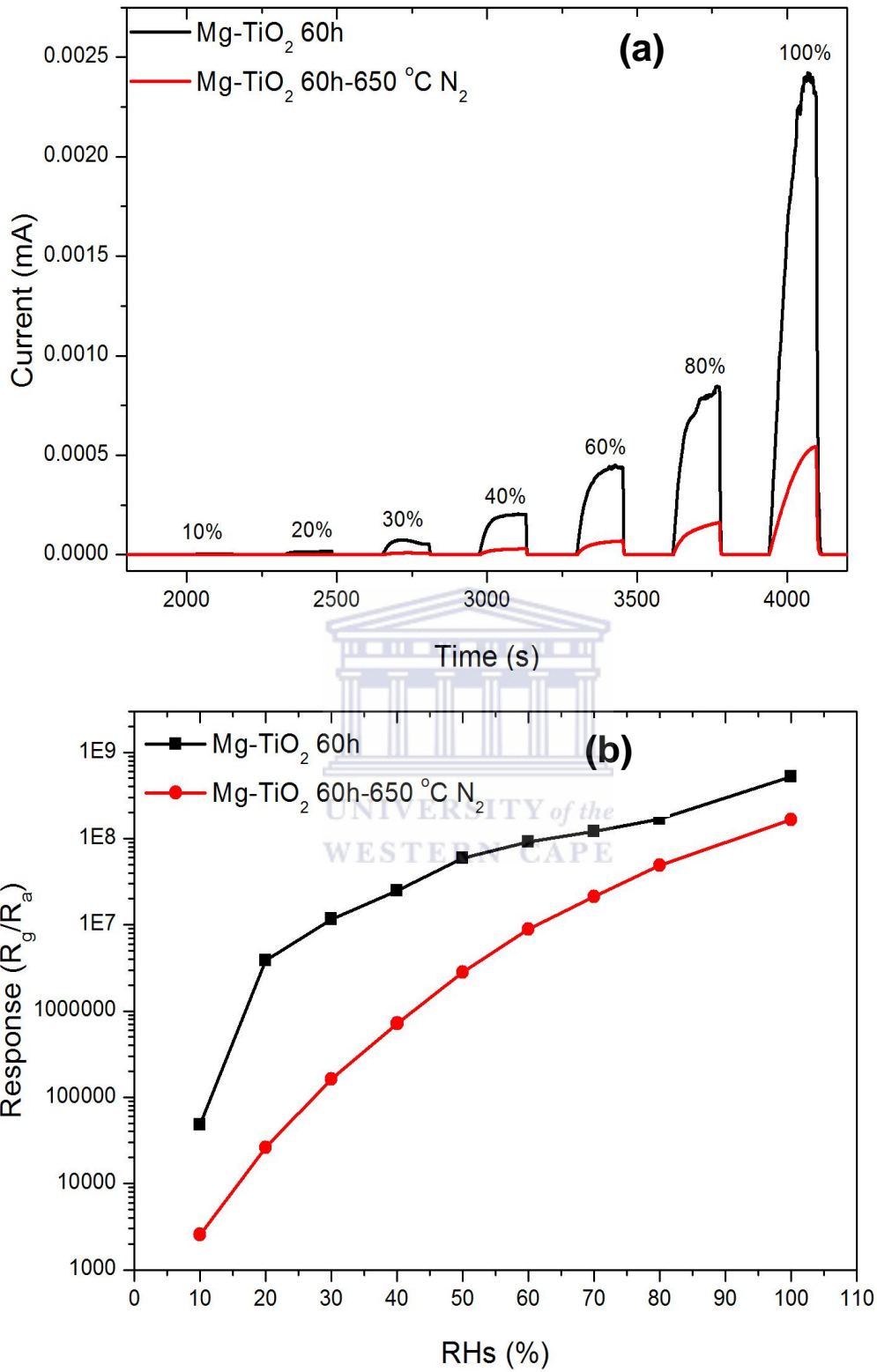
Fig. 8.15: (a) current and (b) response versus time curves of Mg-TiO$_2$ nanostructures exposed to various RHs concentrations.

8.4. CONCLUSION

Ball milling of Mg-TiO$_2$ has shown no phase transformation but reduced the crystallite sizes of the powders. Upon annealing of milled powder, two types of FCC phases yielded different lattice parameters. The induced FCC structures are attributed to the non-stoichiometric structure of the TiO$_x$N$_y$ and (Mg$_{1-x}$Ti$_{1-x}$-O$_x$-N$_y$) phases, respectively. Phase transformation was confirmed by the introduction of new Raman vibration modes on annealed samples. The Mg-TiO$_2$ 60h sensing materials revealed high sensing response to NH$_3$ showing fast response (~32 s) and recovery (~48 s) to NH$_3$ and high selectivity to NH$_3$. The 60h-milled Mg-TiO$_2$ also showed improved response when tested to RHs suggesting that they be used as humidity sensors.
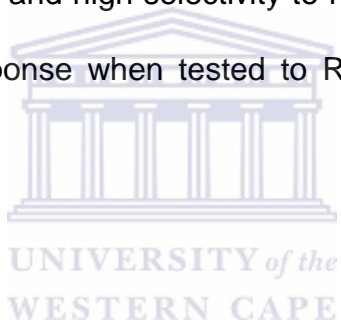
8.6. REFERENCES

[8.1] S. Bagaswi, Y. Niu, M. Nasir, B. Tian, J. Zhang, Applied Surface Science 264 (2013) 139-147.

[8.2] G. Halasi, I. Ugrai, F. Solymosi, Journal of Catalysis 281 (2011) 309-317.

[8.3] B. Choudhury, A. Choudhury, International Nano Letters 3 (2013) 1-8.

[8.4] X. Pan, X. Ma, Materials Letters 58 (2004) 513-515.

[8.5] M.O. Lai, L. Lu, B.Y. Chung, Composite Structures 57 (2002) 183-187.

[8.6] S.Z. Khalajabadi, M.R.A. Kadir, S. Izman, H.R. Bakhsheshi-Rad, S. Farahany, Ceramic International 40 (10) (2014) 16743-16759.

[8.7] N.J. Welham, Journal of Alloys and Compounds 274 (1998) 260-265.

[8.8] M.J. Martinez-Lope, M.P. Baura-Pena, M.E. Garcia-Clavel, Thermochimica Acta 194 (1992) 59-65.

[8.9] M. R. S. Silva, S. C. Souza, I. M. G. Santos, M. R. Cassia-Santos, L. E. B. Soledade, A. G. Souza, S. J. G. Lima, E. Longo, Journal of Thermal Analysis Calorimetry 79 (2005) 421-424.

[8.10] X. Chen, S.S. Mao, Chemical Reviews 107 (2007) 2891-2959.

[8.11] C. Burda, X. Chen, R. Narayanan, M.A. El-Sayed, Chemical Reviews 105 (2005) 1025-1102.

[8.12] L.T. Mancic, B.A. Marinkovic, P.M. Jardim, O.B. Milosevic, F. Rizzo, Crystal Growth Design 9 (2009) 2152-2158.

[8.13] A. Trinchi, Y.X. Li, W. Wlodarski, S. Kaciulis, L. Pandolfi, S. Viticoli, E. Comini, G. Sberveglieri, Sens. Actuators B 95 (2003) 145–150.

[8.14] H. Yang, D. Zhang, L. Wang, Sensors and Actuators B 57 (2002) 674-678.

[8.15] S. Zhuiykov, W. Wlodarski, Y. Li, Sensors and Actuators B 77 (2001) 484-490.

[8.16] Y. Li, W. Wlodarski, K. Galatsis, S.H. Moslih, J. Cole, S. Russo, N. Rockelmann, Sensors and Actuators B: Chemistry 83 (2002) 160-163.

[8.17] K.P. Biju, M.K. Jain, Sensors and Actuators B 128 (2008) 407-413.

[8.18] I. Hayakawa, Y. Iwamoto, K. Kikuta, S. Hirano, Sensors and Actuators B 62 (2000) 55-60.

[8.19] Liu Y, Hang T, Xie Y, Bao Z, Song J, Zhang H, Sensors and Actuators B 160 (2011) 266-270.

[8.20] D. Cullity, Elements of X-ray Diffraction, Addison-Wesley, Reading (MA), 1956, p. 363.

[8.21] E.A.V. Ferri, J.C. Sczancoskia, L.S. Cavalcantea, E.C. Paris, J.W.M. Espinos, A.T. de Figueiredo, P.S. Pizani, V.R. Mastelaro, J.A. Varela, E. Longo, Materials Chemistry and Physics 117 (2009) 192-198.

[8.22] H-K Shin, H Shin, H.S. Jung, S-Y Cho, J-R Kim, K.S. Hong, Materials Research Bulletin 41 (2006) 1206-1214.

[8.23] S. Onder, F.N. Kok, K. Kazmanli, M. Urgen, Materials Science and Engineering C 33 (2013) 4337-4342.

[8.24] K. Huo, X. Zhang, J. Fu, G. Qian, Y. Xin, B. Zhu, H. Ni, P.K. Chu, Journal of Nanoscience and Nanotechnology 9 (2009) 3341-9.

[8.25] A. Hodroj, O. Chaix-Pluchery, P. Steyer, J.F. Pierson, Surface & Coatings Technology 205 (2011) 4547-4553.

[8.26] T.S. Kumar, R.K. Bhuyan, D. Pamu, Applied Surface Science 264 (2013) 184-190.

[8.27] M. Egashira, Y. Shimizu, Y. Takao, S. Sako, Sensors and Actuators B 35 (1996) 62-67.

[8.28] J.-M. Wu, H.C. Shih, W.-T. Wu, Y.-K. Tseng, I.-C. Chen, Journal of Crystal Growth 281 (2005) 384-390.

[8.29] Y. Lei, L.D. Zhang, G.W. Meng, G.H. Li, X.Y. Zhang, C.H. Liang, W. Chen, S.X. Wang, Applied Physics Letters 78 (2001) 1125-1127.

[8.30] X. Yang, C. Li, B.Yang, W. Wang, Y. Qiam, Chemical Physics Letters 383 (2004) 502-506.

[8.31] M. Drygas, C. Czosnek, R.T. Paine, J.F. Janik, Chemical Materials 18 (2006) 3122-3129.

[8.32] A. Rizzo, M.A. Signore, L. Mirenghi, T.D. Luccio, Thin Solid Films 517 (2009) 5956-5964.

[8.33] M.H. Chan, F.H. Lu, Thin Solid Films 517 (2009) 5006-5009.

[8.34] X. Song, D. Gopireddy, C.G. Takoudis, Thin Solid Films 516 (2008) 6330-6335.

[8.35] X.Y. Du, Y. Wang, Y.Y. Mu, L.L. Gui, P. Wang, Y.Q. Tang, Chemical Materials 14 (2002) 3953-3957.

[8.36] J. Yang, H. Bai, X. Tan, J. Lian, Applied Surface Science 253 (2006) 1988-1994.

[8.37] X. Pan, X. Ma, Journal of Solid State Chemistry 177 (2004) 4098-4103

[8.38] N.C. Saha, H.G. Tompkins, Journal of Applied Physics 72 (1992) 3072-3079.

[8.39] M. Braic, M. Balaceanu, A. Vladescu, A. Kiss, V. Braic, G. Epurescu, Applied Surface Science 253 (2007) 8210-8214.

[8.40] M. Zukalova, J. Prochazka, Z. Bastl, J. Duchoslav, L. Rubacek, D. Havlicek, L. Kavan, Chemical Materials 22 (2010) 4045-4055.

[8.41] M.R. Mohammadia, D.J. Fray, Sensors and Actuators B 150 (2010) 631-640

[8.42] X. Zhang, X.M. Li, T.L. Chen, J.M. Bian, C.Y. Zhang, Thin Solid Films 492 (2005) 248-252.

[8.43] D.E. Motaung, P.R. Makgwane, S.S. Ray, Materials Letters 139 (2015) 475-479.

[8.44] Y. Liu, H. Zhang, Z. Zhang, Y. Xie, E. Xie, Applied Surface Science 257 (2010) 1236-1238.

[8.45] A.A. Tomchenko, G.P. Harmer, B.T. Marquis, J.W. Allen, Sensors and Actuators B 93 (2003) 126-134.

[8.46] Y. Mao, S.I. Ma, X. Li, C. Wang, F. Li, Xiaohong Yang, Jing Zhu, Lin Ma, Applied Surface Science 298 (2014) 109-115.

[8.47] J.-C. Chou, H-Y Yang, C-W Chen, Microelectronics Reliability, 50 (2010) 753-756.

[8.48] Y. Tian, J.C. Li, H. Xiong, J.N. Dai, Applied Surface Science 258 (2012) 8431-8438.

[8.49] S.H. Wei, M.H. Zhou, W.P. Du, Sensors and Actuators B 160 (2011) 753-759.

[8.50] D.E. Motaunga, G.H. Mhlongo, I. Kortidis, S.S. Nkosi, G.F. Malgas, B.W. Mwakikunga, S.S. Ray, G. Kiriakidis, Applied Surface Science 279 (2013) 142-149

[8.51] O. Lupan, G. Chai, L. Chow, Microelectronic Engineering 85 (2008) 2220-2225.

[8.52] D. Gopalakrishna, K. Vijayalakshmi, C. Ravidhas, Journal of Materials Science: Materials Electronics 24 (2013) 1004-1011.

[8.53] A.D.S. Basu, A Dutta, Materials Chemistry and Physics 47 (1997) 93-96.

[8.54] G.K. Mani, J.B.B. Rayappan, Applied Surface Science 311 (2014) 405-412.

[8.55] A.S. Bolokang, F.R. Cummings, B.P. Dhonge, H.M.I. Abdallah, T. Moyo, H.C. Swart, C.J. Arendse, T.F.G. Muller, D.E. Motaung, Applied Surface Science 331 (2015) 362-372.

CHAPTER NINE

Structure-property relationship of the ball-milled and nitrided Mg-Sn-TiO$_2$ composite

ABSTRACT

Nitridation of the milled Mg-Sn-TiO$_2$ at 650 °C has crystallized into (Mg-Sn-Ti)ON powder. Raman peaks of the 30 h milled powder appears at 142, 196, 396, 514 and 634 cm^{-1}. Raman peaks for the 30 h-nitrided samples appear at 153, 229, 324, 543, and 707 cm^{-1}. This phase is attributed to (Mg,Ti)ON solid solution phase. Raman peaks of (Sn,Mg,Ti)ON are evident at 204, 253, 279, 325, 351, 397, 446, 516, 605, 640 and 788 cm^{-1}. The peak at 279 cm^{-1} belongs to MgON in addition to 446 and 640 cm^{-1}.

9.1 INTRODUCTION

Ball milling (BM) triggers the phase transformation in powder mixtures such as carbides **[9.1-9.3],** solid solutions and new metastable phases after annealing **[9.4]**. However, the reduction of TiO_2 by Mg and Al by BM was reported to be unfeasible but feasible when milled powders is annealed yielding $MgAl_2O_4$ with some traces of MgO and Al_2O_3 **[9.5]**. On the other hand, the unmilled Mg-Al-TiO_2 powders showed no phase transformation when heated to about 500 °C, but structural change has occurred on mechanically milled powders around 390 °C as proven by the complete disappearance of TiO_2 due to the reduction process **[9.5]**. The Mg-based metastable cubic spinel Mg_2TiO_4 powder is used as a heat resistor, dielectric for microwave technology, capacitor for temperature compensation and refractory material **[9.6]**. Yang and Shen **[9.7]** reported the nanosized spinel particles precipitated on MgO after annealing at 900 °C for specific time period**.** It has been reported that Mg was incorporated into the solid solution $Zn_2(Ti,Sn)O_4$ which led to the formation of the spinel-type solid solution $(Zn_{0.95},Mg_{0.05})_2(Ti_{0.88},Sn_{0.12})O_4$ **[9.8].** Additionally, tin (Sn)-based spinel composites such as Co_2SnO_4 powders are successfully produced by the sol–gel method followed by calcining at 900 and 1500 °C for 1 h. This spinel forms slightly above 900 °C when SnO_2 and CoO reacts **[10.9]**. Characterization of Sn-doped spinel ferrite using x-ray diffraction (XRD) revealed the co-existence of cubic (*Fd-3m*) spinel and trigonal–hexagonal (*R-3c*) structure **[9.10]**. Solid-state reaction is a capable process for synthesis of spinel ceramic powders. In the synthesis of $Ni_{0.6}Mn_{2.4-x}Sn_xO_4$ the calcination temperature, and the lattice

parameter increases with increasing of Sn content **[9.11]**. The spinel materials have expanded to nitrides with smaller lattice parameter when compared to oxide materials. Oxynitride materials have attracted a lot of attention from researchers. The titanium oxynitride powder was formed by BM and annealing in air **[9.12]**. In addition, titanium-tin oxynitride was synthesized after BM followed by annealing in air **[9.13]**. A cubic spinel structure has recently been shown to exist in several chemical structural forms such as Si_3N_4 **[9.14].** For spinel materials, cubic gallium oxide–nitride (Ga-O–N) thin film exists with spinel structure **[9.15].** It can be synthesized using a solvothermal processing route and stabilize up to temperatures of 500 °C in both oxidative and reductive atmospheres due to the high disorder in nitrogen and oxygen at anion sites **[9.16]**. The Aluminium oxynitride (AlON) ceramic with good high temperature properties, thermal shock and oxidative resistance and chemical inertness can be prepared by combustion synthesis using Al and Al_2O_3 under high nitrogen pressure **[9.17].** Moreover, the sintered Mg-doped (AlMg)ON ceramic show good mechanical properties **[9.18]**. In the present work, an investigation of ball-milled Mg-Sn-TiO_2 followed by nitridation is presented.

9.2. EXPERIMENTAL WORK

Magnesium (Mg), tin (Sn) and Titanium dioxide (TiO_2) were ball milled for 30 h and annealed at 650 ºC in a tube under nitrogen (N_2) flow for two hours. The powder morphology was studied using a LEO 1525 field-emission scanning electron microscope (FE-SEM) coupled with a Robinson Backscatter Electron

Detector (RBSD) and an Oxford Link Pentafet energy dispersive x-ray spectroscopy (EDS) detector. Electron micrographs and selected area diffraction patterns (SAED) were collected with an FEI Tecnai G^{2}20 FE-TEM. Phase evolution was traced with a PANalytical X'pert PRO PW 3040/60 X-ray diffraction (XRD) machine fitted with a Cu K$_\alpha$ radiation source. Optical properties were measured using a Jobin-Yvon NanoLog photoluminescence (PL) spectrometer. Raman spectra were collected using a Horiba Jobin-Yvon HR800 Raman microscopy equipped with an Olympus BX-41 microscope attachment. An Ar+ laser (514.5 nm) with energy setting 1.2 mW from a Coherent Innova Model 308 was used as an excitation source. The topography of Mg-TiO$_2$ powders was analyzed using atomic force microscopy (AFM, Veeco, and Digital Instruments).
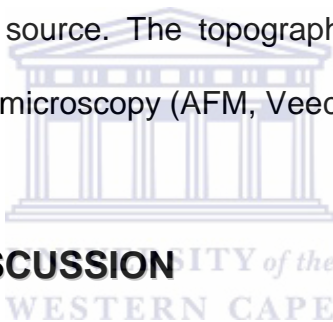
9.3. RESULTS AND DISCUSSION

The TGA results of the 30 h milled Mg-TiO$_2$ and Mg-Sn-TiO$_2$ powders under N$_2$ are shown in **Fig. 9.1** for comparison. The analysis shows the mass loss value of 9.81 mg for Mg-Sn-TiO$_2$ and 21.116 mg Mg-TiO$_2$ in N$_2$ after reaching 1000 °C. At 650 °C, it is clear that the samples are still gaining mass. It is logical to conclude that phases that will be induced at 650 °C might be intermediate and metastable in nature.
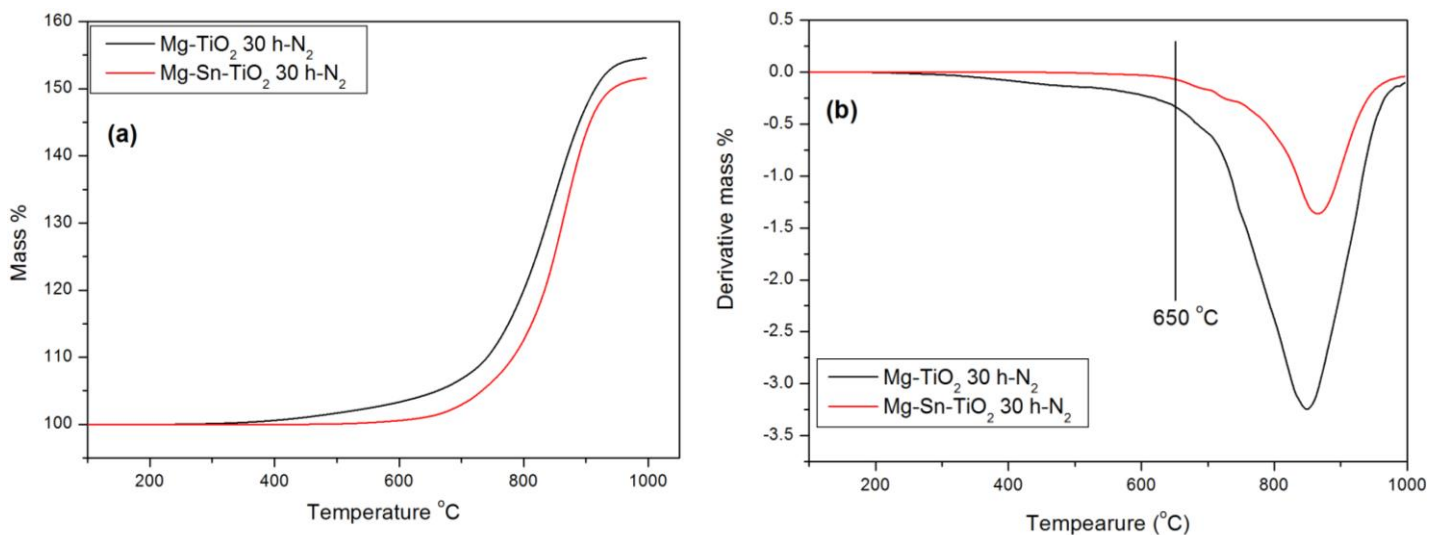
Fig. 9.1: TGA curve of the 60 h milled Mg-Sn-TiO$_2$ powder.

Fig. 9.2a and shows the XRD pattern of the 30h-milled Mg-Sn-TiO$_2$ and nitrided Mg-Sn-TiO$_2$ powder at 650 °C, respectively. XRD patterns of the milled Mg-Sn-TiO$_2$ powder shows that there is no phase transformation that has occurred since the XRD peaks of elemental Mg, Sn, and TiO$_2$ were retained. **Fig. 9.2b** shows the XRD pattern of the 30 h-milled and nitrided Mg-Sn-TiO$_2$ powder. Elemental Mg and TiO$_2$ phases are attributed to their corresponding solid solutions, since pure Mg could have formed Mg$_3$N$_2$ phase after nitridation **[9.19].** Crystallization of FCC (Mg-Sn-Ti)ON yields lattice parameters a= 4.212 Å; *Fm-3m # 225* space group and number. Rhombohedral MgTiO$_3$-types has emerged with a=5.055 Å; c=13.899 Å lattice parameter. The space group and number of the rhombohedral are *R-3 # 148,* respectively. The formation of FCC and rhombohedral phases confirm the partial reduction of TiO$_2$ by Mg during nitridation. Normal MgTiO$_3$ has a rhombhohedral crystal structure with lattice

220

parameters a=b= 5.056 Å; c = 13.900 Å **[9.20]**. Silva et al. **[9.21]** reported the crystallization of spinel from 600 ºC and appearance of $MgTiO_3$ above 800 ºC. Hence, due to BM effect, Sn doping and nitridation, rhombohedral and FCC structures were obtained after annealing at 650 °C in N_2. The reported free energy formation ΔG_f of MgO, $MgTiO_3$ and Mg_2TiO_4 are -504.255 to -442.919, -1308.779 to -1158.464 and -1815.309 to -1610.318, respectively **[9.22]**. Accordingly, spinel formation is more favourable than MgO and $MgTiO_3$-type structures. It thus implies that the presence of N_2 inhibits the spinel formation during annealing in the milled Mg-Sn-TiO_2 powder. Traces of tetragonal tin solid solution peaks and minor SnO_2 peaks were detected.
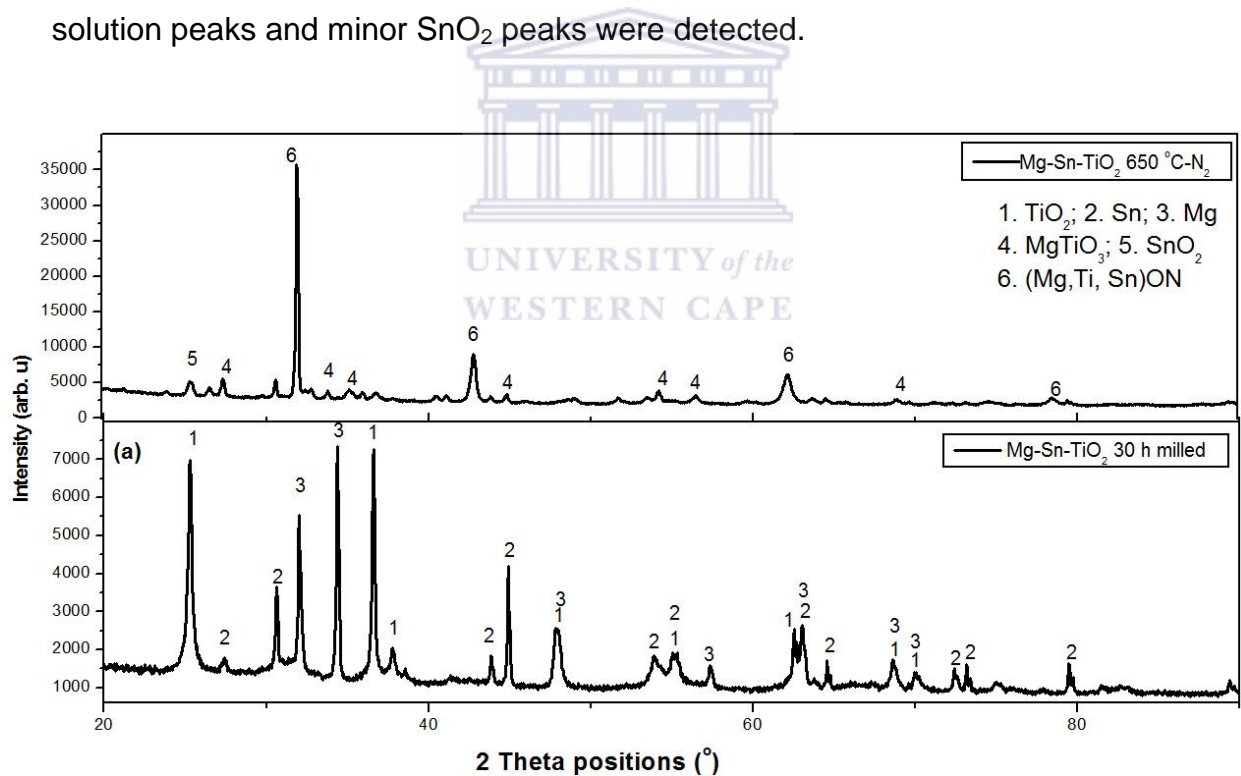

Fig. 9.2: XRD pattern of the (a) 30 h-milled Mg-TiO_2 (b) Mg-Sn-TiO_2 powders.

Fig. 9.3 shows the Raman spectra of the 30 h milled and nitrided Mg-Sn-TiO_2 powders. The Raman vibration modes of the 30 h-milled Mg-Sn-TiO_2 powder appear at 143, 170, 196, 396, 516 and 642 cm^{-1}. These Raman peaks exhibit Raman active modes ($1A_{1g}$ at 516 cm^{-1}, $2B_{1g}$ at 396 and 516 cm^{-1}, $3E_g$ at 143, 196 and 642 cm^{-1}) [9.11,9.23]. The bends corresponding to $MgTiO_3$-type phase in the Raman spectra of nitrided sample occur at: 280 cm^{-1} (E_g), 352 cm-1 (E_g), 398 cm^{-1} (A_g), 638 cm^{-1} (E_g), 787 cm^{-1} (A_g) [9.25]. Moreover, it has been reported that the Raman modes that originate from spinel Mg_2TiO_4 have similar positions as the modes of $MgTiO_3$ with a slight overlapping [9.25].
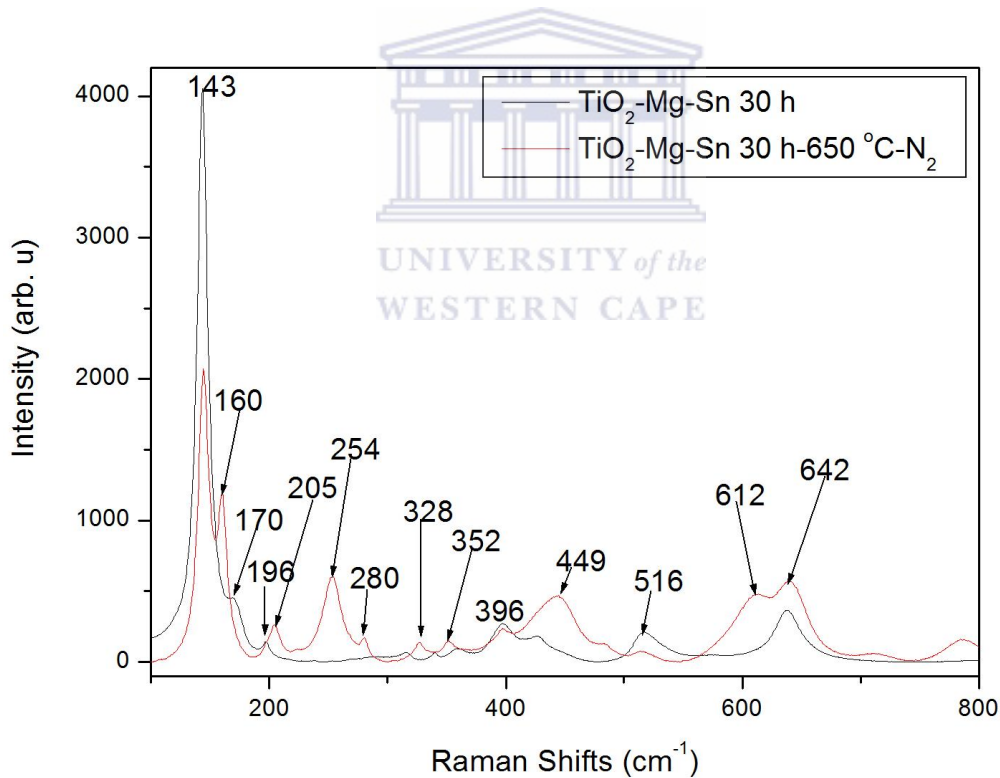

Fig. 9.3: Raman spectra of milled and milled-nitrided Mg-Sn-TiO_2 powder

Fig. 9.4 shows the FTIR spectra of the 30 h-milled and nitrided Mg-Sn-TiO$_2$ powders recorded in the range of 1000-4000 cm^{-1}. The absorption band appears at 1201, 1384, 1963, 2008, 2056, 2331 and 2981 cm^{-1}. The stretching vibrations of N–O in (Mg-Sn-Ti)ON occurred at 1646, 2161 and 2320 cm^{-1} on nitrided Mg-Sn-TiO$_2$ powder **[9.26]**.
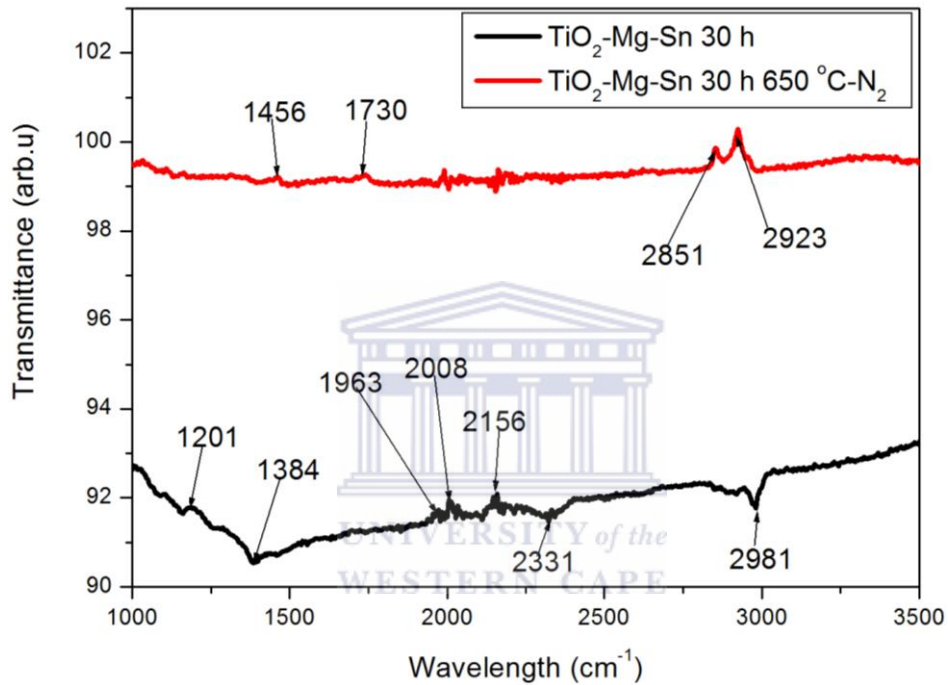

Fig. 9.4: FT-IR spectra of the Mg-TiO$_2$ 30 h milled powder annealed in N$_2$

Figs.9.5 a-c show the SEM images of pure TiO$_2$, Mg and Sn powders, respectively. TiO$_2$ are spherical as shown in **Fig. 9.5a,** while Mg particles display the irregular shapes in **Fig. 9.5b.** The Sn particles appear as elongated tubes with sharp edges in Fig. 10.5c.
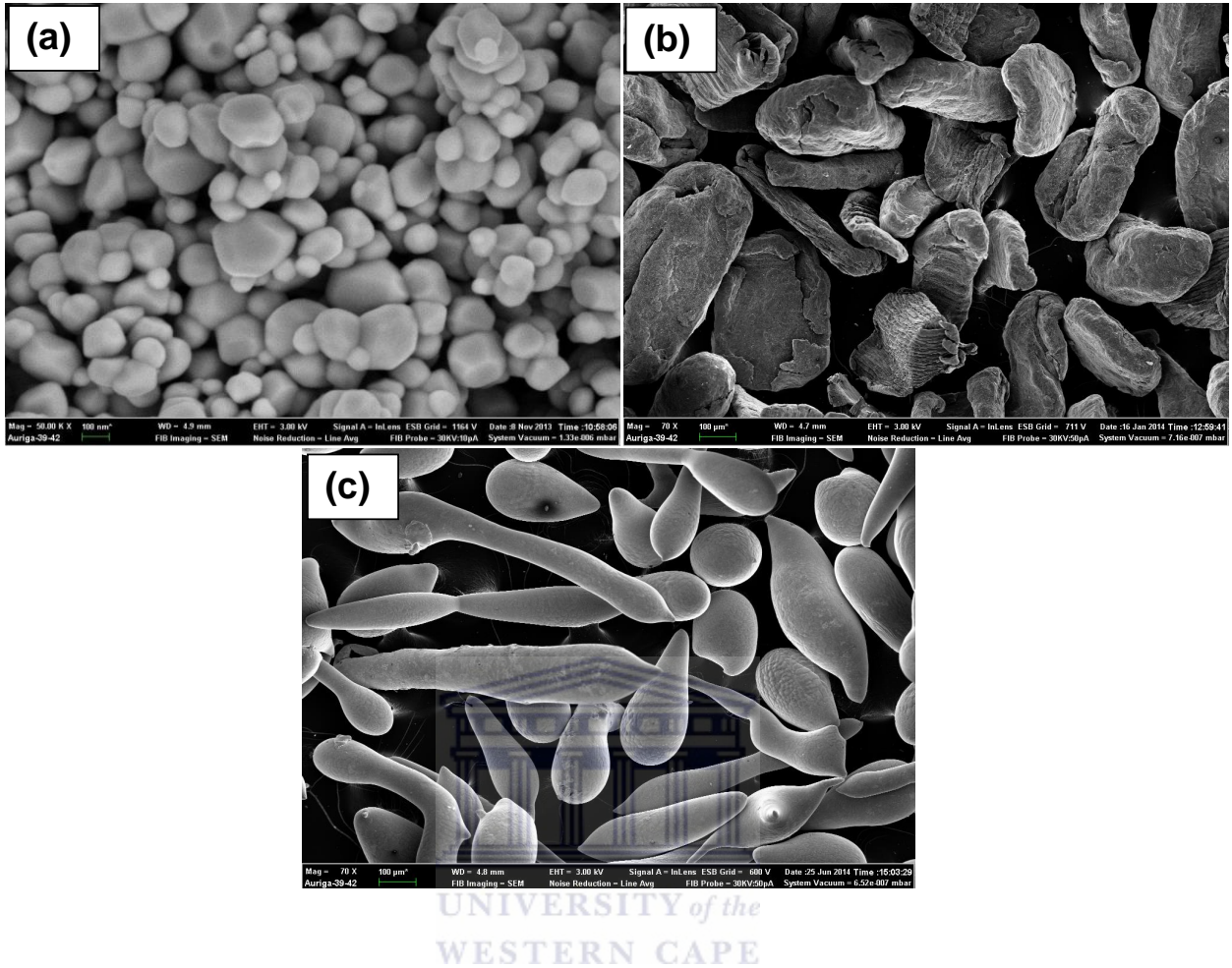
Fig. 9.5a-c: SEM images of (a) TiO_2, (b) Mg and (c) Sn powders.

Figs.9.6 a-b show the SEM images of the, 30 h-milled Mg-Sn-TiO_2 and nitrided 30 h-milled Mg-Sn-TiO_2 after nitridation at 650 °C. **Fig. 9.6a** displays the morphology with fine particle agglomerates induced by milling. In **Fig. 9.9b** the 30 h-milled nitrided Mg-Sn-TiO_2 powder is shown. The SEM image reveals the particles as interconnected and welded, thus forming large and small pores. These pores are irregular in shape and comprised of sizes range from 200 μm (small pores) to approximately 800 μm (large pores), respectively. The

224

compositional analysis in **Fig. 9.7** displays the EDS of elements Sn, Ti, O, Mg, N with compositions 39.1, 30.8, 19.7, 9.1, and 1.3 weight percentages, respectively.
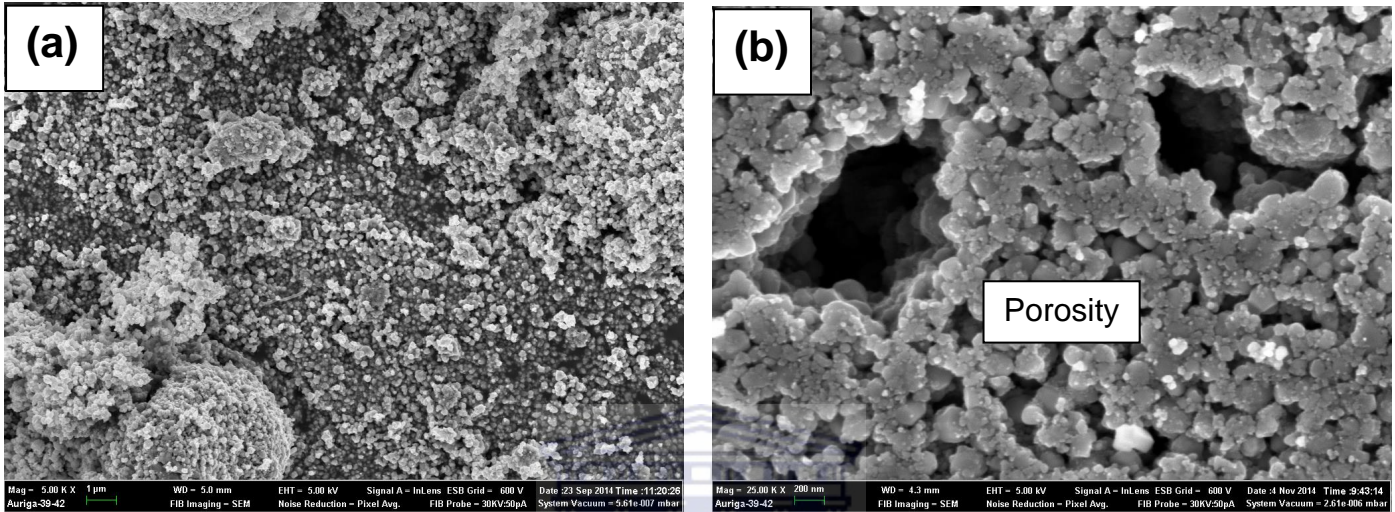

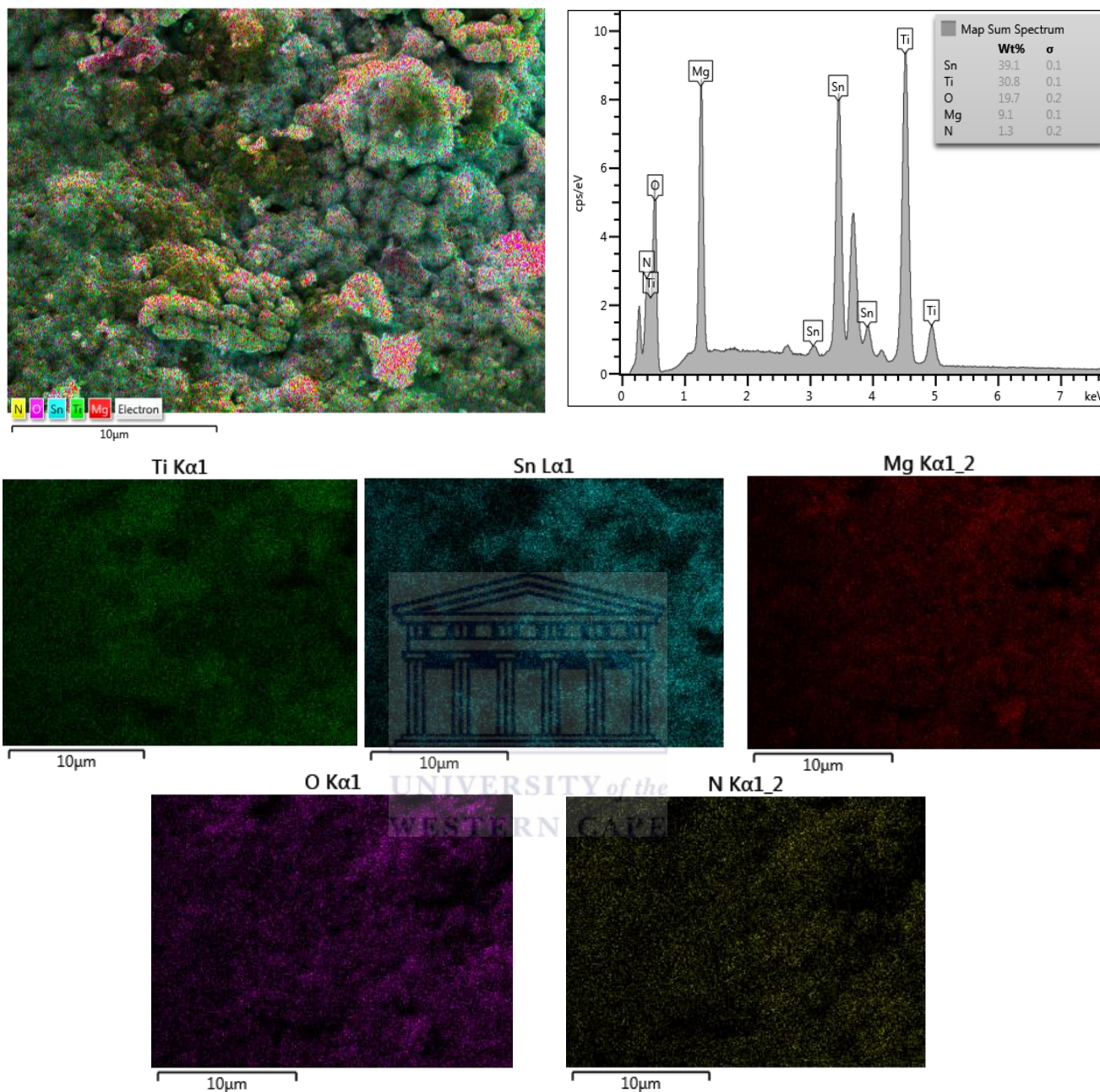**Fig. 9.6:** SEM images of (a) 30 h-milled Mg-Sn-TiO$_2$ and (b) nitrided Mg-Sn-TiO$_2$ powders at 650 °C.

Fig. 9.7: EDS images and spectra of Mg-Sn-TiO$_2$ sample annealed in air

Fig. 9.8 shows AFM micrographs of the mixture and 30h-milled Mg-Sn-TiO$_2$ and nitrided Mg-Sn-TiO$_2$, respectively, displaying surface topography of powders and their corresponding 3D AFM images. AFM images confirm the existence of

different particle shapes and orientations on milled and nitrided Mg-Sn-TiO$_2$ powders. Images clearly show the existence of ultrafine and large powder particles for both samples while 3D images illustrate the grains of nitrided Mg-Sn-TiO$_2$ powder to be more irregular when compared to those of milled samples.
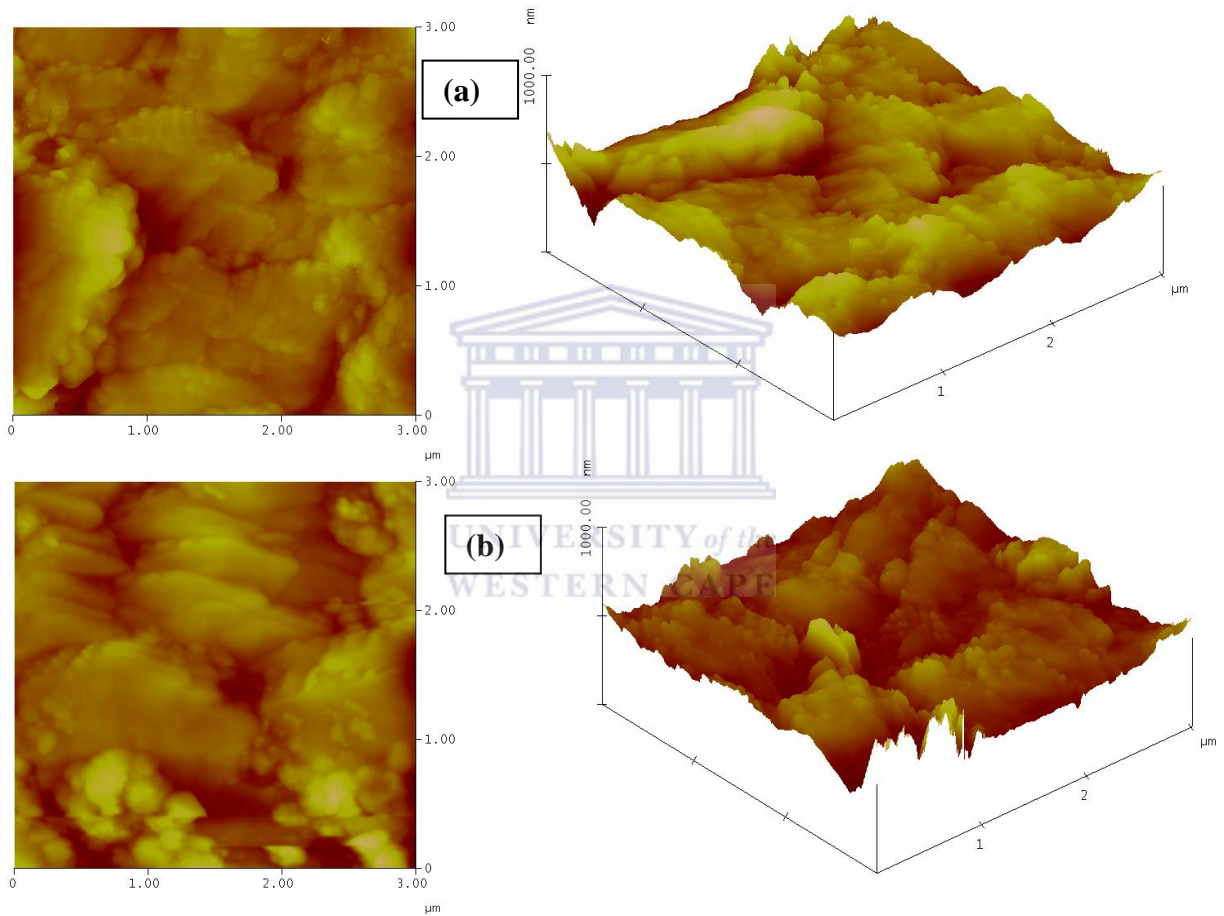

Fig. 9.8:   AFM micrographs of the nitrided 30 h milled (a) Mg-TiO$_2$) and (b) Mg-Sn-TiO$_2$ powders.

9.4. CONCLUSION

Nitridation of the ball-milled Mg-Sn-TiO$_2$ has crystallized into Mg-Sn-Ti)O$_x$N$_y$ powder. After nitridation, Mg-Sn-TiO$_2$ was crystallized into a rhombohedral MgTiO$_3$-type phase with lattice parameters a=5.055 Å; c=13.899 Å; space group and number R-3 # 148. Raman peaks for the nitrided Mg-Sn-TiO$_2$ sample appear at 143, 160, 204, 253, 279, 325, 351, 397, 446, 516, 605, 640 and 788 cm^{-1}. The bends corresponding to MgTiO$_3$-type phase in the Raman spectra of nitrided sample occurs at: 280 cm^{-1} (E_g), 352 cm^{-1} (E_g), 398 cm^{-1} (Ag), 638 cm^{-1} (E_g), 787 cm^{-1} (A_g) **[9.25]**. The SEM image of the 30 h-milled nitrided Mg-Sn-TiO$_2$ sample shows powder particles appear as interconnected, welded and grouped, resulting in small to large pores.
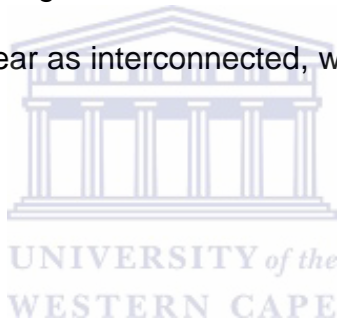
9.6. REFERENCES

[9.1]   S. Bagaswi, Y. Niu, M. Nasir, B. Tian, J. Zhang, Applied Surface Science 264 (2013) 139-147.

[9.2]   G. Halasi, I. Ugrai, F. Solymosi, Journal of Catalysis 281 (2011) 309-317.

[9.3]   B. Choudhury, A. Choudhury, International Nano Letters 3 (2013) 1-8.

[9.4]   X. Pan, X. Ma, Materials Letters 58 (2004) 513-515.

[9.5]   M.O. Lai, L. Lu, B.Y. Chung, Composite Structures 57 (2002) 183-187.

[9.6]   S.Z. Khalajabadi, M.R.A. Kadir, S. Izman, H.R. Bakhsheshi-Rad, S. Farahany, Ceramic International 40 (10) (2014) 16743-16759.

[9.7]   N.J. Welham, Journal of Alloys and Compounds 274 (1998) 260-265.

[9.8]   M.J. Martinez-Lope, M.P. Baura-Pena, M.E. Garcia-Clavel, Thermochimica Acta 194 (1992) 59-65.

[9.9]   M. R. S. Silva, S. C. Souza, I. M. G. Santos, M. R. Cassia-Santos, L. E. B. Soledade, A. G. Souza, S. J. G. Lima, E. Longo, Journal of Thermal Analysis Calorimetry 79 (2005) 421-424.

[9.10] X. Chen, S.S. Mao, Chemical Review 107 (2007) 2891-2959.

[9.11] C. Burda, X. Chen, R. Narayanan, M.A. El-Sayed, Chemical Reviews 105 (2005) 1025-1102.

[9.12] H. Milani Moghaddama, S. Nasirian, Applied Surface Science 317 (2014) 117–124.

[9.13] A. Trinchi, Y.X. Li, W. Wlodarski, S. Kaciulis, L. Pandolfi, S. Viticoli, E. Comini, G. Sberveglieri, Sensors and Actuators B 95 (2003) 145-150.

[9.14] H. Yang, D. Zhang, L. Wang, Sensors and Actuators B 57 (2002) 674-678.

[9.15] S. Zhuiykov, W. Wlodarski, Y. Li, Sensors and Actuators B 77 (2001) 484-490.

[9.16] S. Nasirian, H. Milani Moghaddam, Applied Surface Science 328 (2015) 395-404.

[9.17] K. Dutta, et al., A highly sensitive BTX sensor based on electrochemically derived wall connected TiO_2 nanotubes, Appl. Surf. Sci. (2015), http://dx.doi.org/10.1016/j.apsusc.2015.05.077.

[9.19] Y. Liu, T. Hang, Y. Xie, Z. Bao, J. Song, H. Zhang, Sensors and Actuators B 160 (2011) 266-270.

[9.20] D. Cullity, Elements of X-ray Diffraction, Addison-Wesley, Reading (MA), 1956, p. 363.

[9.21] E.A.V. Ferri, J.C. Sczancoskia, L.S. Cavalcantea, E.C. Paris, J.W.M. Espinos, A.T. de Figueiredo, P.S. Pizani, V.R. Mastelaro, J.A. Varela, E. Longo, Materials Chemical Physics 117 (2009) 192-198.

[9.22] H.-K. Shin, H Shin, H.S. Jung, S.-Y. Cho, J-R Kim, K.S. Hong, Materials Research Bulletin 41 (2006) 1206-1214.

[23] S. Onder, F.N. Kok, K. Kazmanli, M. Urgen, Materials Science Engineering C 33 (2013) 4337-4342.

[9.24] K. Huo, X. Zhang, J. Fu, G. Qian, Y. Xin, B. Zhu, H. Ni, P.K. Chu, J. Nanoscience and Nanotechnology 9 (2009) 3341-9.

[9.25] A. Hodroj, O. Chaix-Pluchery, P. Steyer, J.F. Pierson, Surface & Coatings Technology 205 (2011) 4547-4553.

[9.26] T.S. Kumar, R.K. Bhuyan, D. Pamu, Applied Surface Science 264 (2013) 184-190.

[9.27] M. Egashira, Y. Shimizu, Y. Takao, S. Sako, Sensors Actuators B 35 (1996) 62-67.

[9.28] J.-M. Wu, H.C. Shih, W.-T. Wu, Y.-K. Tseng, I.-C. Chen, Journal of Crystal Growth 281 (2005) 384-390.

[9.29] Y. Lei, L.D. Zhang, G.W. Meng, G.H. Li, X.Y. Zhang, C.H. Liang, W. Chen, S.X. Wang, Applied Physics Letters 78 (2001) 1125-1127.

[9.30] X. Yang, C. Li, B.Yang, W. Wang, Y. Qiam, Chemical Physics Letters 383 (2004) 502-506.

[9.31] M. Drygas, C. Czosnek, R.T. Paine, J.F. Janik, Chemical Materials 18 (2006) 3122-3129.

[9.32] A. Rizzo, M.A. Signore, L. Mirenghi, T.D. Luccio, Thin Solid Films 517 (2009) 5956-5964.

[9.33] M.H. Chan, F.H. Lu, Thin Solid Films 517 (2009) 5006-5009.

[9.34] X. Song, D. Gopireddy, C.G. Takoudis, Thin Solid Films 516 (2008) 6330-6335.

[9.35] X.Y. Du, Y. Wang, Y.Y. Mu, L.L. Gui, P. Wang, Y.Q. Tang, Materials 14 (2002) 3953-3957.

[9.36] J. Yang, H. Bai, X. Tan, J. Lian, Applied Surface Science 253 (2006) 1988-1994.

[9.37] X. Pan, X. Ma, Journal of Solid State Chemistry 177 (2004) 4098-4103

[9.38] N.C. Saha, H.G. Tompkins, Journal of Applied Physics 72 (1992) 3072-3079.

[9.39] M. Braic, M. Balaceanu, A. Vladescu, A. Kiss, V. Braic, G. Epurescu, Applied Surface Science 253 (2007) 8210-8214.

[9.40] M. Zukalova, J. Prochazka, Z. Bastl, J. Duchoslav, L. Rubacek, D. Havlicek, L. Kavan, Chemical Materials 22 (2010) 4045-4055.

[9.41] M.R. Mohammadia, D.J. Fray, Sensors Actuators B 150 (2010) 631-640.

[9.42] X. Zhang, X.M. Li, T.L. Chen, J.M. Bian, C.Y. Zhang, Thin Solid Films 492 (2005) 248-252.

[9.43] D.E. Motaung, P.R. Makgwane, S.S. Ray, Materials Letters 139 (2015) 475-479.

[9.44] Y. Liu, H. Zhang, Z. Zhang, Y. Xie, E. Xie, Applied Surface Science 257 (2010) 1236-1238.

[9.45] A.A. Tomchenko, G.P. Harmer, B.T. Marquis, J.W. Allen, Sensors Actuators B 93 (2003) 126-134.

[9.46] Y. Mao, S.I. Ma, X. Li, C. Wang, F. Li, Xiaohong Yang, Jing Zhu, Lin Ma, Applied Surface Science 298 (2014) 109-115.

[9.47] J.-C. Chou, H-Y Yang, C-W Chen, Microelectronics Reliability, 50 (2010) 753-756.

[9.48] T.T. Trinha, N.H. Tu, H.H. Le, K.Y. Ryu, K.B. Le, K. Pillai, J. Yi, Sensors and Actuators B 152 (2011) 73–81.

[9.49] B. Saruhan, A. Yüce, Y. Gönüllü, K. Kelm, Sensors and Actuators B 187 (2013) 586– 597.

[9.50] Y. Tian, J.C. Li, H. Xiong, J.N. Dai, Applied Surface Science 258 (2012) 8431-8438.

[9.51] S.H. Wei, M.H. Zhou, W.P. Du, Sensors Actuators B 160 (2011) 753-759.

[9.52] D.E. Motaung, G.H. Mhlongo, I. Kortidis, S.S. Nkosi, G.F. Malgas, B.W. Mwakikunga, S.S. Ray, G. Kiriakidis, Appl. Surf. Sci. 279 (2013) 142-149

[9.53] O. Lupan, G. Chai, L. Chow, Microelectronic Engineering 85 (2008) 2220-2225.

[9.54] D. Gopalakrishna, K. Vijayalakshmi, C. Ravidhas, Journal of Materials Science: Materials Electronics 24 (2013) 1004-1011.

[9.55] A.D.S. Basu, A Dutta, Materials Chemistry and Physics 47 (1997) 93-96.

[9.56] G.K. Mani, J.B.B. Rayappan, Applied Surface Science 311 (2014) 405-412.

[9.57] A.S. Bolokang, F.R. Cummings, B.P. Dhonge, H.M.I. Abdallah, T. Moyo, H.C. Swart, C.J. Arendse, T.F.G. Muller, D.E. Motaung, Applied Surface Science 331 (2015) 362-372.

SUMMARY

The structural engineering industries, gas sensors and detectors of hazardous gases are crucial due to their enormous diversity of applications such as in environmental quality control, public safety, and automotive applications and for air conditioning systems in aircrafts, spacecrafts, vehicles, and houses. As a result, research in the field of biomaterial, engineering and gas sensing has been at the highlight over the years. Therefore, in this thesis, structural, optical, surface morphology, chemical composition and gas sensing properties of pure titanium, Ti-Sn and titanium mixed metals oxynitrides (Ti-TiO_2, TiO_2, Mg-TiO_2 and Mg-Sn-TiO_2) synthesized using ball milling (BM) and annealing process were studied using XRD, Raman, HR-TEM, SEM, PL, UV-vis, XPS and gas testing station.

In this thesis, we showed that it is feasible to form titanium oxynitride by only annealing the milled pure Ti in air and under nitrogen gas and by mixing pure Ti with Sn and as well as mixing Ti with TiO_2. Therefore, structural properties of ball–milled pure titanium did not show any phase transformation in its hexagonal closed-packed crystal structure, however, only a broadening on the intensity peak heights and slight shifts in XRD intensity peaks were observed, denoting that BM reduces the crystallinity of the nanostructures. Furthermore, when Ti was mixed with pure Sn, HCP and tetragonal (Ti,Sn) oxynitride powders with lattice parameters a=4.985 Å; c=2.962 Å, c/a=0.594 and a=4.582 Å; c=2.953

Å and *c/a*=0.644 were observed, respectively. When, the pure Ti was mixed with TiO$_2$ in order to reduce the TiO$_2$ to TiO$_x$ phase and to titanium oxynitride through milling and annealing in argon and in nitrogen gas, respectively. As a result, nitridation of TiO$_x$ resulted to TiO$_x$N$_y$ phase as confirmed from the XPS analyses. Finally, when the pure TiO$_2$ was mixed with Mg, and milled for 60 h and annealed in nitrogen at 650 °C, no has shown no phase transformation was observed for Mg-TiO$_2$, only a reduction on the crystallite sizes of the powders was noticeable. The milled and nitrided Mg-TiO$_2$ showed two types of FCC phases revealing different lattice parameters. The induced FCC structures are attributed to the non-stoichiometric structure of the TiO$_x$N$_y$ and (Mg$_{1-x}$Ti$_{1-x}$-O$_x$-N$_y$) phases, respectively. Phase transformation was confirmed by the introduction of new Raman vibration modes on annealed samples.
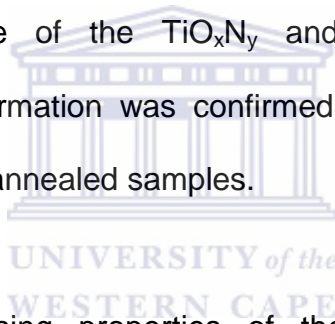
Furthemore, the sensing properties of these milled and oxynitrides structures were carried out at different operating temperatures and at various gas concentrations. The sensing analyses also demonstrated that the sensing response of the TiO$_2$, Mg-TiO$_2$ and Mg-Sn-TiO$_2$ materials improved upon milling. However, the nitrided sensing materials demonstrated low sensing responses compared to the milled samples, due to nitrogen which fills up holes and reduces defects which were promoted for sensing by milling and the presence. More remarkably, the Mg-TiO$_2$ showed improved response compared to other sensing materials. This is due to incorporation of Mg, which might have resulted in a decrease of charge carrier concentration. The Mg-TiO$_2$ sensing materials showed

fast response-recovery time of ~32 s and ~48 s, respectively, as well as high selectivity to NH_3 gas compared to other gases (H_2, and CH_4). In addition, the improved response observed for the milled samples is due to increased surface area and pore diameter, providing more active sites for the target gas and allowing more gas adsorption with an increase in point defects related to oxygen vacancies (V_O), which are the most favorable adsorption sites for oxygen species and thus can enhance the possibility of interaction with gas molecules. A combination of photoluminescence, x-ray photoelectron spectroscopy, vibrating sample magnetometer and sensing analyses demonstrated that a direct relation exists between the magnetization, sensing and the relative occupancy of the V_O present on the surface of TiO_2 nanoparticles. Therefore, based on these finding we conclude that the milling process promotes particle refinement resulting in increased BET surface and partial breaking of Ti–O bonds on the TiO_2 surface layer, which results in the formation of oxygen vacancies in the TiO_2 lattice, therefore anticipating improved sensing response.